Controllable inkjet printing of graphene oxide and hydrophilic nanomaterials

Thomas Alexander Bamford

Doctor of Philosophy

School of Engineering

January 2020

Abstract

Graphene oxide (GO) ink has been widely researched but problems still exist with regards to its printability and conductivity. The following work aims to combat both these issues, leading to the formulation of a glycol-based GO ink with optimised rheology for use with a Dimatix inkjet system. Results show superior print quality and resolution, with films characterised by robust AFM, Raman, XRD, FTIR and optical studies. Through the application of a two- step reduction process, incorporating both chemical and thermal treatments, the conductivity of films are able to exceed 50,000 S/m. This is the highest value reported to date for an inkjet-printed graphene film yet the corresponding sheet resistance (740 Ω/sq) and transmittance (29 %) remain poor compared to indium tin oxide films currently used in optoelectronic devices.

This work also aimed to apply the techniques of printing GO to alternative hydrophilic nanomaterials. The synthesis of cadmium sulphide/DNA nanowires via a wet chemical method allows for the easy formulation of a novel semiconducting ink that is also compatible with an inkjet printing system. The printing of highly resolved cadmium sulphide/DNA droplet arrays on glass is reported with characterisation by fluorescence microscopy, AFM and Raman. The fabrication of conductive nanowire devices is also accomplished by the printing of CdS/DNA features over interdigitated electrodes and sintering of material. Findings show that inkjet printing could be a successful method of processing these semiconducting nanowires towards labelling and gas sensing applications.

Acknowledgements

I'd like to take this opportunity to thank everyone involved at Newcastle University who has made this work possible. A special mention to both my supervisors Dr. John Hedley and Dr. Andrew Pike for their invaluable guidance and supervision throughout the project. I'd also like to acknowledge the researchers on the nanoscience corridor, past and present, for making it an enjoyable environment to work in, particularly the Pike group who I've worked alongside over the years: Sam Lunn, Rachel Little, Colette Whitfield, Bee-Min Goh and Liz Hierons. A thank you to the School of Engineering for the funding goes without saying.

I also wish to thank those outside from work. There's too many family members and friends to name individually but you know who you are. I must reserve a few words for my Mum and Dad though. The amount of support and security you two have given me, both emotionally and financially, has been above and beyond. Not just over the course of these four years but throughout my whole life and education leading up to this point. I couldn't have done this without you.

A notable mention to the cat who has kept me company throughout the vast majority of the writing.

Last but not least, before she thinks I've forgotten her, I need to pay tribute to Fiona. I know I can be difficult at times, especially over the last year, but you've always been there and I'm so grateful. I know you're looking forward to getting your boyfriend back.

Table of contents

Chapter 1. Introduction

1.1 Project motivation

The printed, organic and flexible electronics market is a relatively new and rapidly expanding technology. IDTechEx currently values this market at nearly $30 billion with this figure expected to rise over the next decade to over $73 billion. At present, the conductive ink market alone stands at over $3 billion.[1] Graphene exhibits high performance in terms of conductivity and this property, as well as its low cost, has led to graphene being identified as a promising material for use in conductive inks.[2–10] However, graphene-based inks are still at an early stage of development meaning that more expensive metal nanoparticle inks still dominate this market.[1,11]

The material also exhibits high transmittance and is being touted as a replacement material for indium tin oxide (ITO) in the fabrication of transparent conductive electrodes.[12–16] This market value is forecast to grow to over $8 billion by 2026, with the increasing demands for films in smartphones, tablets, notebooks, wearable devices and other optoelectronic applications.[17] Yet, problems still persist with the use of graphene for these technologies, with electrodes exhibiting poor conductivity in comparison to ITO.

Meanwhile the global semiconductor sector is experiencing rapid growth in all application markets, with the top 25 chipmakers annually amassing revenue amounting to 74 % of the total $300+ billion industry.[18] Samsung electronics alone generated $60 billion in 2017 from semiconductor sales.[19] This market is expected to reach just short of $500 billion by the end of 2019, with continual innovation within automotive, consumer electronics, mobile, medical and industrial segments.

Cadmium sulphide is a II-VI semiconductor and has been identified as a potential material for use within photovoltaic devices, light emitting diodes and as components in labelling and sensing technologies.[20–26]

1.2 Inkjet printing

Inkjet printing is a promising technique for the fabrication of electronic components from conductive ink.[27–29] It works similarly to a normal computer printer, recreating a digital image by propelling droplets of ink onto a substrate. There are several advantages of utilising inkjet printing compared to other deposition or printing methods. For example, the procedure can be carried out at low temperatures and without the need for vacuum conditions.[2,7] This reduces production costs while also making the process viable for a wide range of substrates, particularly for low-melting point polymer films commonly used for flexible electronics.[7,30–32] Due to the drop-on-

demand nature of inkjet technology, meaning ink is only expelled where required, no masks or stencils on surfaces are needed and this gives greater flexibility with regards to device fabrication.[33,34] Inkjet printing also allows for the noncontact patterning of substrates, avoiding potential damage to fragile surfaces. This is not the case with offset, gravure, flexographic and screen printing which rely on the application of pressure to stamp patterns.[34–37] Crucially, the technology is able to achieve much higher resolution than other deposition techniques, such as airbrushing, dip coating or spin coating, with the volumes of droplets being on the order of picolitres.[27,38–41] Consequently, microscale components with controlled morphology can be routinely manufactured.

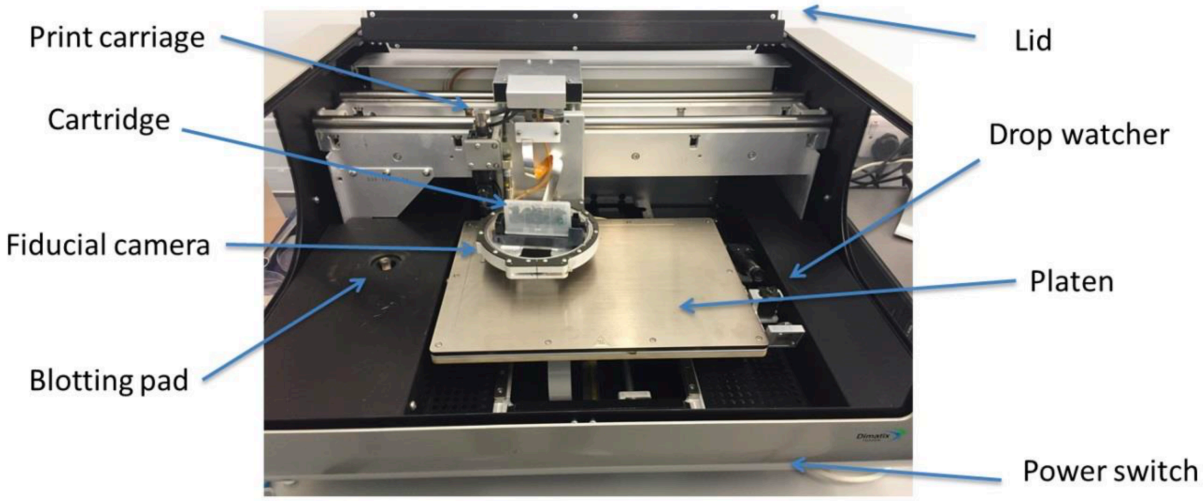

Figure 1.1 Photograph of a Dimatix Materials Printer (DMP) 2800 series, with key features labelled.

One of the inkjet systems available at Newcastle University is a Dimatix Materials Printer (DMP) 2800 series. The ink cartridge is held within a carriage that moves over the substrate as ink is deposited. The substrate is held on the printer's platen that can be heated up to 60 ^{O}C. The Dimatix cartridges each contain 16 nozzles, with commercially-available diameters of either 1 µm or 21.5 µm.[27,42] These cartridges are piezo-driven, meaning material behind nozzles change shape upon application of a voltage in order to eject ink as a result of pressure pulses. The sequence of pulses required to achieve this is known as the jetting waveform and can be altered depending on ink properties, along with other printing parameters such as droplet and printing speeds, through use of the system's Drop Watcher option. This application allows real-time visualisation of droplets being jetted from the nozzle plate prior to printing. The printer also has a built-in fiducial camera, allowing for substrate

and cartridge alignment and for the observation and measurement of printed features.

1.3 Formulating inks for inkjet technology

An ink is typically composed of particulates dispersed within solvent.[2,7,43–46] The sizes of particles have to be carefully controlled in order to prevent clogging of nozzles during printing. In order to avoid this scenario, a general rule is that the lateral sizes of these should not exceed 1/50th of the nozzle diameter.[2,47] In some cases, processing of inks through sonication or centrifugation is required in order to reduce the size of particles and remove larger species. The concentration of material within solvent also has to be carefully tailored in order to obtain a homogenous dispersion. Overloading of inks can result in aggregation and ultimately nozzle blockage. The concentrations of inks viable for printing can vary significantly depending on the nature of the material being printed and its dispersibiltiy within the chosen medium. Stabilisers or binders, usually a resin compound, are often needed for certain materials to enhance the uniformity of dispersions and increase concentrations.[48–51] The rheological properties of inks have to be taken into account in order to achieve high jetting performances. The physical fluid property of a dispersion can be characterised by a dimensionless unit called the Ohnesorge number, relating its viscous, inertial and surface tension forces through Equation 1 below.[2,52]

$$Oh = \frac{\sqrt{We}}{Re} = \frac{\mu}{\sqrt{\rho\sigma L}} \qquad \text{Equation 1}$$

The Reynolds (Re) number is the ratio of inertial to viscous forces while the Weber number (We) number corresponds to a balance between inertial and capillary forces.[53] These parameters can be broken down into distinct viscosity (μ), density (ρ), surface tension (σ) components of the liquid as well as the nozzle diameter (L). In some cases, the reciprocal of the Ohnesorge number is denoted instead (Z, Equation 2).[52–54]

$$Z = \frac{1}{Oh} \qquad \text{Equation 2}$$

It is generally stated that an optimal ink for inkjet technology exhibits a surface tension in the range of 32-42 dynes and a viscosity between 8-12 centipoise.[27,42] Inks with properties outside these boundaries can still be printed but tend to suffer from reduced jetting efficiency. The sizes and concentrations of particulates can favorably alter rheology to some extent, with higher concentrations and sizes increasing both viscosity and surface tension.[55–57] For highly viscous inks, the temperature within the printing cartridge can also be elevated to induce fluid thinning. However, the small diameters of nozzles imposes limits on the sizes particles can take while certain materials cannot be prepared as inks in high loading.[2,58] Thus, the tuning of rheology through the use of an appropriate solvent or combination of suitable solvents is required. Glycol-based liquids are a common choice, with these displaying low surface tensions and high viscosities.[2,30,58–61] The addition of resin or surfactant compounds previously mentioned can also improve fluid physical properties as well as material dispersion.

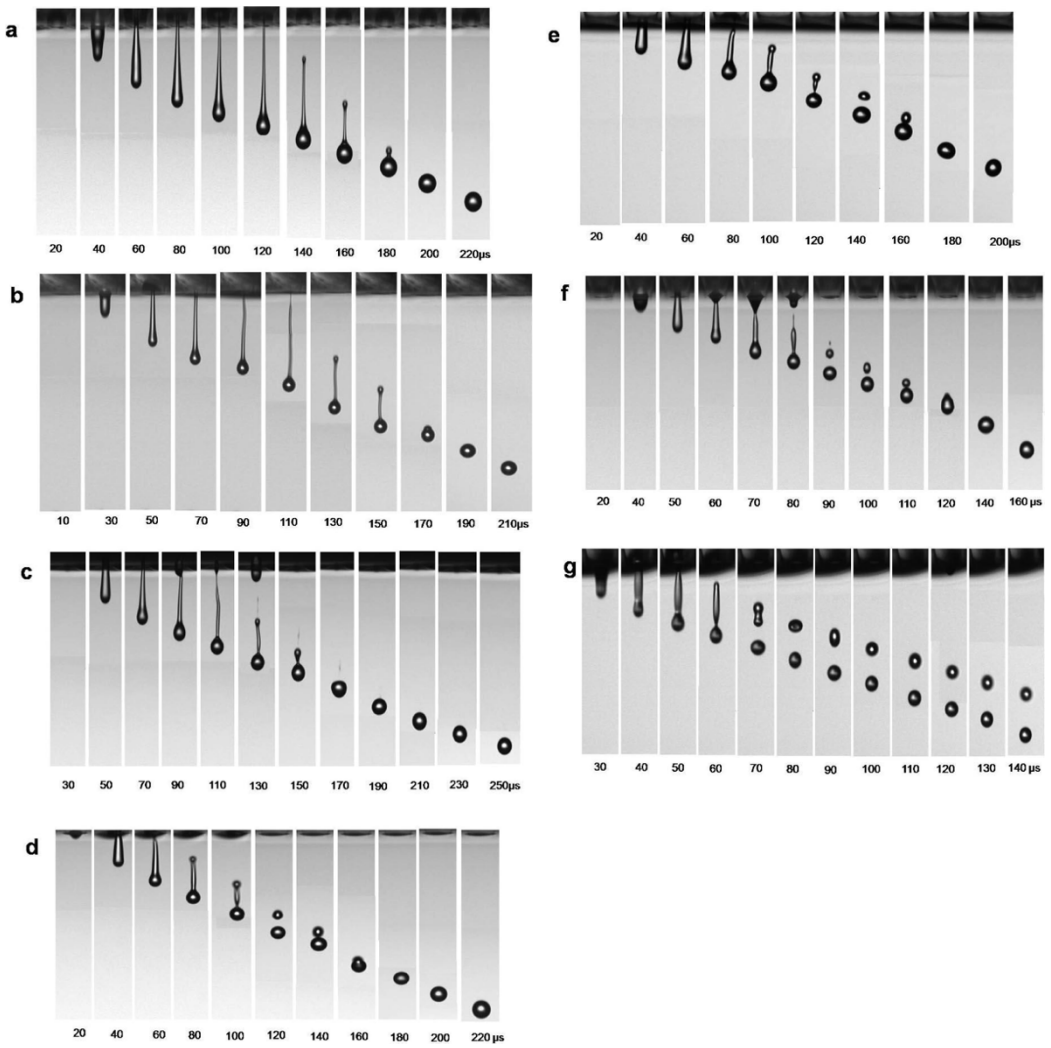

Figure 1.2 Influence of ink rheology on droplet generation for a series of fluids with *Z* numbers 2.17 (a), 3.57 (b), 4.08 (c), 6.57 (d), 7.32 (e), 13.68 (f) and 17.32 (g).[53]

The relationship between an ink's Ohnesorge number and its jetting performance can be observed directly through the characteristics of the droplets produced, see Figure 1.2. A well-tailored ink generates whole, spherical droplets during flight, with unwavering angles and speeds on the order of 7-10 m/s.[27,53] Any deviance from these conditions can result in a loss of film resolution and homogeneity. Inks with too large an Ohnesorge number (small Z, Image a and b) suffer from droplets with large tails. These require extended flight times in order to form droplets before hitting the substrate, resulting in a loss of positional accuracy in drop placement due to the higher cartridge height needed.[53] For fluids with small Ohnesorge numbers (high Z, Image g), droplets fragment, forming satellites that do not recombine. Different Ohnesorge ranges for high-fidelity printing have been reported in literature, with Derby et al. suggesting 0.01-0.1 (Z=1-10), Jang et al. proposing 0.07-0.25 (Z=4-14) and Fromm et al. stating only a highest threshold of 0.5 (Z=2).[52,53,54] Inks lying outside these ranges tend to demand unconventional jetting waveforms and high nozzle voltages, resulting in inconsistency between generated droplets.[62]

1.4 Wetting phenomena

Wetting describes the interaction of a liquid upon contact with a surface and is governed by a balance of the interfacial tension between the surface and liquid (adhesive forces) and the surface tension of the liquid (cohesive forces).[63] The degree of wetting can be characterised through the measurement of the angle formed between a droplet of the liquid and the surface, known as the contact angle (θ_c).[64–66]

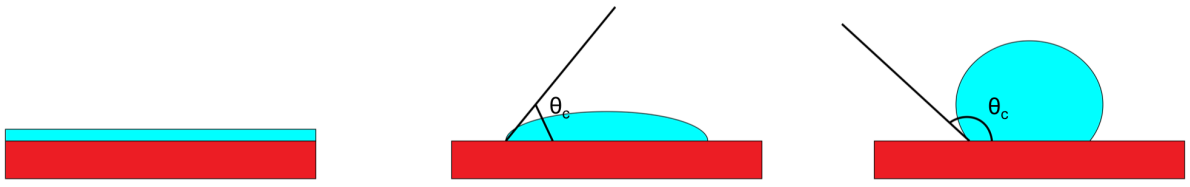

Figure 1.3 Illustrations of the different wetting regimes.

Wetting can be grouped into three main regimes depending on θ_c, depicted above in Figure 1.3. Complete wetting occurs when the droplet spreads fully on the surface, giving a θ_c of 0^O. Partial wetting results in a finite angle, $\theta_c < 90^O$, between liquid and

solid giving a droplet with a spherical-cap shape. Any θ_c above 90 ^{O}C results in a bead-like droplet and is determined to be a non-wetting scenario.[67] In the case of water, any surface that gives complete/partial wetting is said to be hydrophilic while those that don't wet are said to be hydrophobic. Any substrate that results in the θ_c of water exceeding 150 ^{O}C is classed as superhydrophobic.[68]

Alteration of the surface's energy or fluid's surface tension will lead to a change in wetting behavior. An increase in surface energy will give an increase in the adhesive forces, lowering θ_c. Conversely, an increase in liquid surface tension will enhance cohesive forces, raising θ_c.[63] Contact angles are also sensitive to the viscosity of the liquid, the roughness of the surface and temperature. Lower temperatures, higher surface roughness and higher viscosities all lead to a reduction in wetting.[69–71]

Careful control of wetting behavior is crucial for the fabrication of high-quality devices through inkjet printing. Partial wetting of ink on the substrate is most derisible. Total wetting results in a loss of all resolution, with ink unable to be contained and spreading away from where its deposited.[2,72,73] On the other hand, poor wetting of ink results in droplets not adhering to the surface, preventing droplets from overlapping to give a continuous film of material.[74] In order to achieve partial wetting, printing surfaces can be treated beforehand to optimise the balance between surface and ink energies. Low energy surfaces, such as polymer films, can be exposed to plasma treatment to improve ink adhesion while high energy surfaces, such as glass or silicon oxide, can be silanised to prevent uncontrolled wetting.[2] Other factors needed to be considered with respect to wetting include printing density and surface temperature. Higher wetting on the substrate requires a lower density print, with the spacing between adjacent droplets widened to account for larger droplet areas.[74,75] Meanwhile, too low or too high a temperature can both lead to poor quality films, with uncontrolled wetting brought about from prolonged solvent evaporation rates or from low contact angles at high temperature.[74]

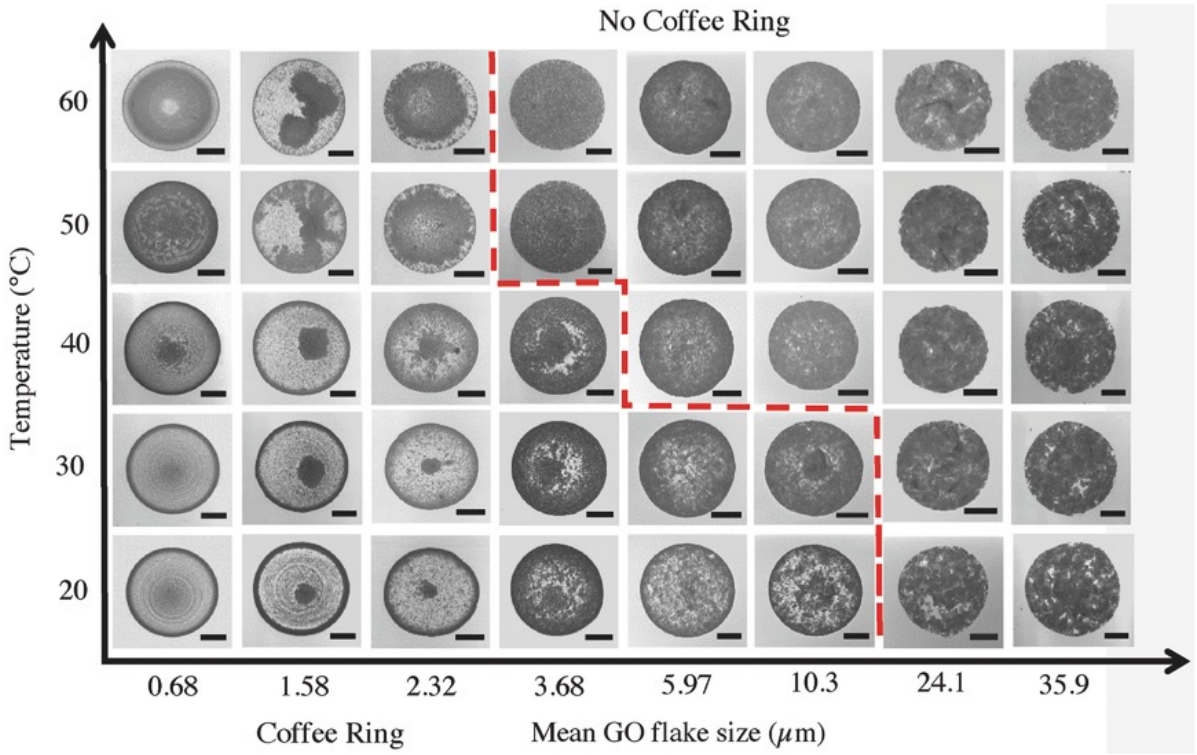

Figure 1.4 Photographs of dried graphene oxide droplets. Droplets containing smaller sized flakes and dried at low temperature tend to exhibit coffee-ring structures. Increase in flake sizes and temperature is found to suppress coffee-ring formation.[55]

The evaporation of a droplet on a surface promotes the movement of particulates within. Local variations in temperature exist throughout a droplet, with greater evaporation rates occurring at its peripheries.[2,68] This induces a capillary flow of material from the bulk of the droplet to its edges as the liquid mass loss is balanced by new liquid flowing outwards. The evaporative flux also produces surface tension gradients within the droplet which can give rise to the Marangoni flow of material.[68,76,77] This involves the movement of particles from regions of low surface tension to high surface tension. The areas of high surface tension are governed by the relative thermal conductivities of liquid and surface but are most commonly located where evaporation rates are greatest, at the contact line. The end result of capillary and Marangoni flow can be a dense ring of material rather than an even film, recognised as the coffee-ring effect (see Figure 1.4).[55,74,78,]

In some reports, coffee-ring formation is desirable for the fabrication of thick, resolved features.[58,78–81] However, it can also drastically reduce the homogeneity of printed films, impacting on mechanical and electrical performance. The phenomenon can be suppressed through tailoring of ink composition, with both higher viscosity and lower surface tension minimising capillary and Marangoni flow.[2] The addition of

chemical species, such as low surface tension surfactants or alcohols, can also alter surface tension gradients to change the direction of Marangoni flow, with material deposited in the centres of droplets.[82,83] The sizes of particles can also be tailored to some extent, with larger sizes better immobilised during droplet evaporation to inhibit the coffee-ring effect.[55,56] Another approach to hamper flows is through the control of the evaporation rate, with increased temperature able to increase the rate of liquid removal relative to the rate of particle movement.[55,74]

1.5 Graphene, graphene oxide and reduced graphene oxide

Graphene was first isolated in 2003 by Geim and Novoselov and consists of a single layer of planar sp^2-hybridised carbon atoms arranged in a hexagonal lattice (Figure 1.5, Image a).[84] This 2D nature bestows a number of interesting and unique properties to the material, including high tensile strength (130 GPa), high Young's modulus (1 TPa), a large specific surface area (2630 m^2/g), high flexibility and high transparency (2.3 % %transmittance at 550 nm). The compound also exhibits high conductivity (theoretically able to reach 10^8 S/m) due to its remarkable electron mobility and intrinsic carrier density (up to 200 000 $cm^2.V.s^{-1}$ and 10^{12} cm^{-2} respectively at room temperature).[5,85–87] This has led to graphene being identified as an ideal candidate for use in a wide range of applications, including transistors, light-emitting diodes, supercapacitors, photovoltaic devices, sensors and flexible components.[10,62,88–91]

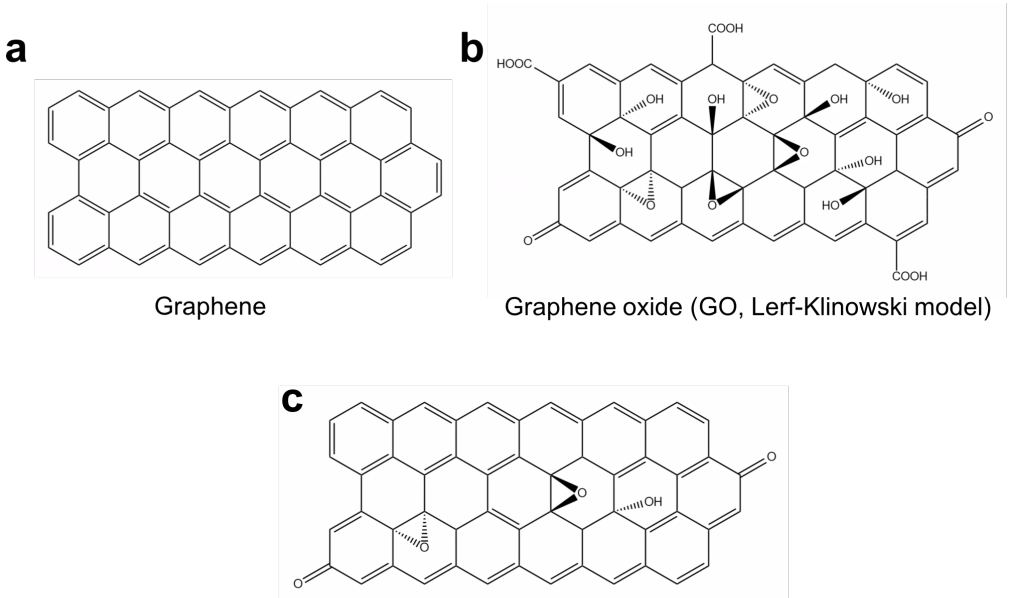

Graphene

Graphene oxide (GO, Lerf-Klinowski model)

Reduced graphene oxide (rGO)

Figure 1.5 Chemical structures of graphene (a), graphene oxide (GO, b) and reduced graphene oxide (rGO, c).

Graphene oxide (GO) is a derivative of graphene, where the carbon lattice is decorated with high densities of oxygen-containing functionalities. The model proposed by Lerf-Klinowski appears to be the most accepted structure for GO, consisting of epoxide and alcohol moieties predominantly located above and below the basal plane and carboxyl and carbonyl species located at sheet edges.[92–94] GO is commonly synthesised by the Hummer's method, using strong reagents such as potassium permanganate to oxidise the carbon structure.[95,96] The defective nature of GO's structure severely hinders its electrical activity, rendering the material insulating and unsuitable for use in most electronic applications.

Material conductivity can be regained through the conversion of GO to reduced graphene oxide (rGO, Image c). Three main methods of GO reduction exist, chemical reduction, thermal reduction and photochemical reduction, but other techniques such as exposure to plasma or irradiation have been proven.[97–101] The type and conditions of the reduction technique determines the extent of GO deoxygenation and resulting electronic properties of the material.

1.6 Challenges faced with the use of graphene inks

Graphene ink is difficult to formulate with the material exhibiting poor dispersibility in most solvents. Harmful solvents, such as NMP, DMF and cyclohexanone, are commonly needed along with binders, such as ethyl cellulose, to prevent material agglomeration.[49–51,102] These binders often need to be removed after printing, generally involving high-temperature annealing which can impair graphene quality. The production of graphene for use in inks is also challenging, typically achieved via the liquid-phase exfoliation of 3D graphite.[2,103] This process involves harsh, extended sonication which can damage the material and yield platelets with a range of layer numbers.

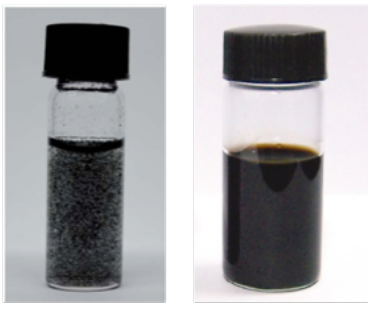

Figure 1.6 Dispersions of graphene and GO in water. The GO sample has a high concentration of 9 mg/mL, with the picture taken several months after preparation.[7,104]

Relative to graphene, the formulation of GO inks is far simpler. Due to the presence of hydrophilic functional groups on its carbon lattice, GO is readily dispersible and exfoliated into single-layer species in water (Figure 1.6).[4,105,106] The use of aqueous inks is an attractive prospect due to their green nature, yet problems still persist with their printability. The rheological properties of water, with its high surface tension and low viscosity, is not suited for inkjet technology.[27,53] Inks tend to exhibit poor jetting performance whilst material immobilisation on the surface is difficult to achieve, with platelets experiencing harsh capillary flows.[7,62,72,88] The end result is a printed feature with reduced resolution and homogeneity. These issues can be pacified through the addition of more viscous, lower surface tension solvents within inks, such as glycols.[10,30,59,60] However, this approach is restricted by the temperatures applied to the substrates during printing (typically below 60 ^{O}C), with too much co-solvent prolonging ink drying times.[27]

The other main challenge with using GO ink is the need for a highly efficient reduction technique after printing to attain conductivities comparable to pristine graphene. The reparation of the graphene lattice is difficult to achieve, with temperatures exceeding 1800 ^{O}C required for the complete removal of defects.[107] GO films are commonly printed on flexible polymer substrates that are not compatible with high temperature annealing processes.[7,30–32] Chemical and low temperature annealing processes are usually chosen in the production of rGO, yielding conductive components with poor sheet resistances compared to those of graphene.[100,101,108–110]

A common issue of using both graphene and GO inks is the requirement of platelets with small lateral dimensions, often ranging from a few hundred nanometers to several micrometers.[2,7,88,102] This is necessary for inks to be jetted through inkjet nozzles without causing blockage but hinders charge transport through the material.[56,72]

1.7 Feasibility of graphene for transparent conductive electrodes

Transparent conductive electrodes (TCEs) are essential components within optoelectronic devices, such as solar cells, light emitting diodes, touch screens and liquid crystal displays.[111–113] It is vital that films for these applications exhibit high transmittance and low sheet resistance. Indium tin oxide (ITO) currently dominates the market, with the material exhibiting transmittances greater than 80 % and sheet resistances below 40 Ω/sq.[114] However, the fabrication of ITO is expensive, with raw materials in short supply and vapour deposition processes requiring high

temperature.[115] The material also displays poor mechanical flexibility, making it impracticable for use in emerging foldable, stretchable and wearable devices, and poor chemical resistance, impacting device durability.[116]

Alternative materials have already been explored in the search for a replacement to ITO. Similar conducting oxides, based on tin, indium, zinc and cadmium oxide, have been widely researched with and shown to exhibit comparable conductive and optical properties to ITO in some certain cases.[117–120] However, these films are still brittle and require the same high energy processes for fabrication. TCEs composed of metal nanowires, predominantly silver and copper, and conducting polymer networks have also demonstrated high transparencies and low resistivity but with enhanced flexibility.[121–124] Yet, metal nanowires are fragile and easily damaged by moisture or external impact while their adhesion to plastic substrates is poor. Meanwhile, the sheet resistances of polymer devices are typically higher than ITO and unstable at high temperatures.

Carbon nanotubes have also been highlighted as a potential candidate for TCEs, with films exhibiting excellent mechanical properties and high flexibility compared to ITO.[125–128] However, the sheet resistances of these examples are still high (exceeding 10^2 Ω/sq), affecting carrier motilities and shortening the lifetime of devices.

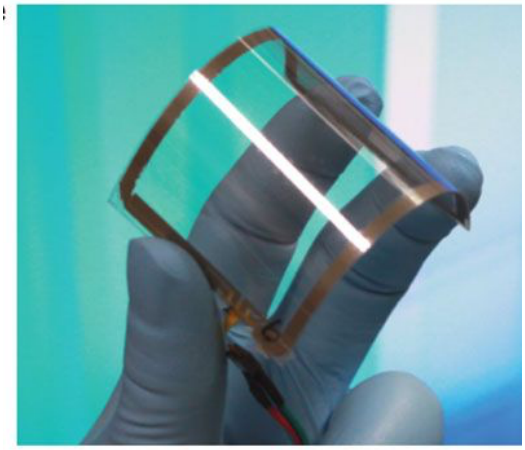

Figure 1.7 An assembled graphene/PET touch panel demonstrating high flexibility.[12]

Due to its low sheet resistance (~30 Ω/sq) and high transmittance (97.7 % for single layer), graphene is also a viable replacement to ITO in TCEs.[12,129] It is also highly flexible and can offer superior chemical and mechanical stability (Figure 1.7). Importantly, graphene-based materials can be dispersed in solution thus offering low-cost routes of TCE production, such as spin coating, roll-to-roll processing and

printing.[16,109,130] Despite these advantages, the sheet resistances of graphene devices (both CVD grown and rGO) tend to be inferior to those currently on the market, often lying between 10^2-10^3 Ω/sq and sometimes higher.[131] The material has been incorporated with metals, polymers and carbon nanotubes to form hybrids with enhanced conductivities.[132–135] Notable success has been achieved with graphene and metal hybrids, with transmittance and sheet resistance properties that meet the requirements for TCEs.[136–138]

1.8 Morphology characterisation of graphene materials

Atomic force microscopy (AFM) can be used to measure the lateral sizes and layer number of graphene features, such as individual platelets within dispersions (Figure 1.8) or films deposited on a substrate.[139–141]

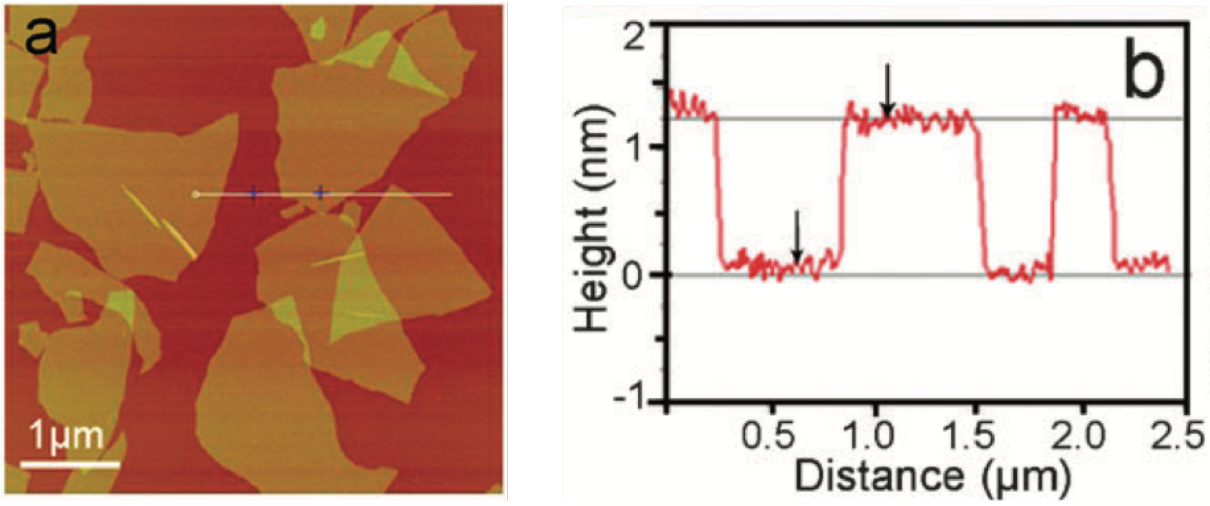

Figure 1.8 Tapping mode AFM image of GO platelets deposited on mica (a) with corresponding height data across three platelets (b).[142]

High resolution AFM imaging can also be used distinguish surface features of GO and rGO. It works by the scanning with a mechanical probe, or the cantilever, moving in a raster pattern over the surface. Changes in sample height cause deflections to the cantilever that are detected through the changes in reflection of a laser beam positioned on the cantilever. Topological mapping is achieved by help of a feedback loop that controls the height of the tip and maintains the laser position. AFM can be run in either contact or tapping modes. In tapping mode, the cantilever vertically oscillates as it is lifted off and on the surface during scanning with changes in oscillation amplitudes caused by deviations in height measured by the detector. The heights of single-layer GO and graphene can vary depending on the substrate and

mode of AFM, due to the variation in interactions between the tip and surface, but typically exhibits heights around 1-2 nm and 0.3-0.7 nm respectively.[139,140,143,144] The heights of single-layer platelets, and the interlayer spacing between multi-layered sheets, are both found to decrease upon GO reduction to rGO.

1.9 Electronic and optical characterisation of graphene materials

The ability of materials to conduct an electrical current can be evaluated through the calculation of its bulk electrical conductivity (σ, S/m), derived with Equation 3 below.[59,60,141]

$$\sigma = \frac{RA}{l} \qquad \text{Equation 3}$$

Where R (Ω) is film resistance, A (m^2) is the cross-sectional area of the film and l (m) is film length. The resistance is typically obtained through probe station measurements, using the gradients of current/voltage (I/V) plots. The area is calculated by simply multiplying the height and width of the film, found by methods such as AFM and optical imaging. The inverse of bulk conductivity gives bulk resistivity (ρ, Ω.m) which can be used to determine sheet resistance (R_s, Ω/sq). This term provides the lateral resistance through a thin square of material and is importantly independent of the square size. This is not the case for bulk measurements. The calculation of R_s can be seen below in Equations 4 and 5.

$$\rho = \frac{1}{\sigma} \qquad \text{Equation 4}$$

$$R_s = \frac{\rho}{t} \qquad \text{Equation 5}$$

Where the unit of ρ is converted to ohm/centimetre (Ω.cm) and t (cm) corresponds to film thickness.

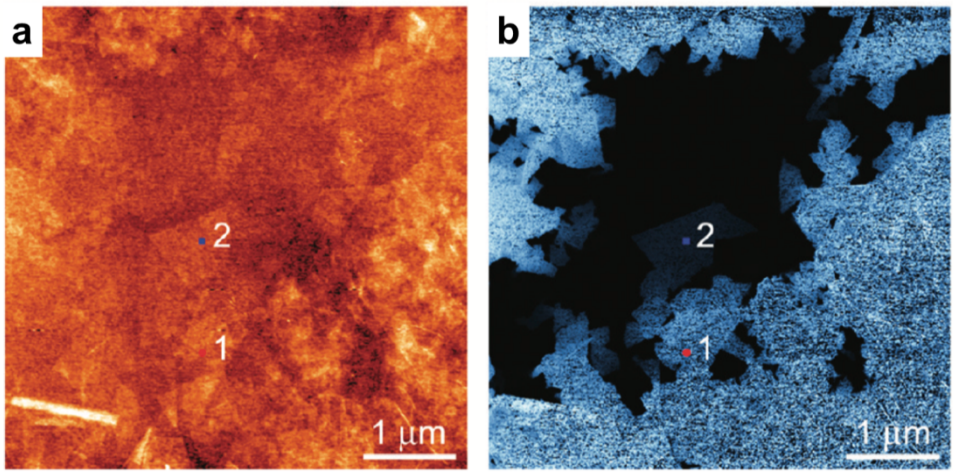

Figure 1.9 Contact mode topological AFM image (a) and corresponding current image (b) of a defective region within a rGO film.[145]

Conductive AFM (cAFM, Figure 1.9) can also be used to electrically characterise materials.[145–147] This method provides information on electronic transport phenomena with regards to localised areas on sheets rather than bulk electronic properties. cAFM works in contact mode, using a conductive cantilever and an applied bias between the cantilever's tip and sample. As the cantilever scans the topography of a surface, in an analogous manner to non-conductive operating modes, the current between sample and cantilever is measured simultaneously and used to create an electrical map.

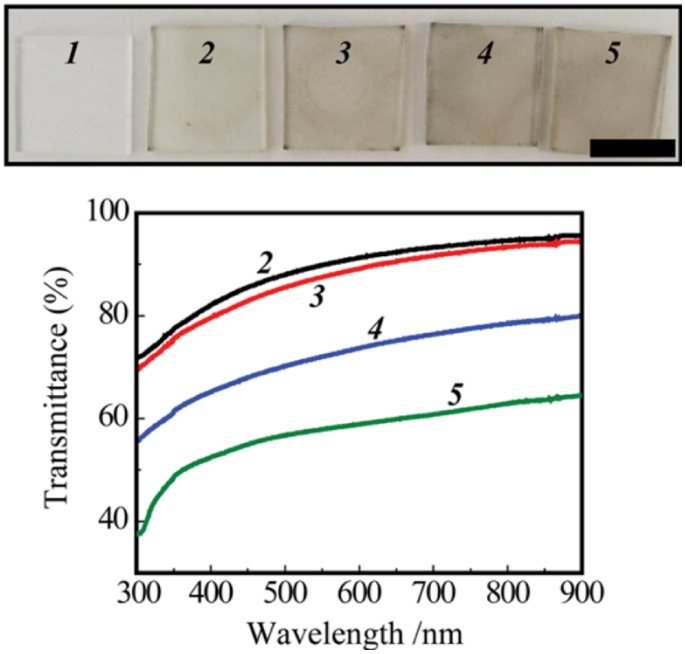

Figure 1.10 Photographs of a bare glass chip (1), GO on glass (2) and rGO on glass (3-5) and obtained through varying the chemical treatment of GO. Shown also is the corresponding % transmittance of samples, measured through UV-Vis spectroscopy.[148]

Upon oxidation of graphene to GO, a colour change from black to brown is observed.[95,96] As can be seen in Figure 1.10, this colour change is reversed upon reduction of GO to rGO, with films appearing darker. The change in colour originates from narrowing of GO's band gap upon reduction, thus altering its absorbance behaviour.[149] A more detailed discussion of band gap and its effect on material properties can be found in Section 1.11. The absorbance of a graphene film can be measured through ultraviolet-visible (UV-Vis) spectroscopy and used to evaluate film transparency with calculation of % transmittance (%T), seen below in Equation 6.

$$\text{Absorbance} = 2 - \log(\%T) \qquad \text{Equation 6}$$

Usually, the transparency of a graphene-based device is characterised by its %T value at 550 nm.[5,102,150] The %T value at this wavelength of light can also be used to determine layer number, with single layer graphene known to have a %T value of 2.3 % at 550 nm.[5] For small area films, the use of UV-Vis becomes problematic due to issues of positioning the sample with respect to the pathway of light. Optical images can be collected through microscopic means, with a constant exposure time of light, and the brightness of the film compared to the substrate (%T = 100 %) to estimate transparency.[151]

1.10 Structural defect characterisation of graphene materials

X-ray photoelectron spectroscopy (XPS) can be used to determine the elemental composition and nature of chemical bonding within graphene layers.[152–155] The technique works through irradiation of the material with X-rays, exciting and ejecting core-level electrons which are measured by a detector. The kinetic energy of the electron is dependent on the binding energy of the atomic orbital it was emitted from and can be used to identify the element and its bound state.

For GO and rGO, the C1s and O1s regions of XPS spectra are of particular interest, being predominantly composed of oxygen and carbon (Figure 1.11). Spectra can be deconvoluted on the basis of functionality, with areas corresponding to quantities. The atomic percentages of chemical groups can be obtained by dividing the area of its deconvoluted peak by the area of the whole region.[153,156,157] Additionally, carbon/oxygen (C/O) ratios can be calculated by the ratio of areas of carbon and oxygen regions after multiplication with their relative sensitivity factors.[153,158] These

methods of quantification are routinely used to evaluate the extent of GO reduction and identify any selectivity of the reduction protocol used.

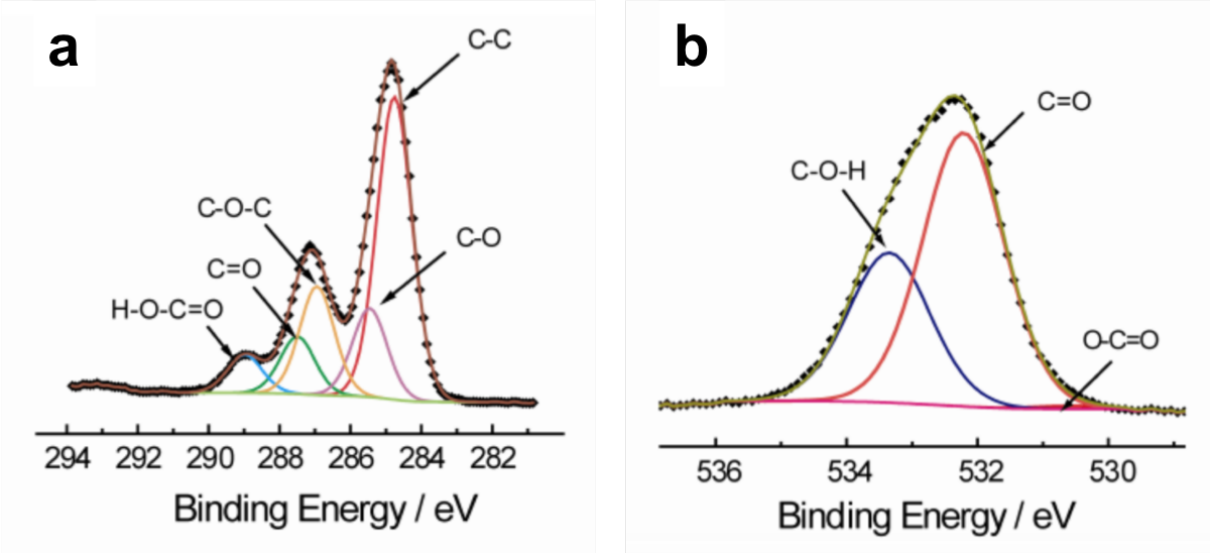

Figure 1.11 XPS spectra of C1s (a) and O1s (b) components of GO.[152]

Raman spectroscopy is one of the most significant techniques that can be used with regards to carbon-based materials, able to provide insight into layer numbers and orientations, edge structures, functional groups, doping, strain or stress and defect density and type.[159–162] The technique works by irradiating the sample with a monochromatic light source, a laser, and measuring the scattering of inelastic light. Depending on the molecular vibrations, phonons and other excitons within the sample, the energies of inelastic photons are altered by varying degrees, the Raman shift, and these can be used to build a structural fingerprint for the material.
The Raman spectra of GO and rGO materials generally show three distinct features that can be observed in Figure 1.12, the D band (~1350 cm^{-1}), the G band (~1580 cm^{-1}) and a less intense 2D band (2500-3500 cm^{-1}).[161] The intensities, areas, shifts and widths of bands can all be used to obtain information regarding graphene materials. The D band is defect-activated and is thus used as measure of disorder within the planar, delocalised lattice. It is not present with pristine graphene, unlike the G band which does not need a defect for activation.[160] The G band arises from the bond stretching of sp^2 chains or rings and is associated with the level of graphitisation within materials. The 2D region occurs from double resonance processes and namely contains a 2D peak (~2700 cm^{-1}) and a D+G peak

(~2950 cm^{-1}). The 2D peak is also present in pristine graphene while the D+G signal is defect activated.[160]

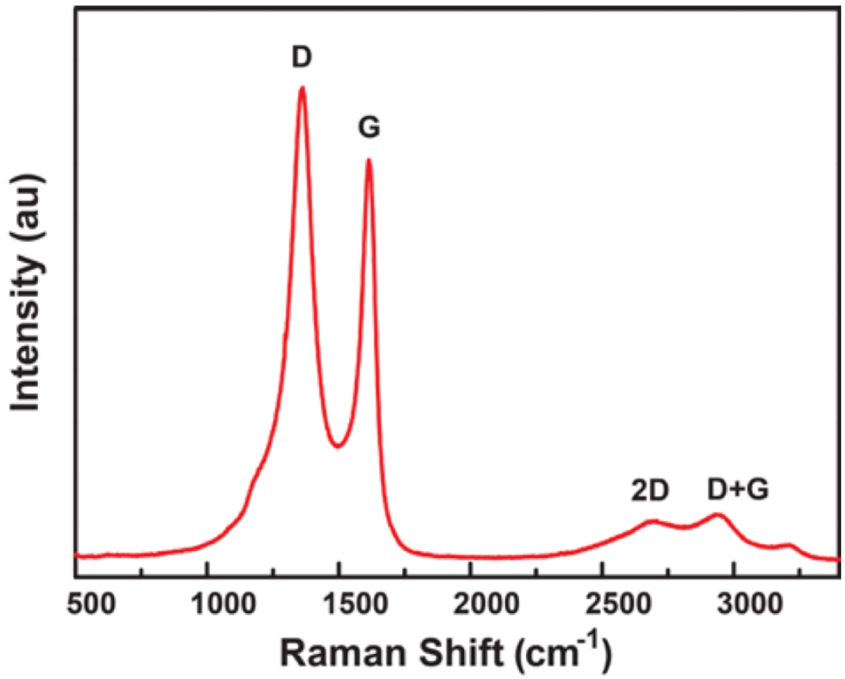

Figure 1.12 Raman spectrum of GO with labelled D, G, 2D and D+G peaks.[163]

The most common method of graphene analysis with Raman is the comparison of peak intensities. The ratio of intensities between D and G bands (I_D/I_G) is predominantly reported, with higher I_D/I_G values typical for more defective structures. If the sp^2 domains within GO and rGO are larger than 2 nm, then this parameter can be inserted into the Tuinstra-Koenig relation, seen below in Equation 7, in order to estimate the average crystallite size (L_a, nm).[162,164] λ (nm) denotes the energy of the light source used.

$$L_a=(2.4 \times 10^{-10})\lambda^4 \left(\frac{I_D}{I_G}\right)^{-1} \qquad \text{Equation 7}$$

Reports have also suggested that I_{2D}/I_{D+G} ratios can also be used as an indication of film quality, with higher values expected for more pristine material.[165,166] In the case of graphene, the 2D peak is also frequently used in conjunction with the G peak to distinguish between single and few layer films (I_{2D}/I_G).[167–169]

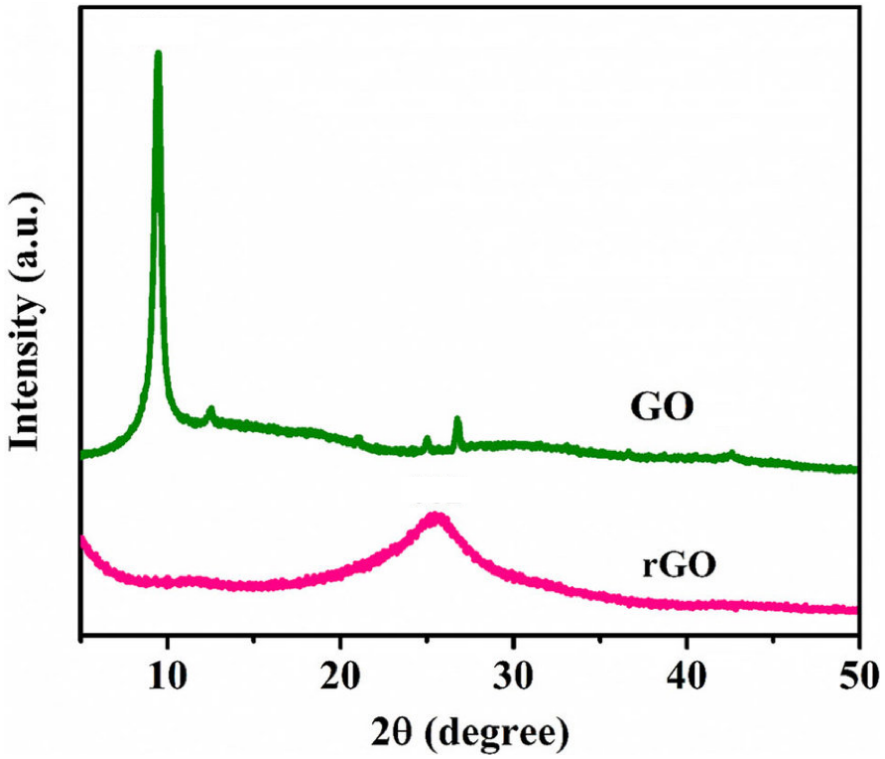

Figure 1.13 XRD spectra of stacked GO and rGO sheets.[170]

X-ray diffraction (XRD) is a powerful tool for identifying the layer ordering within multi-layered graphene films. It works by the irradiation of material with a monochromatic X-ray beam and collecting those diffracted by atoms within the crystal structure using a detector. The X-ray beam and detector is rotated through a range of angles, with the angles at which X-rays diffract corresponding to the planes of the lattice. The interlayer distance (d, nm) can be calculated through use of Bragg's law shown below in Equation 8.

$$d = \frac{\lambda}{2 \sin \theta} \qquad \text{Equation 8}$$

Where λ (nm) is the wavelength of X-rays used and θ (°) is the position of the peak maximum, obtained by dividing the x-axis by two. Stacked GO sheets display a sharp peak maximum around $2\theta = 10^{O}$, which broadens and shifts to higher angles upon reduction to rGO (Figure 1.13) .[98,171] Multi-layered graphene, or graphite, also exhibits a sharp peak with a maximum at $2\theta = 26.7^{O}$ The peak shift with GO upon reduction corresponds to a decrease in interlayer spacing as oxygen functionalities are stripped from the lattice. The width of XRD peaks can also provide information on

the crystallinity of GO and rGO, with broader signals associated with a more amorphous structure.[171]

1.11 II-VI semiconductors

A semiconductor is a material that exhibits some degree of conductivity between that of an insulator and a conductor. They are defined by having a band gap in their electronic structure that separates the valence and conduction bands.[172]

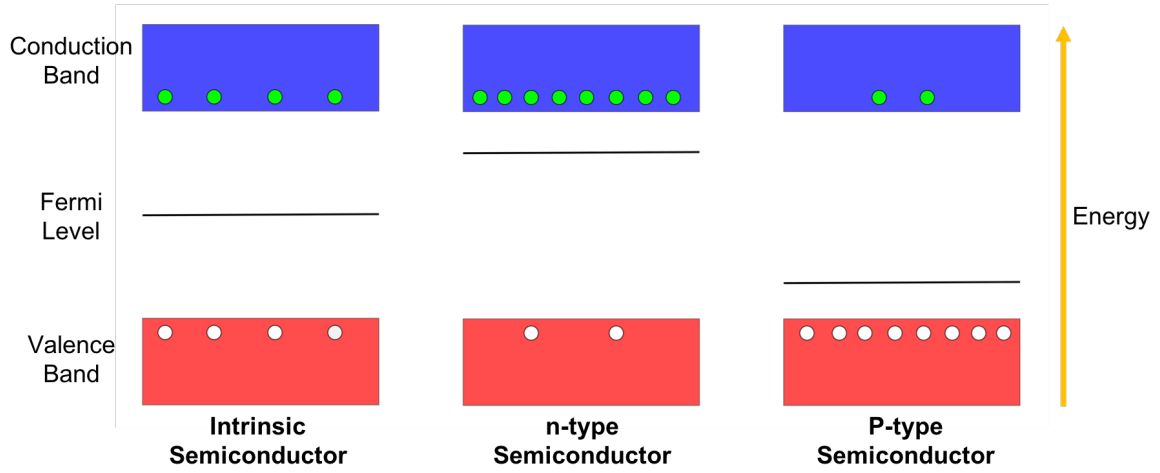

Figure 1.14 Electronic band structures for intrinsic, n-type and p-type semiconductors. Green circles represent electrons and white circles represent holes.

The electronic structures of semiconductor types can be seen above in Figure 1.14. In order to exhibit conductivity, charge carriers require enough energy to transition between the valence and conduction bands. In a conductor, such as metals or graphene, the conduction and valence bands overlap while in an insulator, such as ceramics or GO, the band gap is widened. The Fermi level is defined as the top collection of energy levels at absolute zero. With semiconductors, the excitation of free charge carriers and resulting conductivity can be enhanced through increased temperature or by irradiation.[173,174]

In an intrinsic, or undoped, semiconductor, the Fermi level is found in the middle of valence and conduction bands. Conductivity is induced by the transition of electrons from the valence to conduction band and both electrons and holes are charge carriers.[172] Extrinsic, or doped, semiconductors also exist and are formed by the introduction of electron rich or deficient foreign atoms.[172] N-type doping occurs from electron rich impurities, usually pentavalent species such as nitrogen and phosphorus, and causes a shift in the Fermi level towards the conduction band. The

dominant charge carriers are electrons from the donor atoms excited into the conduction band. P-type doping originates from electron deficient impurities, commonly trivalent atoms such as boron or aluminium, and causes an opposing shift in the Fermi level towards the valence band. The dominant charge carriers are holes in the valence band, generated by the acceptor atoms.

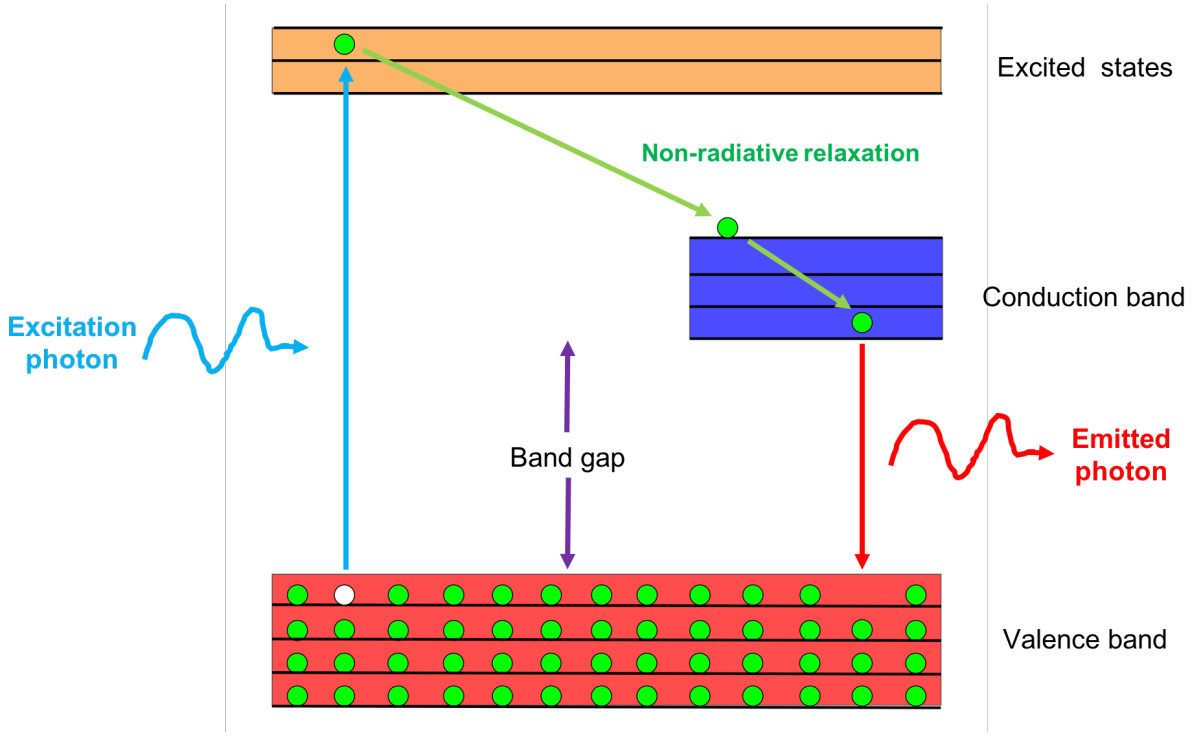

Figure 1.15 Diagram showing how a II-VI semiconductor emits luminescence.

A II-VI semiconductor is a material containing a metal from either group two or twelve of the periodic table and a non-metal from group sixteen, a chalcogen.[175] The band gaps of these semiconductors lie within the UV-visible region, bestowing a host of interesting optical and fluorescent properties. The fundamental principles of fluorescence origin in these semiconductors is depicted above in Figure 1.15. The phenomenon occurs through the absorption of photons by the material, which can result in the excitation of electrons from ground to excited states. The larger the band gap, the higher the energy needed for these transitions to occur. Once excited, these electrons must relax back down to the ground state which can occur through a combination of non-radiative and radiative processes. Non-radiative processes occur by the loss of energy through heat and vibrations while a radiative process results in the loss of energy through emission of a photon. If the energy of this emission resides in the visible range, then fluorescence can be observed. The quantum yield

of the semiconductor is defined by the ratio of the number of photons absorbed to the number of photons emitted.

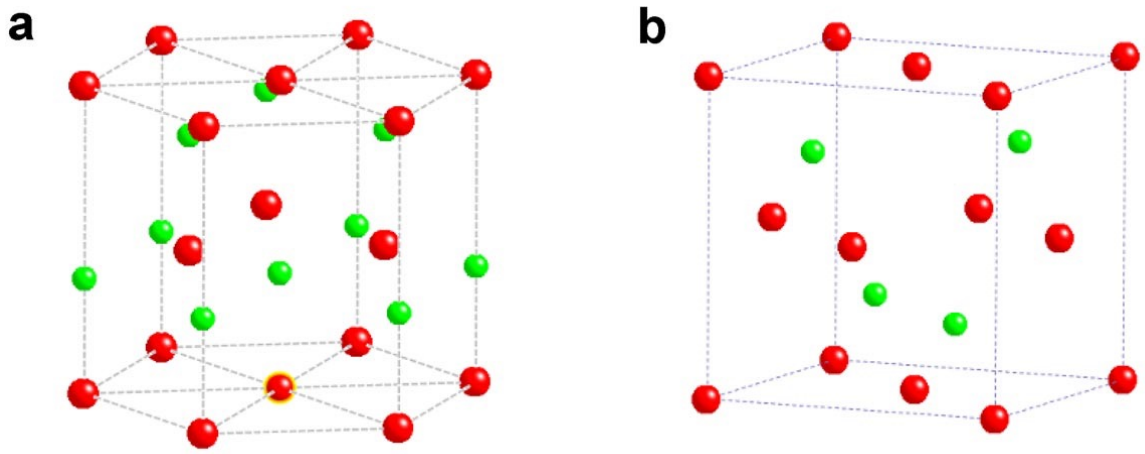

Figure 1.16 The two types crystal structure displayed by CdS, wurtzite (a) and zinc blende (b).[176] Red circles indicates cadmium atoms and green circles indicate sulphur atoms

Cadmium sulphide (CdS) is a well-known example of a binary II-VI semiconductor, possessing a bulk band gap energy of 2.5 eV.[177] The compound appears yellow in colour and its crystal structure can exist in either wurtzite (hexagonal) or zinc blende (cubic) forms (Figure 1.16).[176] The potential applications of the material are many and varied, with uses in solar cells, hydrogen production, light emitting diodes, sensors and labelling all reported.[22–24,178,179]

1.12 Templation of II-VI semiconductors to DNA

The structure of double-stranded, or duplex, DNA is well known, consisting of four nucleotides, cytosine, guanine, adenine and thymine.[180] These nucleotides are each composed of a phosphate group, a pentose sugar and a nitrogen base. Nucleotides are linked together in a strand through the sugar phosphate backbone, with hydrogen bonding between complementary base pairs holding the two strands together in a helical structure.

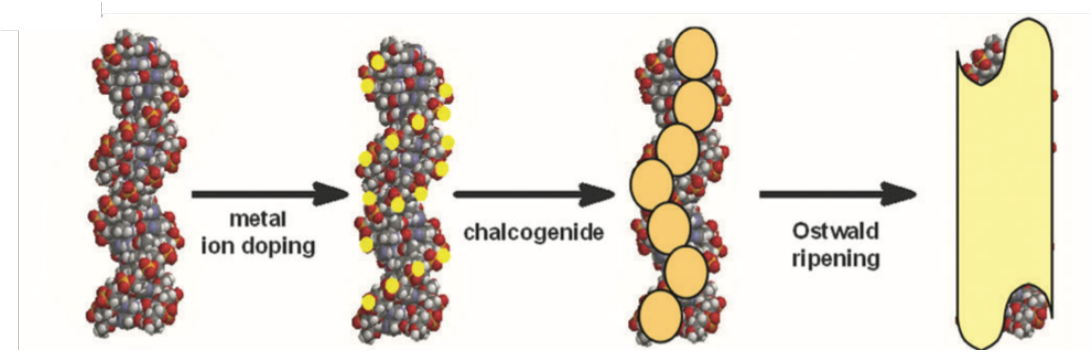

Figure 1.17 Scheme showing the synthesis of II-VI semiconductors on duplex DNA.[181]

The structure of DNA is able to provide a long, thin, chemically-robust template to direct the growth of semiconductors as 1D features, or nanowires.[181] This is achieved through doping of the DNA with sources of the appropriate metal and chalcogenide ions, see Figure 1.17.[182] Typically, metal ions are first introduced onto the DNA. These able to bind to the negatively charged sugar-phosphate backbone through electrostatic interactions, and also coordinate with donor atoms from bases, such as oxygen and nitrogen.[183,184] The chalcogenide is then added, with nucleation of CdS occurring at the binding sites of the metal. The growth of nanoparticles in then believed to occur through a phenomenon similar to Oswald Ripening, energetically forming larger particles from smaller ones.[181,185] Synthesis of the semiconductor can take place with the DNA immobilised on a surface or via a wet chemical method, with DNA dispersed within water.[182] The advantage of the wet chemical technique with regards to inkjet fabrication is that the templating of DNA yields a semiconducting ink.

1.13 Applications and challenges of semiconducting DNA nanowires

Semiconductor nanowires are expected to play a critical role in the development of future electronic and optoelectronic devices. However, due to their granular and uneven nature, DNA nanowires are unsuitable for applications requiring high conductivity.[186,187] This eliminates the use of these materials for optoelectronic or single nanowire devices with vapour-liquid-solid (VLS) nanowires, composed of single crystal units, being more viable candidates.

DNA semiconducting nanowires could still have applications in sensing technologies, where only a measurable change in electrical signal needs to be exhibited upon changes in the environment. For example, cadmium sulphide has been demonstrated to be photoconductive and a strong absorber of volatile gases, making

it a suitable candidate for light and gas sensing applications.[20,25,188,189] DNA coated with materials exhibiting optical band-gaps within the UV-visible region, such as II-VI semiconductors, could also be used for fluorescent labelling technologies, with no electrical activity needed (Figure 1.18).[24,26,190]

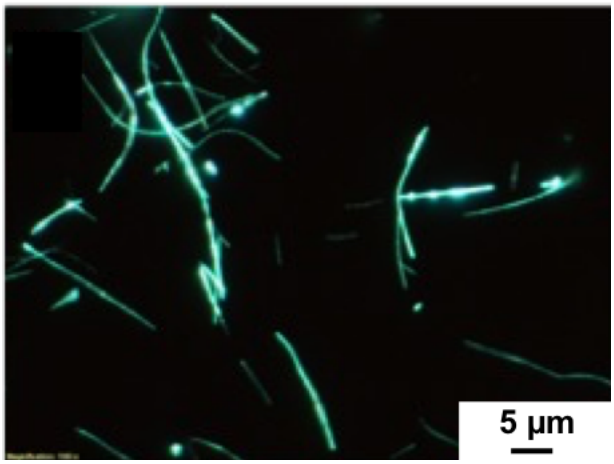

Figure 1.18 Fluorescent microscopy image of zinc oxide nanowires.[191]

The main advantage of using DNA nanowires compared to VLS nanowires, is that the wet chemical method used for synthesis is a low energy, low maintenance process.[181,182] It is also achieved in aqueous solution, providing a ready-made, green ink that can be tailored for use with inkjet technology. This technique allows the fabrication of nanowire components with greater resolution than other deposition methods, such as spin coating, drop casting or Langmuir-Blodgett. Other nanoparticles synthesised through sol gel processes typically require harmful solvents whilst capping agents or stabilisers are also needed to control particle growth.[43,192] However, one of the main challenges with using DNA is the low loading of material within the ink.[193,194] This means more printing passes are needed to obtain desired film thicknesses thickness, requiring a robust printing protocol to maintain resolution. Features for sensing applications may also need to be sintered, to achieve sufficient device conductivity, while DNA conformations will need to be carefully controlled in order to prevent supercoiling of wires, thus minimising the number of barriers to intrinsic charge carriers between contacts.[43,187,195]

1.14 Morphological characterisation of semiconducting DNA nanowires

AFM can be used as a tool to confirm the presence of CdS on DNA and gain insight into the morphologies and lengths of resulting wires.[181,182,185] The height of bare duplex DNA can vary depending on mode of AFM used and the substrate it lies on

but will typically exhibit heights below 1.5 nm.[196] The thickness of DNA decorated with nanoparticles will exceed this threshold and can be used to estimate the size of particle growth. The technique can also be used to look into the extent of coverage, with areas of material growth appearing granular rather than smooth. Depending on the conditions for synthesis used, such as DNA concentration, stoichiometry of reagents and incubation times, the morphology of wires can vary.[182,185,187] In one extreme, the DNA can be merely decorated with isolated particles, giving a 'beads on a string' appearance, while in the other it can be evenly coated throughout its length, giving a continuous wire (Figure 1.19). AFM also allows for the analysis of wire conformation once deposited or printed on a surface which could have implications on the performance of electrical devices.[187,197]

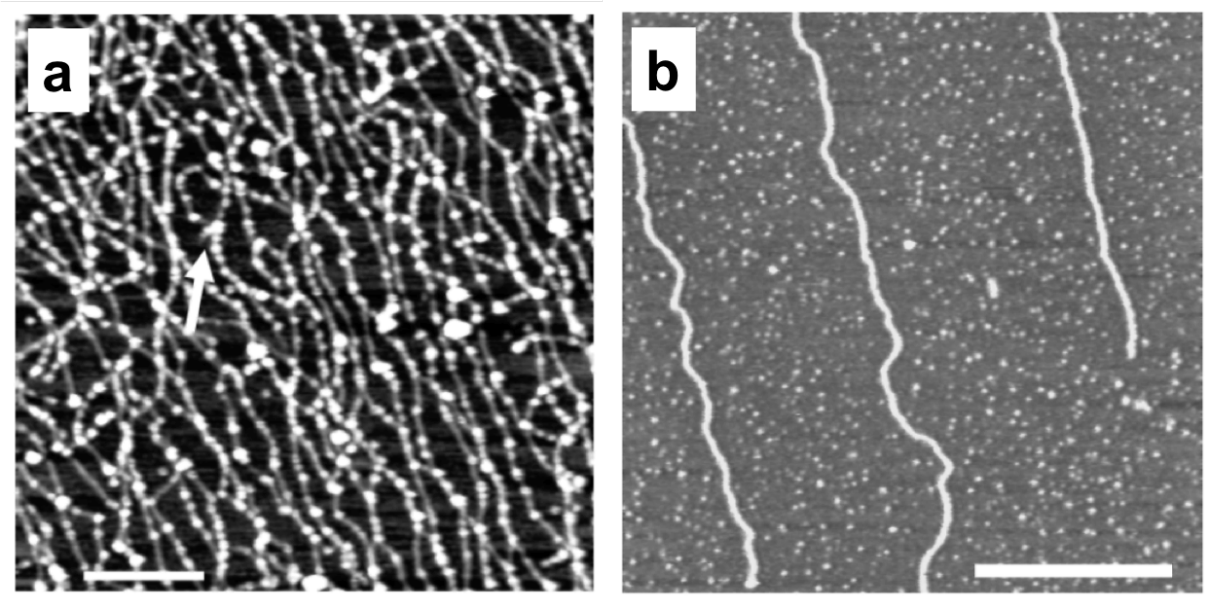

Figure 1.19 AFM images of DNA strands coated with CdS nanoparticles.[198] a) DNA nanowires exhibiting a 'beads on a string' morphology. b) DNA nanowires with a continuous coverage of CdS nanoparticles.

1.15 Characterisation of optical and fluorescent properties of DNA nanowires

Bare DNA shows a strong absorption band at around 260 nm but no absorption above 300 nm.[199] The UV-Vis spectrum of semiconducting DNA wires displays notable absorbance behavior at higher wavelengths, appearing as a knee that extends out from the DNA signal (Figure 1.20).

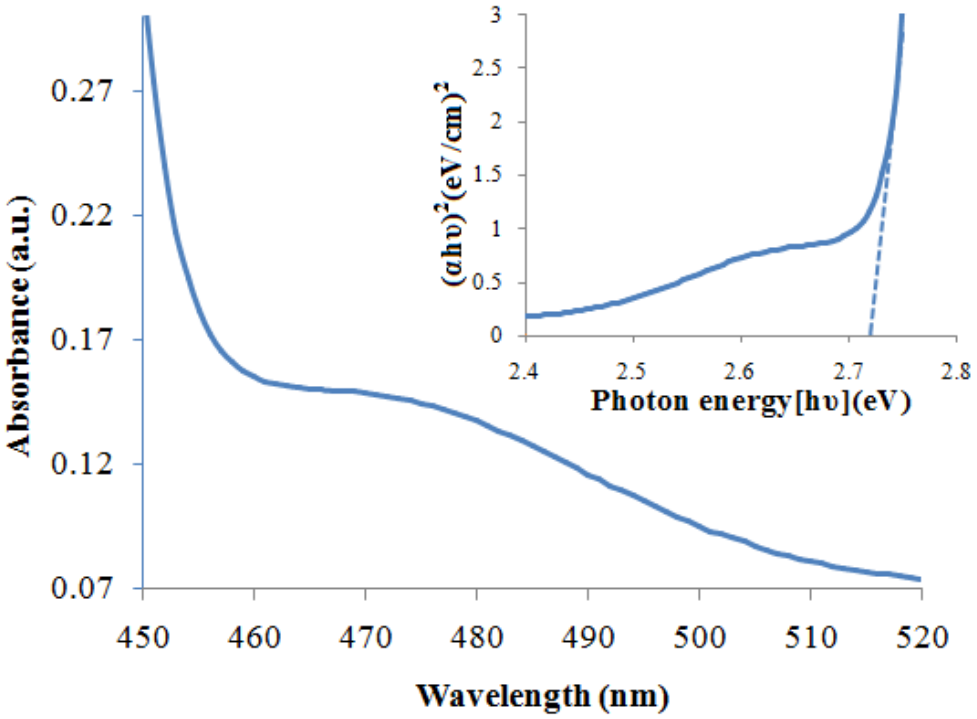

Figure 1.20 UV-Vis spectrum of CdS nanoparticles, with corresponding Tauc plot shown in the inset.[200]

The wavelength at which this absorbance knee extends to correlates to the size of the semiconductor's band gap, calculated through use of the Tauc equation, seen below in Equation 9.[200,201,202]

$$(Ah\upsilon)^2 = \beta(h\upsilon - E) \qquad \text{Equation 9}$$

Where A is absorbance, h is Planck's constant (6.63×10^{-34} J s), υ is frequency (s^{-1}), β is a proportionality constant, and E is the band gap energy. The absorption coefficient (α) is sometimes used instead of absorbance, if material thickness is a factor, while $Ah\upsilon$ is squared due to the measurement of bandgap being a direct, allowed transition. $h\upsilon$ corresponds to the energy of the photon, with υ calculated with Equation 10 below, where c (3×10^8 m/s) is the speed of light and λ is wavelength (m).[203] The energy obtained in Joules can then be converted into electron volts (eV).

$$v = \frac{c}{\lambda} \qquad \text{Equation 10}$$

Plotting $(Ah\upsilon)^2$ on the y-axis and $h\upsilon$ (eV) on the x-axis using the UV-Vis data gives the Tauc plot (see Figure 1.20). Extrapolation of the linear regime of the plot down to the x-axis yields the optical band gap of the material.

Fluorescence studies are fundamental for the characterisation of II-VI semiconductors. Excitation of DNA nanowires at wavelengths above 300 nm can reveal the presence of templated material on DNA, with bare DNA known not to absorb at these wavelengths.[199] The excitation energy required is dependent on the band gap of the semiconductor. Fluorescence microscopy can be used to directly visualise nanowires deposited on a surface.[197,204] If the semiconductor is localised on the DNA itself and not just free in solution, the luminescence of images should correspond to the shapes of DNA strands and networks.

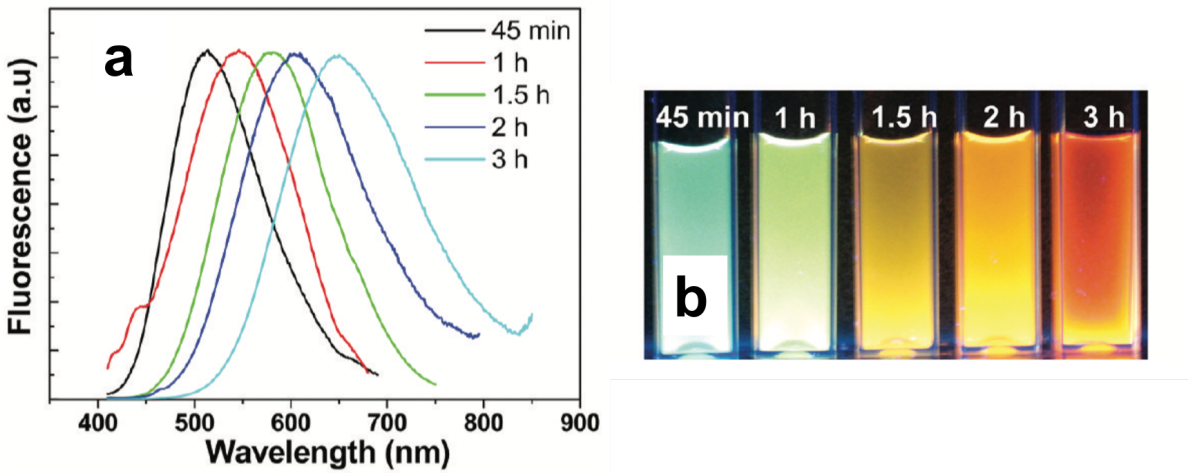

Figure 1.21 Emission spectra of CdS quantum dots of varying band gaps (a) with a digital image of the quantum dot solutions under UV excitation (b).[205]

Emission spectra of nanowire solutions can also be obtained (Figure 1.21), and should exhibit a signal corresponding to the semiconductor.[58,205] The breadth of and shape of emission signals can be interpreted to gain insight into the quality of material formed, with broader and more complex signals generally representative of more defective particles displaying trap state and surface state emission.[205,206] This is where transitions occur from additional energy levels created below the conduction band as a result of material defects or boundaries, rather than from conduction to valence bands. Additionally, time resolved photoluminescence experiments can infer material quality. This technique uses a short laser pulse for excitation and measures the rate of emission decay, with less defective semiconductors with higher quantum yields tending to luminesce over longer timescales.[58,207]

1.16 Raman and XRD characterisation of DNA nanowires

XRD can differentiate between the two different phases of II-VI semiconductors on DNA, with differing peak positions seen for zinc blende and wurtzite structures and corresponding to lattice planes.[208] The XRD spectrum for zinc blende CdS can be seen below in Figure 1.22.

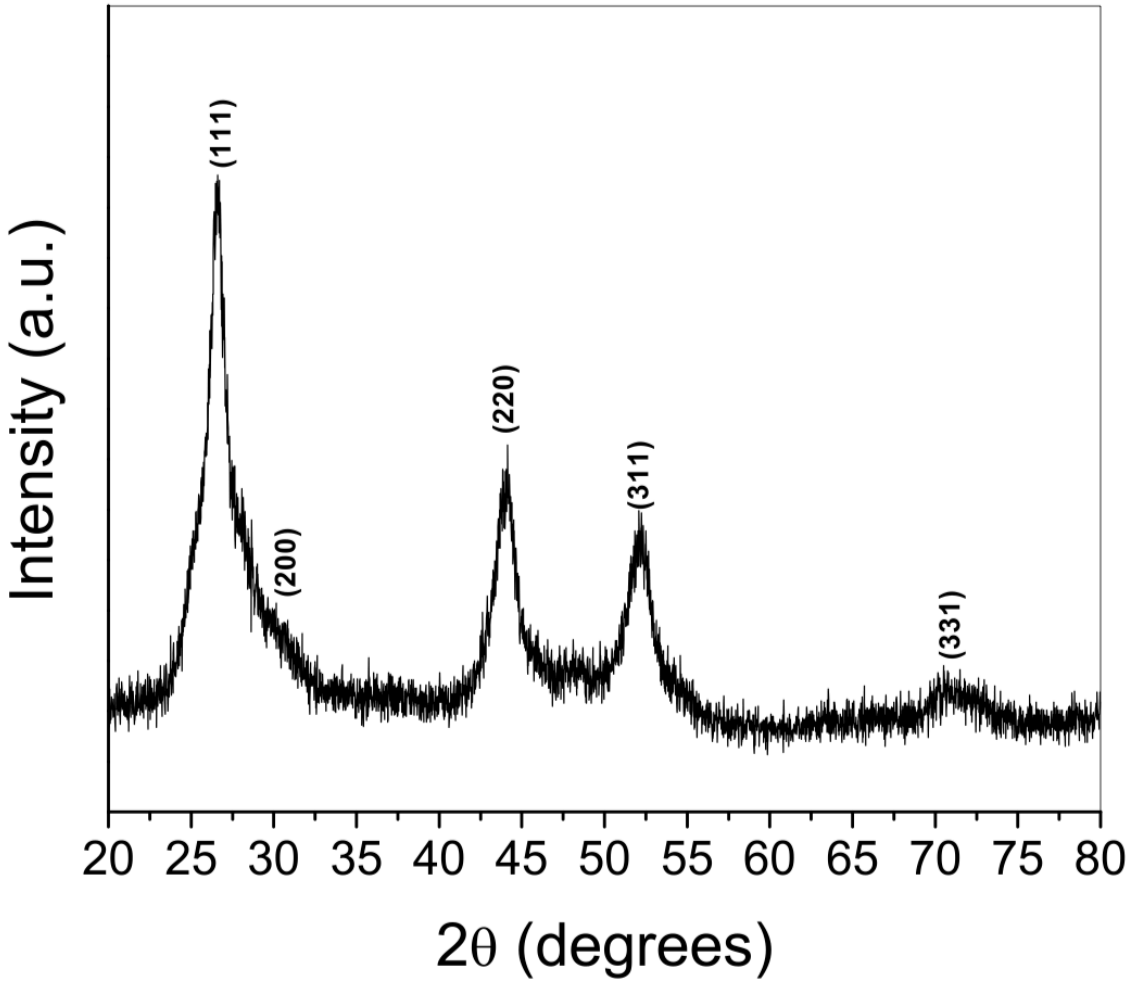

Figure 1.22 XRD spectrum for cubic phase (zinc blende) CdS crystal structure.[209]

XRD can also be used to estimate the average size of particles through use of the Scherrer equation, Equation 11.[210,211]

$$\tau = \frac{K\lambda}{\beta \cos\theta} \qquad \text{Equation 11}$$

Where τ (nm) is the average size of crystallites, K is a dimensionless shape factor (0.9 for spherical particles), λ (nm) is the X-ray wavelength, θ (radians) is the Bragg angle and β is the full width at half maximum (FWHM, in radians) of the XRD peak.

For spectra which show multiple peaks, the dominant peak is typically used for analysis.

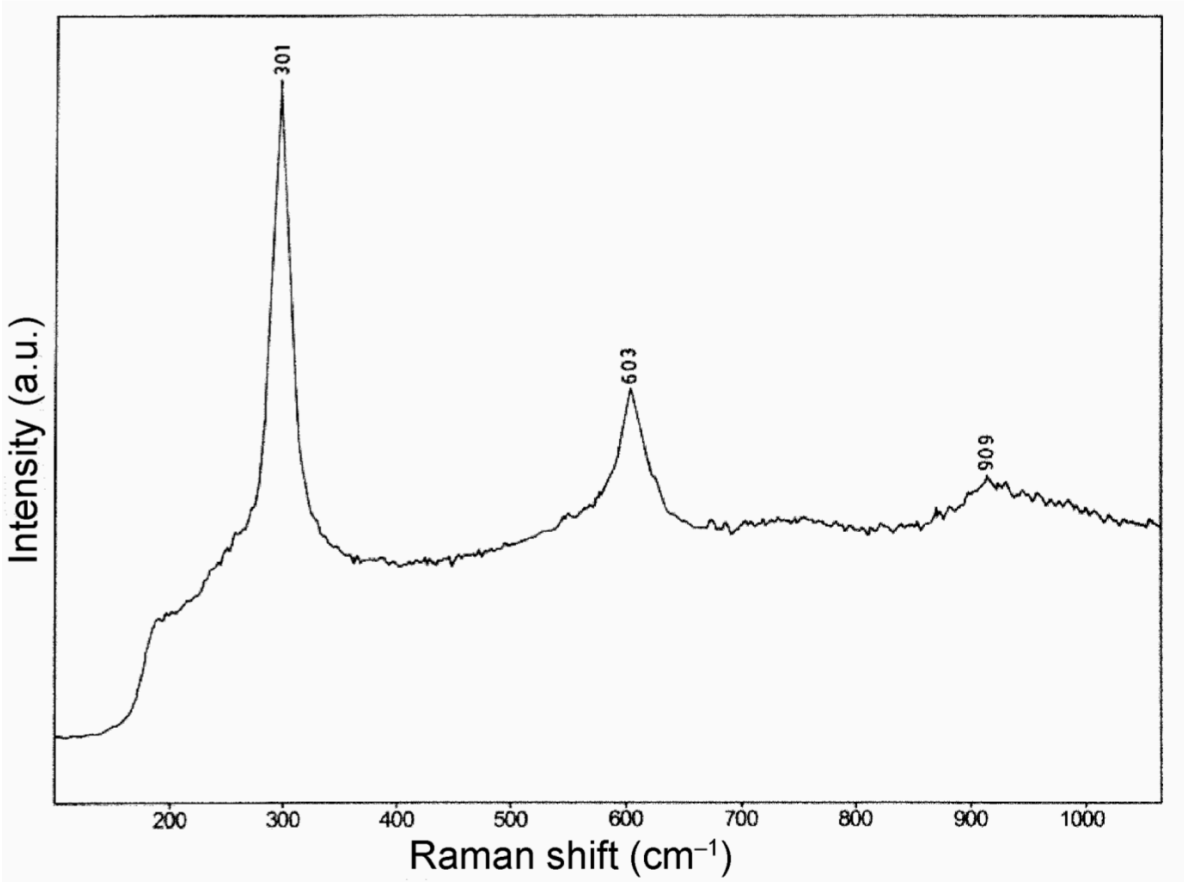

Figure 1.23 Raman spectrum of CdS nanoparticles.

The presence of semiconducting nanoparticles on DNA can also be determined through Raman spectroscopy.[212–214] Through this technique particular phonons, or lattice vibrations, can be observed. The wavenumbers at which these vibrations occur differ between materials, hence providing a fingerprint for identification. In particular, the longitudinal (LO) phonons of II-VI semiconductors can be distinguished and used for characterisation. These are lattice vibrations occurring between two different atoms moving in opposite directions as a result of the electric field of the radiation. Cadmium sulphide exhibits an intense 1LO phonon around 300 cm^{-1}(Figure 1.23) with second and third order resonances (2LO and 3LO) potentially also visible.[213] CdS can also exhibit broad signals, stretching over 1000's of wavenumbers, as a consequence of its photoluminescence.

1.17 Calculation of the activation energies for DNA nanowire devices

The activation energies (E_a) of semiconducting DNA devices can be determined through the application of the Arrhenius Law, shown below in Equation 12.[58,174,215]

$$k=Ae^{\frac{-E_a}{RT}} \qquad \text{Equation 12}$$

Where k is the rate constant, A is a pre-exponential factor, R (8.31 J K^{-1} mol^{-1}) is the gas constant and T (K) is the temperature. Activation energies can be deduced from the measurement of device conductance (G) over a range of temperatures. G is just the reciprocal of resistance, with units of Siemens (S), and thus can be obtained from the slope of I/V curves from probe station measurements. The conductance of semiconductors increases with increasing temperature as more charge carriers are generated within electronic bands. The values of G can be substituted into the Arrhenius Law in place of the rate constant and the natural logarithm applied to give Equation 13.

$$\ln(G) = \ln(A) - \frac{E_a}{RT} \qquad \text{Equation 13}$$

The plotting of lnG vs. 1/T yields a graph with a gradient corresponding to $-E_a/R$ and a y-intercept denoting ln(A). If a factor of 1000 is applied to the x-axis beforehand (1000/T), then the activation energy can be calculated in kJ/mol simply by multiplying by the gas constant in J K^{-1} mol^{-1}. The value for E_a can then be converted into electron volts by dividing by Avogadro's number (6.022×10^{23} mol^{-1}) and converting J into eV (1 eV = 1.60×10^{-19} J).[203]

1.18 Thesis aims

The first aim of the thesis is to address the issues encountered with graphene oxide inks with regards to their printability. This is primarily caused by the hydrophilicity of graphene oxide meaning most stable inks are developed as aqueous-based systems.[7,10,56,88] The rheology of water is unsuited for inkjet technologies and often leads to problems with jetting and control of material once deposited on the surface.[27,53,55] Commonly, the final consequence is a printed film lacking the resolution and homogeneity required to be considered as high-quality.

The second aim of the following work seeks to improve the conductivity of films printed using graphene oxide inks. Due to the high density of defects located on its carbon lattice, graphene oxide is found to be insulating and a reduction step is usually incorporated after printing to restore conductivity for electronic applications. These reduction procedures, generally chemical or thermal processes, are often inefficient at repairing the 2D lattice and yield films that are inadequate for use as components requiring high conductivity or low sheet resistance.[148,216]

The third and final aim of the project will assess the versatility of the techniques designed for the printing of graphene oxide by transferring these to the printing of other hydrophilic nanomaterials. In particular, hydrophilic DNA nanowires templated with II-VI semiconductors have been identified as promising materials for use in future electronic and optoelectronic devices.[58,181,182]

2. Methodology

2.1 Materials

Ultra-highly concentrated single-layer graphene oxide solution (GO, 6.2 mg/mL, platelet size 0.5-5 μm, single layer > 80 %) was obtained from Graphene Supermarket. Lambda DNA (λ.DNA, 500 μg/mL, catalog number N3011S) was bought from New England Biolabs UK Ltd. Ethanol (99.5 %), 2-propanol (99.5 %), tetrahydrofuran (99.9 %), N,N-dimethylformamide (99.8 %), ethylene glycol (99.8 %), propylene carbonate (99.7 %), hydrazine hydrate (50-60 %), silver nanoparticle ink (Suntronic Jet Silver U5603), cadmium nitrate tetrahydrate ($Cd(NO_3)_2.6H_2O$, 98 %), sodium sulphide (Na_2S, product number 407410), concentrated sulphuric acid (H_2SO_4, 99.9 %), hydrogen peroxide (H_2O_2, 30 % w/w in H_2O) and eutectic (gallium-indium, 99.99%) were all purchased from Sigma Aldrich. Deionized water was provided by a NANOpure® Diamond™ Life Science ultrapure water system equipped with a DIamond™ RO Reverse Osmosis System (Barnstead International). Silicon (Si, 111, product code SILI0106) and Silicon Oxide (Si/SiO_2) wafers were purchased from PI-KEM Ltd, glass microscope slides (product code 631-1550) were bought from VWR International, sapphire wafers (Al_2O_3, product code ALC100D065C2) were purchased from MTI Corporation and interdigitated platinum electrodes on glass substrate (Pt-on-glass IDEs, 10 μm band gap, product code DRP-G-IDEPT10) were acquired from DropSens. The Peltier plate (stock number 618 - 724) was sourced from RS Components while DMC-11610 cartridges (16 nozzles, 21.5 μm nozzle diameter, 10 pL droplet volume) were obtained from Printed Electronics Ltd.

2.2 Instrumentation

For processing of GO dispersion into a printable ink, a Langford Sonomatic Cleaner (230 V) and a Jouan A14 Centrifuge were utilised. A Lambora Vortex Genie-2 (Scientific Industries) was used for mixing of reagents during CdS/λ.DNA synthesis. Printing of all graphene oxide, CdS/λ.DNA and silver inks was carried out on a Fujifilm Dimatix DMP-2800 system while a Diener Electronic Plasma -Surface - Technology unit used to treat substrates beforehand. Chemical reduction of GO films was carried out in a covered glass basin heated with a Heidolph MR Hei-Tec hotplate. Low-temperature thermal reduction (<200 ^{O}C) of GO samples was performed in a Fistreem vacuum oven while high-temperature thermal reduction (>600 ^{O}C) was achieved using an Edwards 306 vacuum station with a Tectra ceramic heater. Sintering of CdS/λ.DNA was achieved on a Heidolph MR Hei-Tec hotplate.

Contact angle and surface tension measurements were taken with a KSV-CAM 101 tensiometer while UV-VIS spectra were recorded with a NanoDrop One^{c} absorption spectrometer (ThermoFisher Scientific). Small-scale atomic force microscopy (AFM) imaging of DNA strands and semiconducting nanowires (<16 μm) was performed using a Multimode 8 AFM with a Nanoscope® V controller (Bruker), 'E' scanner, isolation table and silicon-coated silicon nitride cantilevers (Bruker, tip radius 2 nm, force constant 0.7 N/m). All other AFM and conductive AFM (cAFM) studies were carried out on a Nanoscope® V, equipped with Veeco diDimension Controller and isolation table. For tapping mode AFM, aluminum-coated TAP300Al0-G cantilevers were used (Budget Sensors, tip radius <10nm, force constant 40 N/m) while cobalt chromium-coated MESP-LM-V2 cDiantilevers were used for cAFM (Bruker, 25 nm tip radius, force constant 3 N/m). A Cascade Microtech probe station with an Agilent B1500A parameter analyser was employed for the electronic characterisation of printed components. This instrument was also combined with an ETC-200L (ESPEC, Japan) thermal chuck system and a UVP Dual Tube Handheld UV lamp for the electronic studies on DNA/CdS devices. Optical imaging was performed using an Axioskop 2 Plus Microscope twinned with an AxioCam HRM camera. Raman spectra were obtained with a WiTec Confocal Raman Microscope (model CRM200, Ulm, Germany), using a diode laser (488 nm excitation source) and a Peltier cooled CCD as the detector (-60 ^{O}C). X-ray photoelectron spectroscopy (XPS) analysis was undertaken with a Kratos Axis Nova photoelectron spectrometer equipped with a monochromatic Al Ka X-ray excitation source (1486.7 eV, NEXUS Newcastle University). Fourier-transform infrared (FTIR) spectra were recorded with a Shimadzu IRAffinity-1S spectrophotometer equipped with a DLATGS detector. X-ray diffraction (XRD) analysis was carried out using a PANalytical X'Pert Pro Multipurpose Diffractometer (MPD), combined with a X'Celerator detector and a Cu K_{α} X-ray radiation source (λ = 0.15418 nm).

2.3 Processing of graphene oxide into a printable dispersion

The concentration of the dispersion bought from Graphene Supermarket was confirmed to be 6.2 mg/mL through evaporating a known volume of the solution to dryness (50 ^{O}C, 48 h) and measuring the mass of residual solid. This stock solution was diluted (2 mg/mL) and sonicated in a bath (<35 ^{O}C, 4 h) to shear the size of the platelets. The dispersion was then centrifuged (4 x 15 min cycles, 6500 rpm) with the

brown supernatant collected each time and dark-brown pellets, consisting of the largest platelets, discarded. The final supernatant was passed through a syringe filter (1 μm pore size) to give the aqueous based ink. Through using the same evaporation technique as with the starting dispersion, the concentration of the processed dispersion was found to be 2 mg/mL.

2.4 Characterisation of graphene oxide dispersion

The sizes of GO platelets before and after processing were analysed through tapping mode AFM. Samples were diluted 500-fold prior to drop casting 1 μL onto cleaned Si chips (Section 2.5). Samples were left to dry naturally in air. The heights and average diameters of platelets were measured using Nanoscope Analysis version 1.5 software (Bruker). The average dimensions of 300 platelets after processing were measured to provide the size distribution.

UV-Vis spectra for the commercial GO dispersion before and after processing were recorded using a quartz cuvette (1 mm path length) after dilution with denoised water (to 0.2 mg/mL). Absorbances over the range of 200-800 nm were collected.

2.5 Preparation of substrates for use with graphene oxide

Si, Al_2O_3 and Si/SiO_2 wafers were cut into square chips (1 cm x 1 cm) prior to rinsing with water, ethanol and 2-propanol, wiping with a cotton bud and drying under a nitrogen stream. Chips were then given oxygen plasma treatment (5 min, 90 W, 150 sccm) directly before use to remove any solvent residue and increase surface energy to promote ink adhesion.

Glass surfaces were washed and wiped with water, ethanol and 2-propanol prior to sonication in 2-propanol (15 min). Substrates were dried under a nitrogen stream before plasma treatment (10 min, 90 W, 150 sccm). To assess the surface energy of the glass after this treatment, contact angle measurements over the course of 90 minutes were taken afterwards in air, using the methodology described with GO inks in Section 2.7 but without need for repeats.

2.6 Formulation of aqueous-based graphene oxide inks

The additives selected for testing in Section 3.2.2 were ethylene glycol, N,N-dimethylformamide, tetrahydrofuran and propylene carbonate. To the processed dispersion (produced via the method outlined in Section 2.3) the required solvent was

added in a 9 % v/v manner. A 100 % aqueous reference ink was also made to the same concentration through the addition of extra water. To ensure adequate mixing of solvents after addition, inks were sonicated in a water bath (5 min).

2.7 Characterisation of aqueous-based graphene oxide inks

The wettability of inks was measured through contact angle measurements in air. Measurements were taken on clean glass surfaces (see Section 2.5) but without plasma treatment to avoid complete wetting scenarios. Droplet size was kept constant between sets, with 10 measurements recorded for each to obtain an average. The time at which each measurement was taken was kept at 3 s to allow droplets to equilibrate on the surface, with the average contact angle from both sides of the droplet taken in each case using KSV CAM2008 software.

2.8 Printing of films using aqueous-based graphene oxide inks

Inks were degassed under vacuum (10 min) prior to injection into a DMC-11610 cartridge through a syringe filter (1 μm pore size). Each ink was used to print a set of 10 wires differing in length (0.6-2.4 mm x 0.1 mm, 20 μm drop spacing, 20 print passes) onto a glass slide (held at 55 ^{O}C on the platen) directly after being cleaned (Section 2.5). For droplet generation, a highly modified jetting waveform with extreme nozzle voltages (26-29 V) was used. A slow print speed (1 kHz) was applied during printing to help droplet accuracy along with a cartridge height and temperature of 0.8 mm and 28 ^{O}C respectively.

2.9 Formulation of optimised glycol-based graphene oxide ink

A four-fold dilution with ethylene glycol was carried out on the processed dispersion (see protocol outlined in Section 2.3). For preliminary experiments (Chapter 3, Sections 3.2.6 to 3.2.8) the ink concentration was kept at 0.5 mg/mL. For all other studies, the processed dispersion was first concentrated to roughly 8 mg/mL in a vacuum oven (<60 ^{O}C) before the addition of glycol (75 % v/v) and mixing by sonication in a water bath (5 min).

2.10 Characterisation of optimised glycol-based graphene oxide ink

The physical properties and performance of glycol-based GO ink (0.5 mg/mL) were compared to an aqueous GO ink, processed using the method described in Section

2.3 and diluted with denoised water to the same concentration. The wettability of both inks on glass was analysed using the same protocol given in Section 2.7. The same instrument was also used to experimentally compare the surface tensions of inks, using the pendant drop method. This involved expelling ink droplets from the needle as images were recorded. The images which captured the droplet just before ejection were used to calculate surface tension with KSV CAM 2008 software. Five measurements for both inks were taken to obtain an average value.

The jettability of inks was analysed through the printer's Dropwatcher application, allowing real-time visualization of droplets being expelled from the cartridge nozzles. Inks were degassed under vacuum (10 min) prior to injection into a DMC-11610 cartridge through a syringe filter (1 μm pore size). Jetting waveforms and nozzle voltages for both inks were tuned beforehand in order to generate spherical droplets, with speeds between 7-10 m/s. To obtain this scenario, the glycol ink was jetted using a model waveform and low nozzle voltages (17-18 V) whilst the aqueous ink required a highly modified waveform and high nozzle voltages (26-29 V). Droplet images were captured 100 μs after ejection and at a firing frequency of 5 kHz. For the optimized glycol ink, droplets were imaged over a range of 50 print cycles.

For comparisons in print resolution and homogeneity, lines composed of a single row of droplets (8 mm long, 20 μm drop spacing) were printed onto Si chips directly after cleaning (Section 2.5). When using the glycol ink, the printing system was modified with a Peltier plate fixed on the platen, on which the silicon surface (heated to 80 ^{O}C with an external power pack) was held. The aqueous ink was printed with the substrate rested on the platen (at 55 ^{O}C). The same jetting waveforms and nozzle voltages as used in the jettability analysis were applied while print speed (1 kHz), cartridge height (0.8 mm) and cartridge temperature (28 ^{O}C) were kept constant between both inks. Analysis of platelet density within lines was carried out through tapping mode AFM. Images within the lines were collected at three similar points spanning from the edge to the centre in both cases. The edge heights of patterns were calculated from averaging 20 measurements taken using Nanoscope software. The widths of the tracks were measured using images taken on the AFM microscope.

2.11 Low density-printing

Print patterns were specifically designed on Photoshop software, to a scale where each pixel represented one droplet and dependent on the drop spacing needed for

printing. Four patterns were generated, each one printing one in every four neighboring droplets and combining to give one print pass (quarter density printing). Patterns were exported in .bmp format for use with the Dimatix software.

A preliminary test of the technique was undertaken involving the printing of two tracks (2.4 mm x 0.1 mm, 20 μm drop spacing, 20 print passes) with optimised glycol ink (0.5 mg/mL) on a clean glass slide (held at 80 ^{O}C). One track was printed with the quarter density method whilst the was printed conventionally, with each pass printed in one cycle. All other parameters were kept constant (see Section 2.12 for printing with glycol ink). The resolution of tracks was assessed by the optical microscopy approach given in Section 2.14 whilst electronic characterisation was carried out by the procedure stated in Section 2.15, after chemical reduction with hydrazine (Section 2.13).

2.12 Printing of films using glycol-based graphene oxide ink

The ink was degassed and introduced into the printer cartridge using the same procedure described with the aqueous-based inks (Section 2.8).

For the studies in Chapter 3, glycol ink (2 mg/mL) was used to print a set of wires of varying thickness (2.4 mm x 0.1 mm, 25 μm drop spacing, 5-30 passes). Films were printed onto glass slides (treated by the method given in Section 2.5), held at 75 ^{O}C by resting on a Peltier plate fixed on top of the printer platen. Prior to printing, the substrates were kept under a nitrogen atmosphere after plasma treatment for 30 min. A model waveform and low nozzle voltages (17-18 V) were used for the jetting of ink along with a print speed of 5 kHz, a cartridge height of 0.8 mm and a cartridge temperature of 28 ^{O}C. Films were fabricated using the low-density printing technique (provided in Section 2.11) with no drying times between print cycles required. In addition to the set of tracks, a line of droplets (1 cm long, 10 passes) was also printed under identical conditions to determine print resolution.

For the work explored in Chapter 4, printing conditions and techniques were largely kept constant. The protocol was used to generate 13 sets of samples, each containing three identical lines of droplets (2 mm long, 20 μm drop spacing, 10 passes). Printing was carried out on Al_2O_3 substrates, directly after plasma treatment (Section 2.7), whilst applying a slower print speed (2 kHz) to enhance ink adhesion to the surface.

2.13 Reduction of graphene oxide films

The chemical reduction of GO films in Chapter 3 was achieved using hydrazine vapour (500 µL hydrazine hydrate, 75 ^{O}C, 45 min), contained within a sealed glass basin on a hotplate. The formation of reduced graphene oxide (rGO) was signaled by a colour change of films from brown to black.

Out of the thirteen sets of tracks printed in Chapter 4, five were first chemically reduced using the same protocol used in Chapter 3. Each sample then underwent a second reduction at different temperatures under vacuum (~5 × 10^{-6} Torr), ranging from 600-910 ^{O}C (600 ^{O}C, 700 ^{O}C, 800 ^{O}C, 860 ^{O}C and 910 ^{O}C, 1 h each). Five GO samples were also reduced at identical temperatures for the same length of time, giving thermally reduced graphene oxide (trGO). A set of GO tracks was kept unreduced while another was solely chemically reduced, in an analogous manner with hydrazine, to act as references. Lastly, one sample was treated under vacuum at low temperature (170 ^{O}C, 6 h) to investigate the extent of reduction able to be achieved under mild conditions.

2.14 Characterisation of graphene-based film morphologies

The widths of printed tracks in Chapters 3 and 4 were measured using AxioVision 4.8 software on images collected through optical microscopy. Twenty measurements were taken at random on each set of printed films in order to calculate averages and standard deviations.

The heights of films were obtained through tapping mode AFM studies. In Chapter 4, whole cross-sections were analysed by collecting one large image (75 µm x 75 µm). In Chapter 3, only the thicknesses of films printed with the glycol ink were measured. Tracks were too wide to image all at once, with complete cross-sections obtained through acquiring and overlaying three separate images (each 80 µm x 80 µm). Average film heights across the whole profile of films were calculated using Nanoscope Analysis version 1.5 software. Ten cross-sectional measurements were taken at random for each sample to give averages and standard deviations. For the tracks printed in Chapter 3, heights were measured before and after reduction with hydrazine.

In Chapter 4, the analysis of film surface was also carried out through tapping mode AFM. Four small-scale images (5 µm x 5 µm) were collected for each set of tracks and used to determine surface roughness. This was achieved through use of root

mean square (R_q) measurements taken with Nanoscope Analysis version 1.5 software. Twenty R_q values (over areas of 1 μm^2) were gathered for each sample to calculate averages and standard deviations.
The one-way ANOVA analysis on widths, heights and surface roughness of printed films in Chapter 4 was carried out between single and dual step rGO at each annealing temperature using SPSS software.

2.15 Electronic characterisation of graphene-based films

After GO reduction (see Section 2.13), tracks were contacted with silver electrodes (1 mm^2 in Chapter 3 and 0.5 mm^2 in Chapter 4) to produce simple two-terminal devices. Electrodes were fabricated using silver nanoparticle ink, printed over tracks and sintered under vacuum (180 ^{O}C, 15 min). The contact areas between rGO and silver was kept constant within each study to eliminate any influence of contact resistance. A current/voltage (I/V) measurement using two probes (double sweep, from -2 V to 2V) was taken on each graphene-based device, with the gradient of plots between -0.5 V and +0.5 V used to calculate film resistance. The sample chamber was maintained under a dry nitrogen atmosphere and at room temperature (20 ^{O}C) during measurements. For films printed with glycol ink in Chapters 3 and 4, resistance values were used to calculate conductivities and corresponding sheet resistances, using average film heights and widths (see Section 2.14) and with track lengths measured with the aid of the printer's fiducial camera.
In Chapter 4, all three tracks were used to obtain an overall average and standard deviation for both conductivity and sheet resistance at each reduction condition. One-way ANOVA was carried out between single and dual step rGO at each annealing temperature using SPSS software.

2.16 Optical characterisation of graphene-based films

The transparencies of printed films were measured using optical images (collected at a constant exposure time of 100 ms) with ImageJ software.
For films printed with glycol ink in Chapter 3, the greyscale values of ten areas, each spanning the whole cross-section within a track, were recorded relative to the greyscale values of the background substrate (set as 100 % transmittance). This allowed for the calculation of average % transmittance values and standard deviations, with measurements made before and after reduction with hydrazine.

In Chapter 4, the same protocol was used but carried out only after the reduction of films and using five greyscale areas. One-way ANOVA was carried out between single and dual step rGO at each annealing temperature using SPSS software.

2.17 Characterisation of graphene-based films by XPS

XPS analysis was carried out on the films printed in Chapter 4. Carbon (C1s), oxygen (O1s), nitrogen (N1s) spectra as well as a survey scan were recorded for each set of tracks. Due to the high-resolution of films, spectra were recorded over a small area (27 μm x 27 μm) in order to best minimise any signal originating from the Al_2O_3 substrate. Measurements were taken with an operating power of 225 W (15 kV, 15 mA), a chamber pressure of ~3 Å~ 10−9 Torr and a step size of 0.1 eV. Binding energies were calibrated using the lowest C1s component (284.6 eV) as a reference while peaks were fitted using the CasaXPS software version 2.3.16, after a Shirley background subtraction and using a mixture of Guassian and Lorentzian functions (20:80 Guassian : Lorentzian). Atomic percentages of C1s components were calculated using the ratio of areas between components and the whole C1s envelope.

2.18 Characterisation of films through Raman spectroscopy

In Chapter 3, the Raman spectra of a GO and rGO track were collected using the Image spectrum option on Scan Control Spectroscopy Plus 1.38 software (50 μm x 50 μm area, 400 points, 2 s integration time, 150 g/mm grating). Spectra were analysed on WiTec Project 2.10 software, using the points of highest signal intensity to collate data into one average spectrum in each case. No peak deconvolution was carried out prior to the comparison of D and G band intensities.

In Chapter 4, Raman characterisation of samples was performed using the Line spectrum option on Scan Control Spectroscopy Plus 1.38 software. Three measurements (150 collated spectra over a 20 μm length, 2 s integration time) were taken for each set of tracks, with three average spectra generated with WiTec Project 2.10 software. This methodology was carried out using two different gratings, 600 g/mm to obtain information on material D and G bands and 150 g/mm for the analysis of 2D regions. Peak deconvolution was carried out with OriginLab software, using the Multiple Peak Fit tool after background subtraction and normalisation of spectra, according to Kayinor et al.[217] Reported peak intensities, shifts, areas and ratios for each film are averages of all three spectra. One-way ANOVA was carried out

between single and dual step rGO at each annealing temperature using SPSS software.

2.19 Additional characterisation of graphene-based materials

In Chapter 3, complementary FTIR and XRD data was obtained from GO drop-cast samples (20 µL x 20 layers) prepared on cleaned Si chips (see Section 2.5). During preparation, samples were held at 50 ^{O}C on a hotplate to prevent GO reduction. Spectra were acquired before and after reduction with hydrazine (500 µL, 75 ^{O}C, 45 min).

FTIR spectra were recorded using the spectrophotometer's attenuated total reflectance (ATR) attachment (1200 scans, 8 cm^{-1} resolution, 400-4000 cm^{-1} range) using a clean Si chip as a background.

XRD spectra (over the range 10-70^{O}, step size of 0.0668^{O}2θ, 1000 s integration time) were collected with the sample mounted in a stainless-steel holder (revolving at 2 RPM). Interlayer spacing was calculated through use of Bragg's Law.

2.20 cAFM of reduced graphene oxide nanoplatelets

The dispersion from Graphene Supermarket was processed (Section 2.3) and diluted (1 mg/mL) prior to further dilution with ethylene glycol (0.25 mg/mL). The glycol ink was sonicated (5 min) and degassed under vacuum (10 min) prior to injection into a DMC-11610 cartridge. Lines composed of a single row of droplets (1 cm long, 25 µm drop spacing, 1 pass) were printed onto a cleaned Si/SiO_2 chip (Section 2.5) held at 60 ^{O}C. The high temperature set-up and other printing parameters used for glycol ink (see Section 2.12) were also applied.

GO lines were reduced to rGO using hydrazine hydrate (500 µL, 75 ^{O}C, 45 min). Silver tracks (1 cm long, 25 µm drop spacing, 1 pass) were printed perpendicular to rGO lines and sintered under vacuum (180 ^{O}C, 15 min). The silver/rGO network was contacted to a metallic AFM chuck with gallium-indium eutectic to complete the cAFM sample. Areas along silver/rGO boundaries were imaged in contact cAFM mode using an extended TUNA (S/N 673) application module. A negative bias was applied while a slow scan rate (0.1 Hz) was used to minimise noise and reduce sample and tip damage. Any areas containing clusters of platelets were rescanned under normal tapping mode AFM to provide a more resolved topological image.

2.21 Synthesis of CdS/λ.DNA nanowires

The solution-based protocol previously reported in literature was followed.[182] An aqueous solution of $Cd(NO_3)_2$ (200 mL, 0.2 mM) was added to an aqueous solution of λ.DNA (200 µL, 500 ng/µL,1.5 mM nucleotide concentration). The solution was gently mixed and incubated for 24 h at 4 ^{O}C. An aqueous solution of Na_2S (200 µL, 0.2 mM) was added to the solution before mixing and further incubation for 24 h at 4 ^{O}C. A second addition of $Cd(NO_3)_2$ (20 µL, 20 mM) was carried out and allowed to interact for 24 h (4 °C) before a second introduction of aqueous Na_2S (20 µL, 20 mM). The formation of cadmium sulphide was signaled by a colour change in the solution from colourless to pale yellow upon the addition of Na_2S. The solution was incubated again for 24 h at 4 ^{O}C before characterisation and formulation into an ink.

2.22 Preparation of substrates for use with CdS/λ.DNA

Si chips and glass slides were cleaned and treated in an analogous manner to those used with GO, with protocols outlined in Section 2.5. After plasma treatment, glass surfaces were held under a nitrogen atmosphere (30 min) prior to printing.
Pt-on-glass IDEs were cleaned in piranha solution (H_2SO_4 to H_2O_2 v/v ratio of 1:4, 5 min) before washing and sonication in water, acetone and ethanol (15 min each). The IDEs were dried under a stream of nitrogen, plasma-treated (10 min, 90 W, 150 sccm) and held under nitrogen (30 min) prior to printing. IDEs were confirmed to be clean and free from contamination through the measuring of background currents on the single picoamp (pA) scale upon application of a bias (-2 V to 2 V).

2.23 Characterisation of CdS/λ.DNA solution

AFM samples of bare λ.DNA and CdS/λ.DNA nanowires were prepared by dilution of solutions (1-5 ng/µL DNA) and drop-casting (5 µL) onto cleaned Si chips (Section 2.22). The droplet was left to sit on the surface (5 min) before being blown off with a gentle nitrogen stream to help align strands. Images were collected with the AFM system operated in ScanAsyst-in-Air mode, with the heights of strands or nanowires measured with use of Nanoscope Analysis version 1.5 software (Bruker).
UV-Vis spectra of λ.DNA and CdS/λ.DNA solutions (1.5 µL) were recorded using the pedestal accessory of the NanoDrop. The absorption behavior over the range of 200-800 nm was measured, with values scaled to a pathlength of 1 cm by the instrument software. An aqueous solution of cadmium sulphide, synthesised in a similar manner

to the nanowires (see Section 2.21) but in the absence of DNA was also measured to provide a reference.

Fluorescence microscopy samples of CdS/λ.DNA and bare λ.DNA were prepared by drop-casting solutions (1 µL, 156 ng/µL DNA) onto clean Si chips (Section 2.22) with droplets allowed to dry naturally in air. Images were collected with AxioVision version 4.8 software (Zeiss) and at an exposure time of 4 mS. A mercury arc lamp was used as the excitation source along with a bandpass filter to give light of wavelengths 300-400 nm. The fluorescence spectrum of the CdS/λ.DNA solution was also recorded using a quartz cuvette (1 cm path length) and under an excitation wavelength of 370 nm.

XPS spectra were recorded using a drop-cast sample of CdS/λ.DNA (20 µL,156 ng/µL DNA) on a clean Si chip (Section 2.22). Spectra were recorded at an operating power of 150 W (15 kV, 10 mA), a chamber pressure of ~3 × 10^{-9} Torr. and with a step size of 0.1 eV. Binding energies were calibrated using the lowest C1s component (284.6 eV) as a reference while peaks were fitted using the CasaXPS software version 2.3.16.

A powder sample for XRD was obtained through a scaled-up synthesis, using calf thymus (CT) DNA solution (10 mL, 1 mg/mL), $Cd(NO_3)_2$, (10 mL, 0.5 M) and Na_2S (10 mL, 0.5 M). Data was collected over the range 10-70^O and with a step size of 0.0668^{O}2θ. During XRD data collection the sample was mounted in a stainless-steel holder (revolving at 2 RPM). Phase identification was carried out with PANalytical High Score Plus software in conjunction with the ICDD Powder Diffraction Database. Particle size was calculated through use of the Scherrer equation on the dominant (1,1,1) peak at 2θ = 26.6^O.

FTIR samples of CdS/λ.DNA and bare λ.DNA were prepared on clean Si chips (Section 2.22) by drop-casting solutions multiple times until a film of material formed. Spectra were recorded using the ATR accessory of the spectrophotometer, at a spectral resolution of 4 cm^{-1}. 32 spectra were gathered and averaged for each sample, with a clean Si chip used as the background.

2.24 Formulation of CdS/λ.DNA ink

The CdS/λ.DNA solution prepared by the method given in Section 2.21 (500 µL, 156 ng/µL) was diluted through the addition of nanopure H_2O (500 µL) and ethylene glycol (1000 µL). The result was a printable ink (2000 µL) composed of water and

ethylene glycol in a volume ratio of 1:1. The ink was degassed under vacuum (20 min) prior to injection into a DMC-11610 printer cartridge.
Other ink formulations were also prepared with varying water to glycol ratios in order to assess the effect of glycol content on nanowire conformation. This was undertaken through AFM imaging of nanowires, with samples prepared and used in an analogous manner to those previously described in Section 2.23.

2.25 Printing of CdS/λ.DNA droplet arrays on glass

Droplet arrays were printed onto a clean glass surface (Section 2.22) using the CdS/λ.DNA ink with 50 % glycol content (Section 2.24). A highly manipulated waveform was required for stable droplet formation with high nozzle voltages (28-30 V). The ink was held in the cartridge at 30 ^{O}C, with a cartridge height of 0.8 mm used during printing over the glass surface (held at 60 ^{O}C). Droplets were printed at a large spacing (150 μm) to prevent merging of droplets and with a slow firing frequency (1 kHz) to help maintain print accuracy. The number of print passes was varied over the range of 25-250 to create a set of CdS/λ.DNA spots of varying thickness.

2.26 Printing of CdS/λ.DNA over Pt-on-glass IDEs

Pt-on-glass IDEs were cleaned and treated by the procedure stated in Section 2.22 whilst samples were printed using the same CdS/λ.DNA ink and printing parameters described previously in Section 2.25.
For the printing of CdS/λ.DNA droplet arrays, a 100 μm drop spacing was used with 100 printing passes carried out to bridge electrode gaps with sufficient amount of material. Droplets were printed over the whole area of electrode fingers (5 mm x 7 mm).
For the printing of continuous CdS/λ.DNA tracks, drop spacing was reduced to 40 μm in the x-direction to allow droplets to overlap while spacing in the y-direction was 150 μm. A low-density technique (explained in Section 2.11) was implemented to maintain pattern resolution by preventing uncontrolled wetting of ink. This involved printing one in every four droplets within rows per print cycle.

2.27 Characterisation of CdS/λ.DNA droplet arrays on glass

AFM images of printed droplets were collected by tapping mode AFM with typical cross-sectional profiles obtained through use of Nanoscope Analysis version 1.5

software. The same software was also used to measure the maximum heights and widths of CdS/λ.DNA rings at droplet peripheries. 20 measurements were taken in each case to calculate averages and standard deviations.

Fluorescence images of droplets were collected with AxioVision version 4.8 software and at a constant exposure time of 3.18 s. A mercury arc lamp was used as the excitation source along with a bandpass filter to give light with wavelengths 300-400 nm. To quantify fluorescence, the mean brightness over the whole image was measured with ImageJ software, in order to keep the area between samples constant. This was followed by subtraction of the background brightness and normalisation of values to that of a 25-print pass droplet. 10 droplets for each thickness were analysed in this manner to give average fluorescence values.

Raman images of droplets were collected using Scan Control Spectroscopy Plus 1.38 software (WiTec, 100 μm area scan, 50 x 50 spectral points, 2 s integration time). The spectra from the bright areas of intense signal, relating to CdS material, were co-added to give an average Raman spectrum. Images were collected using gratings of both 150 g/mm and 600 g/mm in order to see the material's broad luminescence as well as its LO phonons.

2.28 Characterisation of CdS/λ.DNA over Pt-on-glass IDEs

AFM imaging of samples was carried out under tapping mode, with height and width measurements of CdS/λ.DNA bands measured with Nanoscope Analysis version 1.5 software. 20 measurements of for each sample was made in order to calculate averages and standard deviations.

Fluorescence images of droplets were collected with AxioVision version 4.8 software with exposure times within the range of 1-5 s. A mercury arc lamp was used as the excitation source along with a bandpass filter to give light with wavelengths 300-400 nm.

Electrical characterisation of samples was carried out through the recording of current/voltage (I/V) sweeps (double sweep, -2 V to 2 V) at controlled temperatures (20–80 ^{O}C) and under a dry nitrogen atmosphere in the absence of illumination. Arrhenius plots were determined through the calculation of the zero bias conductance G, using forward scans.

2.29 Sintering of CdS/λ.DNA

Samples printed over Pt-on-glass IDEs were held on a hotplate under ambient conditions (150 ^{O}C, 1 h). Samples were then electrically characterised by I/V sweeps (double sweep, -2 V to 2 V) at a temperature of 20 ^{O}C, under a dry nitrogen atmosphere and in ambient air.

The XRD sample of CdS/λ.DNA before and after sintering was prepared on a clean Si chip (Section 2.22) by drop-casting of solution multiple times until a thin film of material formed. An XRD spectrum of the film was recorded before and after the sintering step (over the range 10-70^{O}, step size of 0.0668^{O}2θ, 1000 s integration time). During XRD data collection the sample was mounted in a stainless-steel holder (revolving at 2 RPM). Phase identification was carried out with PANalytical High Score Plus software in conjunction with the ICDD Powder Diffraction Database. Changes in particle size were calculated through use of the Scherrer equation on all peaks.

2.30 Photoconductivity of CdS/λ.DNA

I/V curves (double sweep, -2V to 2 V) of printed and sintered samples over Pt-on-glass IDEs were recorded at 20 ^{O}C under a dry nitrogen atmosphere with and without external illumination by a UV lamp, balanced over the top of the probe station chamber. I/V curves were collected at UV light wavelengths of 254 nm and 365 nm.

Chapter 3. Overcoming the printability issues of graphene oxide

3.1 Introduction

Graphene has been identified as a promising candidate to replace indium tin oxide (ITO), a n-type semiconductor widely-used as conductive, transparent electrodes in optoelectronic devices.[12–16] ITO films exhibit excellent conductivity (in the range of 10^5-10^6 S/m), low sheet resistance (<40 Ω/sq) and high transparency in the visible range (>80 % transmittance at 550 nm).[114] However, ITO is a scarce commodity whilst film fabrication, typically achieved through physical vapour deposition processes, are expensive.[115] ITO films also struggle to meet the increasing demands of optoelectronic devices, with the material having limited flexibility and chemical stability.[116,218] Graphene has the potential to provide the high conductivity and transparency needed for optoelectronic films, with sheet resistances as low as 30 Ω/sq and single-layer sheets only absorbing 2.3 % of visible light at 550 nm.[12,129] The material is also cheaper than ITO and can give the improved flexibility for devices that need to bend or stretch. Graphene can also be developed into inks suitable for inkjet technology, allowing for a low-cost method of production for conductive and transparent films.

The formulation and inkjet printing of graphene platelets is widely reported in literature with inks containing a range of graphene-based derivatives.[3,48,56] The use of graphene have been extensively studied but problems still persist with the processing of the material into a viable ink. The mechanical exfoliation of graphite to single or few layer graphene can be time-consuming and requires the use of harmful solvents such as NMP or DMF.[2,102,219] The stability of the material in solution is also poor, with inks typically of low concentration and requiring binders or stabilisers to prevent precipitation.[49–51,102] The presence of these species can help tailor ink rheology for inkjet technology but ultimately have to be removed post-printing to enhance film conductivity, usually requiring extreme temperature. [32,49,102,220,] The same issues with material dispersion are also encountered when using reduced graphene oxide (rGO) platelets, with similar techniques used to help overcome these.[5,8,32,221]

An alternative graphene derivative commonly used for inks is graphene oxide (GO).[56,218–221] One of the main attractions of using GO is that ink formulation procedures are uncomplicated compared to graphene and rGO. The presence of hydrophilic functional groups allows for the production of more concentrated, highly stable aqueous dispersions without any need for binders.[7,10,56,105] These oxygenated groups also allow for more flexibility when tailoring the material towards certain

applications, providing linkage points for the covalent attachment of additional functional groups to the graphene surface to give a functionalised GO ink.[47,226]

However, there are also several issues associated with the inkjet printing of GO. Due to the high surface tension and low viscosity of water, the rheological properties of aqueous inks tend to lie outside the boundaries recommended for reliable jetting.[53,62,88] This means highly manipulated jetting waveforms and extreme nozzle voltages are required for the jetting of distinct, spherical droplets.[53,62] These droplets tend to be highly unstable over time, with satellite formation or changing speeds or angles prevalent, and can often result in a loss of film resolution.[53]

The undesirable physical properties of water also create problems once the ink has been deposited on a surface. Their high surface tensions drive the movement of material towards the edges of drops meaning films often exhibit the coffee-ring effect.[7,55,72] This phenomenon is enhanced on high energy surfaces, such as glass or plasma-treated silicon, where the surface tension gradients and resulting capillary flow of particulates is greater.[2,227] The use of these high energy or hydrophilic substrates with aqueous or low viscosity inks also poses an extra risk of uncontrolled wetting, with droplets forming low contact angles. This impacts on the film resolution able to be achieved with cases in literature reporting printed line widths greater than 100 μm.[2,72,73] For these reasons, surfaces such as glass or silicon are often avoided if possible or modified beforehand to lower surface energy and better immobilise material.[32,228] Less hydrophilic polymer films or papers are extensively used with GO inks, with these also compatible for use as flexible graphene-based devices.[7,30–32]

In order to improve rheology, previous work by other groups has involved the introduction of cosolvents within GO inks.[10,30,59,60] These tend to be highly viscous, low surface tension liquids, such as glycols or glycerol, with the effect of improving jetting performance while reducing film deterioration caused by the coffee-ring effect. Due to the high boiling points of solvents, these are generally introduced in an additive manner, with ink composition still predominantly water.[10,30,59,60] Nearly all inkjet printing processes are carried out below 60 ^{O}C meaning the presence of too much of these solvents can lead to prolonged drying times and loss of all film resolution.[27]

Due to the presence of sp^3 hybridised carbons within GO, printed films often exhibit poor conductivity. In order to enhance this property a reduction step is typically carried out on films to remove oxygenated defects and repair the 2D lattice. RGO can

be formed through several means but chemical reduction, through use of agents such as hydrazine or halogen acids, and thermal reduction are most common.[101,148,216] The electrical activity of the film is dependent on the efficiency of the reduction method employed as well as on the quality of the printed film, in terms of homogeneity and resolution. Film conductivities for inkjet-printed rGO films derived from GO can range from tens to tens of thousands S/m, with many cases higher than those using graphene inks.[56] The highest film conductivities reported to date are 42,000 S/m using GO ink and 25,600 S/m using graphene ink, corresponding to sheet resistances of 25 Ω/sq and 130 Ω/sq respectively.[51,60]

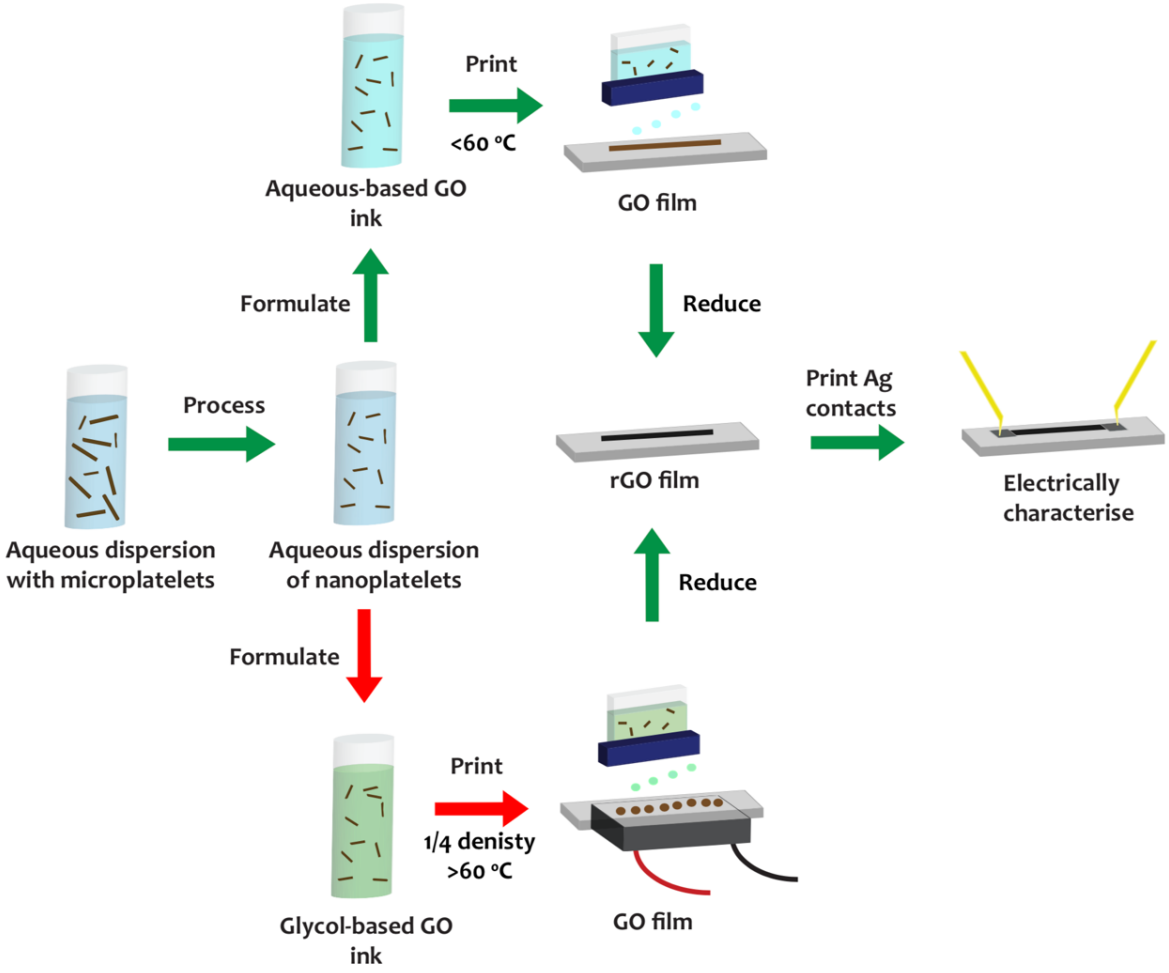

Figure 3.1 Schematic of how to fabricate a conductive rGO film using GO ink. The top pathway shows the traditional method of producing such a film, involving an aqueous-based ink printed at temperatures below 60 ^{O}C. The bottom pathway highlights the protocol introduced in this chapter, involving the formulation of a novel glycol-based ink able to be used in conjunction with a low-density printing technique at high temperature. In both cases, printed GO films still require a reduction step to yield conductive rGO.

The following chapter deals with the first aim of the thesis by presenting efforts to combat the printability issues routinely experienced with the use of GO inks. A method for the production of a highly stable aqueous GO ink from a commercial dispersion is first established and used to print tracks on glass substrate with a Dimatix DMP 2800 inkjet system. This high energy, hydrophilic surface was chosen in order to provide the toughest examination of the robustness of the printing techniques used. Several ink solvent systems are first trialled, through the inclusion of miscible organic additives, with their effects on film resolution and resistance compared after chemical reduction. Subsequent work sees the formulation of a novel, highly optimised GO ink, which can be used at temperatures beyond 60 ^{O}C through the modification of a Dimatix system. A low-density print cycle protocol is also introduced to prevent uncontrolled wetting on the glass surface and increase film resolution. The physical properties of films printed with the optimised ink are extensively characterised before and after chemical reduction with results demonstrating transparent films that exhibit high resolution, improved homogeneity and good conductivity.

3.2 Results and discussion

3.2.1 Processing of graphene oxide dispersion into a printable ink

A highly concentrated GO dispersion in water was bought from Graphene supermarket. Graphene oxide platelets within this solution predominantly exist as single-layer species yet their lateral dimensions, ranging from 500 nm up to several microns, are too large to print using a Dimatix cartridge without causing nozzle blockages. Guidelines state that particles within an ink should be at least one fiftieth the size of the nozzle diameter for efficient jetting.[2,29,72] With the diameter of the cartridge nozzles being just over 21.5 μm, the platelets within this solution should be sheared in size to at least 0.45 μm. The method used to achieve this is outlined in the Methodology, Section 2.3, and consisted of several hours of sonication within an ultrasonic bath to reduce platelet size. During this step, the temperature was kept below 35 ^{O}C to prevent agglomeration of material and evaporation of solvent. Several centrifugation cycles and a final filtration step were then carried out to ensure removal of any larger microscale GO flakes.

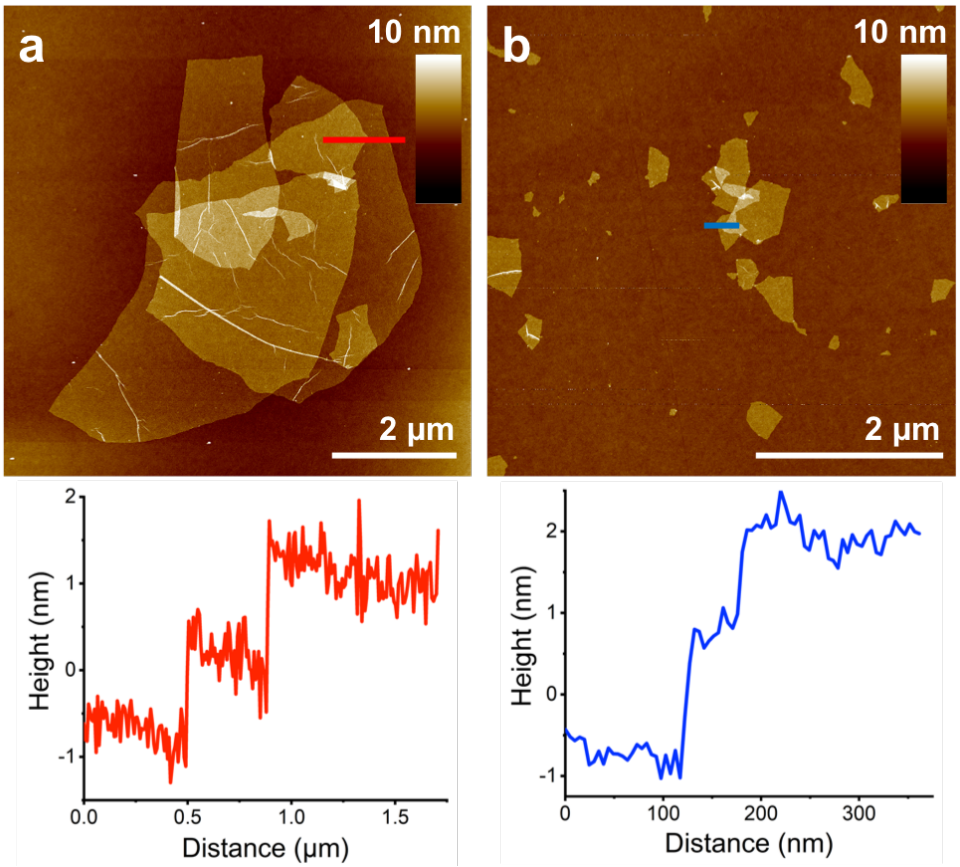

Figure 3.2 AFM images of GO platelets drop-cast on Si chips before processing (a) and after processing (b) with layer heights given below.

The change in flake size as a result of processing can be observed from the AFM comparison displayed in Figure 3.2. Image a shows an area of a few large, overlapping platelets present within the unprocessed dispersion while Image b, from the processed ink, shows smaller and more numerous platelets. In both cases GO's characteristic wrinkles can be observed, likely caused during the drying process.[229] The heights of sheets from both samples were measured, with an example of a step height measurement included below the images in each case. Heights were found to be constant before and after processing, in the order between 1.0 and 1.5 nm high. This is indicative of single-layer GO and proves that the material is well exfoliated and stable in water as expected.[230] The identical step heights seen between samples suggests that the GO shears through the breaking of carbon-carbon bonds within the basal plane, most likely at defect points within the lattice where oxygenated groups have broken the conjugated structure.[231] UV-Vis spectra were also recorded of the dispersion before and after processing (Methodology, Section 2.4) with practically identical absorption behaviour seen (Appendices, Figure 3A). Notably both samples exhibit an intense peak at 230 nm, corresponding to an n-π^* transition, with the absence of any notable shoulder between 226-232 nm. This represents a sample containing single or few-layer (1-3 layer) GO sheets and confirms that dispersion processing is merely needed to shear particle size rather than for exfoliation of layers.[232]

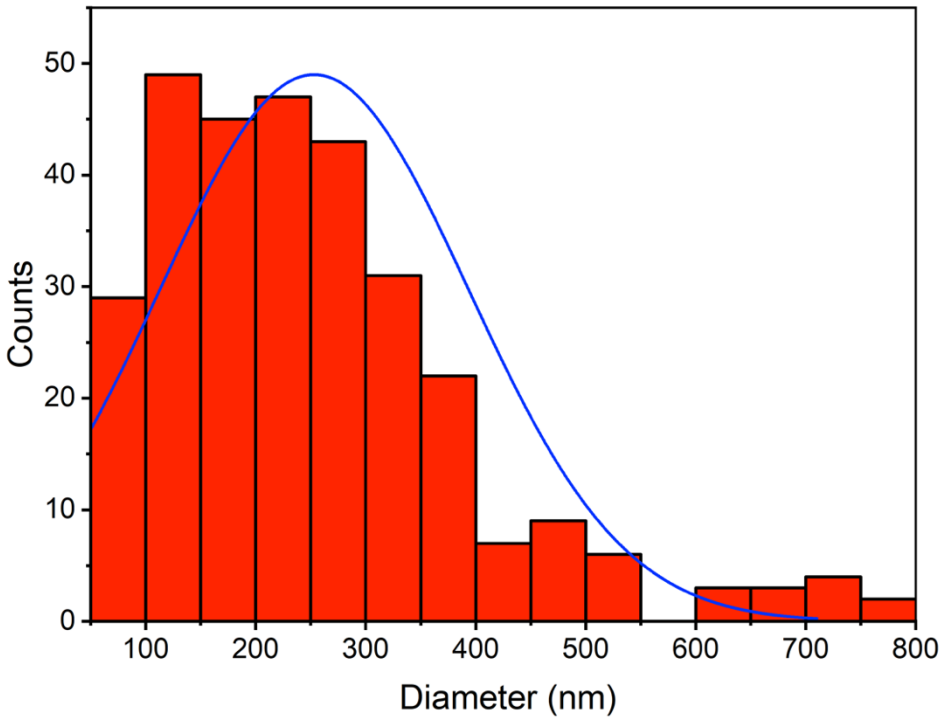

Figure 3.3 Size distribution of average platelet diameters within the processed ink, consisting of 300 measurements and giving an overall average diameter of 253 nm.

To confirm that all platelets within the processed ink were of the required size for printing, extensive AFM analysis of their average diameters was carried out (Methodology, Section 2.4). Measurements on 300 platelets were taken (Figure 3.3) with all sheets exhibiting diameters below 800 nm. 95 % of the flakes were smaller than 450 nm, nearly one fiftieth the size of the nozzle diameter, while an average particle diameter of 253 nm was recorded for the whole data set. This size is almost a hundred times smaller than the nozzle and implies that the shearing and filtration steps used are suitable to provide a dispersion fine enough to be printed without fear of nozzle blockage.[2,29,72] This size range and average also correlates to reports of successfully printed graphene-based inks using the same Dimatix cartridges.[6,88,102]

3.2.2 Formulation and printing of aqueous-based GO inks

With a reliable method for making a printable GO ink in place, research investigating the relationship between ink rheology and print quality was undertaken, with comparison to the 100 % aqueous ink. Water-based GO inks are difficult to work, with poor jetting performance leading to poor resolution and severe capillary flows on the surface disrupting film homogeneity.[53,72] Other groups frequently report the use of organic cosolvents within aqueous GO inks to alleviate these issues through partial tuning of the fluid's physical properties.[10,30,59,60]

In a similar manner, several cosolvent GO inks were trialled (Methodology, Sections 2.6 and 2.8). This involved the printing of an identical set of films with a variety of GO inks, each containing a different additive, followed by an evaluation of resolution through optical measurements and resistances after reduction with hydrazine vapour and contacting with silver. The thickness of all films was kept constant while length was altered within sets to generate resistance vs. distance relationships and determine the contact resistance between rGO and silver. The additives used were miscible with water and added in a 9 % v/v manner, falling below the suggested threshold of 25 % v/v.[27] At concentrations exceeding this upper limit, high boiling point solvents such as glycols and DMF can prolong the drying time of inks, resulting in the loss of resolution to printed features. Along with the aqueous reference ink, DMF, THF, ethylene glycol (EG) and propylene carbonate (PC) were tested (Appendices, Table 3A). These solutions are known to maintain stable dispersions of GO over a timeline of a few weeks.[233,234] All four organic solvents were chosen on their potential to either raise viscosity, lower surface

tension or both to favourably increase the Ohnesorge number of the GO ink.[235]

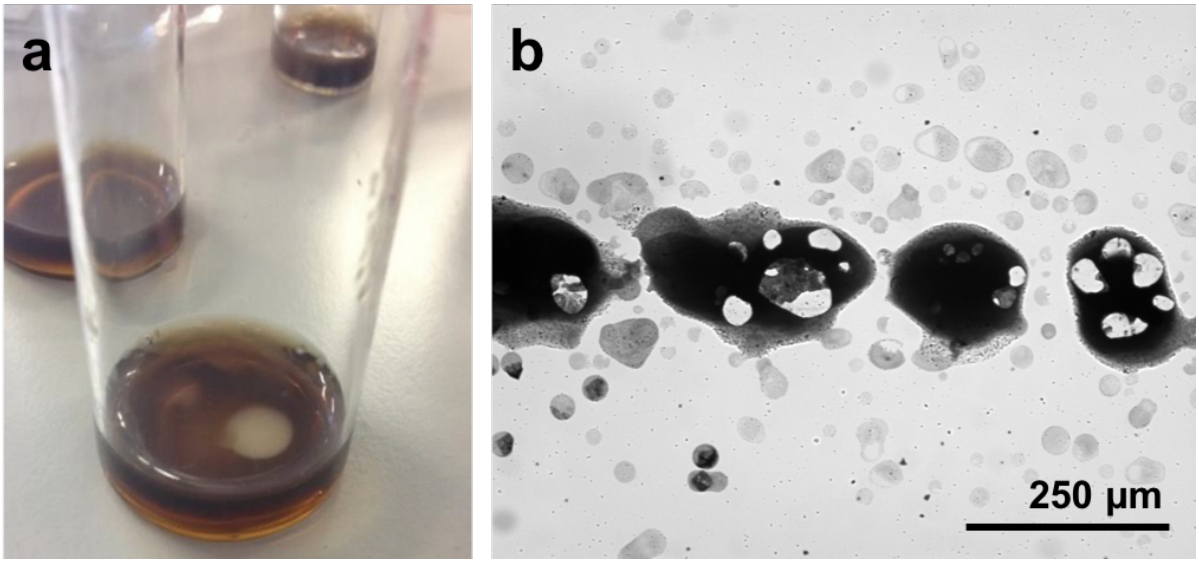

Figure 3.4 Images highlighting the issues encountered with GO.PC and GO.THF inks. a) GO.PC ink was unable to installed into the cartridge with the formation of a phase upon mixing. b) A typical discontinuous track printed on glass when using the GO.THF ink.

Out of the five inks tested, only the GO.PC ink was unsuitable for injection into the cartridge. This was due to the presence of an opaque phase floating on the surface of the ink (Figure 3.4, Image a), suggesting the solvent was not fully miscible at this concentration. Problems were also encountered with the GO.THF ink which failed to reliably print continuous films (Figure 3.4, Image b). The formation of large islands of material is characteristic of uncontrolled wetting, with ink unable to immobilised effectively on the glass surface before drying.[27] THF has the lowest surface tension and viscosity of all solvents used with lowering of either able to give smaller contact angles on a given surface.[2,235] Severe satellite destruction is also evident as a result of misfiring droplets.[53] Given this evidence it can be assumed that THF is an unsuitable candidate for optimising GO ink rheology for printing on high energy, hydrophilic surfaces.

3.2.3 Resistances of films printed with aqueous-based inks

GO (ref), GO.EG and GO.DMF inks were all capable of producing a set of continuous tracks under the selected conditions. Their resistance vs. length plots, after reduction with hydrazine vapour and contacting with silver (Ag), are shown below in Figure 3.5,

fitted with linear trend lines and with y-intercept denoting the rGO/Ag contact resistance (Methodology, Sections 2.13 and 2.15).

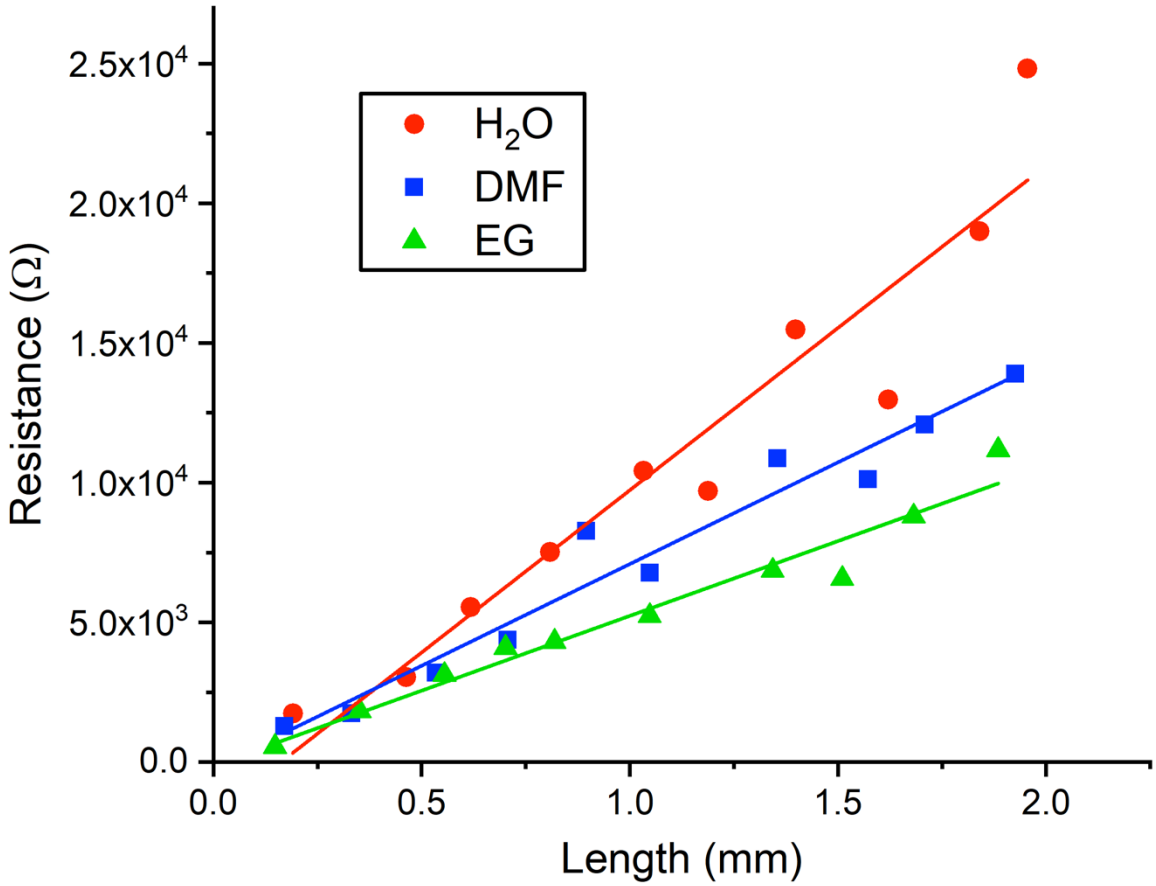

Figure 3.5 Resistance (Ω) vs. length (mm) plots for rGO/Ag two-terminal devices, printed on glass using GO (ref), GO.DMF and GO.EG inks. Plots are fitted with linear trend lines, with gradients of 11.6 Ω/μm, 7.28 Ω/μm and 5.35 Ω/μm calculated for H_2O, DMF and EG additives respectively.

As expected, the resistances of samples are found to decrease with decreasing length between the electrodes in all three cases. With the thickness of films kept constant, a linear relationship should be obtained but deviations from this are observed.[236] This is probably a result of unstable jetting of inks combined with the change in surface energy of the glass over time. Tracks for each ink were printed on the same glass slide one at a time, longest to shortest, directly after surface plasma treatment. From contact angle studies taken on glass after exposure to oxygen plasma (Appendices, Figure 3B), the surface energy is found to gradually decrease over a 90-minute period. This will impact on the wettability of inks and ultimately the quality of the printed film. The negative y-intercepts for all three sets, suggest that this value is negligible compared to the resistance of the rGO films themselves. Both GO.EG and GO.DMF inks gave rise to less resistive films than the aqueous

reference ink, where tracks had a resistance of 11.6 Ω/μm (Figure 3.5). Films printed with the glycol additive gave the best electrical performance, where resistance more than halved to 5.35 Ω/μm. Less of an improvement in film quality was seen with the GO/DMF ink, where tracks exhibited resistances of 7.28 Ω/μm.

3.2.4 Resolution of films printed with aqueous-based inks

For both GO.EG and GO.DMF cosolvent inks, a reduction in the width of films was seen (Appendices, Table 3A). A decrease of over 20 μm was observed for the GO.DMF ink while a more significant drop of over 60 μm was measured for the GO.EG ink. The difference in film diameter can be explained by the wetting properties of the inks on the glass surface (Methodology, Section 2.7). From measurements shown in Figure 2.6, both cosolvent inks exhibited higher contact angles on the surface compared to the aqueous reference. A 5^{O} increase in contact angle was seen with GO.DMF ink and a more substantial increase of 11^{O} for GO.EG ink. In the case of GO.EG ink, this can be explained by the high viscosity of the glycol component, which is sixteen times more viscous than water.[235] This reasoning cannot be applied for the DMF cosolvent ink, with both viscosity and surface tension of the additive lower than that of water. However, wetting is also dependent on the polarity of the surface and liquid, with more hydrophilic solvents adhering better to hydrophilic surfaces due to lowering of interfacial surface tension.[237] With this in mind, it could be theorised that higher contact angles are observed due to the reduction in ink polarity, with DMF having a dielectric constant of 19.9 and water 80.1.[238] Using the electrical and wetting data, there seems to be a relationship of increasing ink contact angle giving films with lower resistances. It would appear that the improvement in film conductivity seen with cosolvent inks is a consequence of better immobilisation of material on the surface.

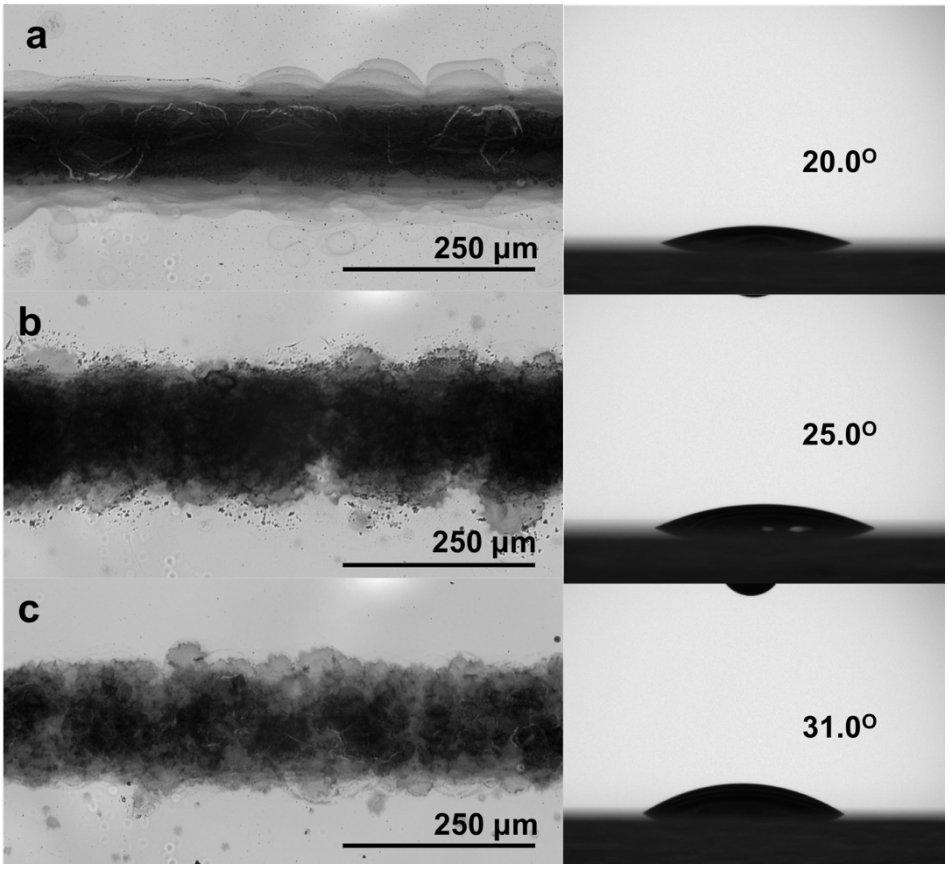

Figure 3.6 Optical images of rGO tracks printed with GO reference ink (a), GO.EG ink (b) and GO.DMF ink (c) with corresponding ink contact angles on glass before plasma treatment shown.

Even though films printed with cosolvent inks exhibited smaller widths compared to those with the aqueous reference, they are still of poor resolution. The calculated diameters exceeded 200 µm, over twice the width programmed on the printer, while standard deviations were large (Appendices, Table 3A). This is due to the highly wetting nature of the inks on the surface combined with too small a drop spacing.[2] From observation of optical images in Figure 3.6, satellite destruction can also be highlighted, albeit not as severe as seen with the GO.THF ink (Figure 3.4, Image b). This implies a slight improvement in jetting performance when using these inks, although highly manipulated waveforms and extreme nozzle voltages were still required to minimise droplet inaccuracy. This suggests that the rheological properties of these inks still lie outside the boundaries required for reliable droplet generation.

3.2.5 Allowing for the printing of optimised GO inks

The additive studies concluded that the presence of ethylene glycol within the ink solvent system yielded the biggest improvement with regards to conductivity and

resolution of printed films. This was attributed to a dual effect of the glycol; increasing the viscosity of the graphene oxide ink while also lowering its surface tension.[53] The alteration of these physical properties favourably heightens the Ohnesorge number of the ink and at the same time reduces uncontrolled spreading on the surface to better maintain film morphology. However, this water-glycol dispersion is far from being an optimised ink with only slight improvements in jetting performance and wettability observed and films lacking homogeneity and resolution still persisting. These issues could be alleviated through the addition of more glycol into the solvent system to further tailor rheology but the maximum platen temperature of 60 ^{O}C places limits on this approach. Mixtures comprising of larger quantities (>25 % v/v) of high boiling point solvent suffer from prolonged drying times upon the substrate leading to loss of all film resolution.[27]

Figure 3.7 Photograph of the high-temperature printing set-up involving a Peltier plate, connected to an external power pack and taped to the platen of the printer to raise the system's maximum temperature. The substrate to be printed on is placed on the hot plate rather than the platen.

With this in mind, a new printing technique was trialled involving temporary modification of the inkjet system with a Peltier plate (Figure 3.7). This is a miniature two-sided plate, able to be used as a thermoelectric generator when a current is passed through it. The plate acts as a heat pump, generating a higher temperature on its top surface compared to its bottom. The temperature measured is dependent upon the bias applied and the temperature underneath. When placed on the printer's

platen and connected to an external power source, higher temperatures could be established on surfaces held on top through utilisation of a 'hot-plate on a hot-plate' setup. The previous restrictions imposed on the quantity of high boiling point solvent are now lifted, allowing for the formulation of GO inks with rheology better suited for inkjet technology. The use of this tactic with a Dimatix system does not appear in current science.

3.2.6 Jetting performance of optimised GO ink

As the best candidate from additive trials, ethylene glycol was chosen again as the ink's cosolvent. It was discovered that when mixed with the aqueous GO ink in a 75 % v/v manner a stable ink resulted (Appendices, Figure 3C), with viscosity and surface tension properties suited for high-fidelity droplet formation. The preparation of this ink (Methodology, Section 2.9) signifies the movement from aqueous-based GO ink systems to an organic, glycol-based system.

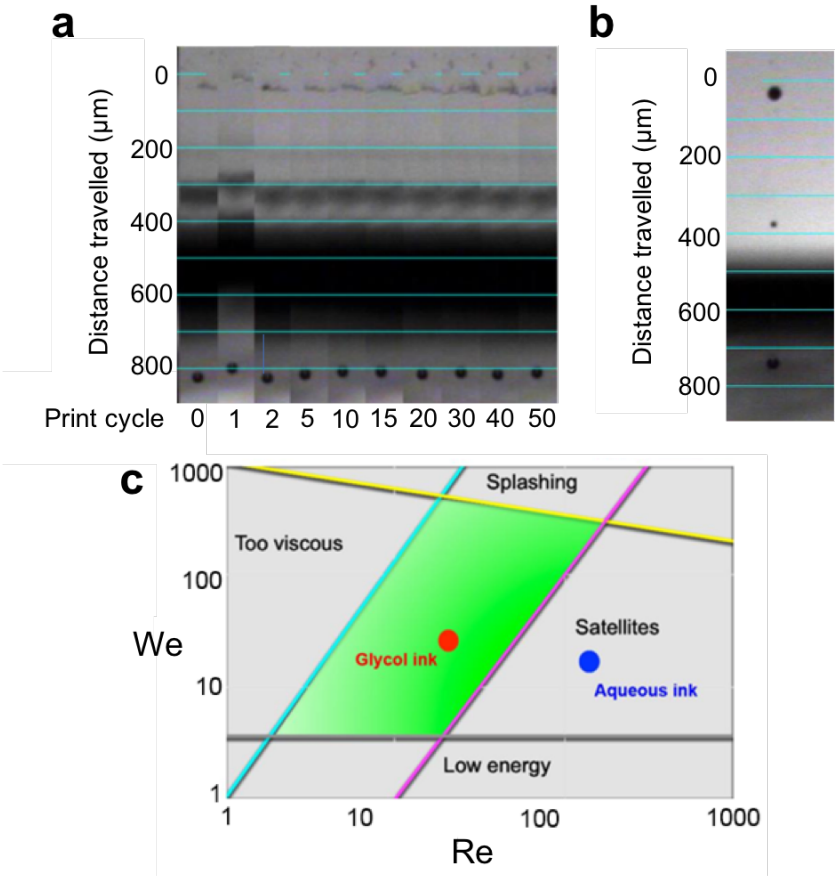

Figure 3.8 a) Snapshots taken of GO.EG (75 % v/v) ink droplets taken over 50 print cycles, without nozzle reoptimisation. Images were taken on the Dimatix Drop Watcher application, 100 µs after ejection. b) Typical droplet generated using an aqueous GO ink, exhibiting satellite formation. c) Characterisation of the jetting performance of aqueous and glycol GO inks with use of an Ohnesorge chart, based on Weber (We) and Reynold (Re) values.

Upon analysis with the printer's Drop Watcher camera, spherical droplets with speeds of 8 m/s were able to be expelled from the cartridge (Figure 3.8, Image a). Droplet speeds between 7-10 m/s are necessary in order to hit the substrate in their targeted positions.[27] Importantly, these drops, roughly 30 μm in diameter in flight, were ejected with more conventional printing parameters, with the ink operating with a model fluid waveform and low nozzle voltages. A preliminary experiment proved that the droplet ejection was stable over extended printing periods, with no change in droplets seen over fifty print cycles and with no re-optimisation of the nozzle in between (Methodology, Section 2.10). This scenario is unattainable with the aqueous inks or other cosolvent inks trialled previously, where satellites were visible at the target droplet speeds. (Figure 3.8, Image b).

This improvement in jetting performance can be attributed to the optimisation of the ink's physical properties towards inkjet technology. The large quantity of glycol present in the solvent system significantly increases the ink's Ohnesorge number, bringing its value to within the boundaries outlined for precise jetting. This change can be visualised with aid of an Ohnesorge chart (Figure 3.8, Image c), with the Weber and Reynold components calculated for both aqueous and glycol ink solvent systems from literature.[239,240] A change in Ohnesorge number from 0.027 (Z = 37.4) for the aqueous ink to 0.237 (Z = 4.2) for the glycol is determined, with this value within the range suggested for reliable jetting (the green area within the Ohnesorge chart). The larger volume of glycol notably increases the viscosity of the solution from 0.89 cp to 8 cp, while lowering surface tension from 72 dynes to 51 dynes, to cause this. Calculations were proven to be accurate through experimentally measuring the surface tensions of both inks through pendant drop measurements (Methodology, Section 2.10) while also measuring the viscosity of the glycol ink (Appendix, Figures 3D and 3E). The agreement between theoretical and experimental calculations show that the GO platelets within solution have a negligible contribution to the ink rheology. This can be expected with platelets being on the nanoscale and in concentrations not exceeding 2 mg/mL.[241]

3.2.7 Homogeneity and resolution of tracks printed with optimised GO ink

AFM analysis on the distribution of platelets within printed patterns was undertaken with both aqueous and glycol-based inks (Methodology, Section 2.10). This was done by printing identical lines, one droplet in diameter, onto Si chips, with the aqueous GO ink diluted to the same concentration as glycol ink (0.5 mg/mL). The

glycol-based ink was printed with aid of the Peltier plate at a temperature of 80 ^{O}C while the reference ink was printed under standard inkjet printing conditions on the platen at 50 ^{O}C.

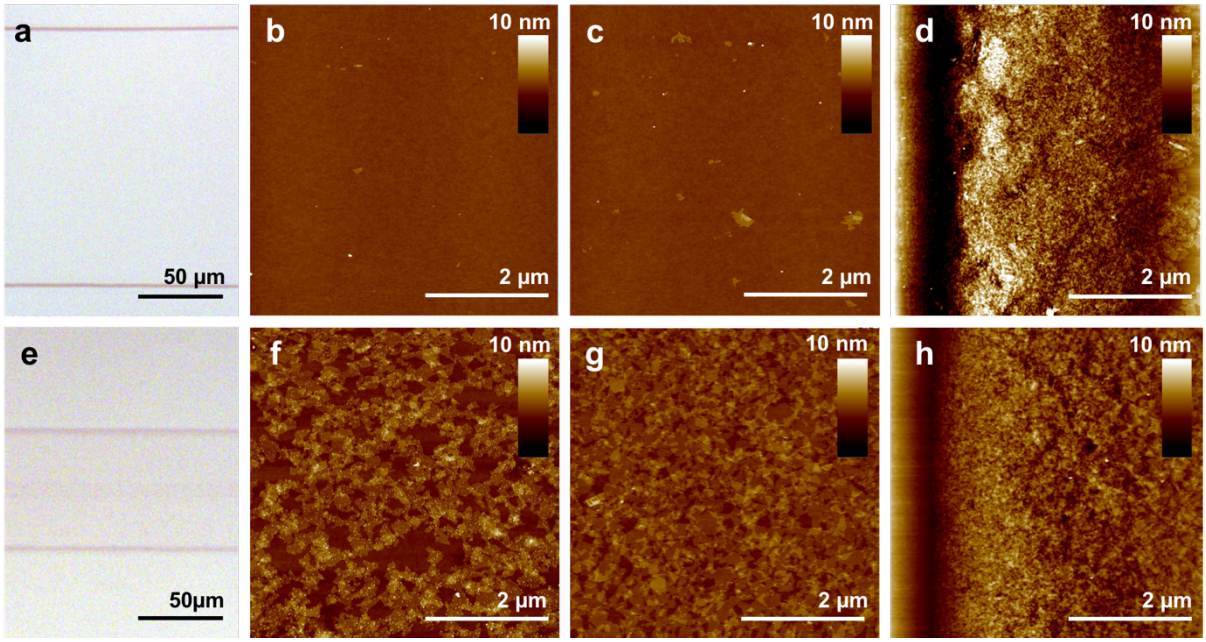

Figure 3.9 Tapping mode AFM analysis of platelet densities within single-pass, one-drop diameter lines printed with aqueous and glycol GO inks. a) Optical image of track printed with aqueous ink. b) Platelet density at centre of aqueous track. c) Platelet density towards edge of aqueous track. d) Platelet density at edge of aqueous track. e) Optical image of track printed with glycol ink. f) Platelet density at centre of glycol track. g) Platelet density towards edge of glycol track. h) Platelet density at edge of glycol track.

From Figure 3.9, it can be seen that lines printed with the aqueous ink suffered from a severe mismatch in platelet density, with all material concentrated at the edges of lines (Images b, c and d). This was expected due to the harsh capillary flows experienced by platelets within the aqueous media as evaporation takes.[55,227] Tracks printed with the glycol-based exhibited a much more even coverage of platelets throughout the pattern (Images f, g and h), demonstrating suppression of material flow and quelling of the coffee-ring effect. Ethylene glycol has also been demonstrated to induce an opposing Marangoni flow of material away from the solvent periphery.[60] Over a three-fold decrease in edge thickness, from 17.2 nm in the case of aqueous ink to 5.22 nm for glycol ink, was recorded. The density of material was still greatest at line peripheries when using the glycol, but this could be a result of the plasma treatment used on silicon directly prior to printing to help ink adhesion. This raises the energy of surfaces significantly and accelerates the coffee-

ring effect.[60] The optical images of tracks in Figure 3.9 (Images a and e) show a large increase in resolution when using the glycol ink. The line printed with glycol ink measures around 70 μm in diameter, nearly three times thinner than that printed with the aqueous reference. This is due to the viscosity of glycol ink being around eight times higher than the reference ink, with ethylene glycol previously shown to reduce wettability in Section 3.2.2. From this initial test, one would expect to see much greater film resolution and homogeneity than previously recorded when using the additive inks.

3.2.8 Introduction of a low-density printing technique

From previous additive studies, there was a recurring problem of ink control on the substrate resulting in wires with low resolution and poor homogeneity. This was attributed to the hydrophilicity of both ink and surface leading giving uncontrolled wetting scenarios. In order to circumvent this, a quarter density printing technique can be introduced.[27] This works by printing each pass in separate cycles, each one printing every one in four neighboring droplets in a pattern closely resembling a checkerboard arrangement (Figure 3.10). This prevents ink accumulating on the surface and spreading away from where it has been deposited before it has evaporated. A similar technique, whereby the deposition of adjacent droplets has been delayed so that evaporation rate exceeds firing frequency has been demonstrated with a polymer ink.[74] This method is an alternative to increasing drop spacing, where the risk of poor droplet overlap reducing film conductivity is higher.

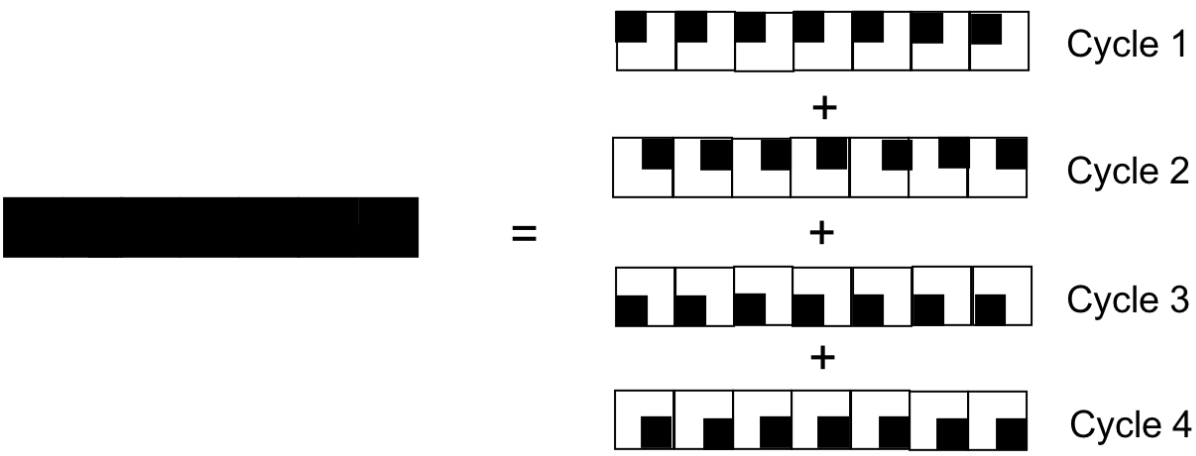

Figure 3.10 Depiction of how quarter density printing works. One layer of a film (left) is printed in four successive print cycles (NW, NE, SE and SW) to improve ink adhesion to the surface. Patterns are generated on Photoshop software.

The quarter density printing method was initially tested in conjunction with the high-temperature protocol (Methodology, Section 2.11). Two identical tracks were printed, one with passes printed at full density and the other printed at quarter density, with drop spacing kept constant at 20 µm. The optical images of both samples can be seen below in Figure 3.11.

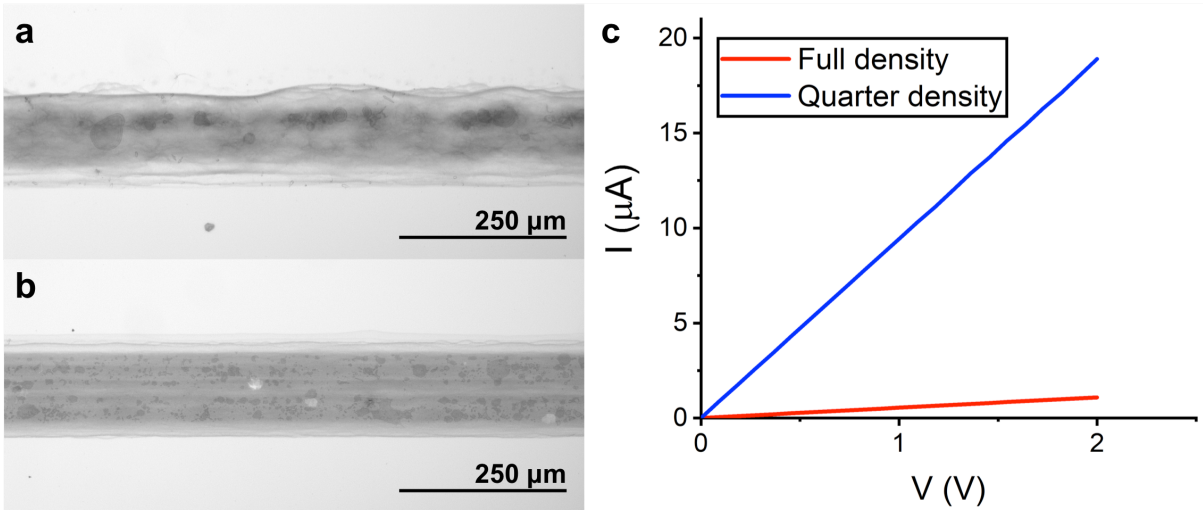

Figure 3.11 Optical images of two identical tracks printed on glass at high-temperature (80 ^{O}C) after reduction to rGO with hydrazine a) Track printed at full density. b) Track printed with the quarter density technique. c) Current (I) vs voltage plots for both tracks, measured on a probe station after reduction with hydrazine and contacting with silver electrodes.

Both tracks exhibit similar widths, with a diameter of 141 µm measured for the full density track compared to 138 µm for the quarter density track. However, a noticeable difference in the standard deviations of widths is calculated with the quarter density track exhibiting a much narrower distribution (±2.4 µm as opposed to ±7.7 µm). This is due to better immobilisation of ink on the surface, with edges of the quarter density film appearing more defined and straighter. Small signs of uncontrolled wetting are still noticeable with some material localised beyond the periphery of the film, but this could be eliminated through slight adjustment of the drop spacing.

Both films were also characterised electrically, after reduction with hydrazine and contacting with silver electrodes. A much greater difference in the conductivity of the two films was measured, with the resistance of the full density track found to be over seventeen times higher than that of the quarter density sample. This result reconfirms the importance of controlling ink adhesion and suggests that the quarter

density method is critical to maximising film quality, especially when printing at high temperature where the wetting of surfaces is known to increase.[69]

3.2.9 Resolution of GO films printed with optimised ink and protocol

With preliminary testing of the newly developed GO ink and printing protocol yielding promising results, a set of tracks of varying thickness were printed (Methodology, Section 2.12). The height of films was controlled through alteration of the number of printing passes, ranging from 5 to 30. Films were printed at a slightly lower temperature of 75 ^{O}C and an increased drop spacing of 25 μm in order to combat the uncontrolled wetting observed previously on glass. Glass slides were also held under nitrogen for 30 minutes in between plasma treatment and printing to allow the surface's energy to fall.

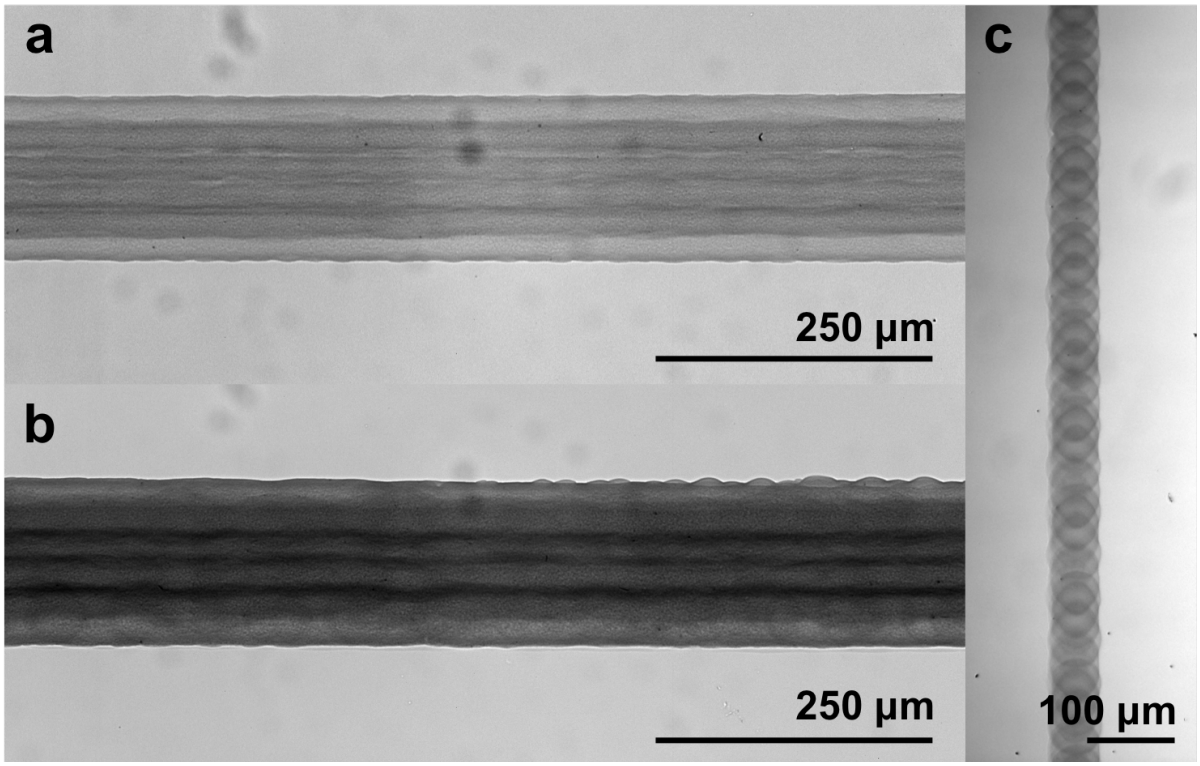

Figure 3.12 Optical images of printed GO films on glass with optimised glycol ink, at a temperature of 75 ^{O}C and using the quarter density technique. a) Film generated from 5 printing passes. b) Film generated from 30 printing passes. c) Film generated from a single row of droplets, giving the maximum resolution able to be achieved with the protocol.

A selection of the printed GO films can be seen in Figure 3.12. Comparable resolution and morphology was observed within the whole range, from 5 printing passes (Image a) to 30 printing passes (Image b). All films exhibited widths between

148-151 μm, with small standard deviations below 3 μm. No evidence of uncontrolled wetting was apparent, with film edges straight and defined. An undulating morphology is present across track cross-sections, which could suggest that the coffee-ring effect has not been completely suppressed.[7]

A single-droplet diameter line was also printed on glass, under the same conditions with the quarter density technique (Figure 3.12, Image c). The width of this line is measured to be 54 μm, giving the highest resolution able to be achieved with the protocol. This resolution is considerably higher than other reports reporting the use of glass or high-energy substrates with graphene inks, with line widths above 80 μm, and is comparable to those printed on lower energy, less hydrophilic surfaces, with widths around 50-60 μm.[2,6,73,228] The maximum film resolution is also dependent on the nozzle size or size of droplets in flight, as well as the ink rheology and surface properties. Generally, a reliable printing method should be able to obtain a resolution two or three times that of the size of droplets in flight.[6] With the diameters of droplets being roughly 25-30 μm (Figure 3.8) this scenario has been reached.

3.2.10 Electrical and optical characterisation of films

The thicknesses of the GO films were characterised using AFM (Methodology, Section 2.14) and are plotted against the number of printing passes in Figure 3.13. A linear relationship is observed, with similar trends reported in literature.[31,60] This demonstrates the reliable build-up of material on a vertical scale, which each printing pass contributing 5 nm of height. The linearity supports the fact that no loss in resolution was seen throughout the sample set, proving that wetting of the ink on glass has been controlled. The AFM images across of one of the films can be found in the Appendices, Figure 3F. As expected from the optical images in Figure 3.12, higher-density ridges across the film were observed, suggesting some platelet movement as a result of the coffee-ring effect is still occurring.[7] Further optimisation of the printing conditions could potentially eliminate this, either through modifying the surface energy of the glass beforehand or printing at temperatures where complete suppression of the phenomenon is reached.[2,55] Alternatively, the rheology of the ink could be further tailored. The optimal surface tension of inks is stated to be between 33-42 dynes, with the glycol ink experimentally measured to be higher at 49 dynes.[2,27] Other glycol solvents exist, such as propylene glycol, which have lower surface tensions than that of ethylene glycol and have already been demonstrated to be suitable for the printing of GO.[59,223]

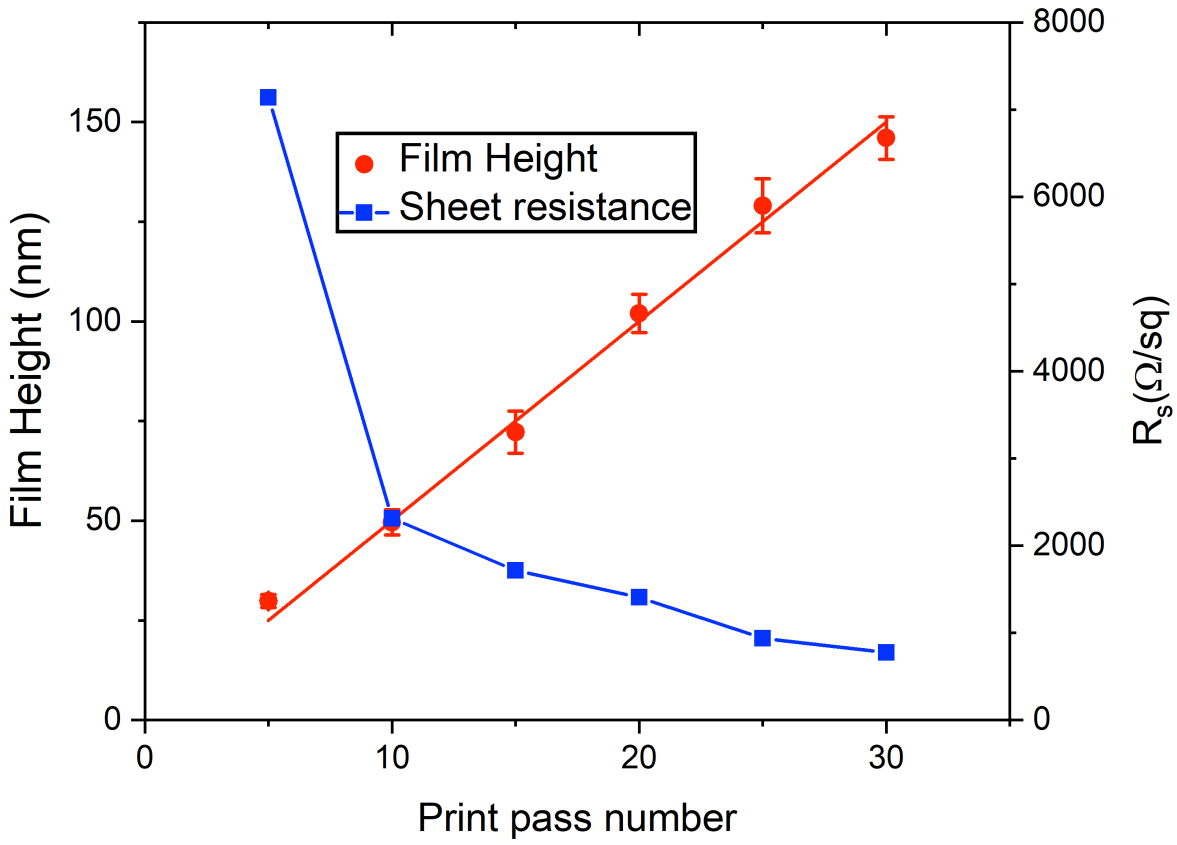

Figure 3.13 Graph showing the plots of film height and sheet resistance vs. number of print passes, for the glycol-based GO ink at 75 ^{O}C on glass with the quarter density printing technique. The standard deviations of film heights are also shown, with data points fitted using a linear trend line (slope = 4.7 nm / pass).

The relation between sheet resistance and the number of printing passes is also displayed in Figure 3.13 (Methodology, Section 2.15). As the number of printing passes is increased, the sheet resistance drops in an exponential manner, with similar observations previously reported.[60,141] The contact resistance between rGO and silver was shown to be negligible through the printing of electrodes at different spacing along the one droplet diameter line, also reduced with hydrazine (Appendices, Figure 3G). A linear relationship is seen between resistance and distance, intercepting the y-axis (denoting contact resistance) just below 0.
Over the range tested, a 10-fold decrease in sheet resistance is measured, from 7140 Ω/sq at 5 layers to 776 Ω/sq at 30 layers. This lowest sheet resistance recorded at 30 printing passes corresponds to a highest bulk film conductivity of 8800 S/m (1.13×10^{-4} Ω.m). This result is almost identical that described by Kim *et al.,* when using nanoscale GO platelets (albeit with an average size twice as big) with similar reduction with hydrazine vapour.[72] The films exhibit higher conductivities than most other printed rGO films after chemical reduction techniques.[5,10,141,59] However, there

are examples were groups have attained conductivities exceeding 10,000 S/m. Many cases involve GO inks with much larger platelet sizes, ranging from a few to tens of microns in diameter, printed using systems able to accommodate cartridges with wider nozzles.[56,72,242] Being able to use larger sheets of GO not only reduces the number of boundaries current has to cross within a film but also improves film homogeneity due to reduction of the capillary flow of material to the peripheries.[55] Crucially, the electrical performance of the rGO films fall short of the ITO films that currently dominate the optoelectronic market. The sheet resistance measured at 30 layers is still around 20-fold higher than typically seen with ITO.[114] The lowest reported sheet resistance for rGO from printed GO (25 Ω/sq) is comparable with ITO and was also obtained chemically, using hydroiodic acid.[60] This was not put down to either the reduction technique or printing, but rather as a result of using a form of 'weakly-oxidised' GO to fabricate a dense film, over 1 μm thick. Once reduced, this led to a final rGO material with significantly fewer defects but with a transmittance outside the viable range for use a conductive, transparent electrode.[114]

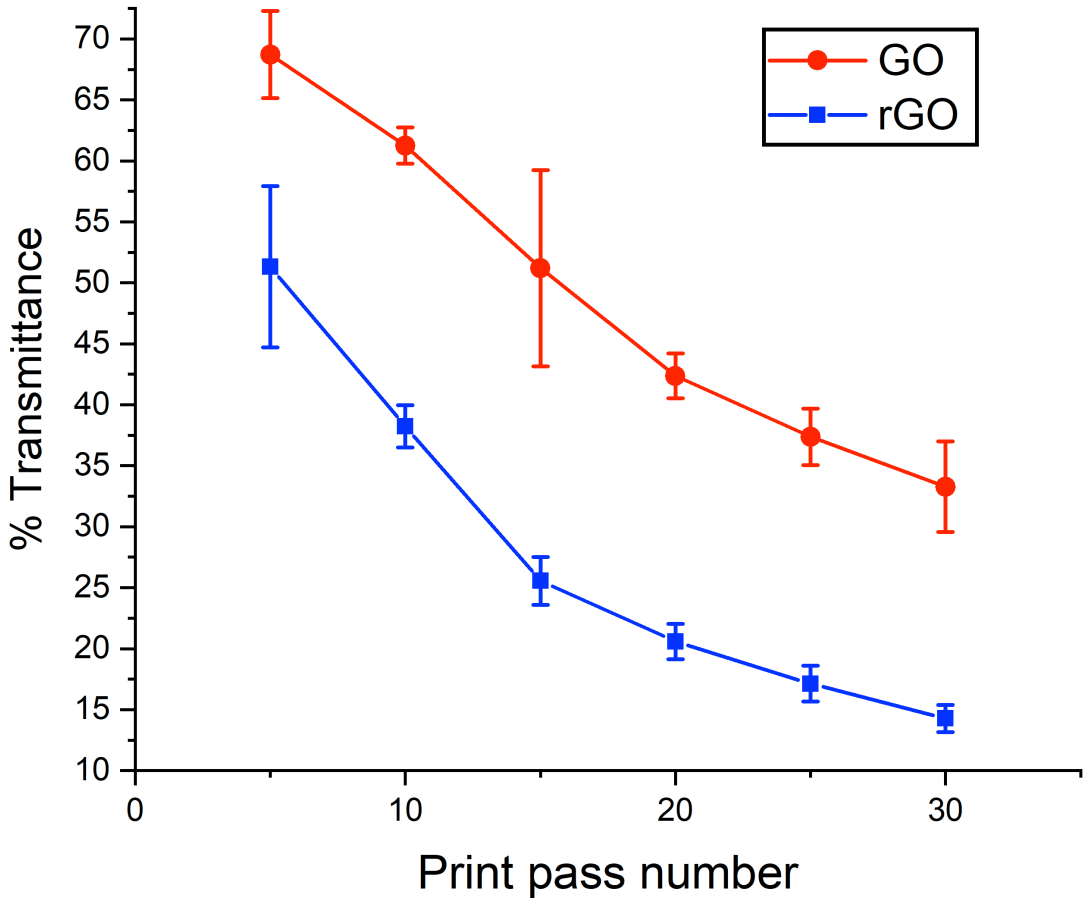

Figure 3.14 % Transmittance vs print pass number for GO films, before and after reduction to rGO with hydrazine vapour, with standard deviations also shown.

The transparency of films, before and after reduction to rGO, can be seen in Figure 3.14. A decrease in transparency, between 18-25 %, is observed when GO is reduced as a result of films turning from dark brown to black. The transparency of GO and rGO films both show a curved dependence on the number of printing passes, as expected from other theoretical and experimental studies.[243] Optical electronics require transparent films of a conducting nature, with rGO films exhibiting transmittances in the range of 14-51 %. These are much lower compared to ITO films which have transmittances ranging from 80 to 95 % at 550 nm.[5] The transparency of films is conventionally measured through UV-VIS to determine % transmittance at this wavelength but the small scale of the tracks prevents the use of this approach.[102,150] Instead measurements were made by optically imaging films, which uses white light with a range of wavelengths between 400-700 nm (Methodology, Section 2.16). Even so, the transparencies of films are relatively low due to the large number of graphene layers stacked upon one another. From XRD data (Appendices, Figure 3H), the interlayer spacing within GO is calculated to be 0.81 nm, meaning the thinnest GO film at around 25 nm is still composed of 30 layers of material. Thinner, more transparent rGO films could be fabricated, through using less printing passes or diluting the ink, but at the expense of increased sheet resistance. Conductive films with transparencies matching ITO have already been demonstrated with printed graphene, with films exhibiting 83-90 % transmittance in the visible range.[5,242]

3.2.11 Assessment of the chemical reduction method used with GO films

The Raman spectra of films, before and after reduction, are shown in Figure 3.15. In both cases the expected signals can be seen, the D and G bands occurring around 1350 cm^{-1} and 1570 cm^{-1} respectively and the broad 2D band at around 2700 cm^{-1}.[244]

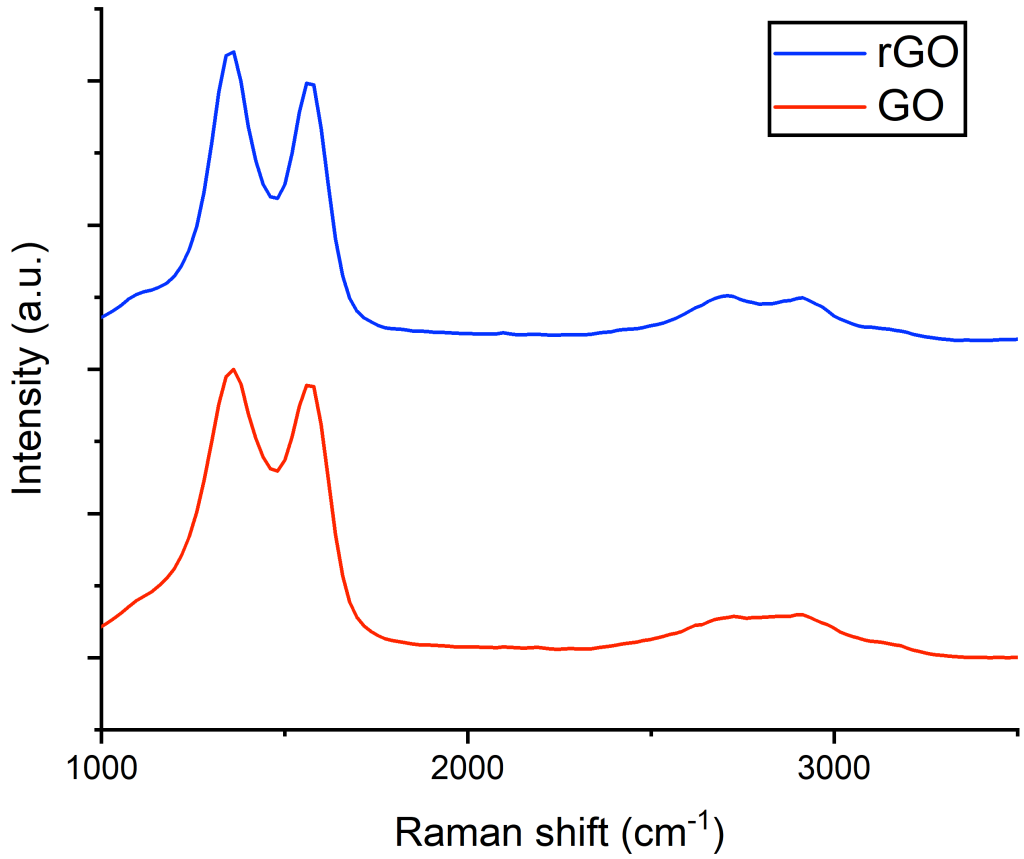

Figure 3.15 Raman spectra for printed films, before and after reduction with hydrazine hydrate.

A change in the I_D/I_G ratio is calculated after treatment of the GO film with hydrazine, with the ratio increasing from 1.05 to 1.14 (Methodology, Section 2.18). With the D band representing defects within the carbon lattice and the G band corresponding to sp^2 planar character, one might expect the I_D/I_G ratio to decrease but similar observations when using hydrazine have been reported by other groups.[30,245] Previous studies have shown that the I_D/I_G ratio can be misleading as a metric for characterising the reduction of GO. The G band of the material and its derivatives also contains an additional defect activated peak, D', around 1620 cm^{-1} that can affect ratios.[244] Ratios in carbon materials have also been shown to rise as the areas of sp^2 domains are increased with the removal of defects.[246] Narrowing of the G and D bands is observed upon reduction to rGO, resulting in a more pronounced trough between, in addition to more prominent 2D and D+D' peaks (at around 2700 cm^{-1} and 2900 cm^{-1} respectively). These two signs are characteristic of a carbon material with increased 2D character.[60]

The XRD data of drop-cast samples (Methodology, Section 2.19) highlight a change in interlayer distance upon the reduction of GO, suggesting the removal of oxygenated groups (Appendices, Figure 3H). The GO sample displays a sharp peak

at 11^{O} (2θ) corresponding to an interlayer distance of 0.81 nm.[171] This peak disappears upon reduction to rGO, shifting to a higher angle as the spacing between stacked platelets narrows. The rGO signal is broad due to its amorphous nature and centred at 20^{O} (2θ), with a calculated interlayer distance of 0.45 nm. The interlayer distance of graphite is known to 0.34 nm, with the difference in values attributed to only partial restoration of graphene's π-network.[171]

FTIR spectra of drop-cast samples (Methodology, Section 2.19) also proved the deoxygenation of GO to rGO, with frequencies corresponding to oxygen containing bonds becoming less intense (Appendices, Figure 3I).[247] In particular, the broad C-O stretch (2500-3600 cm^{-1}) attributed to alcohol and carboxy groups and the C=O stretch (1700 cm^{-1}) weakened from GO to rGO. This C=C aromatic bond stretch (1625 cm^{-1}) also shifted to lower wavenumbers upon reduction, suggesting a higher degree of conjugation within the material.

Importantly, these characterisation techniques signal the persistence of substantial numbers of defects within the rGO lattice and explain the low conductivity compared to ITO.[114] Graphene-based transparent conductive electrodes with sheet resistances as low as 30 Ω/sq and transmittances of 90 % have been reported, suggesting further optimisation of the reduction protocol is required.[12]

3.2.12 Application of the new printing protocol with cAFM

In order further understand graphene materials and best optimise their properties for technologies it is important to study their electronic transport properties on the nanoscale. This is often done through conductive AFM (cAFM) and in the past has been predominantly carried on large-area graphene sheets, grown through chemical vapour deposition or spin coated onto an insulating surface.[145,146,248] The electrical behaviour across overlapping, nanoscale platelets is relatively unknown, with inkjet printing a potential method of fabricating such a scenario. Information on how conductance changes through platelets, with regards to size, overlap or doping with other molecules, could help the optimisation of 'smarter' graphene inks for the future.

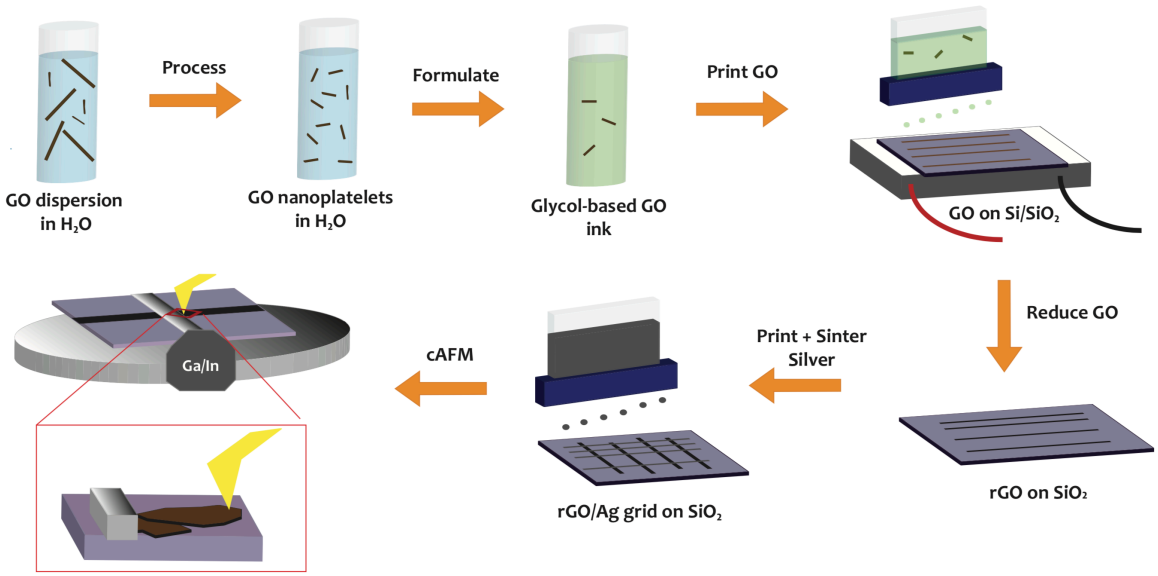

Figure 3.16. Schematic showing the methodology in fabricated a rGO cAFM sample through the printing of GO and Ag inks on Si/SiO_2.

The main challenge faced with using inkjet printing for this approach is the reliable control of material to form regions of overlapping platelets at the appropriate density. However, with the greater control of material able to be achieved with the glycol-based GO ink this obstacle was overcome, along with careful control of temperature and dilution of the ink to a suitable concentration (0.25 mg/mL). The method for producing a working cAFM sample through inkjet printing is depicted in Figure 3.16 and outlined in the Methodology, Section 2.20. In brief, the sample is made through the printing of GO lines onto an insulating Si/SiO_2 surface, reduction to rGO and then the printing and sintering of Ag lines perpendicular. Any regions of platelets contacted to the silver can potentially be characterised once the sample has been fixed to the AFM chuck with eutectic. This method of fabricating an rGO/Ag grid for this purpose is not previously reported in literature.

A cAFM image of platelets can be seen in Image b of Figure 3.17, with the corresponding topological picture alongside, Image a. The Ag contact is located at the top edge of both images. The sample is scanned with a negative bias, meaning areas of higher conductance appear darker. As expected, the conductance falls as the distance from the silver contact increases through the platelets. With the use of Matlab software, specific areas of conductance over platelets can be accurately measured (Image c).

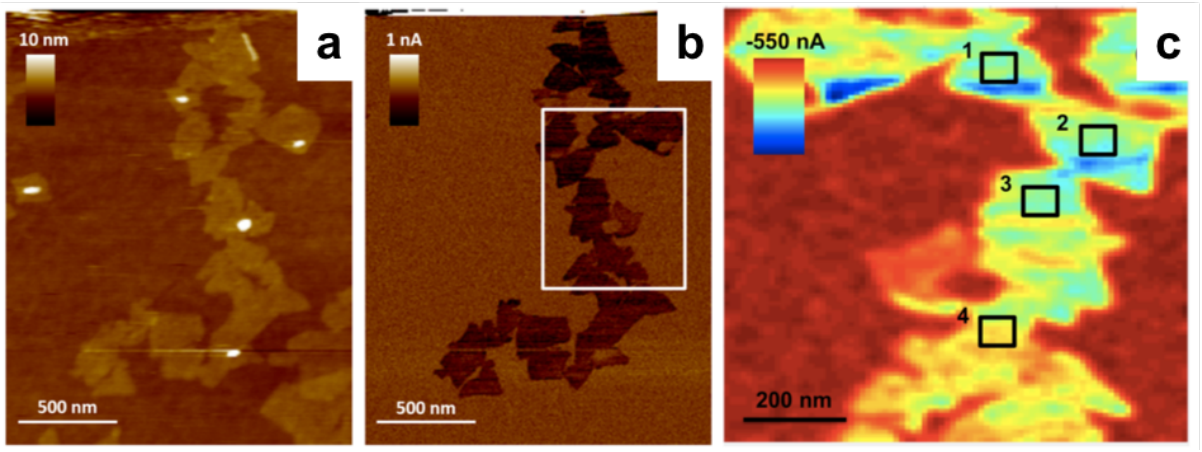

Figure 3.17 a) Topological image of a rGO platelets series obtained through tapping mode AFM. b) Corresponding cAFM image of rGO platelet series. c) Electrical image of platelets from the section outlined in Image b, with data modelled and smoothed using Matlab software. Average currents at point 1 = -337 pA, point 2 = -323 pA, point 3 = -256 pA and point 4 = -209 pA.

3.3 Conclusion

A novel GO printing protocol, tailored for use with a Dimatix system, was used to overcome the printing obstacles posed by GO inks and successfully meet the first aim of the thesis. The process involved the formulation of a highly optimised glycol-based ink (75 % v/v ethylene glycol in water) that demonstrated reliable printing at substrate temperatures exceeding 60 ^{O}C, through the temporary modification of the inkjet system and by use of a low-density printing technique. The resulting GO films on glass exhibited significant improvements in terms of homogeneity, though suppression of the coffee-ring effect, and resolution, due to enhanced jetting performance and the avoidance of uncontrolled wetting, compared to those printed with aqueous-based inks. The maximum resolution able to be achieved was 54 μm, which exceeds previous reports of graphene-based inks on unmodified glass while being comparable to those seen on lower energy surfaces such as polymer films and papers.[2,6,73,228]

Once reduced chemically through hydrazine vapour, films demonstrated good electrical performance, with a highest bulk conductivity of 8800 S/m recorded. This value is higher than most reports of chemically reduced films derived from nanoscale-sized GO platelets synthesised through a conventional Hummer's method but lower than current ITO films used in the optoelectronics market.[5,10,59,72] In particular, the lowest sheet resistance measured (776 Ω/sq) is still 20-fold higher than that typically seen with ITO.[114] This can be attributed to the reduction method used with GO, achieving only limited reformation of graphene's 2D lattice.

This was confirmed through Raman, XRD and FTIR analysis, highlighting the production of highly defective rGO. The transparencies of reduced films (14-51 % transmittance) were also found to be inferior to ITO due to their thick, multi-layered nature. Further work should focus on improving the conductive and transparent properties of printed films to compete with current ITO technology. Investigations into more efficient methods of reduction need to be conducted in order to generate thinner films with lower sheet resistances. The new printing protocol is also suitable for use with polymer substrates and should be tested on these for the fabrication of flexible electronics.

As a consequence of this work, a novel method of fabricating a rGO cAFM sample with a dilute glycol-based GO ink was also highlighted. This paves the way for electronic transport characterisation across overlapping, nanoscale platelets, with potential applications in future ink design.

Chapter 4. Attempts to improve the conductivity of printed films for optoelectronic applications

4.1 Introduction

The simplicity with respect to ink formulation makes graphene oxide (GO) an attractive material for the printing of electronic components. However, the work in Chapter 3 discovered that the presence of oxygenated groups remaining in high densities after reduction perturbed the aromaticity of the carbon lattice and limited material conductivity. It was concluded that a much more efficient reduction protocol was needed to fabricate thinner reduced graphene oxide (rGO) films with lower sheet resistances, in order to compete with the commonly used indium tin oxide (ITO) films as conductive, transparent electrodes.[114]

GO has been reduced through electrochemical methods, resulting in the generation of rGO films on electrode surfaces.[99,249–254] Yet rGO films produced via this route are prone to contamination from electrolyte species while the need for a conductive surface for deposition imposes limitations.[255,256] RGO from GO has also been attained through irradiation and plasma treatments, with both these processes able to impose considerable damage to film structure and substrate.[98,257–260] Solvothermal reduction of GO has also been demonstrated while Williams et al. developed a photocatalyst route, involving the use of titanium oxide particles.[261–263] More recently MacInnes et al. reported reduction of GO through exposure to metallocene compounds.[148] These techniques would involve the submersion of printed films in solution, a potential risk for small-scale inkjet films that can deteriorate or even lift off substrates completely.

The two most routine methods for rGO synthesis are chemical and thermal reduction of GO. Chemical conversion of GO to rGO has been achieved through a range of reductants, including hydrazine, hydroiodic acid (HI), Lawesson's reagent, carbohydrate derivatives, alcohols, urea, thiourea, quinones, alkaline solutions and metal hydrides.[148,264,269–273] Hydrazine and HI are most commonly used out of these choices with other reagents tending to give inferior levels of reduction.

Carbon/oxygen (C/O) ratios of 15 and between 8.8-12.5 have been reported for rGO reduced by HI and hydrazine respectively while the most conductive inkjet film published (43,000 S/m) was achieved through use of HI.[60,101,216,274] Films reduced by chemical means exhibit a wide range of sheet resistances, dependant on the oxidation level of the precursor GO and the reductant used, typically falling between 10^2-10^5 Ω/sq. The main advantage to using chemical routes is that only mild reaction conditions are needed, with rGO synthesis usually able to occur at room temperature or by moderate heating. The reduction of films can also be achieved through with the

vapours of hydrazine and HI in a sealed vessel, a less invasive method than within solution to help avoid material fragmentation.[59,60,141] The drawback to using these chemicals is that they are selective to certain functionalities, placing limits on the extent of reduction and film conductivity able to reached. Hydrazine is known to selectively remove epoxide defects while HI has been theorised to depose both hydroxyl and epoxide groups.[101,275] The use of hydrazine has also been reported to dope rGO with nitrogen species through incomplete conversions of defects to carbon-carbon double bonds and through side reactions.[101,276]

Thermal reduction or annealing of GO is often carried out under inert or vacuum conditions at high temperatures, within the range of 700-1100 ^{O}C, to ensure considerable desorption of functionalities.[216,273–275] This places constraints on the substrate able to be used for film deposition. Most inkjet printing of GO is carried out on low-melting point, flexible polymer films which cannot withstand these extreme conditions.[7,30–32] The highest reported annealing temperature applied to inkjet-printed GO is 400 ^{O}C, with only a moderate conductivity of 870 S/m achieved.[7] This is due to the fact that that only the removal of intercalated water and most labile oxygen species, predominantly carboxylic acids, is achieved, resulting in hampered restoration of sp^2 structure.[153,280] Thermal annealing at temperatures between 900-1100 ^{O}C generally results in films with higher C/O ratios compared to chemical treatment, with calculated values ranging from 14.1-33.[100,109,153] Under these conditions, significant loss of epoxide and hydroxyl moieties can be accomplished, along with complete expulsion of carboxyl and partial desorption of carbonyl functionalities.[110,153,275] As a consequence, conductivities for these graphene materials are superior to those chemically treated, with published electrical performances in the range of 72,000-100,000 S/m and corresponding to sheet resistances between 10^2-10^3 Ω/sq.[100,109,281] The higher efficiency of GO deoxygenation does however come at a cost. The decomposition of functionalities results in the removal of carbon atoms from the lattice, as gases such as carbon dioxide and carbon monoxide are generated.[110,275,282] These new defects reduce the size of crystallites within films, resulting in increased sheet resistances. Films also experience high compressive forces through the rapid removal of water and oxygenated groups, which can lead to cracking and slipping of films and, in severe cases, lead to mechanical and electrical failure.[283,284]

In order to enhance the reduction efficiency of GO, several groups have applied multi-step strategies, incorporating both chemical and thermal treatments.[109,272,285–287]

For example, Eda et al. found that pre-treatment of GO with hydrazine vapour and subsequent thermal annealing at 200 ^{O}C could produce a more conductive film than one solely annealed at 550 ^{O}C, important for flexible devices on polymer substrates.[285] Meanwhile, Gao et al. proposed a three step reduction protocol, involving deoxygenation with sodium borohydride, dehydration with sulphuric acid and a final thermal annealing step. This method was able to eliminate ketone, epoxide, ester, alcohol and carboxyl groups to give a film with a C/O ratio surpassing 246.[272] More recently, Qin et al. reported that the prior treatment of films with HI vapour before annealing at 1100 ^{O}C significantly lowered the sheet resistance of films compared to those directly annealed at the same temperature.[286]

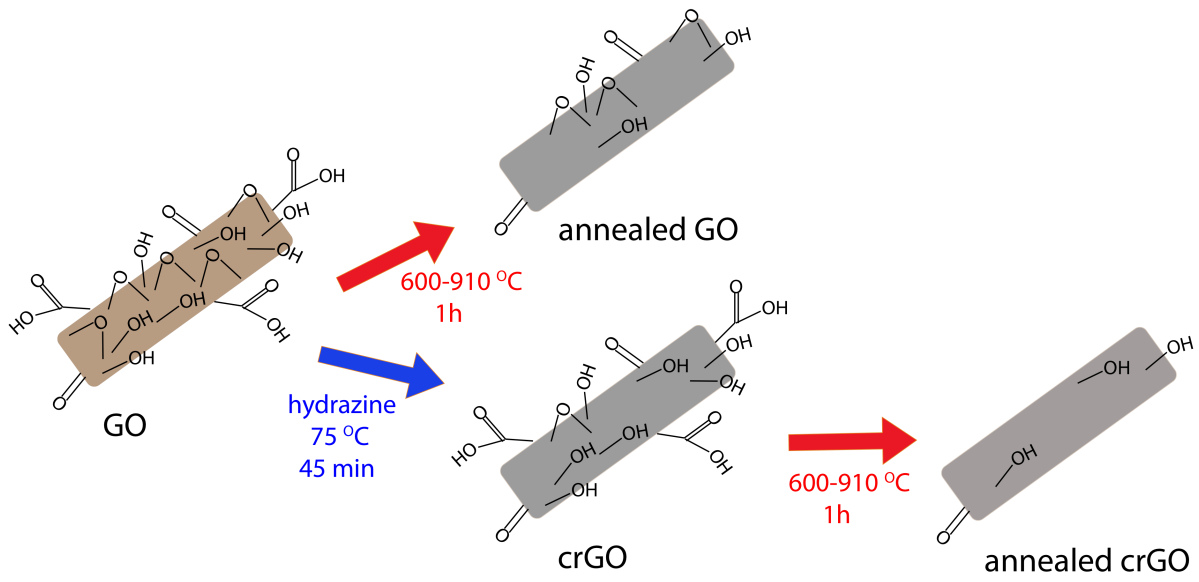

Figure 4.1 Schematic illustrating the single and dual-step reduction protocols to be trialled in this chapter on inkjet-printed GO films. Methods involve thermal annealing of films at high temperature (600-910 ^{O}C) with or without prior reduction of GO to crGO (chemically reduced graphene oxide).

The following work in this chapter is directed at the second aim of the project and seeks to improve the conductivity of films derived from the GO ink developed in Chapter 3. Earlier studies identified the need for a more efficient reduction protocol in order to obtain films with conductive and transparent properties more competitive with ITO currently used in optoelectronic devices. The use of a two-step reduction process will be investigated, involving the thermal annealing of films at extreme temperatures (600-910 ^{O}C) after treatment with hydrazine vapour, and compared to films solely annealed over the same range. The resulting optoelectronic properties of

films are critically analysed in comparison to ITO and other materials being explored for its replacement. Extensive XPS and Raman characterisation is performed in order to probe the efficacy of oxygenated group removal and the density of defects remaining within the lattice. In order for samples to be viable for the thermal annealing step, the printing of GO tracks is carried out on high-melting point sapphire substrates. The use of these annealing conditions with inkjet-printed GO films does not appear in current literature.

4.2 Results and discussion

4.2.1 Characterisation of rGO film thickness

The fabrication of GO films on sapphire substrates was achieved using the optimised glycol-based ink, introduced in Chapter 3 and supplied in the Methodology, Sections 2.9 and 2.12. Once printed, samples underwent either a one or two step reduction process, both involving a thermal reduction, at temperatures ranging between 600-910 ^{O}C, with or without an initial chemical reduction using hydrazine vapour (Methodology, Section 2.13). Information on the morphology of reduced films, such as thickness, width and roughness, was obtained through optical and atomic force microscopy techniques (Methodology, Section 2.14). Similar characterisation of unreduced GO and hydrazine reduced rGO (crGO) films was also carried out to provide references. A thermally reduced rGO sample (trGO) was also prepared by exposure to a lower temperature of 170 ^{O}C, in order to analyse the extent of reduction able to be attained at temperatures viable for polymer films required for flexible devices.

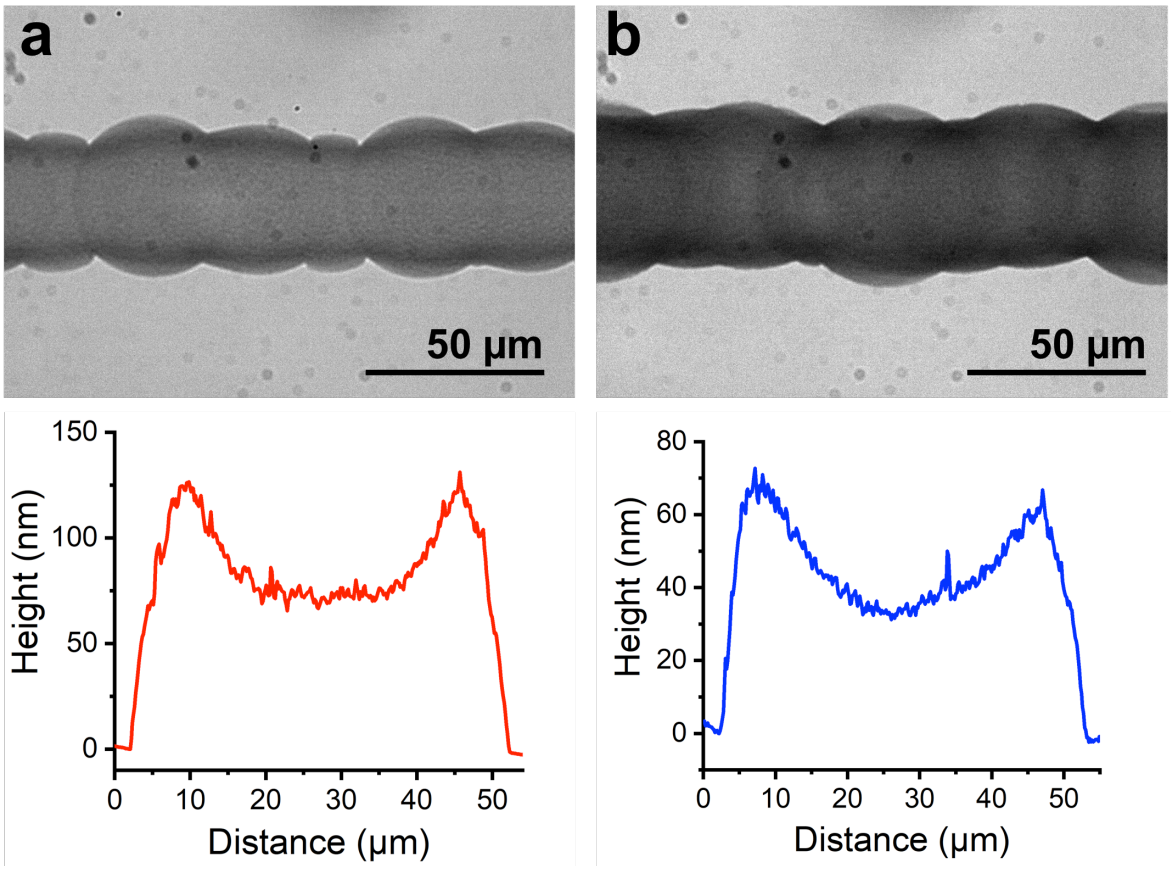

Figure 4.2 Optical images of a GO (a) and a rGO (b) track, reduced under vacuum at 170 ^{O}C for 6 h, with corresponding height profiles across films, measured through tapping-mode AFM.

The appearance of a typical GO track printed on sapphire can be seen in Figure 4.2 (Image a) above. Individual overlapping droplets could be distinguished along the lengths of tracks, giving scalloped morphologies rather than the uniform appearance witnessed on glass in Chapter 3.[288] This is caused by the reduction in wetting behaviour of the ink on sapphire compared to glass and justifies the requirement of a reduced drop spacing of 20 μm to yield continuous films. The contact angles of water and ethylene glycol have been previously reported on glass and sapphire, with higher contact angles of both liquids measured on sapphire.[289] This was attributed to the lower surface energy of sapphire, with a lower contribution of polar component, minimising the adhesion of polar solvents to the substrate. This phenomenon also explains the increase in print resolution observed, with average track widths measuring between 41-51 μm compared to 54 μm on glass.

As well as a change in transparency, the reduction of GO is accompanied by a change in film height, with the compression of films able to be measured through AFM studies (Figure 4.2, cross-section profiles). Even after reduction under the milder temperature of 170 ^{O}C, a height difference of over 30 nm was recorded (from 85.0 ± 5.3 nm for GO down to 52.8 ± 3.1 nm for trGO). These changes in thickness are predominantly driven by the removal of intercalated water and oxygenated defects, effectively decreasing the interlayer distances within films.[283,290,291] The maintenance of a trough-like morphology was seen before and after reduction, with the highest density of platelets found at the peripheries of tracks as a consequence of the coffee-ring effect during printing. The origin of this has been covered extensively in Chapter 3, with the elevated printing temperature, increased surface energy due to plasma treatment and the high surface tension of glycol-based ink all believed to provide contributions.[60,65–67,288]

The film heights of samples undergoing high-temperature thermal reduction with and without prior chemical reduction can be observed below in Figure 4.3. In the case of both GO and crGO films, there is a clear decrease in film height after thermal annealing, suggesting the removal of both intercalated water and oxygenated defects. One-way Analysis of Variance (ANOVA) was carried out between single and dual step treated samples at each temperature, with track width and film thickness values displayed in the Appendices, Tables 4A and 4B. Both differences in film thickness and track width are found to be significant up to 800 ^{O}C (p = <0.05). This suggests that the fluctuations in track widths rather than the reduction protocol are

the cause of the variance seen with samples below 800 ^{O}C. Above this temperature, differences in track width and film height are not significant (p = >0.05).

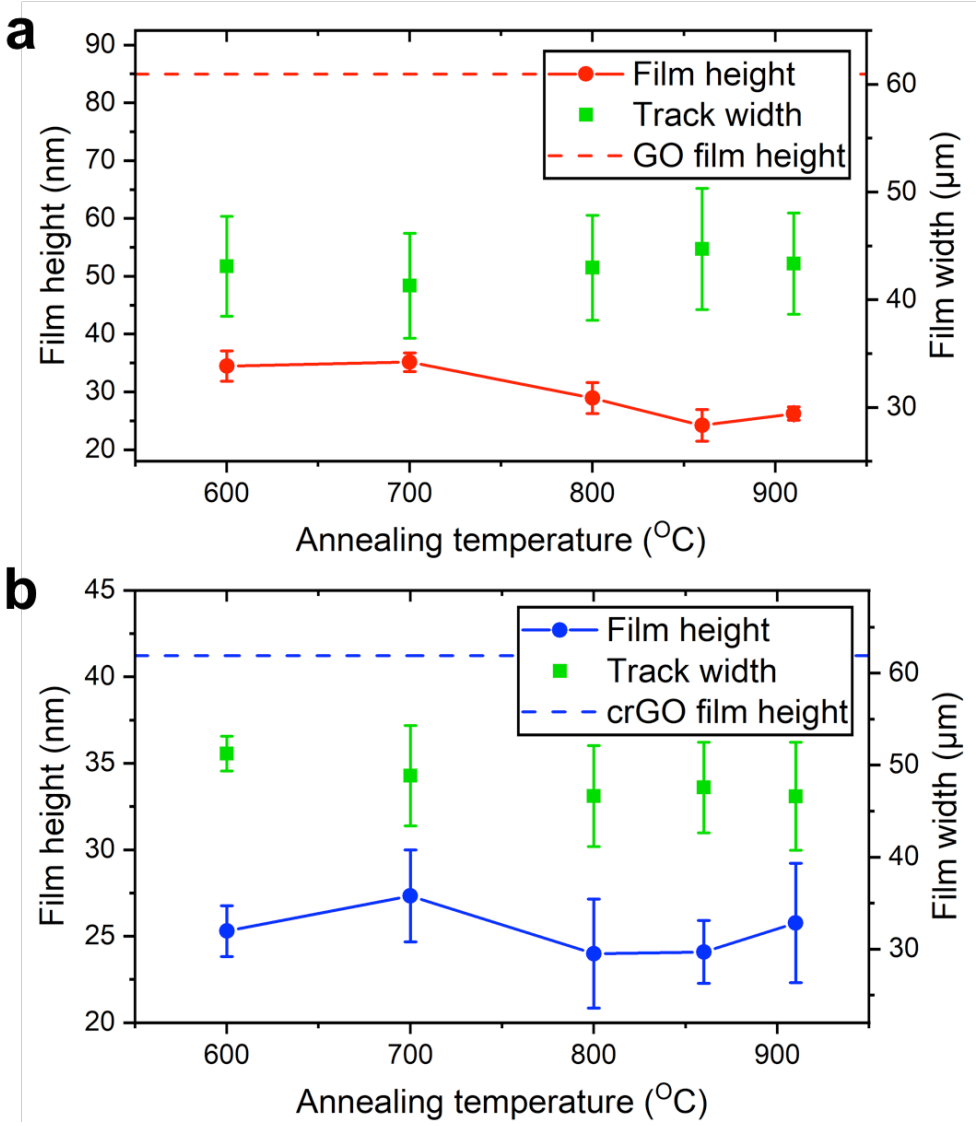

Figure 4.3 Plots of GO (a, red circles) and crGO (b, blue circles) average film heights and standard deviations (nm), after thermal annealing between 600-910 ^{O}C and measured through tapping-mode AFM. Shown also are corresponding average track widths and standard deviations (µm), measured through optical microscopy. The GO and crGO film heights (dashed lines) prior to thermal annealing are included. ANOVA (Appendices, Tables 4A and 4B) confirms differences in the widths and heights between one and two-step treated samples are only found to be significant at 600, 700 and 800 ^{O}C (p = <0.05).

Across the annealing range tested, all films exhibit thicknesses within a narrow range of 10 nm (24-34 nm), with the most drastic changes occurring at lower temperature. The heights of annealed GO and crGO films are comparable and correspond to roughly a third of the unreduced GO height. This disparity coincides with reports of the difference in interlayer spacing between GO (0.8-0.9 nm) and rGO (0.3-0.4 nm).[283,292–294]

4.2.2 Characterisation of rGO surface morphology

The surface morphology of films was also investigated through tapping-mode AFM (Methodology, Section 2.14), with images grouped below in Figure 4.4 and the trGO sample, reduced at 170 ^{O}C, located in the Appendices, Figure 4A.

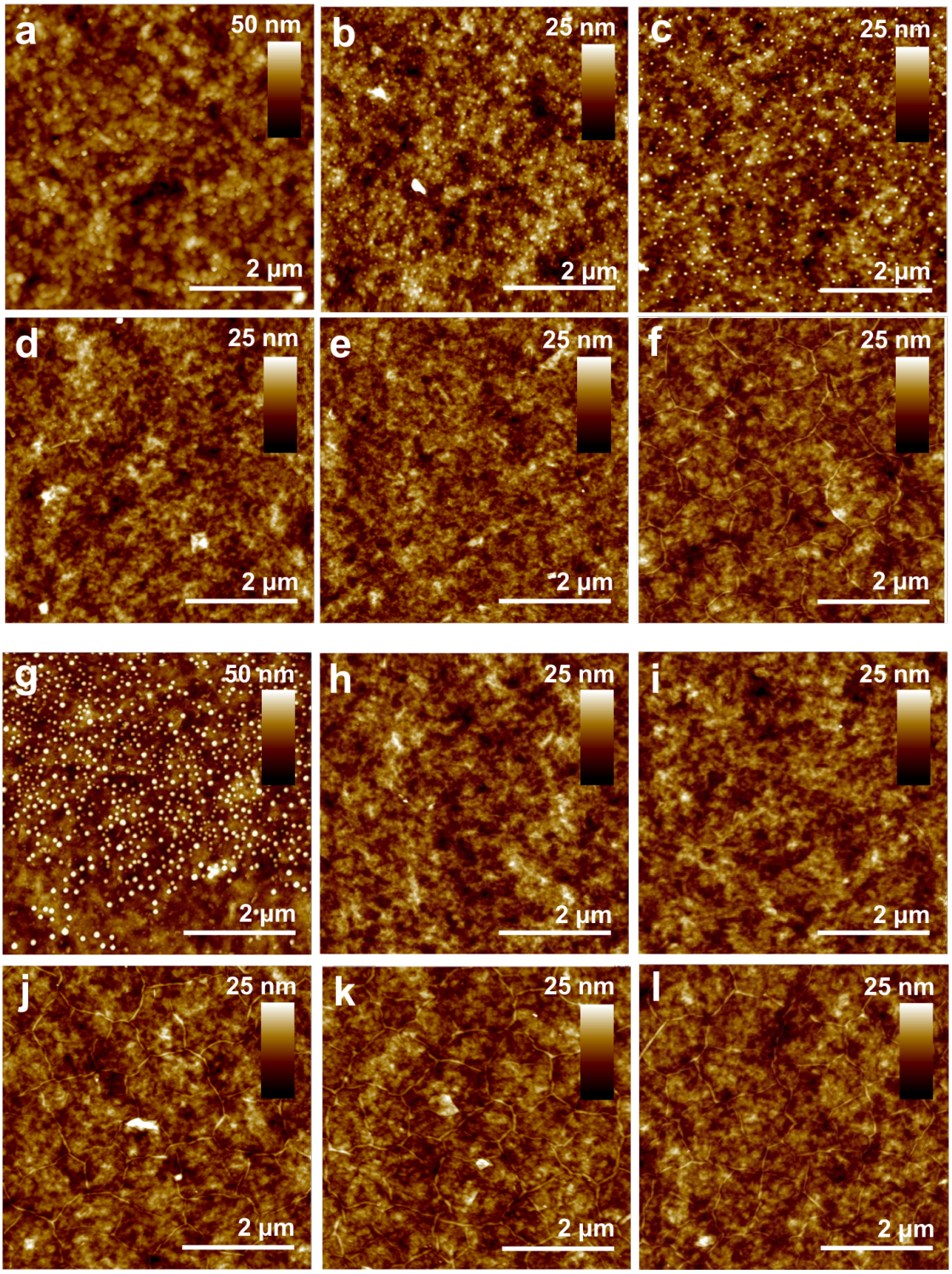

Figure 4.4 Tapping-mode AFM images showing the surface morphology of GO (a) and crGO (g) films after annealing at 600 ^{O}C (b and h), 700 ^{O}C (c and i), 800 ^{O}C (d and j), 860 ^{O}C (e and k) and 910 ^{O}C (f and l) for 1 h.

Both sets of samples display a stark decrease in film roughness compared to references (GO, Image a and crGO, Image g) after treatment at high temperature. In the case of crGO and the sample reduced at low temperature, distinctive bumpy morphologies are observed, possibly caused by the bubbling and expansion of material during reduction as gas and water is evolved.[101,295] Films exhibiting this morphology have been found to be mechanically unstable and prone to fragmentation. GO samples annealed at 600 ^{O}C and 700 ^{O}C (Images b and c) exhibit less severe nano-sized bubbles on their surfaces which could also be caused by the explosive release of gas as a consequence of defect removal.[110,275] These features cannot be identified after treatment at higher temperatures (Images d-f) or with annealed crGO films (Images h-l).

The GO film reduced at 910 ^{O}C displays a marked difference in surface structure with cracks, measuring 2-8 nm high, prevalent across its entirety. This observation is believed to be caused by the mismatch in thermal expansion coefficients (CTE) between graphene and sapphire, with graphene known to have a negative CTE and sapphire a positive CTE.[296,297] This means that as temperature drops after treatment, the substrate contracts while the graphene-based material expands, introducing a compressive strain within the system which is released by the film through buckling or cracking.[297,298] This phenomenon is more common at higher temperatures where the strain is greater and can reduce the mechanical stability of films. This distortion within samples is observed at milder temperatures with crGO (Images j-l), with cracks appearing at temperatures as low as 800 ^{O}C. Reports in literature have previously discovered relationships between defect density and crack propagation, with more defective graphene films found to hinder crack formation.[284,299] The assumption that the two-step reduction protocol yields films with fewer defects supports this argument. Additionally, imposed strain can cause slipping of material on the surface if it is significant enough to overcome the interactions between the two.[296] In the case of more oxidised rGO species one would expect a higher degree of stronger hydrogen bonding compared to weaker Van der Waal's interactions, hence preventing slipping and resulting film buckling.

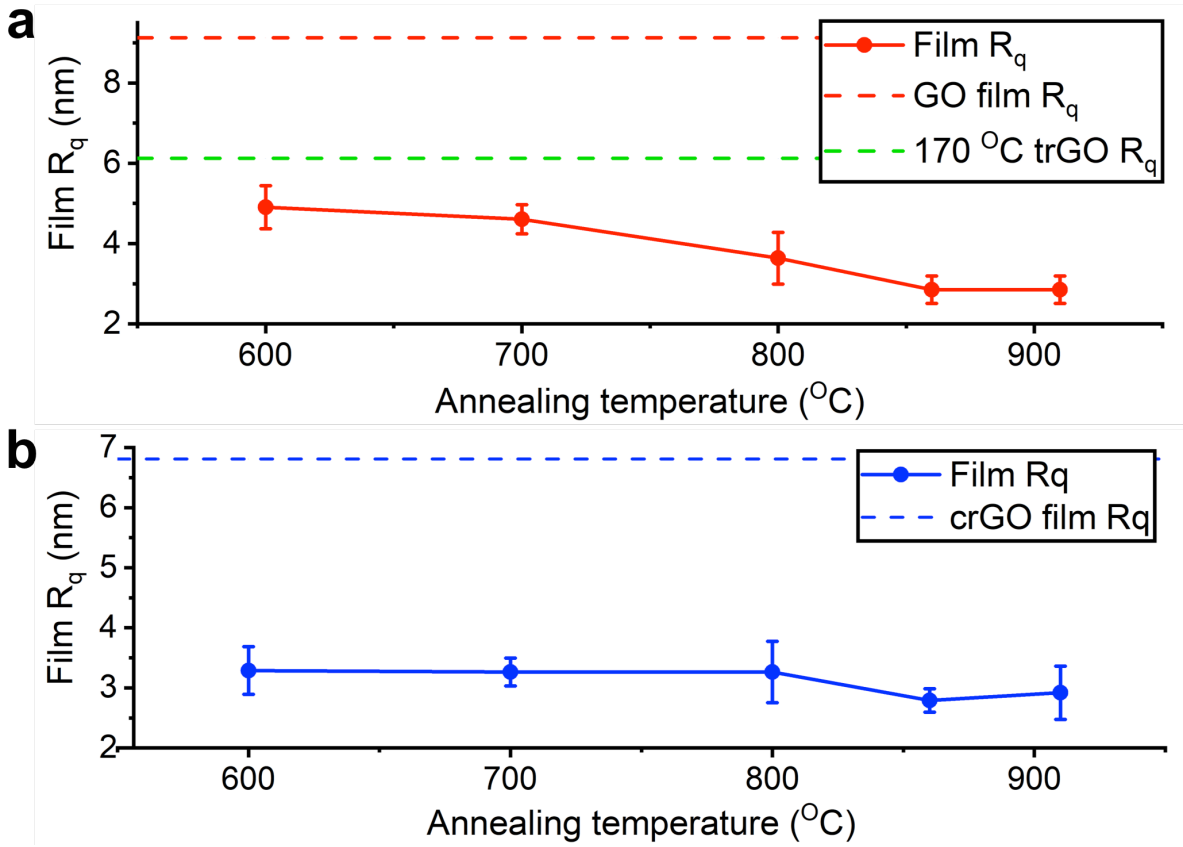

Figure 4.5 Average root-mean-square roughness (Rq, nm) values of GO (a) and crGO (b) films vs thermal annealing temperature (^{O}C), with standard deviations. Measurements were taken on small-scale images obtained by tapping-mode AFM images. GO (red dash line) and crGO (blue dash line) control sample values along with trGO reduced at 170 ^{O}C (green dash line) are also shown. ANOVA (Appendices, Table 4C) confirms differences in film Rq between one and two-step treated samples are only significant at 600 and 700^{O}C (p = <0.05).

The surface roughness of films was quantified through root-mean-square roughness (Rq) measurements performed on tapping-mode AFM images (Methodology, Section 2.14), with plots against annealing temperature shown above in Figure 4.5. A distinct reduction in Rq is observed seen when both GO (Image a) and crGO films (Image b) are thermally treated, coinciding with the sharp decrease in film height discussed earlier (see Figure 4.3). A similar observation was reported by Jernigan et al. with films annealed at high temperature and ultra-high vacuum.[300] The generation of smoother films suggests higher-ordered stacking of platelets within and the reduction in size of sp^3 domains, able to bestow improvements in optical, conductive and mechanical properties.[97,148] ANOVA (Appendices, Table 4C) performed between single and two-step reduced samples at each temperature, show that the difference in roughness is only significant at 600 and 700 ^{O}C (p = <0.05). This can be attributed to the nano-sized bubble features observed on the single-step reduced films at these

temperatures (Figure 4.4, Images b and c), resulting in a rougher surface. Above 700^{O}C, differences in Rq are not significant (p = >0.05) with both sets of films exhibiting similar values, ranging between 2.8-3.6 nm and corresponding to a Rq loss of around 70 % compared to unreduced GO. The cracking of films previously highlighted at temperatures above 800 ^{O}C (Figure 4.4, Images f, k, j and l) does not appear to have a measurable effect on surface roughness. Meanwhile, only a 25 % increase in smoothness was calculated between GO and crGO reference samples due to the highly distorted surface produced through using hydrazine vapour (Figure 4.4, Image g).

4.2.3 Electrical and optical characterisation of rGO films

In order to access the suitability of films for use as in optoelectronic applications, the conductivities of films were measured (Methodology, Section 2.15), with results displayed below in Figure 4.6.

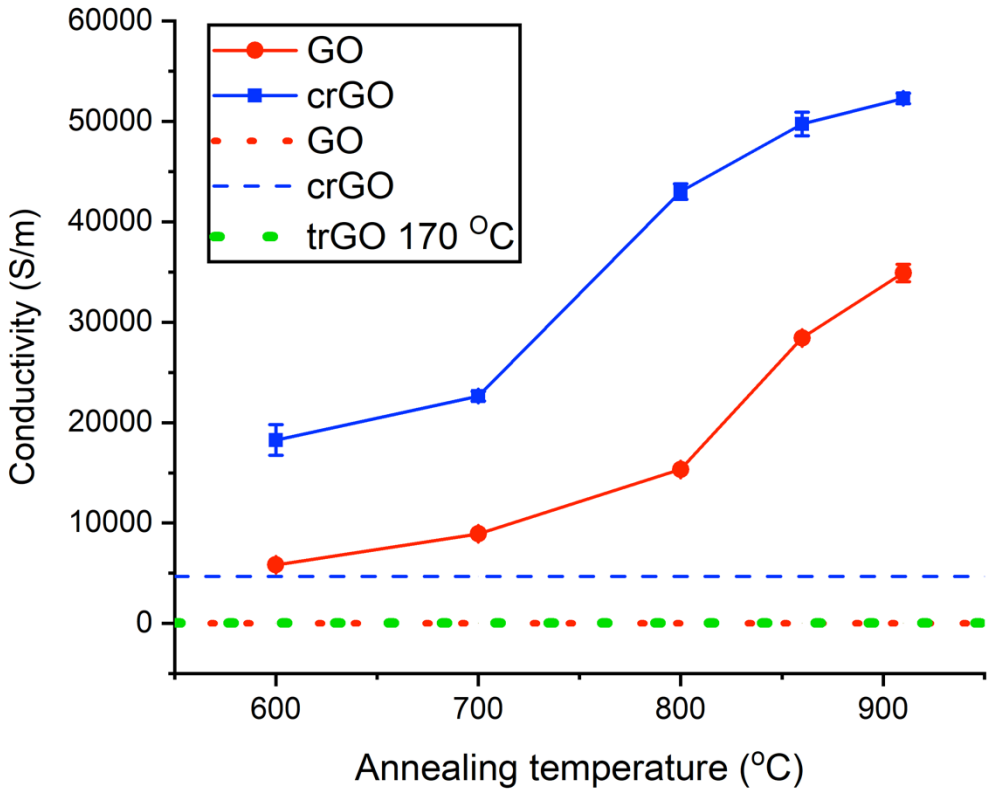

Figure 4.6 Average conductivity (S/m) vs annealing temperature (^{O}C) for GO (red circles) and crGO (blue squares), along with standard deviations. Shown also are values for GO (red dash) and crGO (blue dash) reference samples and the trGO sample (green dash) reduced at 170 ^{O}C. ANOVA analysis (Appendices, Table 4D), confirms differences in film conductivity between one and two-step treated samples are significant at each temperature (p = <0.05).

GO is practically insulating, with a measured conductivity of $2.81 \times 10^{-5} \pm 3.6 \times 10^{-6}$ S/m while the trGO sample, treated at low temperature, displays a low conductivity of 43.0 ± 0.34 S/m. Exposure to films at temperatures at around 200 ^{O}C only remove the most labile oxygenated groups, along with trapped interlayer water, impairing the restoration of the 2D lattice.[301,302] Schneipp et al. reported that a C/O ratio of no more than 7 could be attained at temperatures below 500 ^{O}C.[282] Upon reduction with hydrazine vapour a much more conductive film is obtained (4690 ± 770 S/m), with activity comparable to chemically reduced inkjet-printed samples in literature.[31,141] The higher resistivity of films compared to those printed on glass in Chapter 3 may be attributed to the lower overlap observed between droplets upon the sapphire surface.

The conductivity of GO and crGO films show trends of increasing conductivity with increased annealing temperature. At a given temperature, the electrical performance of samples previously chemically reduced is superior to those that were not, with differences confirmed to be significant by ANOVA (Appendices, Table 4D). This increase in activity through the application of multi-step reduction has been previously observed by other groups and attributed to the increased desorption of oxygen groups.[272,285,287,303] Hydrazine is known to selectively remove epoxide moieties under mild conditions, with extreme heat otherwise needed for this to occur.[275] The presence of epoxides within rGO has still been detected at annealing temperatures beyond 900 ^{O}C. The highest conductivity calculated for thermally reduced GO is 34,900 S/m, a good match for the value of just under 40,000 S/m reported by Wang et al. for trGO at 900 ^{O}C.[100] A maximum electrical performance of 52,300 ± 500 S/m S/m was recorded for crGO, exceeding the highest conductivity achieved with an inkjet-printed rGO film (43,000 S/m) to this date.[60] Most graphene printing is carried out on polymer films, limiting the use of a high temperature process such as this.[7,48,31,5] This value is still smaller than other reported trGO samples which utilised higher temperatures of 1100 ^{O}C (72,700 – 100,000 S/m).[100,109,281,] This suggests that even higher performances could be achieved through further elevation of annealing temperature, with the conductivity of both sets of films yet to plateau over the range tested.

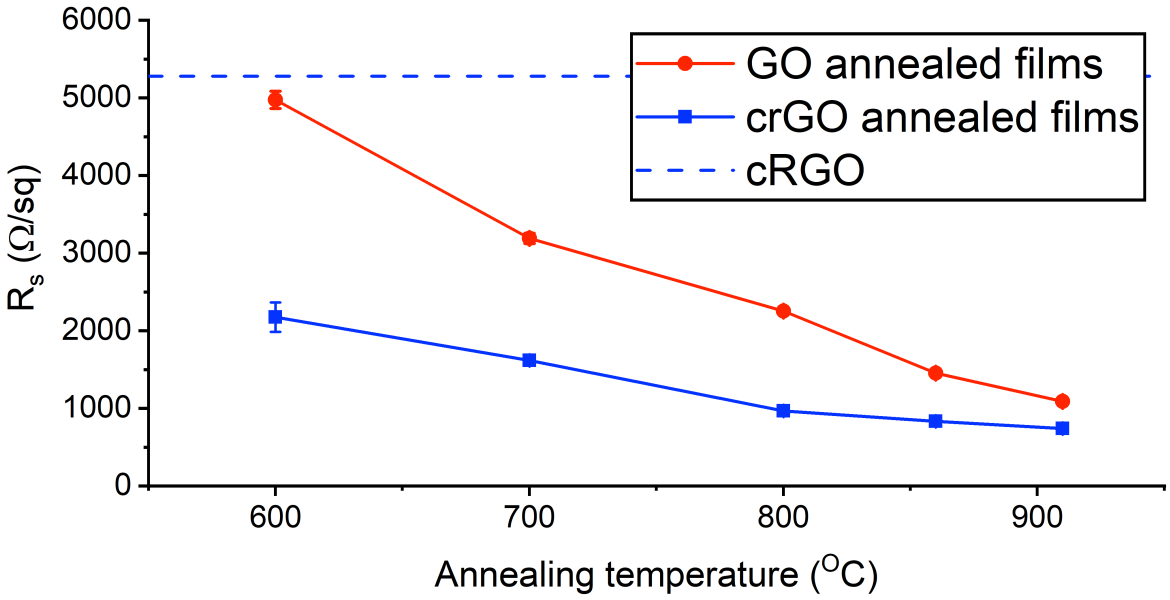

Figure 4.7 Average sheet resistances (R_s, Ω/sq) vs annealing temperature (^{O}C) for GO (red circles) and crGO (blue squares), with standard deviations. Shown also is the crGO (blue dash) reference sample. The R_s of GO and trGO samples (reduced at 170 ^{O}C) were calculated to be 4.24 x 10^{11} and 4.57 x 10^5 (Ω/sq). ANOVA (Appendices, Table 4E) confirms differences in R_s between one and two-step treated samples are significant at each temperature (p = <0.05).

The corresponding sheet resistances of films are displayed in Figure 4.7, with values decreasing as film conductivity rises. Through application of the dual step reduction protocol, with thermal annealing at 910 ^{O}C, the average sheet resistance of films is found to be 740 ± 7.0 Ω/sq. This is comparable to the lowest sheet resistance obtained for the chemically reduced films in Chapter 3 but achieved at a film thickness several times smaller. Even though remarkable improvements in film conductivity have been achieved, sheet resistances are still 20-fold higher to those exhibited by commercial ITO films.[114] Further advancements in GO reduction efficacy would close this gap, but the use of slightly higher annealing temperatures, up to 1100 ^{O}C, would likely give limited progress, with sheet resistances still within the region of 10^2-10^3 Ω/sq.[100,109] Rozada et al. have reported the complete restoration of a graphene lattice from GO but the protocol requires temperatures approaching 2800 ^{O}C.[107] A more viable approach may be to print graphene or carbon nanotubes rather than GO and avoid needing a reduction process all together. This would also allow fabrication of flexible devices where ITO is too brittle to use. Feasible, lower cost replacements for ITO have already been demonstrated using these nanomaterials, with sheet resistances below 100 Ω/sq and transmittances exceeding 80 %.[12,126,304,305] Alternatively, rGO can be combined with other materials, such as

metal nanowires or grids, to form hybrid films with conductive and transparent properties comparable to ITO whilst maintaining high flexibility.[133,306] Typically, these other carbon-based films or hybrids or prepared through processes other than inkjet printing, where the sizes of individual sheets are not restricted to the nanoscale, thus reducing the number of grain boundaries that limit charge transport and increase sheet resistance.

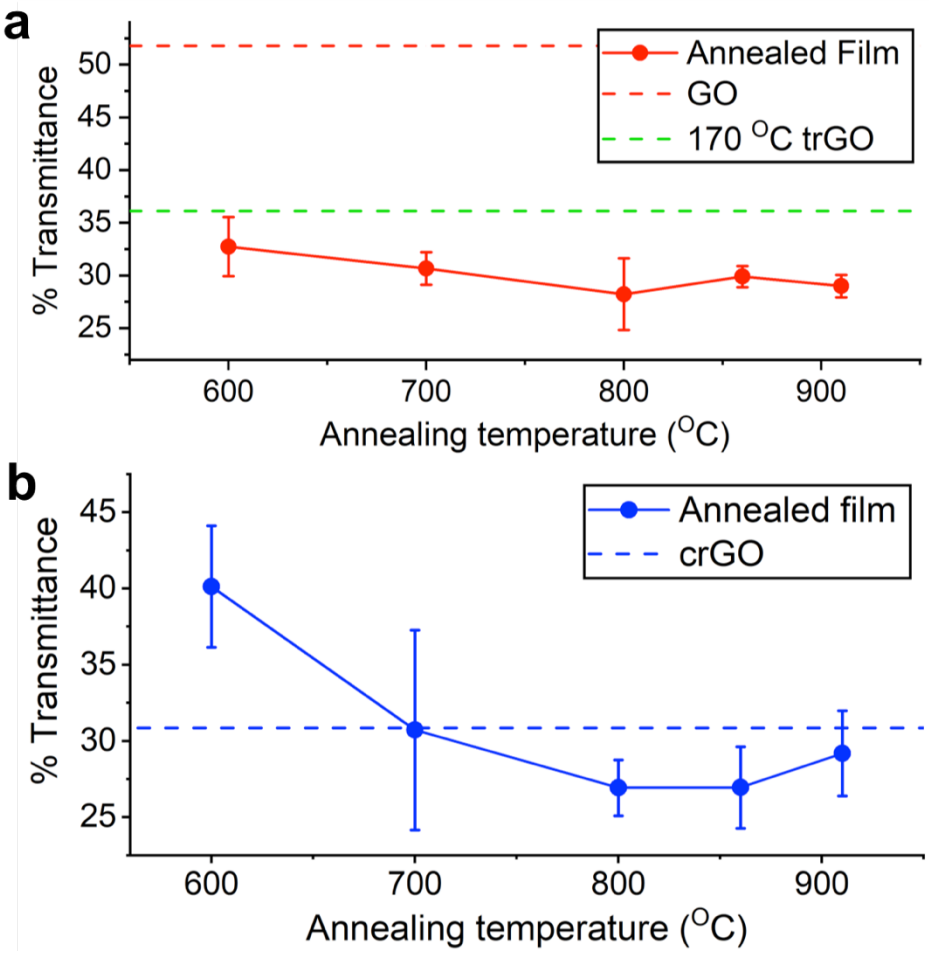

Figure 4.8 Plots of GO (a, red circles) and crGO (b, blue circles) average film % transmittance with standard deviations (nm), after thermal annealing between 600-910 °C. The GO (red dash), trGO at 170 °C (green dash) and crGO (blue dash) references are also included. Measurements were obtained using ImageJ software on optical images. ANOVA analysis (Appendices, Tables 4F) confirms differences in the widths and heights between one and two-step treated samples are only found to be significant at 600 °C (p = <0.05).

The transmittance values of films can be observed above in Figure 4.8 (Methodology, Section 2.16). There appears to be no obvious trends between annealing temperature and % transmittance, with the majority of films exhibiting transmittances between 26-32 %. ANOVA analysis (Appendices, Table 4F) also confirms that the

only significant difference in transmittance between single and dual step reduced films is found at 600 ^{O}C (p = <0.05). This is most likely due to the larger difference in film height recorded at this condition (Figure 4.3). As was the case in Chapter 3, the printed films are too opaque for use as transparent, conductive electrodes. Transparency can be increased by simply printing less layers but will come at the expense of increased sheet resistance. Solution processed rGO films with transmittances of between 78-84 % have been reported in literature but typically exhibit higher sheet resistances, 10^2-10^5 Ω/sq than films prepared using graphene or carbon nanotubes.[100,109,285]

4.2.4 XPS characterisation of rGO films

The characterisation of films through XPS was also undertaken (Methodology, Section 2.17), with C1s and O1s regions of particular interest in order to monitor the loss of oxygenated groups from GO and crGO through annealing. Unfortunately, O1s signals suffered from interfering signals from the sapphire substrate used and hence could not be analysed accurately (Appendices, Figure 4B). Notably sapphire exhibits an intense peak centred at 530.5 eV, overlapping with signals attributed to oxygen doubly bonded to aromatic carbon (531 eV) and oxygen singly bonded to aliphatic carbon (532 eV).[153] The penetration depth of X-rays can reach 10 nm, with regions of films found to be thinner than this, especially after compression with treatment and due to the low number of print cycles used along with the coffee-ring effect reducing homogeneity.[307] Thus analysis within this section will focus predominantly on collected C1s spectra (Figure 4.9 and Appendices, Figures 4C and 4D), which can be deconvoluted into three main peaks assigned to an sp^2 component (284.6 eV), oxygen bonded to carbon in hydroxyl or epoxide configurations (~286 eV) and oxygen related to carboxyl or carbonyl groups (~288 eV), with agreement to literature.[264,274,308]

The distinction between separate hydroxyl and epoxide signals, as well as separate carbonyl and carboxyl signals, could not be reliably made due to the high resolution of the tracks. This meant measurements had to be collected over a small area resulting in increased spectral noise. For annealed GO and crGO films an additional feature at higher binding energy (~290.5 eV) could be fitted, identified as a π-π* satellite peak.[153,272] This indicates the reparation of graphene's delocalized carbon lattice to some extent after chemical and thermal treatment. Another indication of

higher levels of graphitisation in reduced samples was the shifting of C1s peak maxima to lower binding energies (Appendices, Figure 4E).[153]

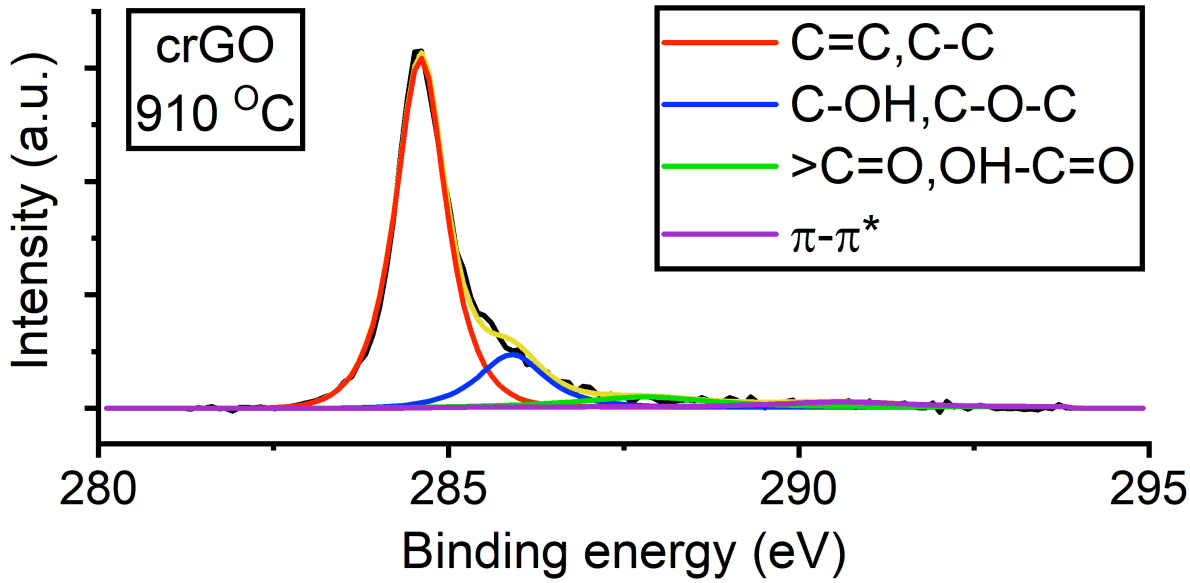

Figure 4.9 C1s XPS spectra of crGO thermally annealed at 910 °C for 1 h. The spectrum was fitted using CasaXPS software, after a Shirley background subtraction and using a mixture of Guassian and Lorentzian functions (20:80 Guassian : Lorentzian). C1s spectra for all other films are located in the Appendices, Figures 4C and 4D.

For crGO, fitting was aided by the introduction of an extra peak at 285.5 eV. This energy can correspond to hydroxyl groups but also to carbon-nitrogen bonding.[264,309,310] During the hydrazine reduction of GO, ring-opening of an epoxy group occurs to form a hydrazine alcohol, followed by a further reaction to form an aziridine species which then undergoes thermal-elimination of diimide to form a carbon-carbon double bond.[275,311] This chain of reactions can potentially stop at any transition state leading to unintentional doping with nitrogen. Park et al. have also reported the insertion of an aromatic N_2 moiety into a 5-membered ring at the edges of rGO sheets through use of hydrazine.[312] The presence of nitrogen bound to carbon within the crGO sample was confirmed through the analysis of its N1s region (Appendices, Figure 4F) with a clear signal at 400 eV discovered. This feature is not evident with trGO samples or with crGO samples after annealing, suggesting nitrogen species are effectively removed at temperatures below 600 °C.

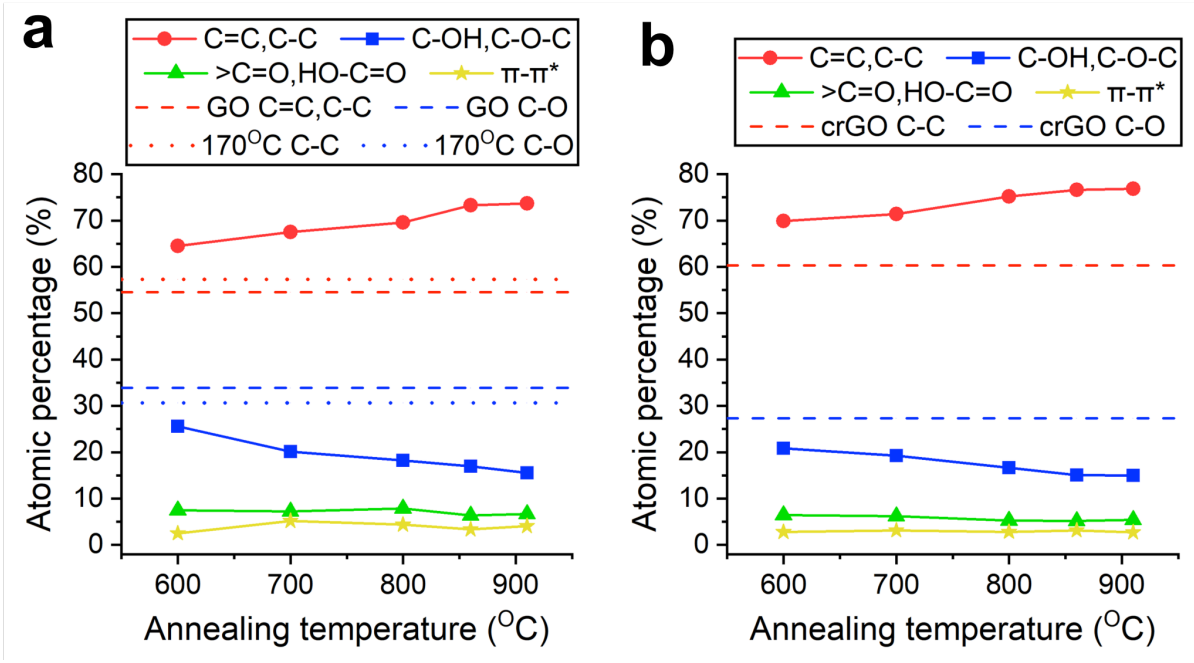

Figure 4.10 Plots showing the temperature-dependence of the atomic percentage (%) of C1s peak components, calculated from dividing the area under each component by whole C1s area for GO (a) and crGO (b) films. C=C,C-C is sp^2 component, C-OH,C-O-C is hydroxyl and epoxide moieties, >C=O,OH-C=O is carbonyl and carboxyl moieties while π-π* satellite peak is also shown. Lines represent sp^2 (C-C) and hydroxyl and epoxide (C-O) values for GO and crGO references (dashed) and for trGO sample reduced at 170 °C (dotted).

The contributions of oxygen moieties on rGO structures can be observed above in Figure 4.10. The sp^2 fraction of GO (Image a) was found to be 54.5 %, which increased marginally to 57.3 % upon reduction at 170 °C. This explains the relatively low conductivity measured for the trGO sample with only slight reparation of the material's 2D framework. This change in sp^2 character was mirrored by a small decrease in the hydroxyl and epoxide component, from 33.9 % down to 30.7 %. A negligible change in these oxygenated species was similarly reported by Ganguly et al. at 200 °C.[153] A more substantial increase in sp^2 fraction, to 60.3 %, was found upon chemical reduction with hydrazine (Image b) along with a corresponding decrease in oxygenated groups singly bonded to the lattice, down to 27.4 %. This is expected with hydrazine known to selectively reduce epoxide species and confirmed by the atomic percentage of carbonyl and carboxyl species remaining constant before and after treatment (11.5 % for GO and 11.1 % for crGO).[275,312] The actual atomic percentage of oxygen singly-bound to carbon for crGO will in fact be lower due to the unintentional doping of material with nitrogen already highlighted and with this component unable to be reliably separated from the hydroxyl feature.

As annealing temperature is increased, the sp^2 fraction of GO and crGO films also increase (Images a and b). At 910 ^{O}C, the sp^2 region of films accounts for 73.7 % and 76.8 % of the total C1s signal for single and dual-step reduction samples respectively. The sp^2 component of films obtained through the multistep reduction at any given temperature is found to be higher than those solely thermally annealed, explaining the higher conductivities observed with these films. This could be a result of the enhanced removal of epoxide functionalities by first treating films with hydrazine. The desorption of epoxide species from GO by thermal annealing is a conflicting topic, with Gao et al. modelling that these cannot be removed at temperatures below 1200 ^{O}C while Larciprete et al. report reversible desorption at temperatures below 500 ^{O}C. [110,275]

The change in sp^2 content is mirrored by a decrease in the amount of hydroxyl and epoxide groups, with a lowest percentage of total C1s area of 15.6 % for GO annealed at 910 ^{O}C and 15.0 % for crGO annealed at the same temperature.

The loss of hydroxyl and epoxide functionalities appears to be the predominant driving force for the restoration of the graphene lattice, with the area percentages of carbonyl and carboxyl groups with respect to C1s envelopes found to remain constant for both sets of films above 600 ^{O}C. A small decrease in values between GO (6.7-7.9 %) and crGO (5.2-6.5 %) was observed which could be attributed to the fact that hydrazine has been theorised to convert carbonyls to hydrazones through side reactions.[276] Below 600 ^{O}C both sets of films exhibit similar losses with regards to the doubly-bound oxygen to carbon fraction, of 4.1 % for GO and 4.7 % for crGO, along with a slight shift of components to lower binding energy. This suggests the preferential loss of carboxyl species within this temperature regime, with carbonyl groups predominant above 600 ^{O}C.[153] The prevalence of carbonyl groups across the range of annealing temperatures agrees with thermodynamic simulations, with decarbonylation of GO found to have the highest activation energy, while Bagri et al. have postulated the favourable conversion of neighbouring hydroxyl and epoxides into carbonyl functionalities at temperatures between 150-1000 ^{O}C. [157,275] Overall, XPS observations are consistent with other reports in which oxygenated defects still persist after annealing at 900-1100 ^{O}C.[153,157,216,313]

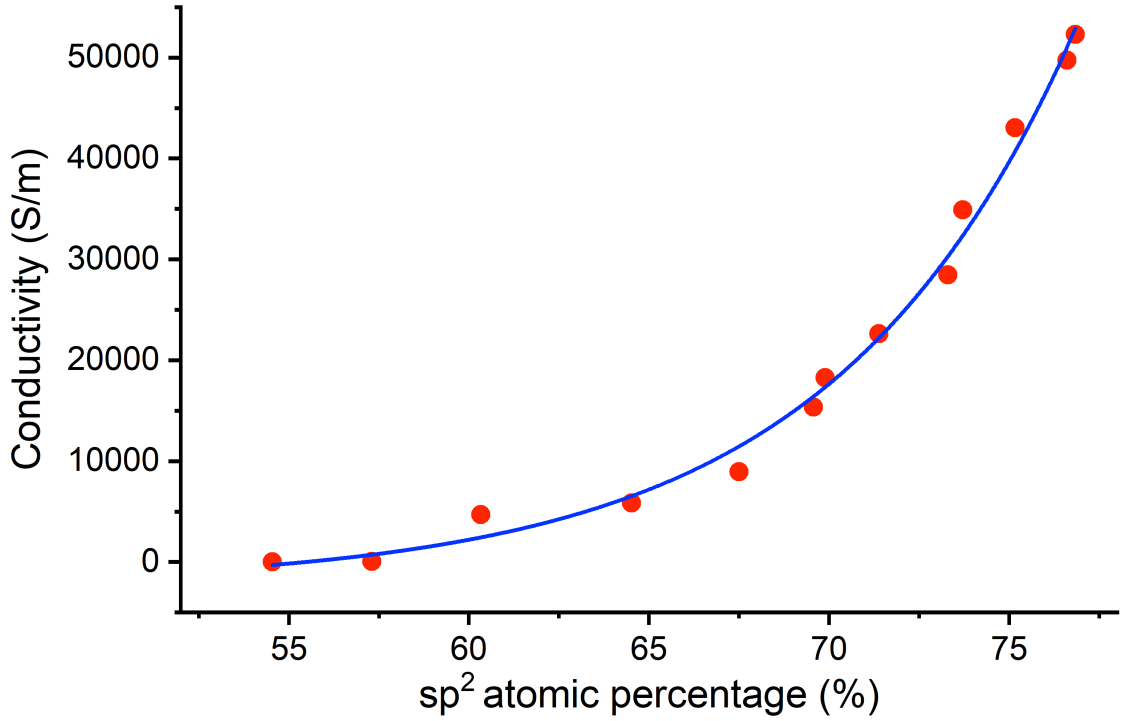

Figure 4.11 Plot of average conductivity (S/m) vs. sp^2 atomic percentage (%) for GO and crGO films, before and after thermal annealing at 170 ^{O}C and at temperatures ranging between 600-910 ^{O}C. The sp^2 atomic % was calculated from the area of sp^2 component relative to the whole area under C1s envelopes. Data is fitted with an exponential growth curve.

An exponential relationship between film sp^2 atomic percentage and conductivity can be derived from the XPS data, with the plot given above in Figure 4.11. As sp^2 content within films is increased, its electrical performance is boosted as a result of the restoration of graphene's delocalised π system, increasing the density of charge carriers and their mobility.[157,314] Due to the influence of the substrate on O1s spectra, areas of carbon and oxygen signals obtained from survey scans could not be converted into accurate carbon/oxygen (C/O) ratios. Ganguly et al. reported a similar sp^2 intensity maximum of 77 % after annealing at 1000 ^{O}C, corresponding to a film C/O ratio of 33.[153] One could assume that the crGO sample annealed at 910 ^{O}C would consist of a similar ratio of the two elements. C/O ratios for GO annealed at 900 ^{O}C have also been reported, with lower values ranging from 14.1-23.4 calculated.[274,315,316] These estimated C/O ratios justify the use of the two-step reduction protocol in order to enhance film graphitisation.

4.2.5 Raman analysis of the D and G region of rGO films

Raman characterisation of films was carried out in order to access the effectiveness of the reduction processes and the quality of graphene films obtained (Methodology,

Section 2.18). The phonon modes of graphene-based materials are able to provide valuable insight with regards to layer structure, defect density, doping, strain and conductivity.[159] This section will cover the analysis of material D and G regions, with the 2D area covered in the following section, with changes in peak intensities, areas and shifts used to deduce the physicochemical properties of films.

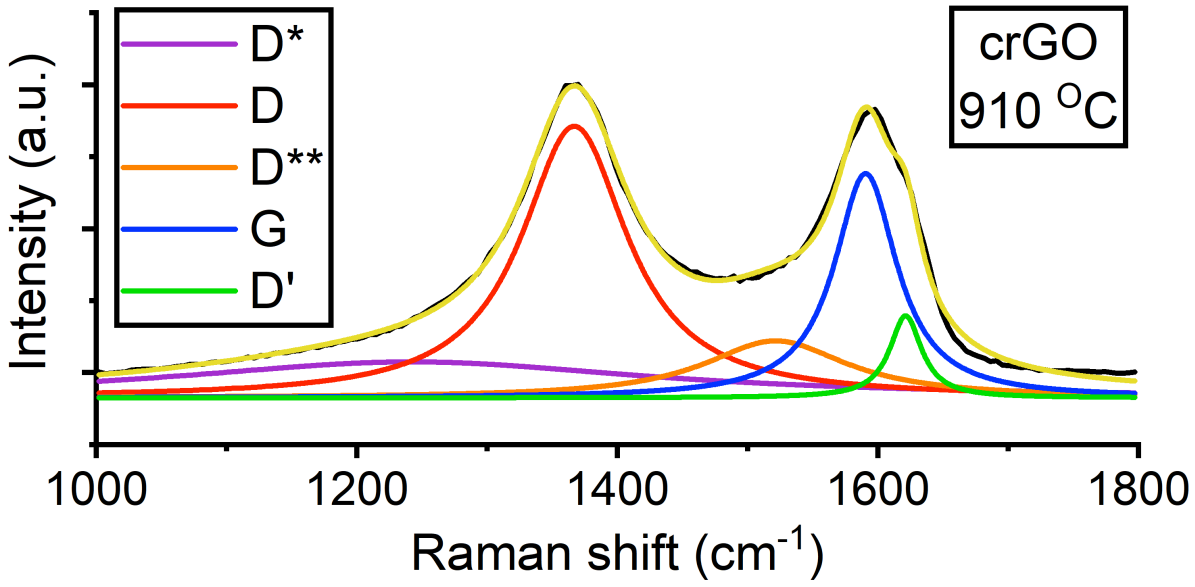

Figure 4.12 Raman spectrum of D and G regions (1000-1800 cm^{-1}) of crGO after thermal annealing at 910 ^{O}C for 1 h. D and G bands have been deconvoluted into D*, D, D**, G and D' peaks according to Kaniyoor et al.[217] Spectra for all other films are located in the Appendices, Figures 4G and 4H.

The Raman spectrum of the crGO film annealed at 910 ^{O}C is displayed above in Figure 4.12, with deconvolution of bands carried out using Origin software and according to the paper published by Kaniyoor et al.[217] The spectra of all the other films can be found in the Appendices, Figures 4G and 4H. Five features can be identified within Raman signals, two prominent D and G modes along with three less intense D*, D** and D' modes. The G band, located at around 1580 cm^{-1}, arises from bond stretching of sp^2 pairs in rings or chains and thus is often associated with the level of graphitisation within carbon-based films.[159,162,317] The lower frequency D peak, positioned near 1350 cm^{-1}, is assigned to the breathing modes of sp^2 atoms in rings but critically requires a defect for its activation.[159] Hence, the D band is absent within pristine graphene and is often used a measure of disorder within defected graphene structures.[168,169,279] The D' feature appearing beside the G peak at higher frequency, near 1620 cm^{-1}, is also defect-induced and observed in amorphous carbon materials.[159,169,279] The D* mode, around 1190 cm^{-1}, has been previously

attributed to the sp^3 rich phase of highly-defective carbons while the D** mode, near 1500 cm^{-1}, could be a result of either finite sized graphitic crystals or due to carbon-hydrogen vibrations.[161,318] Alternatively, Ferrari et al. argued that these two peaks were caused by the presence of trans-polyacetylene moieties, consisting of an alternating chain of sp2 carbons with a single hydrogen bonded to carbon.[168] These two peaks are often disregarded with regards to characterising graphene materials, with changes to the D, G and D' peaks of particular interest.

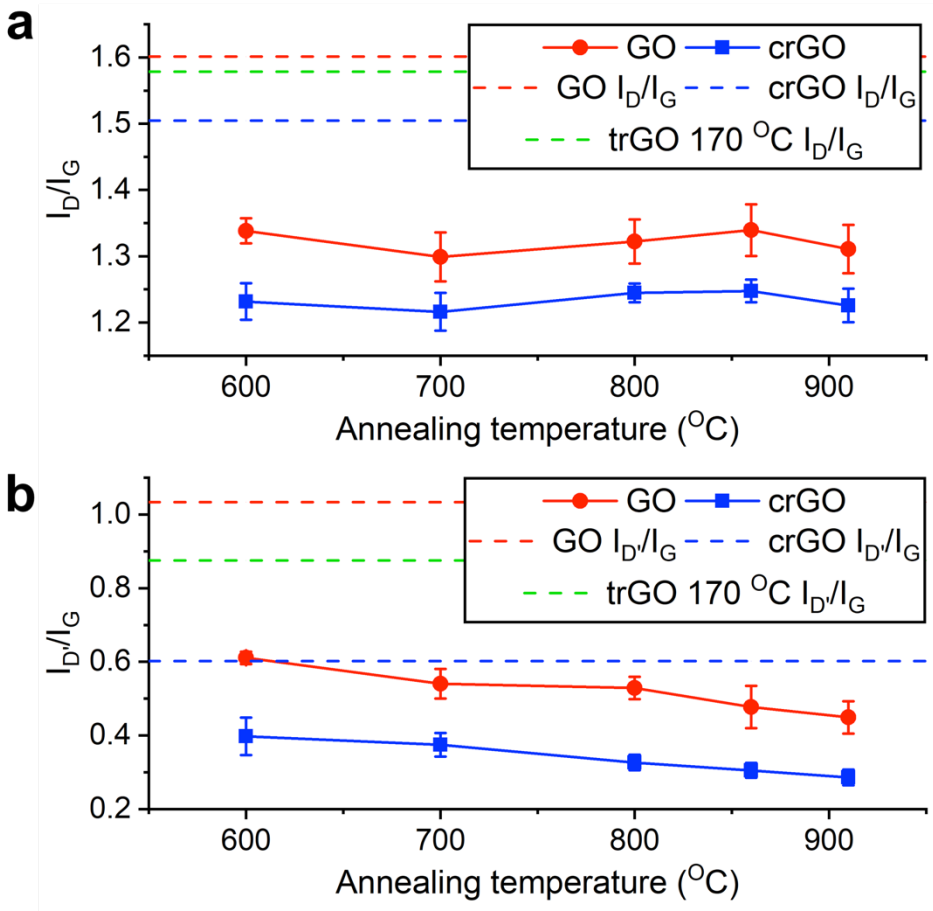

Figure 4.13 Average I_D/I_G (a) and $I_{D'}/I_G$ (b) ratios and standard deviations for annealed GO (red circles) and crGO (blue squares). Shown also are values for GO (red dash) and crGO (blue dash) references and the trGO film annealed at 170 ^{O}C (green dash). Raman spectra were deconvoluted according to Kaniyoor et al.[217] ANOVA analysis (Appendices, Table 4G and 4H) confirm differences in I_D/I_G and $I_{D'}/I_G$ between one and two-step treated samples are significant across the whole temperature range ^{O}C (p = <0.05).

The most common method for analysis of graphene film quality is through the measurement of D and G band intensities to give a ratio between the two (I_D/I_G). I_D/I_G values can be used as a tool to assess defect density and estimate crystallite size within carbon based materials.[159,279,319] The plot of I_D/I_G vs. annealing temperature for

GO and crGO films are shown above in Figure 4.13 (Image a), with data for reference samples and the sample reduced at low temperature also given. Measurable change in I_D/I_G compared to GO (I_D/I_G = 1.61) are seen for all films, regardless of reduction conditions, with all values decreasing. This change is often not seen in literature, or slight increases in I_D/I_G are reported post reduction, as the contribution of D' to the G band is not considered.[30,245,264,274] The lowering of I_D/I_G values can be attributed to the desorption of oxygenated groups from treated films, reducing the D intensity, and the reparation of the sp^2-hydribised lattice, increasing G intensity. Only small changes in I_D/I_G are measured for the sample reduced at low temperature (I_D/I_G = 1.57), coinciding with XPS data showing only a minimal increase in sp^2 character due to inefficient defect removal.[301,302] The chemically reduced film also only exhibited a small decrease (I_D/I_G = 1.51), most likely due to the doping with nitrogen species identified previously through XPS.

More substantial lowering of I_D/I_G ratios was observed for annealed GO and crGO films, with values ranging between 1.30-1.34 and 1.22-1.25 respectively. The smaller values calculated for films treated with the dual-step reduction protocol is in good agreement with the conductivity measurements and XPS analysis, which also implied increased levels of graphitisation compared to thermally annealed GO films. The fact that I_D/I_G ratios are seen to decrease after reduction suggests that crystallite sizes within samples are large enough for the Tuinstra-Keonig equation to be applied.[162,164,317] Utilising this relation, the largest crystallite size calculated for annealed films is 10.5 nm with GO and 11.2 nm with crGO, compared to 8.5 nm for unreduced GO.

For both sets of films, I_D/I_G ratios are found to be similar across the temperature range, yet XPS analysis shows a continual restoration of aromatic character through expulsion of functional groups throughout this same range. These two observations appear to be contradictory but can be explained by the fact that the Tuinstra-Keonig equation gives only the average size of crystallite domains. The thermal reduction of graphene is known to result in the generation of lattice vacancies and topological defects that can disrupt aromaticity, reducing the average size of crystallites.[110,153,275] Additionally, damage to films through cracking has already been highlighted at these extreme temperatures (Figure 4.4). A more accurate measure of GO deoxygenation may be through the calculation of $I_{D'}/I_G$ ratios, with these also expected to be lower in less-defective graphene structures.[280,320] These are also given in Figure 4.13 (Image

b), with values for both sets of films decreasing with increasing temperature to coincide with the loss of oxygen moieties.

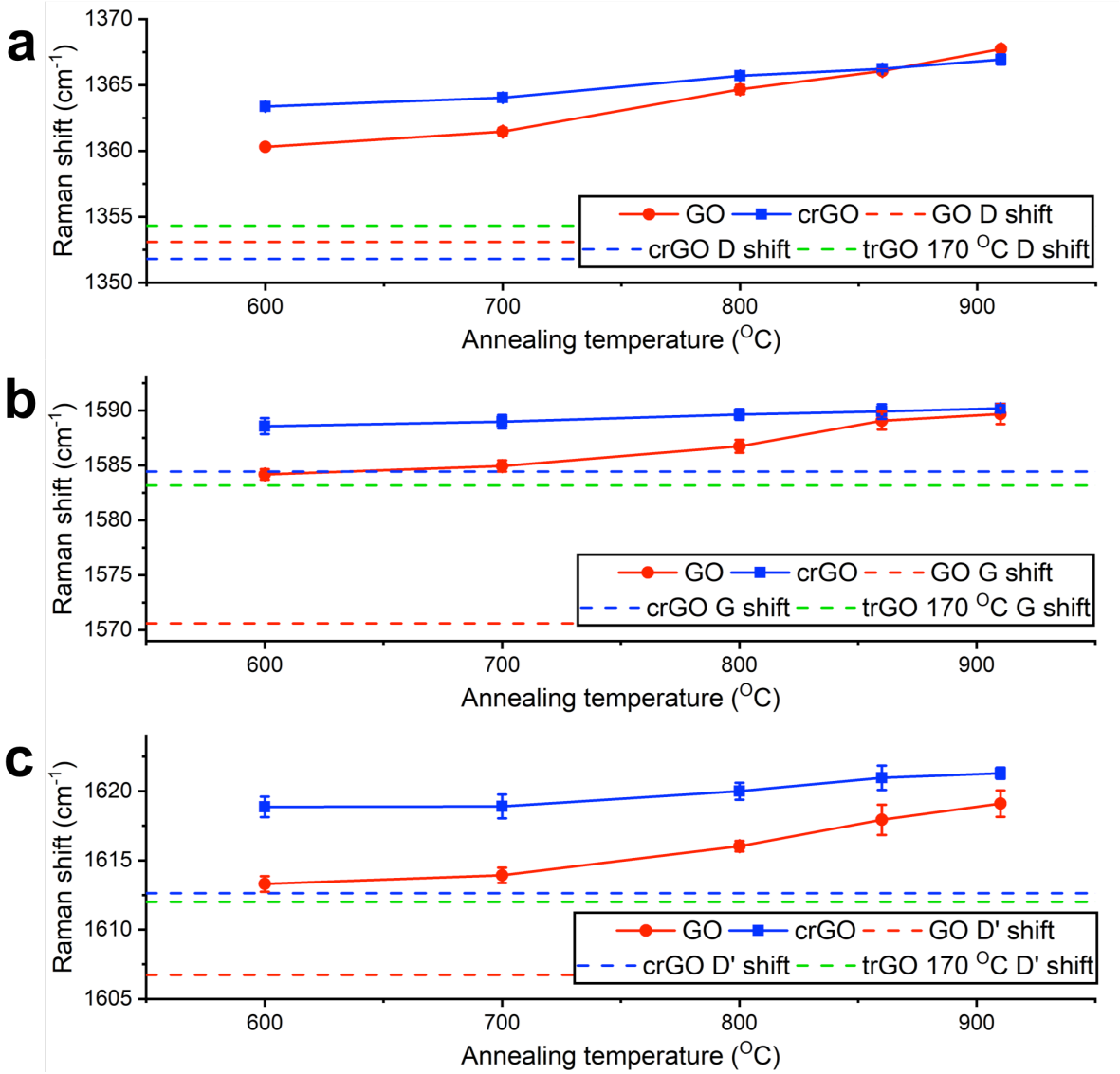

Figure 4.14 Average Raman shifts (cm^{-1}) and standard deviations for D (a), G (b) and D' (c) modes of GO (red circle) and crGO (blue square) films annealed at temperatures ranging from 600-910 ^{O}C. Shown also are values for GO (red dash) and crGO (blue dash) references along with the sample reduced at 170 ^{O}C (green dash). Raman spectra were deconvoluted according to Kaniyoor et al.[217] ANOVA analysis (Appendices, Table 4I, 4J and 4K) confirms that only differences in the D shift at 860 ^{O}C and G shift at 860 and 910 ^{O}C are insignificant (p = >0.05).

The Raman shifts of D, G and D' modes are plotted in Figure 4.14 above. Bands exhibited blue shifts to higher frequency upon reduction, with the only exception being the slight red of the crGO D band. All bands show clear trends of higher frequency resonance with increasing annealing temperature. The shifting of D and G bands to higher frequencies can be correlated to the compressive strain introduced

within films through thermal annealing, with this topic already discussed in Section 4.2.1 and similar observations reported in literature.[321–323] The position of the G band has also been proven to be sensitive to the density of charge carriers, with both electron and hole doping able to result in a blue shift.[322,324,325] The shifting of the G band may therefore be a combination of strain and doping effects. King et al. have published a Raman metric for the characterisation of graphene oxide materials, deriving a relationship between the G and D' positions and the C/O ratio of films.[320] The shifting of G and D' to higher wavenumbers was found to correspond to an increase in C/O ratio, agreeing with the XPS analysis in Section 4.2.4. The shifting of D' closer to the frequency seen with graphite, at 1620 cm^{-1}, has also been reported by Nemanich et al. as a marker for higher levels of graphitisation within carbon structures.[326]

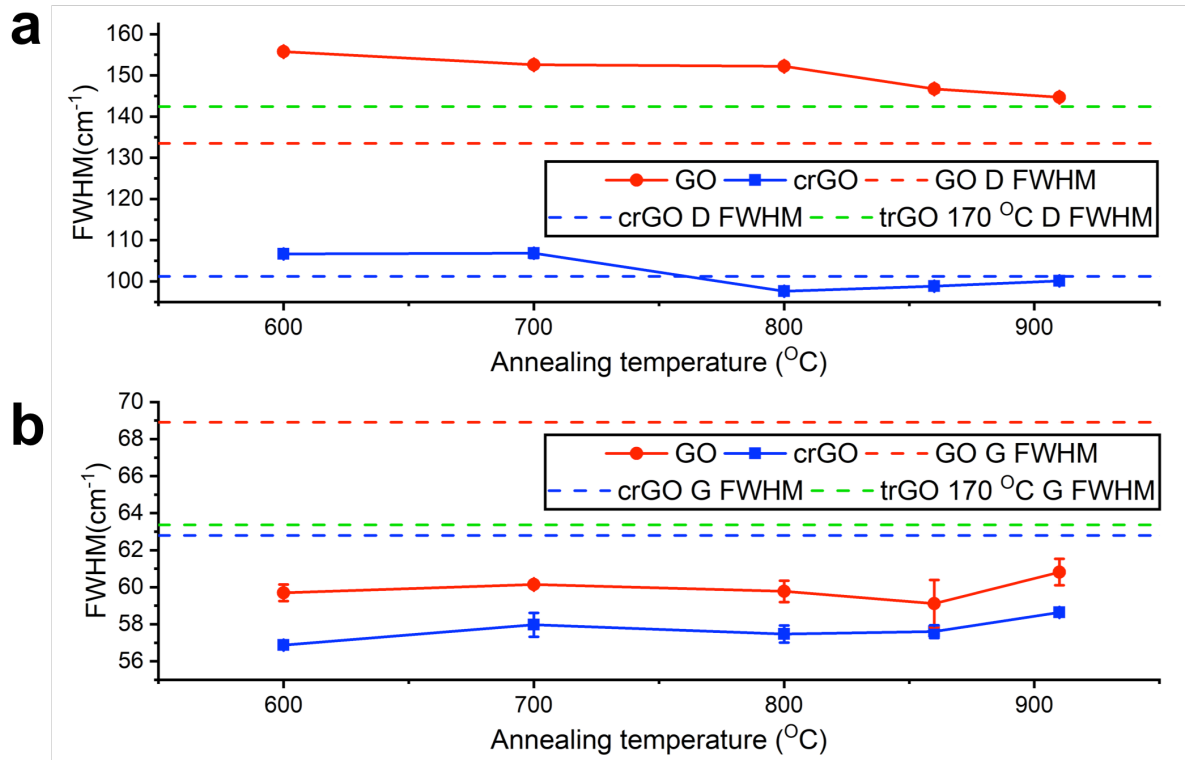

Figure 4.15 Average FWHM and standard deviations (cm^{-1}) for D mode (a) and G modes of annealed GO (red circle) and crGO (blue square) films at temperatures ranging 600-910 °C. Shown also are values for GO (red dash) and crGO (blue dash) references along with the sample reduced at 170 °C (green dash). Raman spectra were deconvoluted according to Kaniyoor et al.[217] ANOVA analysis (Appendices, Table 4L and 4M), confirm only the difference in the G width between one and two-step treated samples at 860 °C is insignificant (p = >0.05).

The FWHM values for D and G bands can be viewed within Figure 4.15. The breadth of these two Raman features can also be interpreted to gauge the efficiency of GO

reduction, with narrowing of both typically expected to occur within more pristine graphene-based films.[327–329] The reduction in G band width can be observed for both GO and crGO films after thermal annealing (Image b), with crGO films displaying smaller FWHM values compared to GO films to suggest greater levels of defect removal.

Interestingly, both sets of films exhibit initial broadening of D modes (Image a) after exposure to heat. Even the sample treated at 170 ^{O}C showed some broadening of the D signal. A similar observation was reported by Diez-Betriu et al. after thermal treatment of GO at 300 ^{O}C and assigned to the evaporation of water and initial compaction of films introducing structural defects.[280] Above 600 ^{O}C, the D peak for both sets of films appears to gradually narrow with increasing temperature, most likely as a result of increased sp^2 character attained through loss of functionalities. Even after thermal annealing at 910 ^{O}C, the D modes of films are still pronounced. This supports XPS studies where the presence of considerable amounts of oxygenated defects were still identified after treatment. The introduction of additional defects through the thermal annealing films, such as lattice vacancies, will also broaden D signals and have been reported to occur over the temperature range tested.[110,275] These observations suggest that the quality of rGO films can be further improved through optimisation of reduction protocols. The complete removal of oxygenated species can require temperatures approaching 1500 ^{O}C, while at even higher temperatures any lattice imperfections gained through the stripping of oxygenated groups can heal.[107]

4.2.5 Raman analysis of the 2D region of rGO films

Graphene-based materials also exhibit Raman features at higher frequency, between 2500-3500 cm^{-1}, with the spectrum for the crGO sample annealed at 910 ^{O}C shown in Figure 4.16 and all other samples grouped in the Appendices, Figures 4I and 4J. This region is often disregarded with defective films, or films composed of many layers, due to its low intensity compared to D and G bands, yet valuable information on their composition can be attained through its analysis.

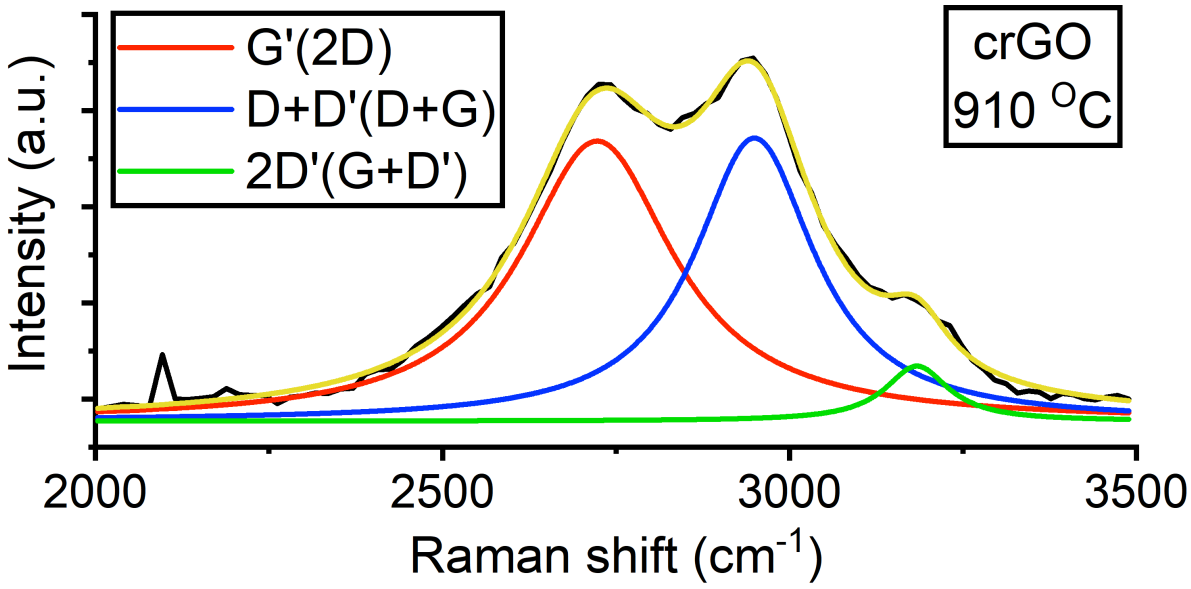

Figure 4.16 Raman spectrum of the 2D band (2000-3500 cm^{-1}) of crGO after thermal annealing between at 910 ^{O}C for 1 h. The band has been deconvoluted into G', D+D' and 2D' peaks according to Kaniyoor et al.[217] Spectra for all other films are located in the Appendices, Figures 4I and 4J.

This area is generally referred to as the 2D region and can be deconvoluted into three overlapping signals, two more intense G' and D+D' bands and a weaker 2D' band.[217,330] The G' band, located around 2700 cm^{-1} is also referred to as the 2D band, originating from a double resonance Raman process and indicative of crystalline graphitic materials.[153,159,217] This peak is also highly sensitive to stacking order and is thus mainly used to distinguish single-layer from few-layer graphene.[167–169] The D+D' band, positioned near 2900 cm^{-1}, has also be assigned as D+G in articles.[153,166,331] This is a combinational mode of signals within D and G features and is defect-activated. The 2D' peak, near 3150 cm^{-1}, is an overtone of the D' peak and has been detected in graphite at low intensity.[330] Kaniyoor et al. also identified an additional weak signal, resonating at 2445 cm^{-1} and labelled G*, but this was unable to be fitted reliably to spectra.[217]

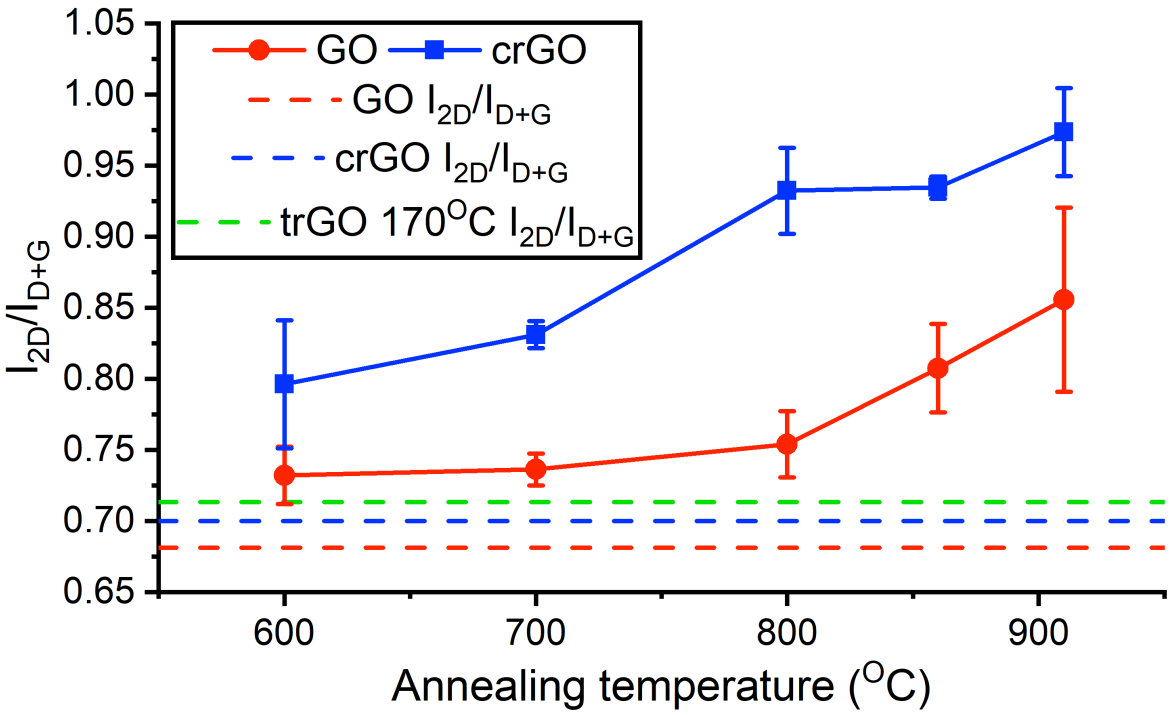

Figure 4.17 Average I_{2D}/I_{D+G} ratios and standard deviations for GO (red circle) and crGO (blue square) films after annealing at temperatures between 600-910 ^{O}C. Shown also are values for GO (red dash) and crGO (blue dash) references along with the sample reduced at 170 ^{O}C (green dash). Raman spectra were deconvoluted according to Kaniyoor et al.[217] ANOVA analysis (Appendices, Table 4N) confirms only the difference in I_{2D}/I_{D+G} ratios between one and two-step treated samples at 600 ^{O}C is found to be insignificant (p = >0.05).

In a similar manner to D and G signals, the ratio of G' (2D) and D+D' (G+D) intensities have also been used to as an indicator of graphene quality (I_{2D}/I_{D+G}).[165,166] The I_{2D}/I_{D+G} ratio is expected to be larger for less-defective structures, with the 2D band sensitive to aromatic nature and the D+G band sensitive to lattice disorder. The I_{2D}/I_{D+G} ratios of samples with respect to annealing temperature are plotted above in Figure 4.17, with increasing temperature resulting in a gain in magnitude of I_{2D}/I_{D+G}. This suggests that the extent of graphitisation achieved in films is greater at higher temperatures, consistent with XPS data in Section 4.2.4. At any given condition, the I_{2D}/I_{D+G} of an annealed crGO film is greater than that for annealed GO. This coincides with XPS and I_D/I_G characterisation that confirmed the more efficient removal of oxygenated groups and the restoration of larger crystallite domains through the two-step reduction protocol. The I_{2D}/I_{D+G} ratios for the film reduced at 170 ^{O}C and the hydrazine reduced reference are found to be similar and smaller than annealed samples, indicating smaller differences in aromaticity between these and unreduced GO.

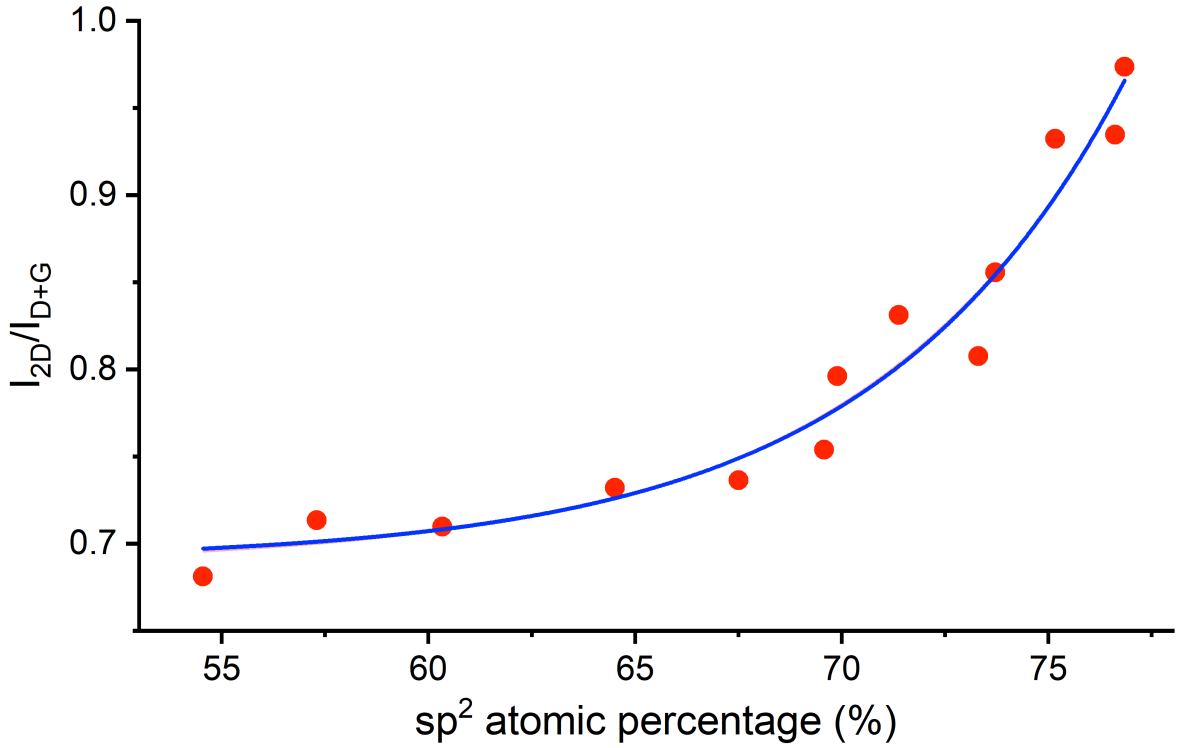

Figure 4.18 Plot of average I_{2D}/I_{D+G} vs. sp^2 atomic percentage (%) for GO and crGO films before and after thermal annealing at 170 ^{O}C and at temperatures ranging between 600-910 ^{O}C. The sp^2 atomic % was calculated from the area of sp^2 component relative to the whole area under C1s envelopes. Data points are fitted with an exponential growth curve.

The plot of film I_{2D}/I_{D+G} against sp^2 atomic percentage is displayed above in Figure 4.18. A clear exponential trend of higher I_{2D}/I_{D+G} values with increased graphitic nature is obtained, suggesting that I_{2D}/I_{D+G} could be used as a more powerful tool for determination of film quality rather than I_D/I_G ratios. The superimposition of the G band with the defect activated D' band could be a reason for this, resulting in more ambiguity with regards to peak fitting. This is less problematic when using 2D and D+G features due to the increased separation, giving two distinctive humps in Raman spectra. As previously mentioned the intensity of the D peak is also highly sensitive to the size of crystallites, with films of higher sp^2 content able to give higher I_D/I_G ratios due to the reduction in the average size of crystallites upon annealing. [110,162,275] This confusion appears to be avoided with the application of I_{2D}/I_{D+G}, with less defective films giving higher values.

3.4 Conclusion

The fabrication of high-resolution and continuous GO films on Al_2O_3 was successfully performed through the formulation of the optimised glycol-based GO ink and application of inkjet printing techniques introduced in Chapter 3. Films were then exposed to either a one-step or two-step reduction protocol, consisting of a thermal annealing process at temperatures ranging from 600-910 ^{O}C with or without prior chemical reduction with hydrazine vapour. The use of the dual step reduction protocol was found to enhance film conductivity, with XPS and Raman studies confirming a greater extent of oxygenated defect removal and sp^2 structural restoration. A highest film conductivity of 52,300 S/m was measured, after chemical treatment and annealing at 910 ^{O}C, exceeding the most conductive inkjet-printed film reported to date by Su et al (43,000 S/m).[60] Upon reflection of this result, the second aim of this study was reached, with significant enhancement of rGO conductivity achieved compared to that attained by the chemical route followed in Chapter 3. However, despite this improvement, the corresponding sheet resistance (740 Ω/sq) and transmittance (29 %) of remain inferior to ITO films currently on the market.[114] XPS proved the persistence of oxygenated defects, with appreciable levels of epoxide, hydroxyl and carbonyl functionalities still remaining, whilst a pronounced defect activated D peak was also observed by Raman spectroscopy. These findings suggest that other avenues may need to be explored in the search for a viable substitute for ITO. Future work could see the formulation of inks containing more pristine carbon-based materials, such as graphene or carbon nanotubes, or mixing of rGO with other materials, such as metal nanowires, to form hybrids with enhanced properties. Inks may be more difficult to formulate but resulting films would not require annealing at high temperatures, also making printing onto polymer substrates for low cost, flexible electrodes feasible.

Chapter 5. Inkjet printing of semiconducting DNA nanowires

5.1 Introduction

The formulation and printing techniques explored with graphene oxide (GO) in Chapters 3 and 4 can also be adapted for use with other hydrophilic nanomaterials, such as DNA nanowires. These can be prepared by nucleating the growth of conductive materials on DNA molecules, with semiconductors, metals and conductive polymers all synthesised in this manner.[177,328–343] The role of DNA within these systems is to provide a long, thin, chemically-robust template to direct the growth of materials as 1D structures. With the diameter of its duplex structure being just over 2 nm, the thicknesses of wires can be confined to only a few nanometers.[181,182] Usually, the conductivity of DNA-templated nanowires is inferior to that of bulk material or of nanowires fabricated through other techniques, such as the vapour-liquid-solid (VLS) method.[186] This is because VLS wires are synthesised as single crystal units while DNA-based wires are composed of many nanoparticles on a chain, giving a highly granular appearance.[182,187] This hinders the use of DNA nanowires as highly conductive components but applications in sensing have still been demonstrated.[187]

Nanowire synthesis is generally carried out with the DNA immobilised on a surface or dispersed within aqueous media before doping with solutions containing the desired species.[181,183,342] The advantage of using the wet chemical method (with DNA in water) is that the final nanowire dispersion can be thought of as an ink and can be tailored for use with inkjet technology, in a comparable method applied with graphene oxide in Chapter 3. The use of DNA to restrict material size also means that the use of capping agents and stabilisers, used routinely in solvent-based synthesis of nanoparticles to control Oswald ripening, can be avoided.[344]

The templating of cadmium sulphide (CdS) to DNA has already been studied in great detail.[181,182,187] CdS is a binary II-VI semiconductor, possessing a bulk band gap energy of 2.5 eV.[177] The material is yellow in colour with this property exploited for use as pigments, historically in art and more recently with plastics.[345,346] More recently potential applications of the material for solar cells, catalytic hydrogen production, light emitting diodes (LEDS) and photosensors have been identified.[22,23,185,346] Notably, CdS can exhibit photoluminescence in the visible region of the spectrum when excited under the appropriate conditions. This fluorescent property has been utilised in biological labelling, primarily using CdS quantum dots.[24,26,190] Another key property of CdS is its ability to strongly absorb volatile

vapours, with gas sensing behaviour reported upon exposure to species such as ethanol, methanol, carbon monoxide and hydrogen sulphide.[20,25,178,348]
Records of using CdS and DNA inks with inkjet technology exist already in literature but the use of CdS-templated DNA nanowires as a practical ink is novel. CdS inks usually consist of capped nanoparticles in organic solvent while DNA is kept within aqueous-based media to avoid degradation of material.[43,192–194] DNA inks are typically used to pattern a surface for assays rather than for the fabrication of continuous films. Examples of other types of printable nanowire-based inks have also been developed by other groups, of both semiconducting and metallic nature as well as conductive polymers.[349–353]

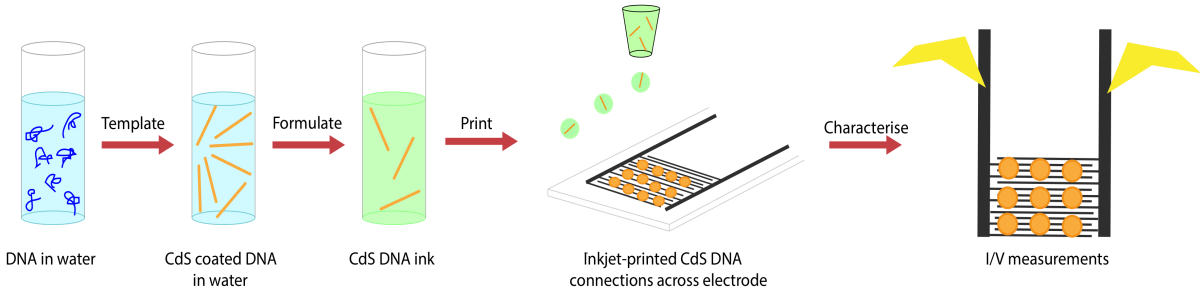

Figure 5.1 Schematic depicting the method of producing a CdS.DNA ink followed by the fabrication of a CdS.DNA conductive device through inkjet printing.

In the following chapter, the synthesis of CdS on lambda (λ) DNA by an established wet chemical method is described.[182] This DNA is linear and double stranded, with strand lengths exceeding 16 μm (over 48,000 base pairs), and is able to bridge the micron-scale electrode gaps in later work.[354] Characterisation of the CdS/λ.DNA through various microscopic and spectroscopic techniques is reported as well as the formulation of the dispersion into an ink suitable for inkjet printing using ethylene glycol. The inkjet printing and characterisation of luminescent multi-wire features on bare glass surfaces and semiconducting devices, using interdigitated electrodes, is also addressed, adapting techniques developed with the printing of GO in Chapters 3 and 4 (Figure 5.1). The following work seeks to address the third and final aim of the thesis, demonstrating the versatility of the methods devised with GO for use with other hydrophilic nanomaterials.

5.2 Results and discussion

5.2.1 Synthesis of CdS/λ.DNA in solution

The solution-based templation of CdS onto λ.DNA was carried out following a protocol previously described in literature and is outlined in the Methodology, Section 2.21.[182] This involved sequential doping of an aqueous solution of DNA with sources of cadmium and sulphide ions over a 4 day period, with incubation of the solution in a fridge in between steps. The production of CdS is signaled by a colour change in the DNA solution from colourless to yellow (Appendices, Figure 5A).[182]

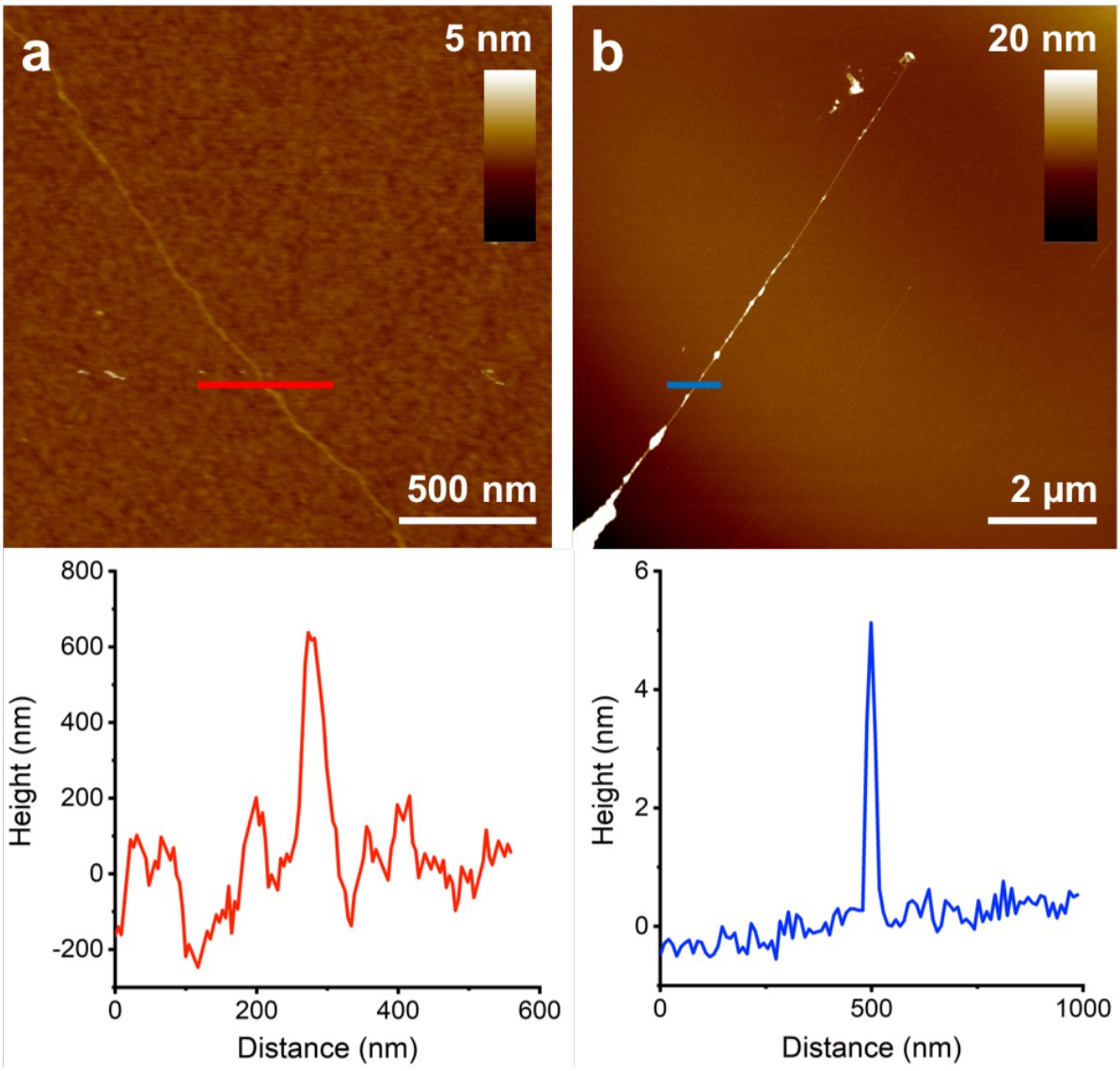

Figure 5.2 Tapping mode AFM images of λ.DNA strands deposited on Si before (a) and after (b) templation with CdS, with corresponding height profile measurements displayed below.

Figure 5.2 shows a typical AFM image of λ.DNA strands before and after templation with CdS (Methodology, Section 2.23). Bare DNA appears uniform in morphology along its length (Image a) with measured heights ranging from a few hundred picometres to one nanometre. This is consistent with reported height of double-stranded DNA (dsDNA) imaged with tapping mode AFM.[196] After incubation with cadmium and sulphide ions the appearance of the DNA is seen to change (Image b) with localised areas of strands, where CdS growth has taken place, appearing granular. The heights of these positions range from a few nanometres to over 10 nm, well exceeding the expected heights of bare dsDNA.[196] The incorporation of CdS onto DNA is far from regular, with large domains on strands and even whole strands themselves still exposed. It is theorised that the growth of particles on DNA occurs through a process similar to Oswald Ripening, where the formation of larger particles from smaller ones is energetically favorable.[182,185] For a single nanowire device this would be problematic but using printing as a method of device fabrication relies on the formation of deposits consisting of many wires in an extended network. Almost complete coverage of CdS onto strands has been demonstrated at much lower DNA concentrations and through the use of higher ratios of metal salt and sulphide.[187] However, for use as a viable ink it is beneficial for the DNA concentration to be as high as possible, meaning suitable amounts of material can be deposited on realistic timescales. Too high a ratio of metal salt and sulphide has also been shown to cause supercoiling of nanowires within solution.[187] This scenario would likely hamper the electrical performance of printed material, with strands unable to bridge electrode gaps.

5.2.2 Optical and fluorescent characterisation of CdS/λ.DNA

The absorbance of λ.DNA and CdS/λ.DNA solutions were recorded over a wavelength range of 200-800 nm, with spectra shown in Figure 5.3. An aqueous CdS solution was also run as a control, with semiconducting material grown in solution without the presence of DNA (Methodology, Section 2.23).

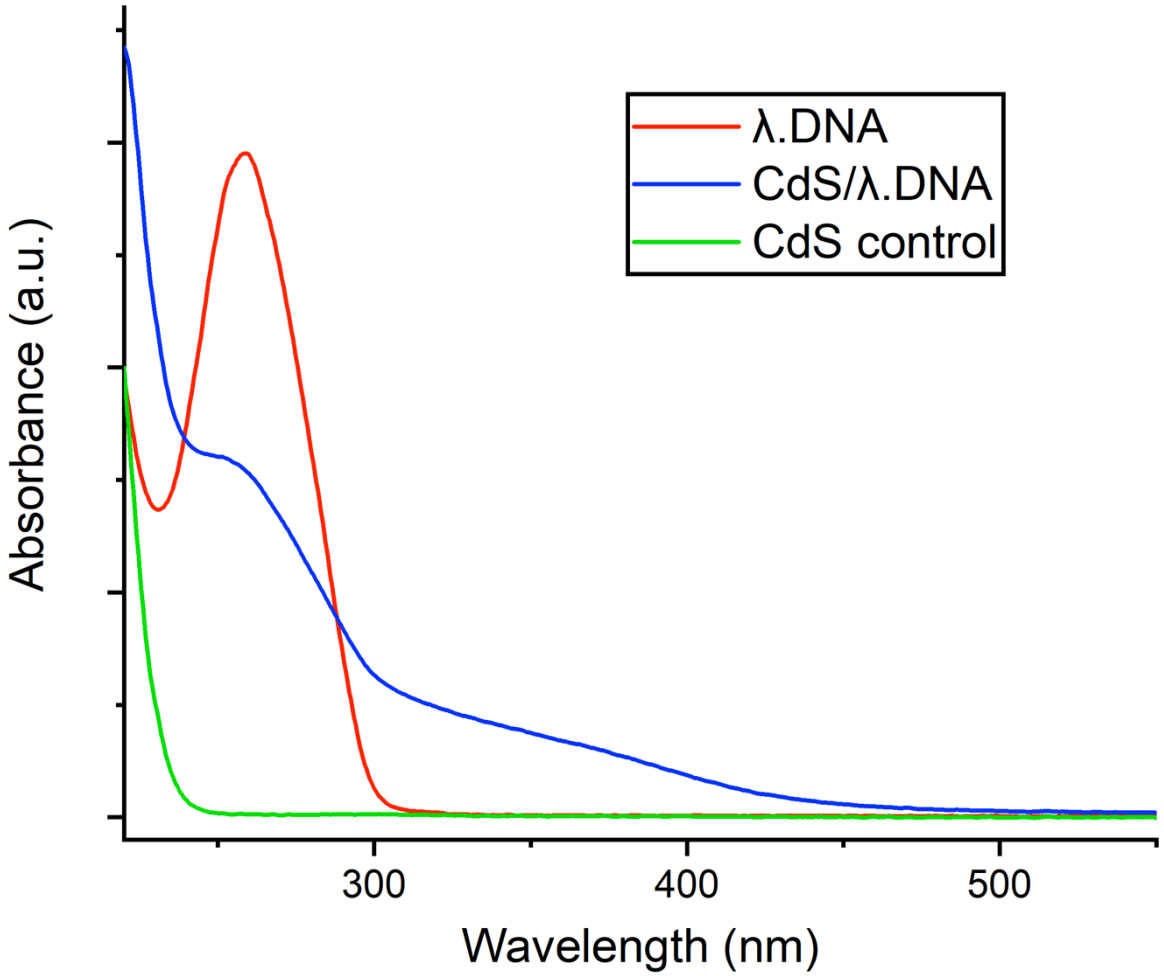

Figure 5.3 UV-Vis spectra of aqueous λ.DNA, CdS/λ.DNA and CdS solutions, recorded using the pedestal accessory of a NanoDrop.

The λ.DNA spectrum shows an expected peak at 260 nm, attributed to transitions involving the nucleobases, and no significant absorbance above 300 nm.[199] The CdS/λ.DNA solution also shows the absorbance peak at 260 nm but with a knee that extends to around 470 nm. This absorption knee is a result of exciton effects within CdS crystals, with the cut-off wavelength corresponding to the material's bandgap.[355] Through Tauc plot analysis the bandgap is calculated to be around 2.65 eV, slightly greater than the bulk value for CdS of 2.5 eV.[177] The absorbance behaviour of the CdS/λ.DNA solution shows a marked difference to the CdS control, which shows no absorbance above 250 nm, suggesting the quantum-confinement of nanoparticles on DNA.

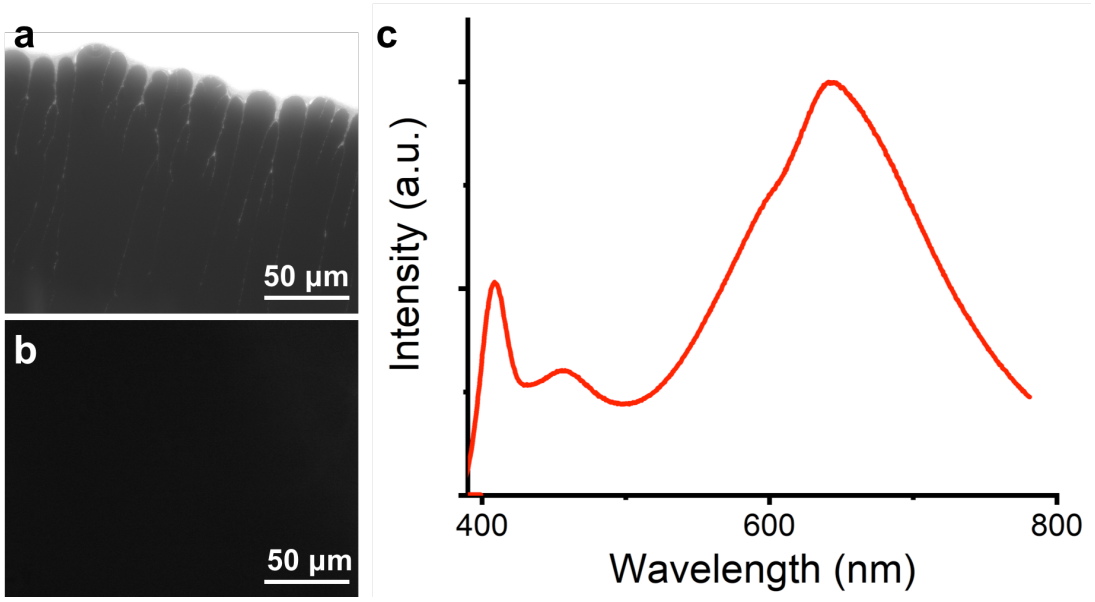

Figure 5.4 Fluorescence microscopy images of CdS/λ.DNA (a) and λ.DNA (b) on Si, at an exposure time of 4 mS and under wavelengths of 300-400 nm. Also shown is the emission spectrum of CdS/λ.DNA (c, excitation wavelength = 370 nm).

The photoluminescent behaviour of λ.DNA strands and CdS/λ.DNA nanowires is provided by the microscopy images in Figure 5.4 (Images a and b, Methodology, Section 2.23). No features are observed with the bare DNA sample (Image b), with the molecule known not to luminesce or absorb light within the excitation wavelengths used (300-400 nm).[199,356] Conversely, CdS/λ.DNA nanowires are clearly visible under these conditions due to the emission of CdS, with the material confirmed to absorb light between 300 and 400 nm through its UV-Vis spectrum in Figure 5.3. The luminescence pattern, observed protruding outwards from the boundaries of the dried droplet, resembles the shape of DNA molecules, suggesting that the semiconductor is confined onto strands. These regions are composed of many CdS/λ.DNA nanowires bundled together, with wire lengths exceeding those of single λ.DNA molecules.[354]

The emission spectrum of the CdS/λ.DNA solution is also given in Figure 5.4 (Image c), measured at an excitation wavelength of 370 nm (Methodology, Section 2.23). Two smaller peaks can be seen at 420 and 480 nm, attributed to 1st and 2nd order Raleigh and Raman scattering.[357] The more intense signal, centered around 650 nm can be identified as CdS luminescence. The signal is broad due to the highly defective surfaces of CdS nanoparticles, typical of growth without the use of capping agents and potentially worsened by the presence of DNA.[206,207,358] The broad

emission is also characteristic of a material with a low quantum yield, with additional photoluminescence dynamics studies calculating this to be 1 %.[58]

5.2.3 Characterisation of CdS/λ.DNA by XPS, Raman and XRD

Key regions of the XPS spectrum for dried CdS/λ.DNA material can be viewed in Figure 5.5 (Methodology, Section 2.23). The data confirms both the presence of DNA and CdS within the sample. The peaks found at 405.0 eV and 411.7 eV (Image a) can be assigned to cadmium, with binding energies close to those for Cd3d5/2 (405.73 eV) and Cd3d3/2 (411.9 eV).[359,360] The Auger parameter (Image b) for Cd of 787 ± 0.8 eV is also in good agreement with that of 786.5 eV for CdS.[361] The presence of sulphide can be determined through the appearance of S2p3/2 and S2p1/2 peaks, at binding energies 161.3 eV and 162.5 eV respectively.[360] Regarding DNA, a N1s signal from nucleobases at 399 eV (Image a) and a P2p band from phosphate groups at 133.3 eV (Image d) can be located and match literature values.[362,363] From the O1s spectrum (Image e), features at 535.5, 532.6 and 531.1 eV correspond to reported values for C-OH bonds, C=O bonds and phosphate oxygens in DNA while the C1s spectrum (Image f) displays bands at 286.2 and 288.1 eV, consistent with work by other groups on DNA.[362]

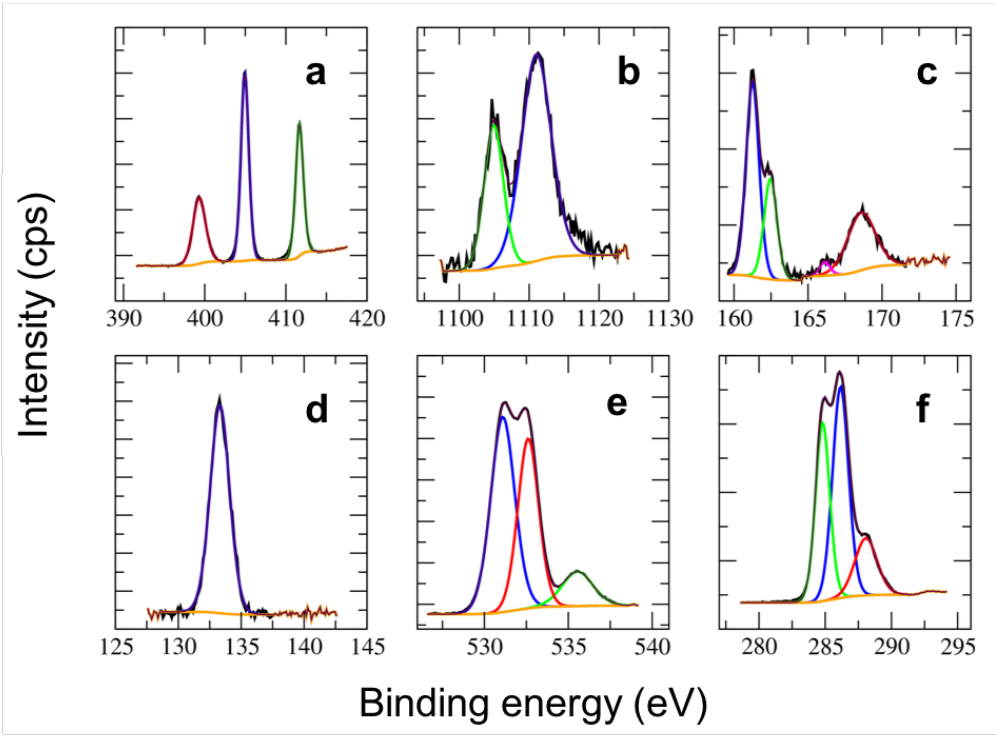

Figure 5.5 Regions with peak fitting of the XPS spectrum of CdS/λ.DNA, recorded with a step size of 0.1 eV. a.) Cd3d and N1s region. b) Cd MNN/15 Auger region. c) S2p region. d) P2p region. e) O1s region. f) C1s region. The energy scale was calibrated by setting the lowest C1s component to a binding energy of 284.8 eV.

The XRD spectrum of the CdS.DNA material can be observed in Figure 5.6. Due to the large amount of material required to provide enough powder for analysis and the high cost of λ.DNA, the use of cheaper calf thymus (CT) genomic DNA was employed (Methodology, Section 2.23). This DNA is composed of a similar percentage of guanine and cytosine (GC) base pairs (42 % GC for CT.DNA compared to 47 % GC in λ.DNA) but exhibits a much larger distribution of strand lengths, which should not greatly affect the templating process.[364,365]

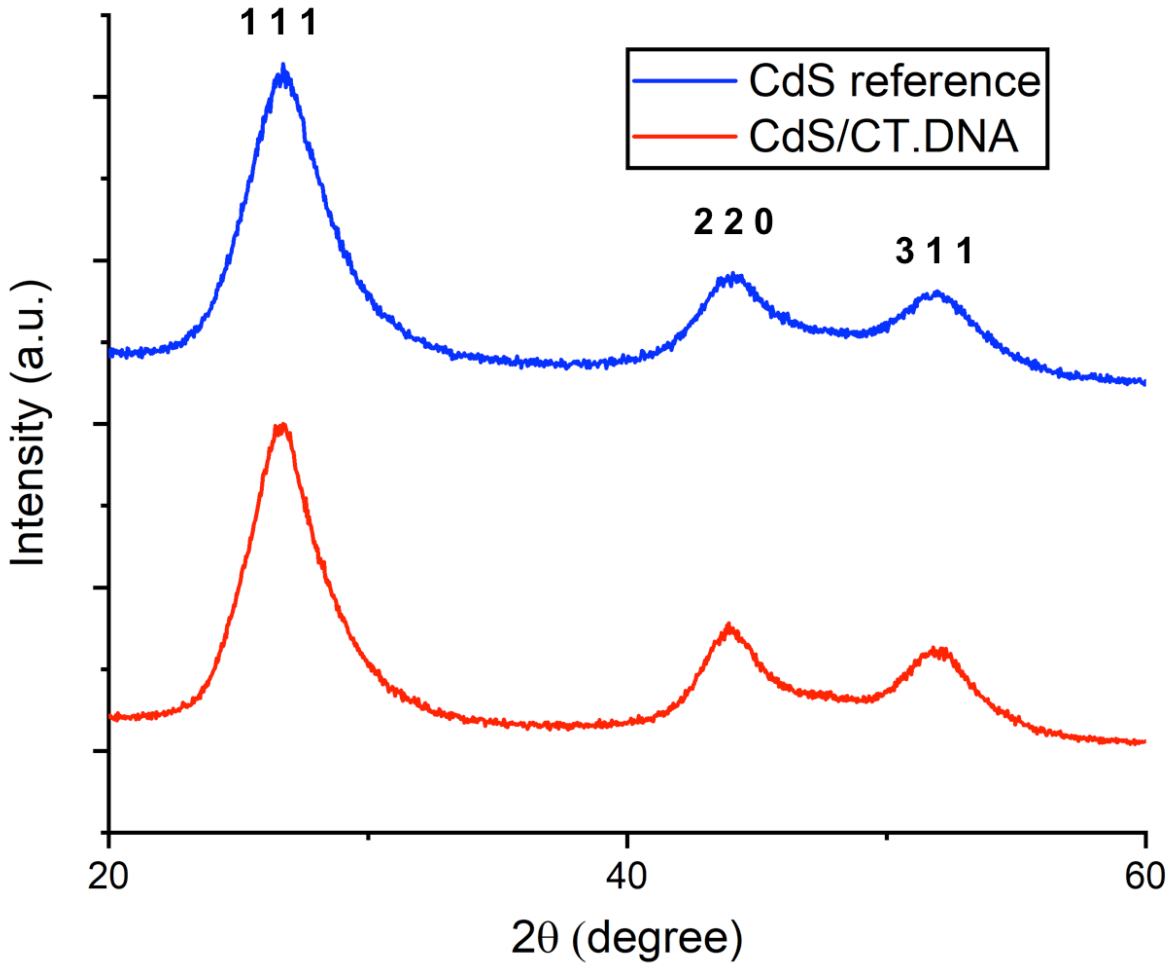

Figure 5.6 XRD spectra of CdS/calf thymus (CT.DNA) and a cubic phase CdS reference, synthesised in aqueous solution without DNA.

The CdS/CT.DNA spectrum shows three distinct bands at 26.6^{O}, 43.9^{O} and 52.0^{O}, corresponding to the (1 1 1), (2 2 0) and (3 1 1) planes of a cubic phase CdS crystal structure.[210] The spectrum also matches that of the cubic CdS reference, also shown in Figure 5.6, synthesised in aqueous solution in the absence of DNA. The average crystallite size grown on CT.DNA can be estimated to be 3.9 nm according to the Debye-Scherrer equation, using the broadening of the dominant (1 1 1) diffraction

peak. This value falls within the range of crystal heights measured through AFM studies (Figure 5.2), where the diameter of the DNA template also needs to be accounted for.

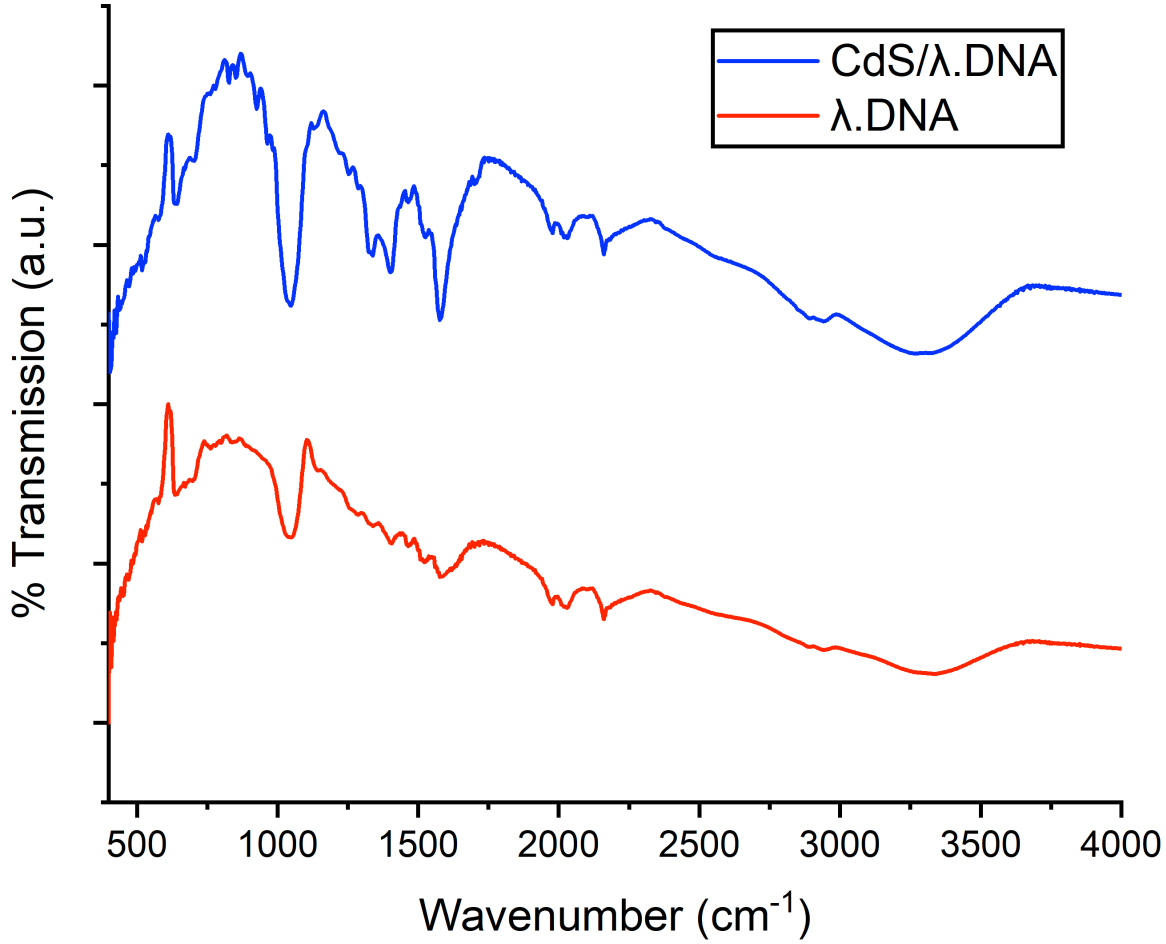

Figure 5.7 FTIR spectra λ.DNA and CdS/λ.DNA, drop-cast as thin films onto Si and recorded using the ATR attachment of the spectrometer.

The FTIR spectra of λ.DNA and CdS/λ.DNA are shown above in Figure 5.7. In both spectra a strong peak around 1040 cm^{-1} can be seen which can be attributed to the P-O stretch of the phosphodiester backbone of DNA.[366] Metal-sulphur stretching frequencies generally lie in the far-infrared range (70-400 cm^{-1}) and thus cannot be identified.[367] However the numerous weaker modes observed between 1000-1500 cm^{-1}, relating to the DNA nucleobases, do appear to change upon the templating of CdS.[368] This suggests a close interaction between both materials rather than just being a mixture. Stretches above 3300 cm^{-1} imply the presence of water within films even after drying, with DNA known to bind strongly to water molecules through its phosphodiester backbone.[369]

5.2.4 Printing of CdS/λ.DNA droplet arrays

In order to tune the CdS/λ.DNA solution's rheology for inkjet technology, ethylene glycol was added (Methodology, Section 2.24). The influence of this solvent with aqueous inks has already been investigated in detail for the printing of GO in Chapter 3. In brief the glycol has the dual effect of increasing ink viscosity and lowering surface tension to improve jetting performance while also increasing immobilisation of fluid on a surface to maintain pattern resolution.[53,59] However with the printing of 1D structures there is the additional problem of maintaining an extended conformation, with previous work indicating that the conductance of nanowire films is dependent on wire length.[197]

In order to investigate the effect of glycol on nanowire morphology, CdS/λ.DNA inks of varying glycol content where drop-cast onto Si chips and material combed with the use of a gentle nitrogen stream prior to AFM analysis.[370]

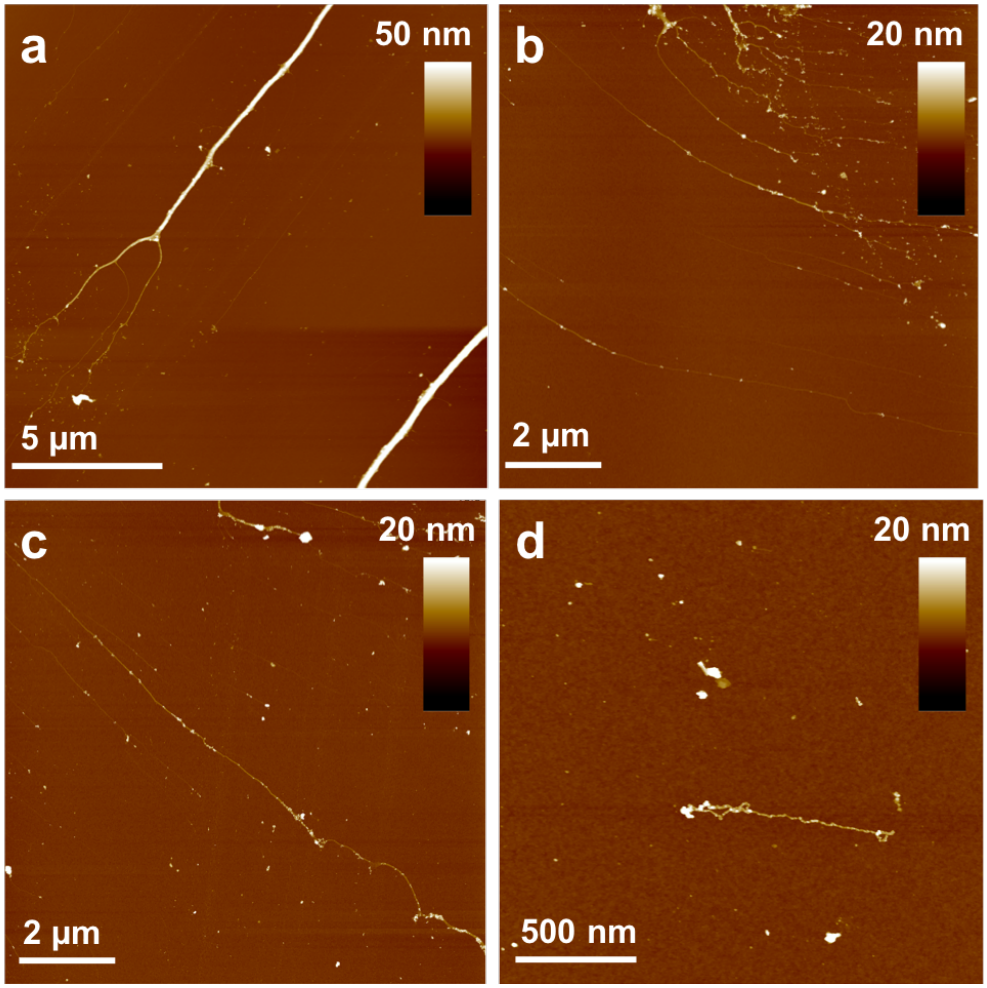

Figure 5.8 Tapping-mode AFM images of CdS/λ.DNA nanowires combed onto Si chips with inks of varying glycol content. a) 0 % glycol. b) 25 % glycol. c) 50 % glycol. d) 75 % glycol.

The conformations of CdS/λ.DNA nanowires within inks varying in ethylene glycol content from 0-75% v/v can be seen in Figure 5.8. Extended nanowire conformations are commonly observed for inks with up to 50 % glycol content (Images a,b and c). At volume fractions above this threshold the CdS/λ.DNA material coils (Image d). This change in morphology is likely caused the poorer stability of DNA in glycol, with water being a superior hydrogen-bond donor and possessing a higher dielectric constant.[371,372] On the basis of these observations, a 50 % v/v ethylene glycol CdS/λ.DNA was selected for printing in order to reduce strand compaction and enhance the chances of printing continuous and conductive features.

The optimal CdS/λ.DNA ink was used to print a set of droplet arrays onto a bare glass slide, cleaned and treated with oxygen plasma (Methodology, Section 2.25). The thicknesses of droplets within the set was altered through changing the number of printing passes, over the range of 25 to 250. This large number of printing passes was required due to the dilute nature of the ink and for the accumulation of sufficient material for labelling or gas sensing devices. Topological information on droplets was acquired through AFM studies (Methodology, Section 2.27), shown in Figure 5.9, with droplets (Images a-f) exhibiting coffee-ring structures with material predominantly located at the peripheries. This can be explained by the high energy of the glass surface and the high surface tension of the ink enhancing capillary flow of nanowires to droplet edges where solvent is evaporating fastest.[2,373] The change in edge morphology with respect to the number of printing passes was characterised by profile measurements (Image g), with both heights (Image h) and widths (Image i) observed to increase with increasing amount of material deposited. An increase in boundary height from 35.2 $\pm$ 7.5 nm to 137.1 $\pm$ 21.4 nm was measured across the range as well as increase in boundary width from 2.9 $\pm$ 0.3 nm to 9.7 $\pm$ 1.4 nm.

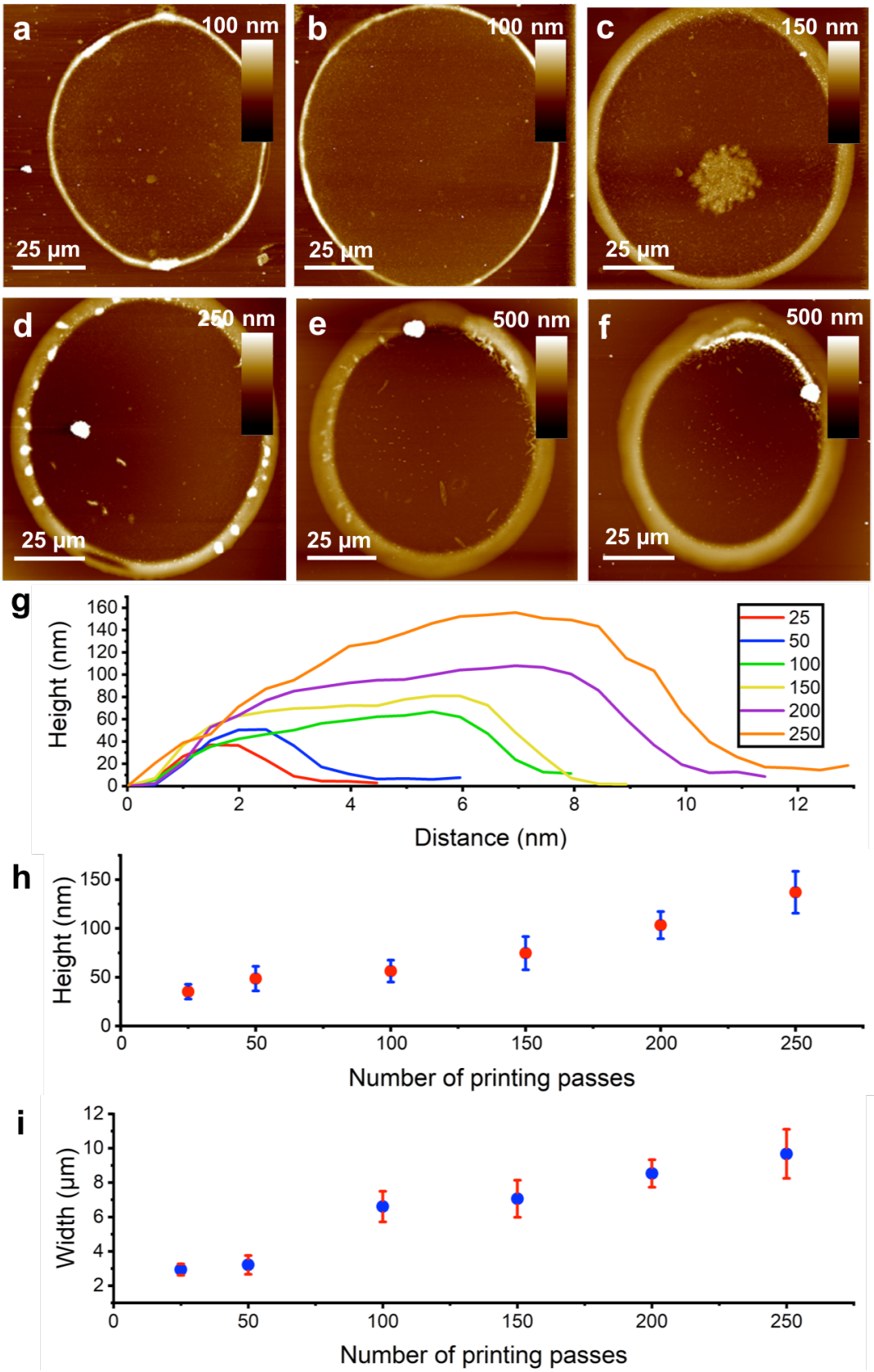

Figure 5.9 Tapping-mode AFM images of CdS/λ.DNA droplets on glass, fabricated from 25 (a), 50 (b), 100 (c), 150 (d), 200 (e) and 250 (f) printing passes. Also shown are typical cross-sectional profiles of droplet edges (g) as well as the relationships between the number of printing passes with droplet edge height (h) and width (i), with calculated standard deviations.

5.2.5 The luminescence of CdS/λ.DNA droplet arrays

The changes in droplet fluorescence, as a function of the number of printing passes, was also investigated with the same set of droplet arrays on glass, with results shown in Figure 5.10 (Methodology, Section 2.27). The intensity of fluorescence is related to CdS/λ.DNA material density, with thicker regions shown to have stronger luminescence.[374]

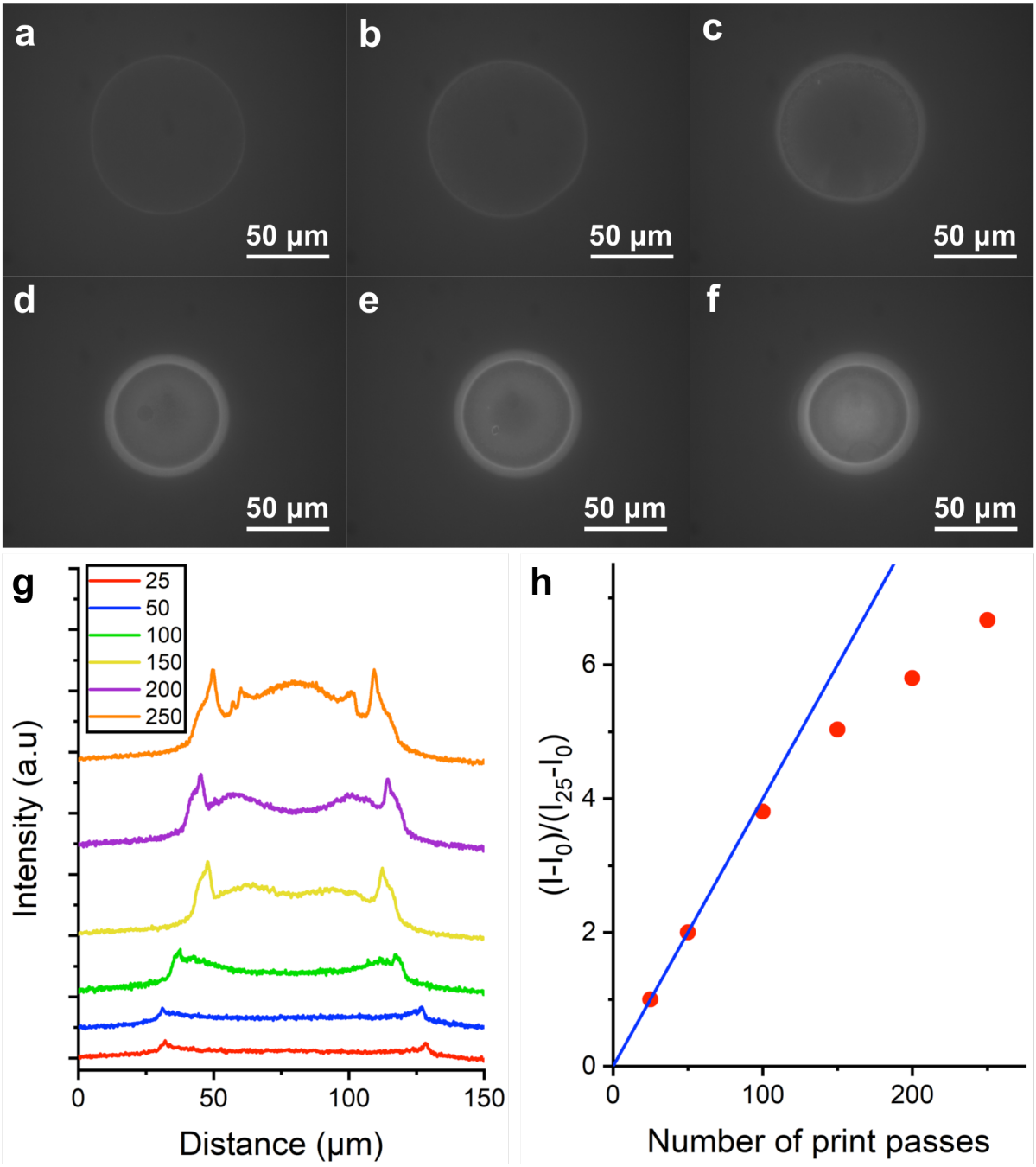

Figure 5.10 Fluorescence microscopy images of CdS/λ.DNA droplets on glass, fabricated from 25 (a), 50 (b), 100 (c), 150 (d), 200 (e) and 250 (f) printing passes. Also shown is the change in fluorescence intensity across droplet cross-sections (plot g) and the integrated intensity (I) over each droplet thickness (plot h), corrected with respect to the background (I_0) and normalised to the 25-print pass sample (I_{25}).

Upon inspection of the fluorescence photographs (Images a-f), taken through the use of a fluorescence microscope with 300-400 nm UV light, the morphology of droplets is seen to change with increasing printing pass number. At print pass numbers up to 100 (Images a, b and c) a clear coffee-ring morphology is observed, supporting the observations seen through AFM in Figure 4.9.[375] At higher pass numbers (Images d, e and f) material is still predominantly localised at pattern edges but droplets more closely resemble a disc morphology, with immobilisation of CdS/λ.DNA also occurring in droplet centres. This is likely part due to the influence of the ring of material altering the drying behaviour of droplets compared to the clean glass surface, with the droplet contact line being pinned at smaller radii. Nanofibres have also been demonstrated to be particularly effective at suppressing coffee-ring morphology with their concentration on the surface increasing with increasing pass number.[376]

The change in morphology is confirmed by the intensity profiles across droplet diameters, shown in Image g. Notably a trend of decreasing droplet size is also seen with increasing pass number. This is probably a result of the decrease in glass surface energy over time giving rise to droplets with higher contact angles. This factor may also contribute to the gradual formation of disc morphology, with lower surface energy known to weaken the coffee-ring effect and help promote opposing Marangoni flows induced by the presence of glycol.[82] The 'wearing-off' of plasma treatment has already been proven in earlier work with graphene oxide in Chapter 3, with a plot of water contact angles over time on glass displayed in the Appendices, Figure 3B. A decrease in diameters from around 110 μm to 80 μm is measured across the set. This printing resolution is lower than that achieved with graphene oxide on glass in Chapter 3 (54 μm) due to the lower amount of glycol used within the CdS/λ.DNA ink. This leads to higher wetting of ink on the surface due to its reduced viscosity.[373]

Image h in Figure 5.10 displays the quantitative relationship of fluorescence intensity against the number of printing passes. Fluorescence values were calculated through measuring the mean image brightness over a square region of constant size (and incorporating the whole droplet), with subtraction of the background brightness (I_0) and normalisation to the 25-print pass sample (I_{25}). The change in fluorescence signal is proportional to print pass number up to nearly 100 layers, expected with no loss of CdS material with increasing pass number. Above 150 layers, the plot becomes sublinear, which cannot be explained on the basis of the change in droplet

radius or morphology with the total amount of CdS material being proportional to pass number. This deviation from linearity could be a cause of inner filter effects where the absorption depth of the excitation light is less than the layer thickness or quenching of emitted light is taking place.[377]

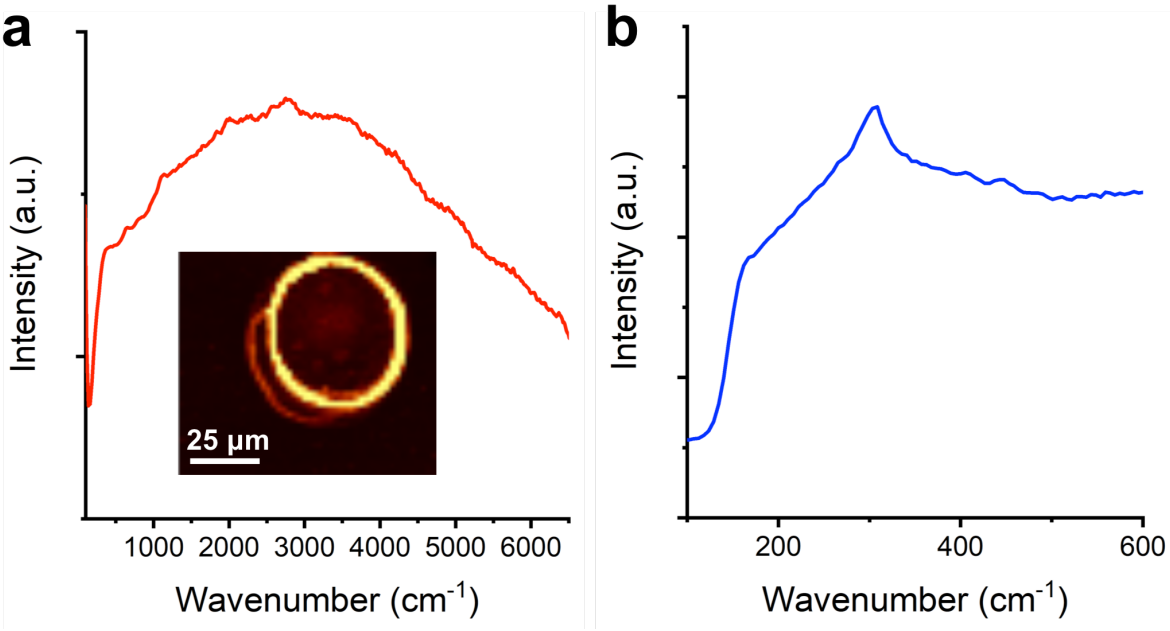

Figure 5.11 a) Raman spectrum over the wavenumber range of 0-6500 cm^{-1} for a printed CdS/λ.DNA on glass, with inset of a Raman image. b) Raman spectrum of the same CdS/λ.DNA, with increased spectral resolution, over the wavenumber range 0-600 cm^{-1}.

The Raman and luminescence spectra of one of the droplet deposits are displayed in Figure 5.11 (Methodology, Section 2.27). The glass substrate and DNA does not absorb the laser light meaning the Raman images are dominated by the luminescence of CdS, as can be seen from the inset in spectrum a. From the lower-resolution spectrum (Image a) the broad photoluminescence of CdS can be seen extending from around 150 cm^{-1} all the way to 6500 cm^{-1} (corresponding to wavelengths of 490 nm-715 nm). This observation is consistent with the broad fluorescence signals of the material measured in solution, Figure 5.4, and with low quantum yield calculated in further work.[58] Upon measuring the same the droplet with a higher-resolution grating (Image b), the CdS LO phonon spike at 305 cm^{-1} can be identified.[213]

5.2.6 Printing of CdS/λ.DNA conductive devices

The CdS/λ.DNA ink was also utilised to print features over interdigitated electrodes in order to fabricate conductive devices (Methodology, Section 2.26). Two types of CdS/λ.DNA patterns were tested, with the final arrangement of material controlled by the spacing between neighbouring droplets. In a similar manner as described in Section 5.2.4, droplet arrays were printed over electrode fingers, with a large spacing used to prevent overlap of droplets. Upon reducing drop spacing in the x-direction to facilitate the merging of material, CdS/λ.DNA tracks were also assembled, running perpendicular to the direction of electrodes. To maintain the resolution of tracks, through the prevention of uncontrolled wetting, the quarter density printing technique, used previously in Chapter 3 with GO, was applied again.

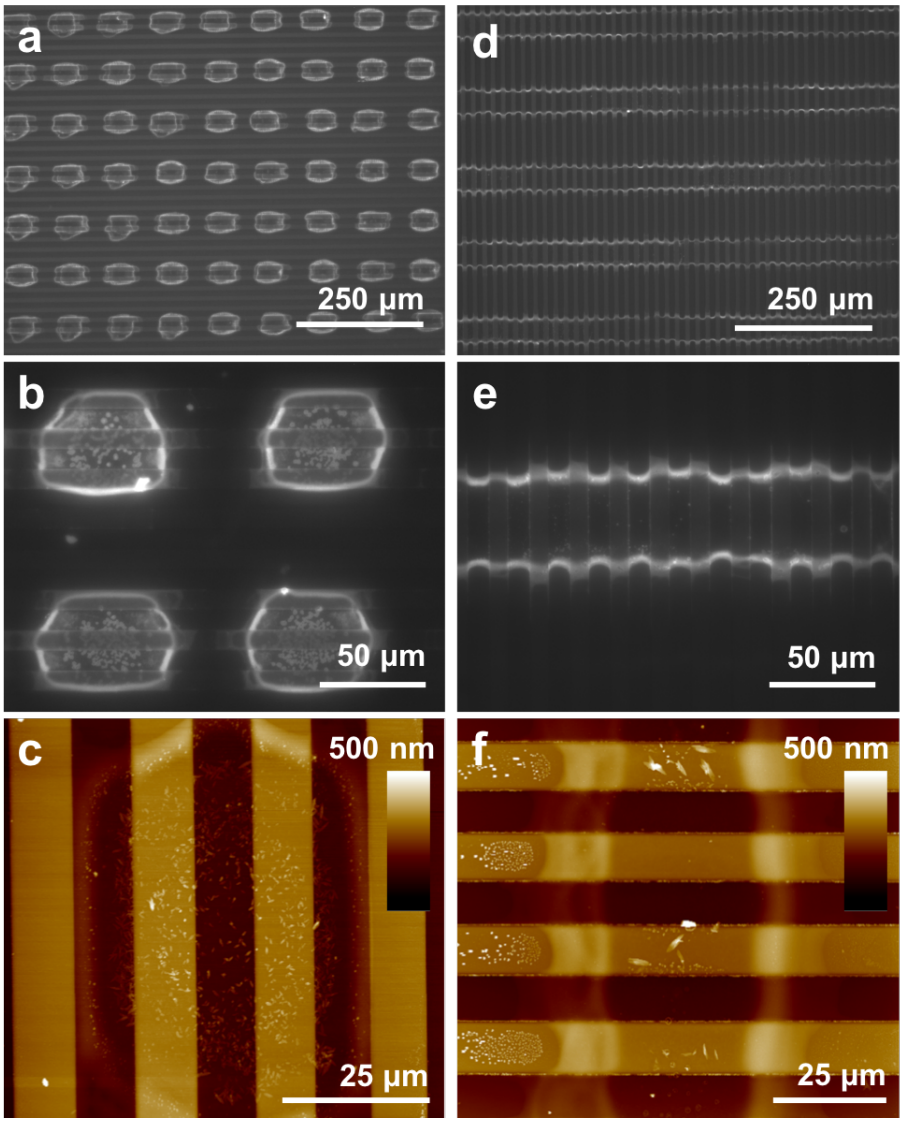

Figure 5.12 Fluorescence microscopy images of CdS/λ.DNA droplets (Images a and b) and tracks (Images d and e) printed over Pt-on-glass IDEs. Also shown are corresponding tapping mode AFM images of CdS/λ.DNA droplets (Image c) and tracks (Image f).

The photoluminescence and AFM images of both printed CdS/λ.DNA patterns over platinum electrodes are shown in Figure 5.12 above (Methodology, Section 2.28). From observation of fluorescence (Images a,b, d and e) both droplets and track morphologies appear to give CdS/λ.DNA features that span the 10 μm electrode gap. Supplementary AFM analysis also confirm that the semiconducting contacts are composed of dense networks of nanowires, where individual strand linearity is preserved (see Appendices, Figure 5B). The appearances of droplets are comparable to those printed onto bare glass, with the vast majority of material located at the edges due to the coffee-ring effect (Images a and b).[375] However, the diameters of drops are significantly smaller, measuring around 50 μm as opposed to over 80 μm. This is likely due to the influence of the platinum electrodes, with noble metal materials known to be more hydrophobic than glass whilst also providing step heights that increase the roughness of the surface.[378–380] The capillary flow of material to pattern boundaries is also seen with the printing of tracks (Images d and e), with the final result being two lines running parallel at a distance of 50 μm. Through AFM studies (Images c and f), the thicknesses of CdS/λ.DNA bundles in both devices were found to be almost identical, with droplets (100 printing passes) measuring 58 ± 13 nm and tracks (50 layers) measuring 60 ± 19 nm. However, a significant difference in the width of contacts was recorded, with tracks (17 ± 3.1μm) nearly four times the breadth of droplets (5.0 ± 1.6 μm).

5.2.7 The electronic properties of CdS/λ.DNA devices

The electrical characterisation of both droplet and track CdS/λ.DNA devices can be seen in Figure 5.13. Current-voltage curves were measured under a dry nitrogen atmosphere over temperatures ranging from 20-80 ^{O}C (Methodology, Section 2.28). For both droplet and track samples the conductance increases with increasing temperature, characteristic of a material with semiconducting nature and reported previously with CdS.[381] This is due to the increase in charge carriers with energy great enough to overcome the barrier between valence and conduction bands. At the highest temperature of 80 ^{O}C, a ten-fold increase in conductance for the track sample (Image b) is seen compared to the droplet array (Image a). This suggests that the track morphology is a superior method to contact the Pt electrodes, with material aligned perpendicular to the direction of electrodes being advantageous to device performance. The increase in width of CdS/λ.DNA bundles observed through the

printing of tracks (Figure 5.12) may also partly explain the improvement in electrical activity.

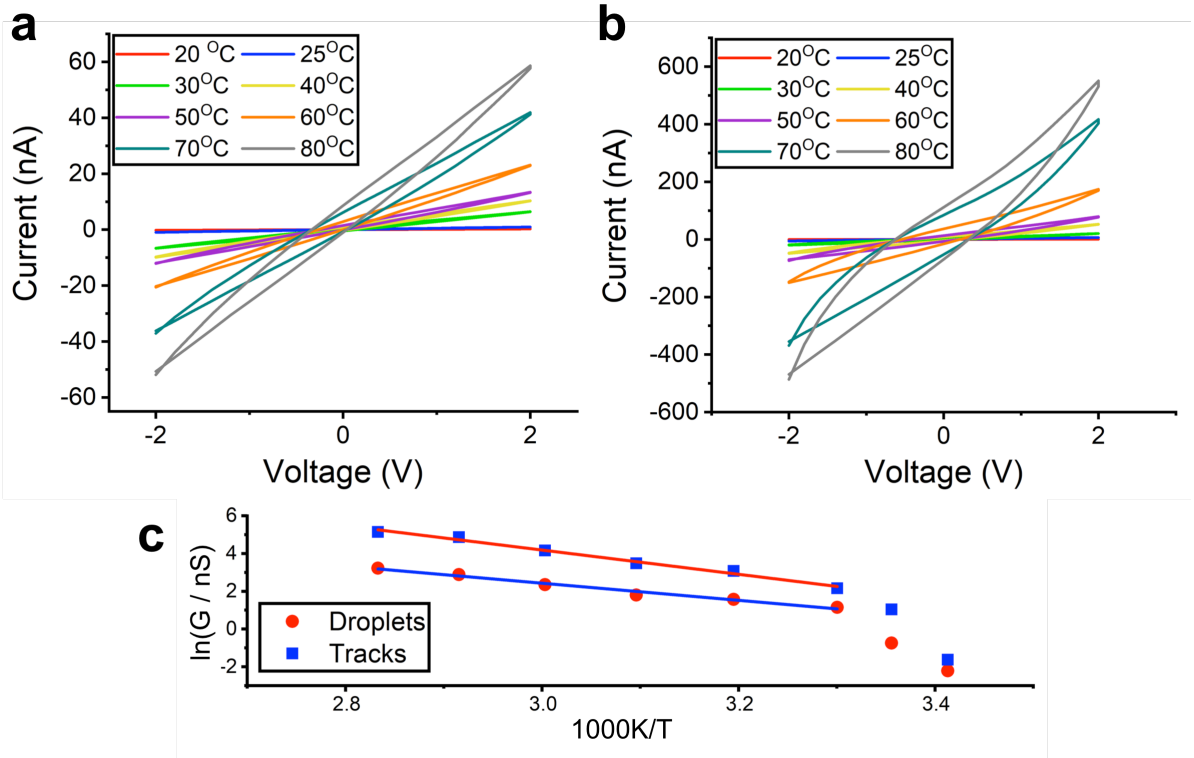

Figure 5.13 Current-voltage curves for CdS/λ.DNA droplet (a) and track (b) devices, measured under nitrogen at temperatures between 20-80 ^{O}C. The Arrhenius plots of both devices (c) is also given, using the gradients of current-voltage slopes for positive scans (between -0.5-0.5 V) to calculate the zero-bias conductance, G.

From calculation of the zero-bias conductance (G), an Arrhenius plot of lnG against inverse of temperature (1/T) can be obtained for both samples (Image c). Above 300 K plots appear linear, with gradients able to be used to calculate activation energies of 0.57 ± 0.03 eV for the track device and 0.39 ± 0.02 eV for the droplet device. These values are much smaller than that reported for a drop-cast sample in earlier work (1.03 ± 0.06 eV), with the additional control of material alignment achieved through printing a feasible explanation for this.[197] Drop-casting generally results in a thick film of loosely adherent material whereas through inkjet printing, and exploitation of the coffee-ring effect, highly resolved and compact deposits of nanowires are formed.

It is important to note that the current–voltage curves for both samples exhibit hysteresis, suggesting some ion motion is involved. A two-terminal metal/semiconductor/metal device would be expected to show current–voltage characteristics in which the forward and reverse scans retrace.[382,383] The hysteresis appears to be more considerable at higher temperature, implying an activated

process. The possibility of ion diffusion in residual water cannot be entirely ruled out, with DNA known to bind strongly to water molecules even during exposure to dry atmosphere.[383]

5.2.8 Enhancing the conductivity of CdS/λ.DNA devices

With both track and droplet devices exhibiting hysteresis and low conductance at room temperature, attempts were made to enhance electrical performance. This is critical for sensing applications in order to obtain measurable changes upon exposure to target molecules against the background current. Many cases of gas sensing in literature report devices displaying superior conductance over the bias range tested with current-voltage curves that retrace over forward and reverse scans.[384–386] Sintering is a common step applied to nanoparticle films in order to boost conductivity, with examples using CdS already published.[43,195] Sintering is the process of applying heat or pressure to particulates to promote coalescence without reaching the melting point of the material.

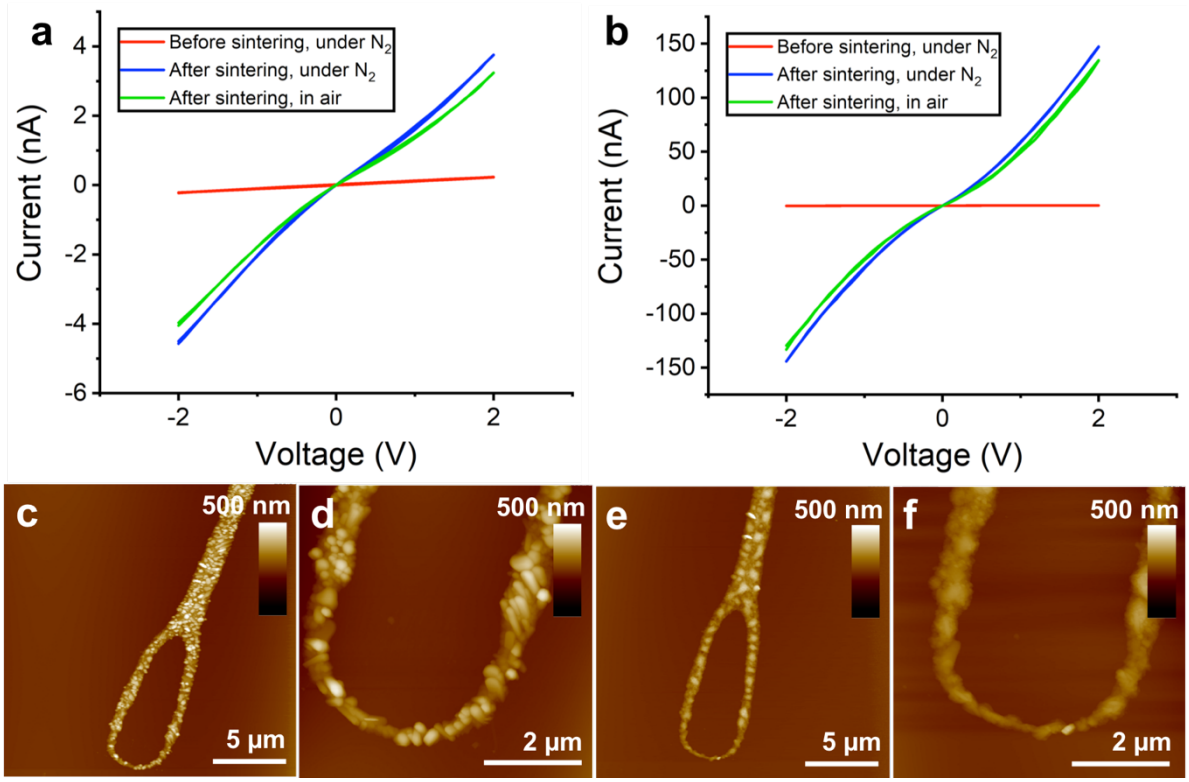

Figure 5.14 Current-voltage curves for droplet (a) and track (b) CdS/λ.DNA devices before and after sintering of material, with measurements taken under a dry nitrogen atmosphere at 20 ^{O}C. Also displayed are current-voltage curves of devices under the same conditions after sintering at 150 ^{O}C. AFM images of the same areas of CdS/λ.DNA nanowires combed into a Si chip before sintering (c and d) and after sintering (e and f) are shown too.

The sintering of CdS/λ.DNA was carried out by resting devices on a hotplate for one hour, at a temperature of 150 ^{O}C in air (Methodology, Section 2.29). The current-voltage curves for both track and droplet samples were measured at room temperature before and after the process, with data shown in Figure 5.14 (Images a and b). A marked difference in response was seen after sintering, with an approximate 1000-fold increase in conductance measured in both cases and with curves displaying greater ohmic character, free from hysteresis. Device sensitivity towards humidity was also tested after sintering, by measuring electrical activity in air rather than under nitrogen, with results also shown in Images a and b. The shapes of curves remained constant as to those taken under nitrogen with only a small change in the magnitude of conductance. Generally, gas sensors composed of semiconducting materials operate at temperatures exceeding 200 ^{O}C in order to improve selectivity to target compounds rather than atmospheric water, as well as to enhance conductivity.[178]

The appearance of CdS/λ.DNA before and after sintering was analysed through AFM, using nanowires combed onto a Si chip, and with images also shown in Figure 5.14 (Images c-f). A change in material morphology can be observed after sintering, with the CdS/λ.DNA bundle appearing much smoother. Root mean square roughness (Rq) measurements were taken over identical areas before and after treatment, with a reduction in the average value from 34.3 ± 7.8 nm to 21.2 ± 7.1 nm recorded. XRD spectra of drop-cast films before and after heating also showed a slight increase in the average particle size from 6.6 nm to 8.3 nm. These results confirm the fusing of CdS grains, with the substantial increase in electrical performance predominantly attributed to the lowering of grain boundary resistances within CdS/λ.DNA contacts.

With CdS being a well-known photoconductor, the electrical performance of CdS/λ.DNA devices was also tested under exposure to different lighting conditions (Methodology, Section 2.30).[385,387] The results can be seen below in Figure 5.15, with current-voltage plots for both devices tested in ambient light and with aid of a UV lamp balanced over samples, emitting 365 nm or 254 nm UV light. The conductance of both samples increased upon exposure to UV light, with highest values recorded under 254 nm radiation rather than 365 nm. This is because the higher energy light is able to excite more charge carriers from the CdS valence band to the conduction band. A more pronounced difference in conductivity under 254 nm UV light was

observed with the track sample, probably as a result of the better contact achieved between Pt electrodes through the printing of this morphology compared to a droplet array.

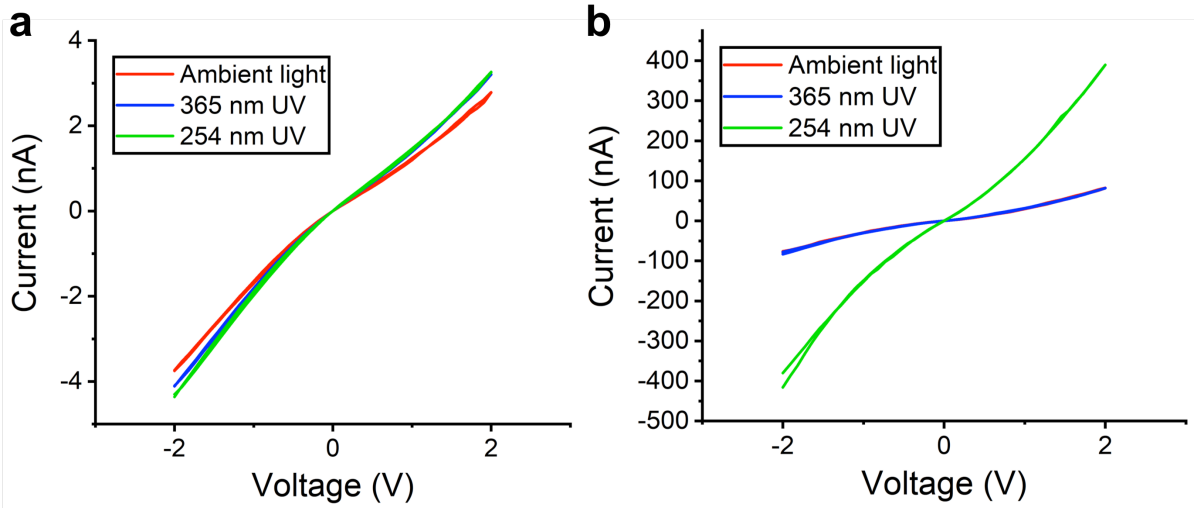

Figure 5.15 Current-voltage curves for droplet (a) and track (b) CdS/λ.DNA devices under nitrogen, with exposure to ambient light and UV light of 254 nm and 365 nm wavelengths.

5.3 Conclusion

The final aim of the thesis was met through work described in this chapter, with techniques applied to the printing of GO successfully adapted for use with CdS/λ.DNA nanowires. The nucleation of CdS nanoparticles on duplex λ.DNA to yield CdS/λ.DNA nanowires was achieved via a wet chemical process. This method avoided the use of capping agents and stabilisers, typically required in sol gel processes to control nanoparticle growth, as well as the need for harmful solvents, with nanowires dispersed in water.[43,192] The CdS/λ.DNA dispersion was subsequently formulated into a novel ink suitable for inkjet technology through the addition of ethylene glycol in a 50 % v/v manner. This ratio of CdS/λ.DNA solution to glycol was chosen in order to maintain extended nanowire conformations and believed to be crucial for the fabrication of conductive contacts between electrodes.

The novel CdS/λ.DNA ink was successfully used to print fluorescent droplet arrays onto bare glass substrates, where photoluminescence intensity could be controlled through alteration of the number of printing passes and the presence of CdS could be confirmed through spectroscopic techniques. This demonstrates the invention of a simple labelling or anti-counterfeiting technology and further work could see the printing of more complex barcodes, using more appropriate paper or polymer film substrates and using multiple semiconductor nanowire inks with varying luminescent properties.

The CdS/λ.DNA ink was also printed across interdigitated Pt-on-glass electrodes to fabricate conductive two-terminal Pt/CdS/λ-DNA/Pt devices. Through manipulation of droplet spacing the arrangement of material could be controlled between a droplet array or track morphology. The coffee-ring effect was used as an advantage to form dense and resolved bundles of CdS/λ.DNA between electrodes. The current-voltage curves of devices originally exhibited hysteresis and low performance but ohmic character, as well as a 1000-fold increase in conductance, could be attained through sintering of material after printing. Further enhancement of device conductivity was shown to be possible through illumination with UV light, evoking the metal sulphide's photoconductivity. CdS has been shown to be a potential candidate for the sensing of volatile organic compounds and future work should see the testing of these printing devices for this application.[178]

Outlook

In summary, the first two aims sought to overcome two fundamental problems associated with the use of graphene oxide (GO). First, its printability using inkjet technology and second, the generation of films with improved conductivity upon their reduction to reduced graphene oxide (rGO). In particular, this material has been identified as a promising candidate for the replacement of indium tin oxide (ITO) in transparent conducting electrodes.[12–16] ITO is in short supply, its fabrication processes are energy intensive and films are too brittle to meet the demands of emerging devices that require high flexibility.[115,116] Graphene materials have the potential to match ITO in terms of transmittance and conductivity, while also being highly flexible, of relatively low cost and superior in terms of chemical stability compared to other ITO alternatives, such as metal oxides and metal nanowires.[12,129,131]

With regards to GO printability, endeavours were successful. A glycol-based GO ink with rheology tailored for use with inkjet printing was formulated, with its printing on a standard inkjet system allowed through the development of a robust, low density printing protocol at elevated temperatures. This approach differed from the work carried out by others, where printing is typically carried out with aqueous-based inks and with each layer of material printed in a single cycle.[7,10,88,141] This is because printing is usually carried out at lower temperatures, restricting the amount of highly viscous solvent able to be incorporated within the ink in order to avoid prolonged drying times and complete wetting scenarios.[27] This means problems, such as unreliable jetting and poor film homogeneity and resolution, still persist.[7,62,72,88] The method developed in this work maintained the benefits of using GO, such as processing the material within water, whist solving problems concerning jetting performance. Printed films also exhibited improved homogeneity and excellent resolution with printing carried out on high-energy, hydrophilic glass surfaces to challenge the robustness of the protocol. A print resolution of 54 μm was achieved on this surface, higher than other reports of printing GO on glass and comparable to resolutions found with lower energy, more hydrophobic substrates.[2,6,72,73] Importantly, the temperatures applied to substrates during printing can still be compatible with higher melting point polymer films, allowing for the fabrication of flexible devices.

The second aim of the work, improving the conductivity of printed GO upon reduction, was also met. Initially, films were chemically reduced using hydrazine vapour, with a highest conductivity of 8800 S/m recorded via this route. This value is greater than those reported by others using inkjet systems with cartridges only able

to accommodate nanoscale GO, rGO or graphene platelets.[5,56,102,141] Better electronic performances were achieved by other groups through using printing systems compatible with materials on the microscale.[56,72] The conductivity achieved through the reduction with hydrazine correlated to a sheet resistance of 776 Ω/sq and a transmittance of 14 %, making the material unsuitable for use as an ITO replacement.[114]

Enhancement of film conductivity was achieved through use of a two-step reduction process, involving a thermal annealing step at temperatures between 600-900 ^{O}C after hydrazine treatment. Through this approach, film conductivities were able to reach over 50,000 S/m, exceeding the highest film conductivity from printed GO previously reported.[60] Films also outperformed those fabricated from printed graphene and rGO, where issues in material exfoliation and dispersion can severely hamper electronic properties.[56] This significant improvement in conductivity was attributed to the greater removal of oxygenated defects and reparation of the carbon lattice, monitored through extensive XPS and Raman studies. Hydrazine is known to selectively desorb epoxy moieties and can also introduce further nitrogen-containing defects in doing so.[101,276] These were found to be removed by the annealing step along with the complete expulsion of carboxyl groups and measurable loss of hydroxyl and residual epoxy species. However, even after this two-step reduction process, rGO films demonstrated poor transmittance and high sheet resistance compared to ITO and other alternatives.[114,131] This was attributable to the appreciable levels of defects within the carbon structure, impairing charge carrier mobility. In addition, these reduction conditions are not compatible for the fabrication of flexible electronics, a growing market in which graphene could make a significant impact.

GO as a material does not lend itself towards optoelectronic applications, requiring a reduction step to regain conductivity. A more viable route worthy of exploration could be the use of more pristine carbon-based materials, such as graphene or carbon nanotubes, which already exhibit low resistivity.[12,126,304,305] Alternatively, rGO could be doped with other highly conductive materials, such as certain polymers or metal nanowires, to deliver hybrid films with lower sheet resistance at higher transmittances.[131,133,306] The choice to inkjet print may also have hindered progress, with the requirement for platelets to be on the nanoscale and increasing the number of barriers to charge transport within films. Typically, TCE fabrication processes allow for the use of macroscale materials and these could also be investigated in future with larger sized GO sheets.[12,16,131]

The final aim of the work sought to transfer the methods applied to GO for the printing of other hydrophilic nanomaterials. A novel CdS/λ.DNA ink was formulated and successfully used to print highly resolved, continuous components with band gap properties suited for labelling and sensing applications.[384–386] This work represents a significant advancement in the field of DNA technology with DNA dispersions generally used to pattern surfaces for assays.[193,194] The use of DNA also allows the synthesis of semiconducting nanoparticles without the need for harmful solvents or capping agents whilst confining sizes to only a few nanometres.[43,192,344]
Continuation of this work is already ongoing and in collaboration with an industrial partner, Touchlight Genetics. The company have developed an enzymatic DNA amplification procedure, able to produce large quantities of DNA at reduced costs. This makes DNA devices more feasible, with the price of DNA, particularly long length DNA for conducting devices, providing a stumbling block to compete with other technologies. Further research into both the fluorescent and conducting nature of a range of metal sulphide nanowires has been investigated, including ZnS, CuS, Fe_2S_3, Bi_2S_3 and PbS, as well as metal alloy sulphides, such as $Cd_xZn_{x-1}S$ and Cd_xPb_{x-1}. Recently, involvement from the Centre for Process Innovation has seen the first discussions aimed indenting the most suitable market for these materials.

Appendices

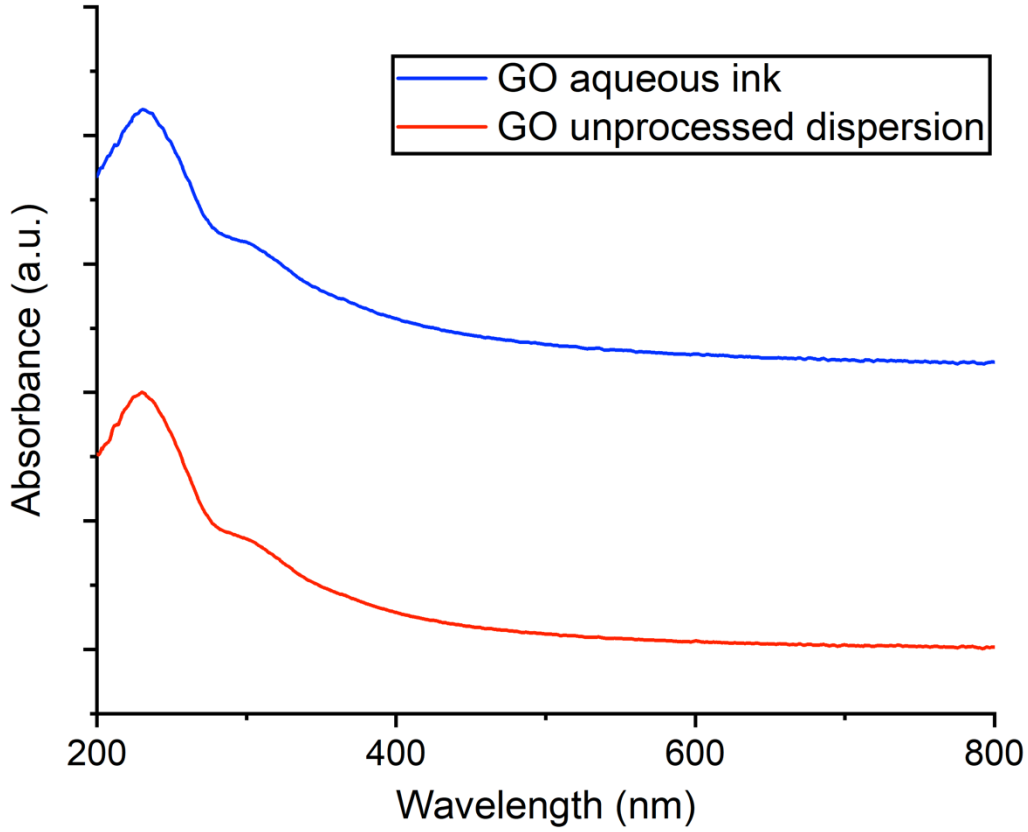

Figure 3A UV-VIS spectra of commercial graphene dispersion and processed aqueous ink.

Ink	Additive viscosity (cP)	Additive surface tension (mN/m)	Wire resistance (Ω/μm)	Wire width (μm)
GO (ref)	0.89	72.7	11.6	276 ± 33
GO.EG	16.1	48.4	5.35	214 ± 21
GO.DMF	0.79	34.4	7.28	253 ± 23
GO.THF	0.46	26.7	N/A	N/A
GO.PC	2.50	40.9	N/A	N/A

Table 3A List of GO cosolvent inks trialled, with ethylene glycol (EG), DMF, THF and water (ref) added in a 9 % v/v manner to processed GO ink. Corresponding viscosities and surface tensions of solvent (at 25 ^{O}C) are included. Resistance and width values were obtained from a set of ten tracks (0.6-2.4 mm long) printed on glass and reduced with hydrazine. GO.THF and GO.PC inks failed to produce any continuous wires (N/A).

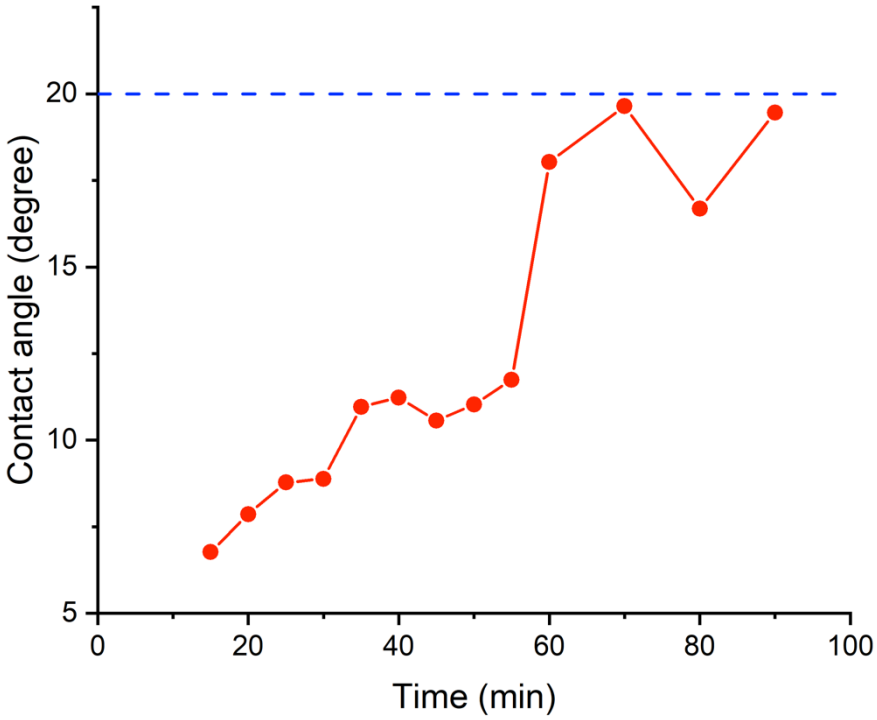

Figure 3B Contact angles of water on glass, directly after plasma taken, taken over the course of 90 min. Blue dashed line represents contact angle of before plasma. Contact angles were too small to measure accurately before 15 min (<5^{O}) due to a complete wetting scenario.

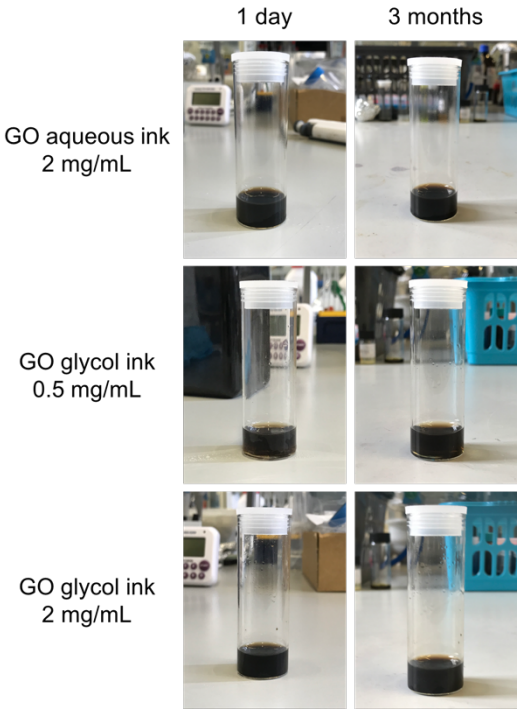

Figure 3C Photographs of formulated GO aqueous and GO glycol-based inks after 1 day and after 3 months. All three inks remained as stable dispersions over this period.

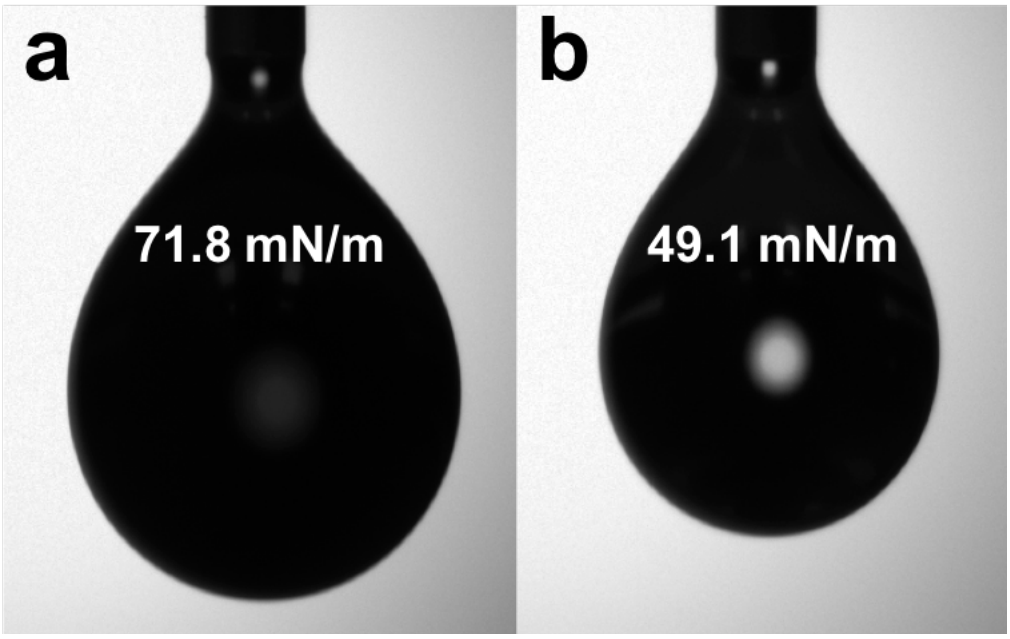

Figure 3D Pendant drop images of both aqueous (a) and glycol-based (b) GO inks taken using a tensiometer. Displayed on the images is the calculated surface tension of the inks, as an average of 5 separate measurements.

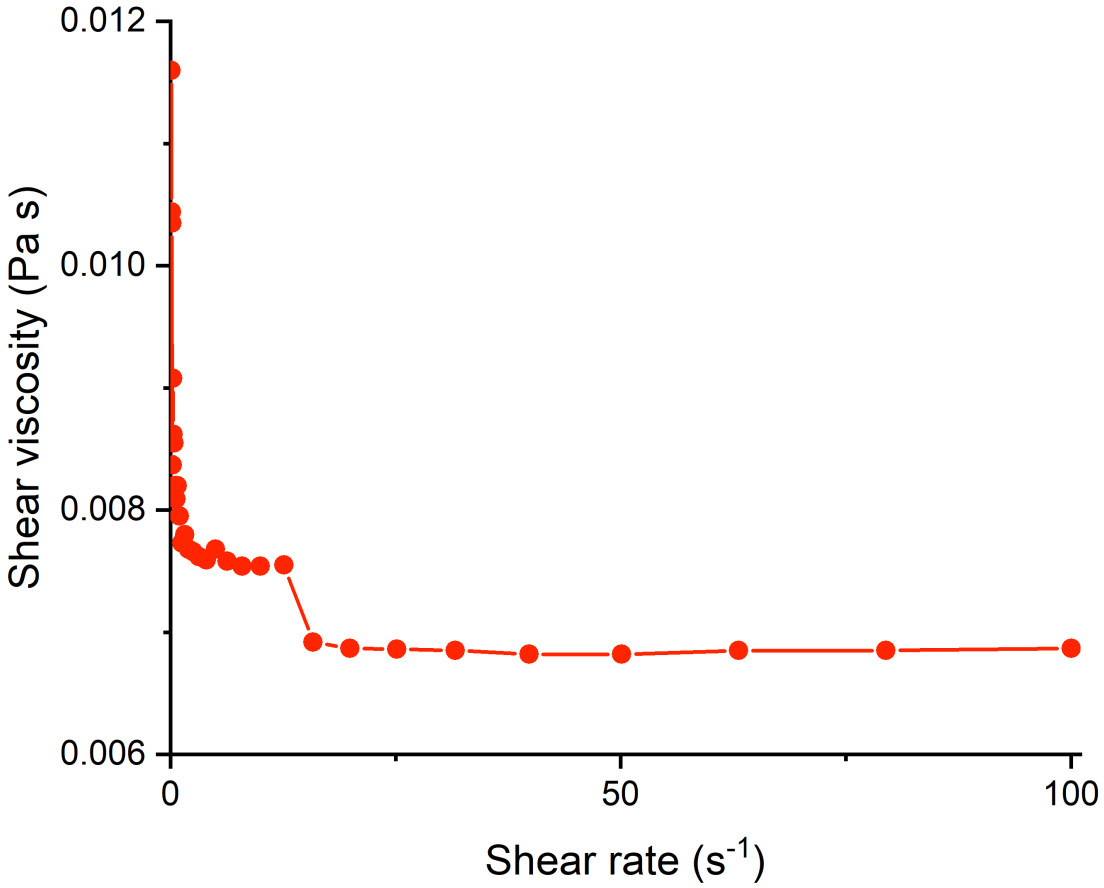

Figure 3E Shear viscosity vs shear rate plot of glycol-based GO ink obtained through use of a rheometer. Shear-thinning of ink is observed as shear rate increases. Viscosities in between the range of 7-8 cP are recorded over rates of 0.1-100 s^{-1}.

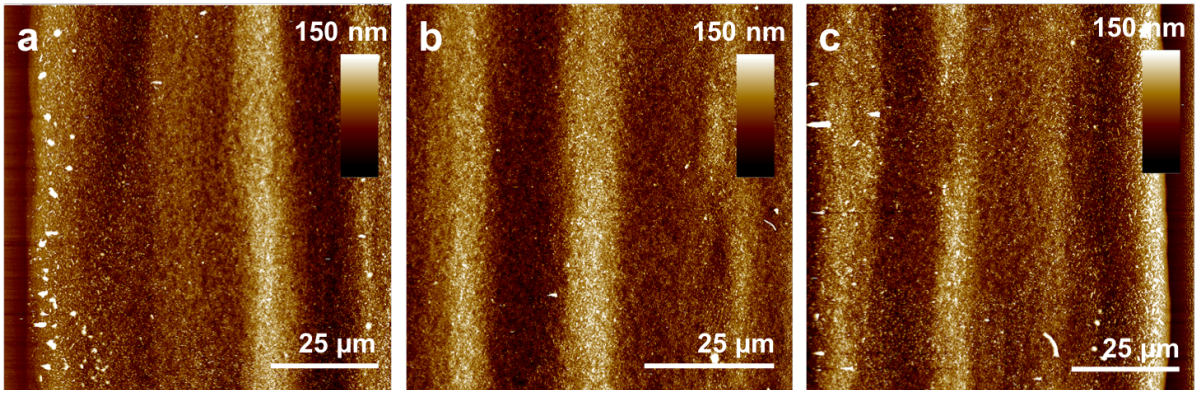

Figure 3F Large-scale AFM images of a track printed with glycol-based GO ink (10 printing passes). From the three images combined (a = left side of track, b = track centre, c = right side of track) the average height over the whole film cross-section can be calculated.

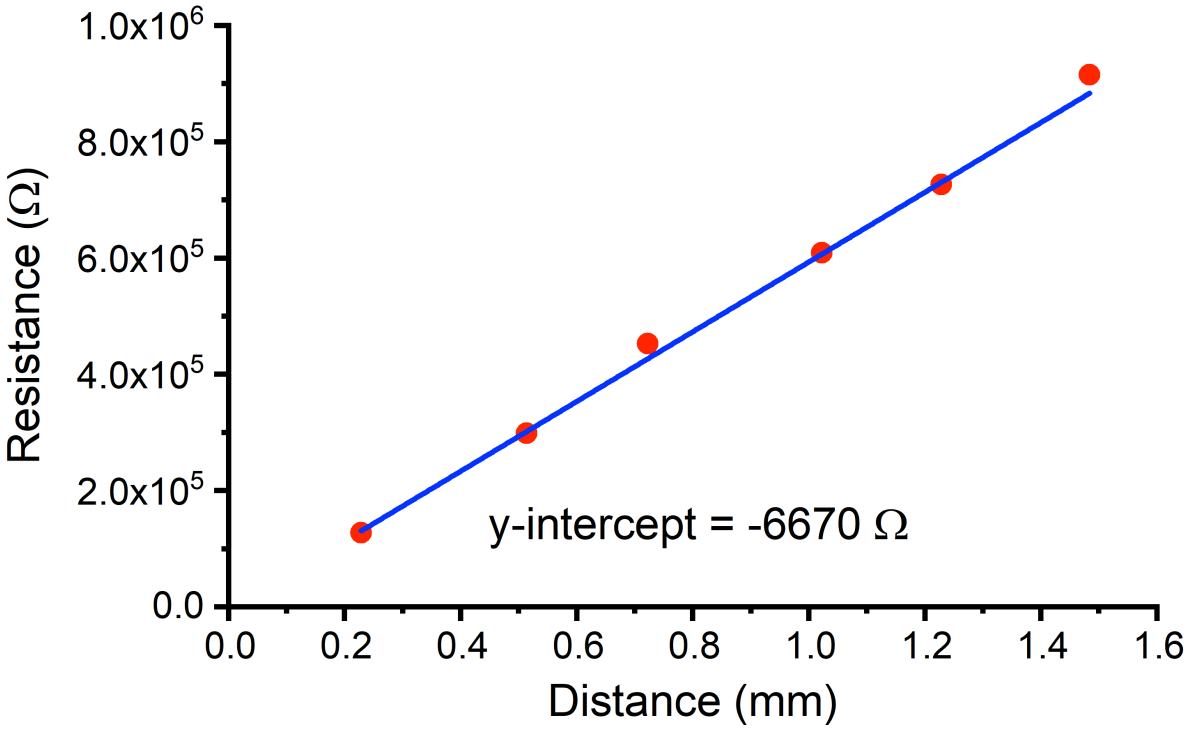

Figure 3G Resistance vs. distance plot, with y-intercept equalling Ag/rGO contact resistance for two terminal graphene devices printed with glycol-based GO ink.

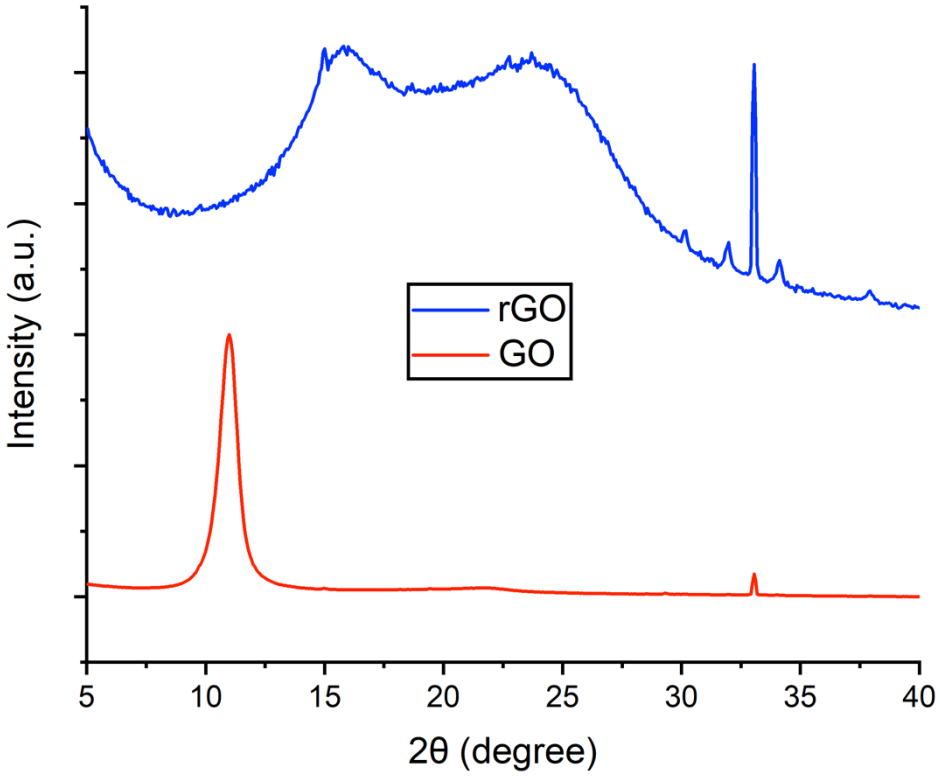

Figure 3H XRD spectra of GO and rGO, reduced through hydrazine treatment, using drop-cast samples on Si chips.

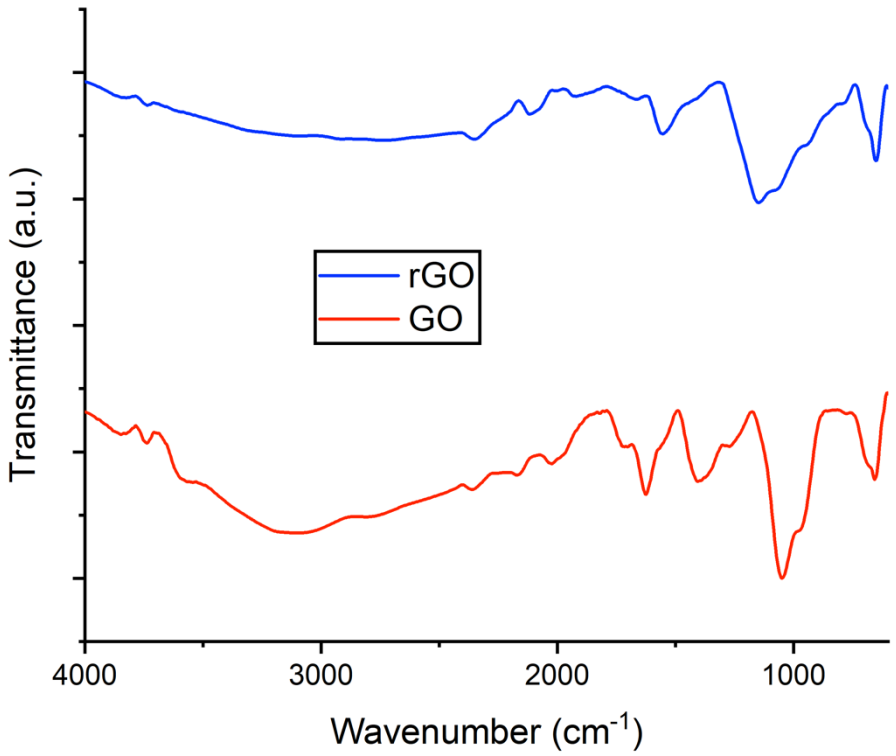

Figure 3I FTIR spectra of GO and rGO, reduced through hydrazine treatment, using drop-cast samples on Si chips.

Temperature (^{O}C)		Sum of Squares	df	Mean Square	F	Sig. (*p*)
600	Between groups	421.314	1	421.314	93.340	0.000*
	Within groups	81.248	18	4.514		
	Total	502.562	19			
700	Between groups	304.078	1	304.078	63.643	0.000*
	Within groups	86.001	18	4.778		
	Total	390.079	19			
800	Between groups	120.941	1	120.941	14.133	0.001*
	Within groups	154.030	18	8.557		
	Total	274.971	19			
860	Between groups	.061	1	0.61	0.11	0.917
	Within groups	97.899	18	5.439		
	Total	97.959	19			
910	Between groups	1.155	1	1.115	0.173	0.682
	Within groups	119.969	18	6.665		
	Total	121.123	19			

Table 4A One-way ANOVA between the heights of one and two-step rGO samples at each annealing temperature, calculated using SPSS software.

Temperature (^{O}C)		Sum of Squares	df	Mean Square	F	Sig. (*p*)
600	Between groups	662.108	1	662.108	52.772	0.000*
	Within groups	476.770	38	12.547		
	Total	1138.878	39			
700	Between groups	568.591	1	568.591	21.282	0.000*
	Within groups	1015.225	38	26.716		
	Total	1583.817	39			
800	Between groups	134.689	1	134.689	4.987	0.032*
	Within groups	1026.337	38	27.009		
	Total	1161.026	39			
860	Between groups	81.539	1	81.539	2.913	0.096
	Within groups	1063.813	38	27.995		
	Total	1145.352	39			
910	Between groups	105.885	1	105.885	3.746	0.060
	Within groups	1074.065	38	28.265		
	Total	1179.950	39			

Table 4B One-way ANOVA between the widths of one and two-step rGO samples at each annealing temperature, calculated using SPSS software.

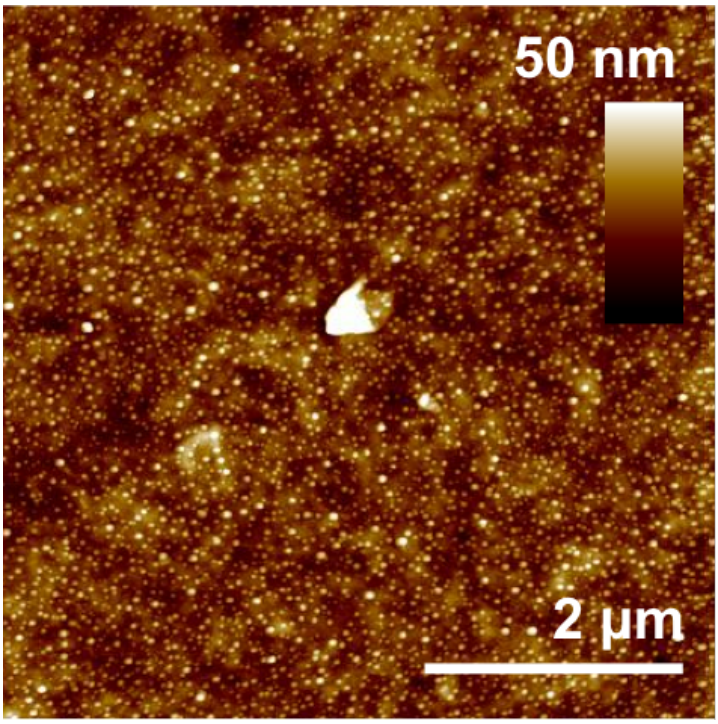

Figure 4A Tapping-mode AFM image of the trGO at 170 ^{O}C for 6 h.

Temperature (^{O}C)		Sum of Squares	df	Mean Square	F	Sig. (*p*)
600	Between groups	26.163	1	26.163	117.816	0.000*
	Within groups	8.439	38	0.222		
	Total	34.602	39			
700	Between groups	18.063	1	18.063	195.078	0.000*
	Within groups	3.519	38	0.093		
	Total	21.582	39			
800	Between groups	1.369	1	1.369	4.067	0.051
	Within groups	12.792	38	0.337		
	Total	14.161	39			
860	Between groups	0.036	1	0.036	0.467	0.498
	Within groups	2.929	38	0.077		
	Total	2.965	39			
910	Between groups	0.048	1	0.048	0.310	0.060
	Within groups	5.915	38	0.156		
	Total	5.963	39			

Table 4C One-way ANOVA between the Rq values of one and two-step rGO samples at each annealing temperature, calculated using SPSS software.

Temperature (^{O}C)		Sum of Squares	df	Mean Square	F	Sig. (*p*)
600	Between groups	232110611.6	1	232110611.6	199.635	0.000*
	Within groups	4650694.351	4	1162673.588		
	Total	23761305.9	5			
700	Between groups	281907375.8	1	281907375.8	2219.450	0.000*
	Within groups	508067.063	4	127016.766		
	Total	282415442.8	5			
800	Between groups	1148715349	1	1148715349	3726.023	0.000*
	Within groups	1233181.135	4	0.337		
	Total	1149948530	5			
860	Between groups	680892925.4	1	680892925.4	923.551	0.000*
	Within groups	2949022.580	4	737255.645		
	Total	683841948.0	5			
910	Between groups	453020053.9	1	453020053.9	909.870	0.000*
	Within groups	1991580.664	4	4.483		
	Total	455011634.6	5			

Table 4D One-way ANOVA between the conductivity of one and two-step rGO samples at each annealing temperature, calculated using SPSS software.

Temperature (^{O}C)		Sum of Squares	df	Mean Square	F	Sig. (*p*)
600	Between groups	11768579.27	1	11768579.27	487.715	0.000*
	Within groups	96520.137	4	24130.034		
	Total	11865099.40	5			
700	Between groups	3711490.942	1	3711490.942	1346.775	0.000*
	Within groups	11023.340	4	2755.835		
	Total	3722514.282	5			
800	Between groups	2476485.363	1	2476485.363	5565.036	0.000*
	Within groups	1780.032	4	445.008		
	Total	2478265.395	5			
860	Between groups	573238.419	1	573238.419	1959.220	0.000*
	Within groups	1170.340	4	737255.645		
	Total	574408.759	5			
910	Between groups	183286.073	1	183286.073	478.459	0.000*
	Within groups	1532.305	4	4.483		
	Total	184818.378	5			

Table 4E One-way ANOVA between the resistivity of one and two-step rGO samples at each annealing temperature, calculated using SPSS software.

Temperature (°C)		Sum of Squares	df	Mean Square	F	Sig. (*p*)
600	Between groups	137.054	1	137.054	11.556	0.009*
	Within groups	94.881	8	11.860		
	Total	231.934	9			
700	Between groups	0.008	1	0.008	0.000	0.985
	Within groups	181.428	8	22.679		
	Total	181.437	9			
800	Between groups	4.209	1	4.209	0.564	0.474
	Within groups	59.743	8	0.337		
	Total	63.952	9			
860	Between groups	21.574	1	21.574	5.292	0.050
	Within groups	32.613	8	4.077		
	Total	54.187	9			
910	Between groups	0.102	1	0.102	0.023	0.884
	Within groups	35.866	8	4.483		
	Total	35.866	9			

Table 4F One-way ANOVA between the % transmittance of one and two-step rGO samples at each annealing temperature, calculated using SPSS software.

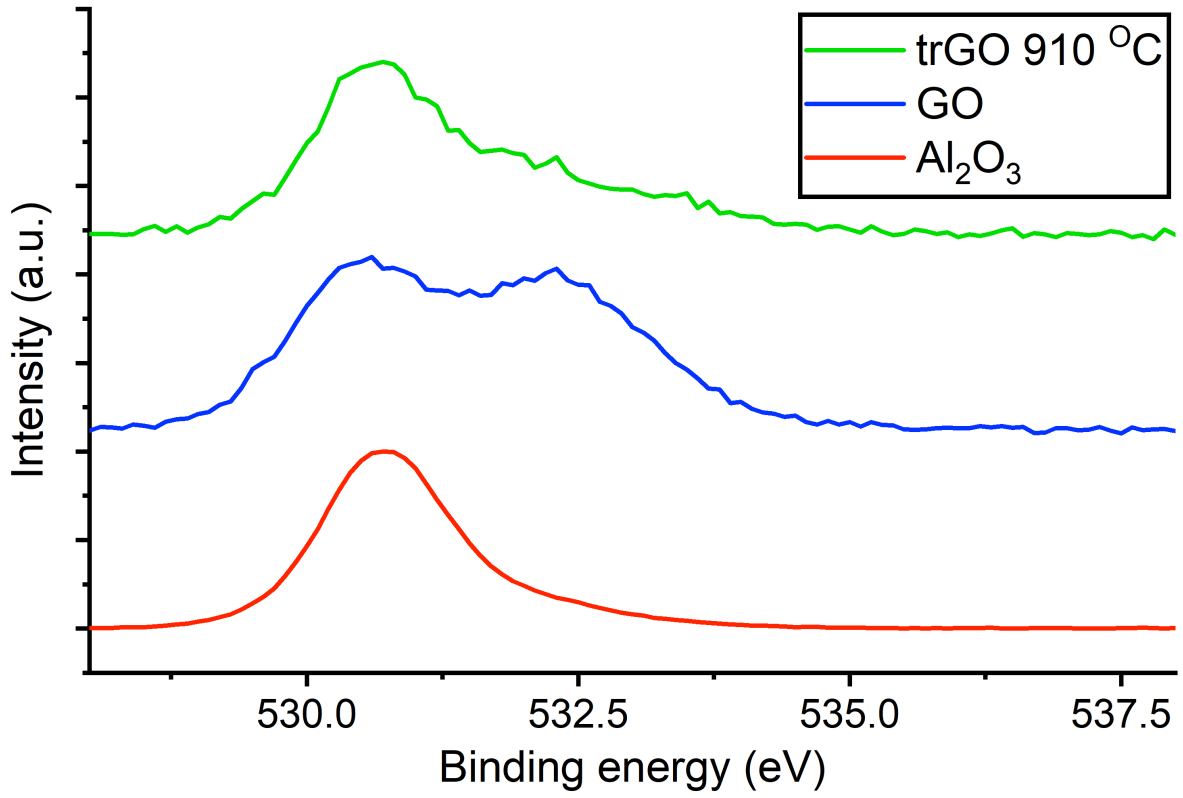

Figure 4B O1s XPS spectra of the Al_2O_3 substrate (red line), GO (blue line) and trGO after annealing at 910 °C (green line). The appearance and area of O1s components are heavily influenced by signals from the Al_2O_3.

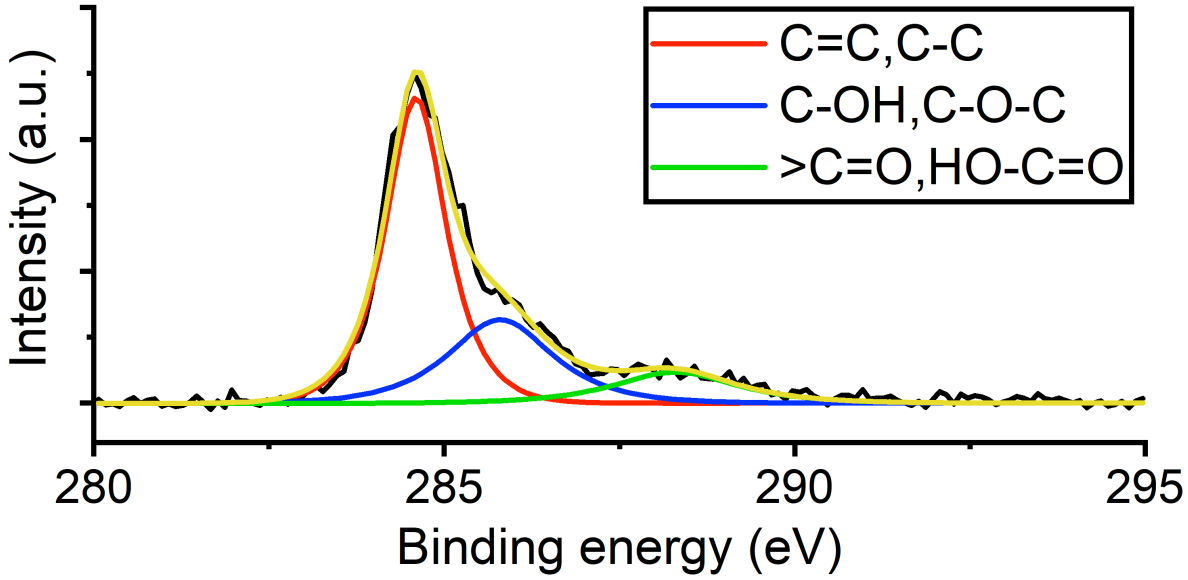

Figure 4C XPS spectrum of C1s component, 280-295 eV, for the trGO at 170 ^{O}C. The spectrum was fitted using CasaXPS software, after a Shirley background subtraction and using a mixture of Guassian and Lorentzian functions (20:80 Guassian : Lorentzian).

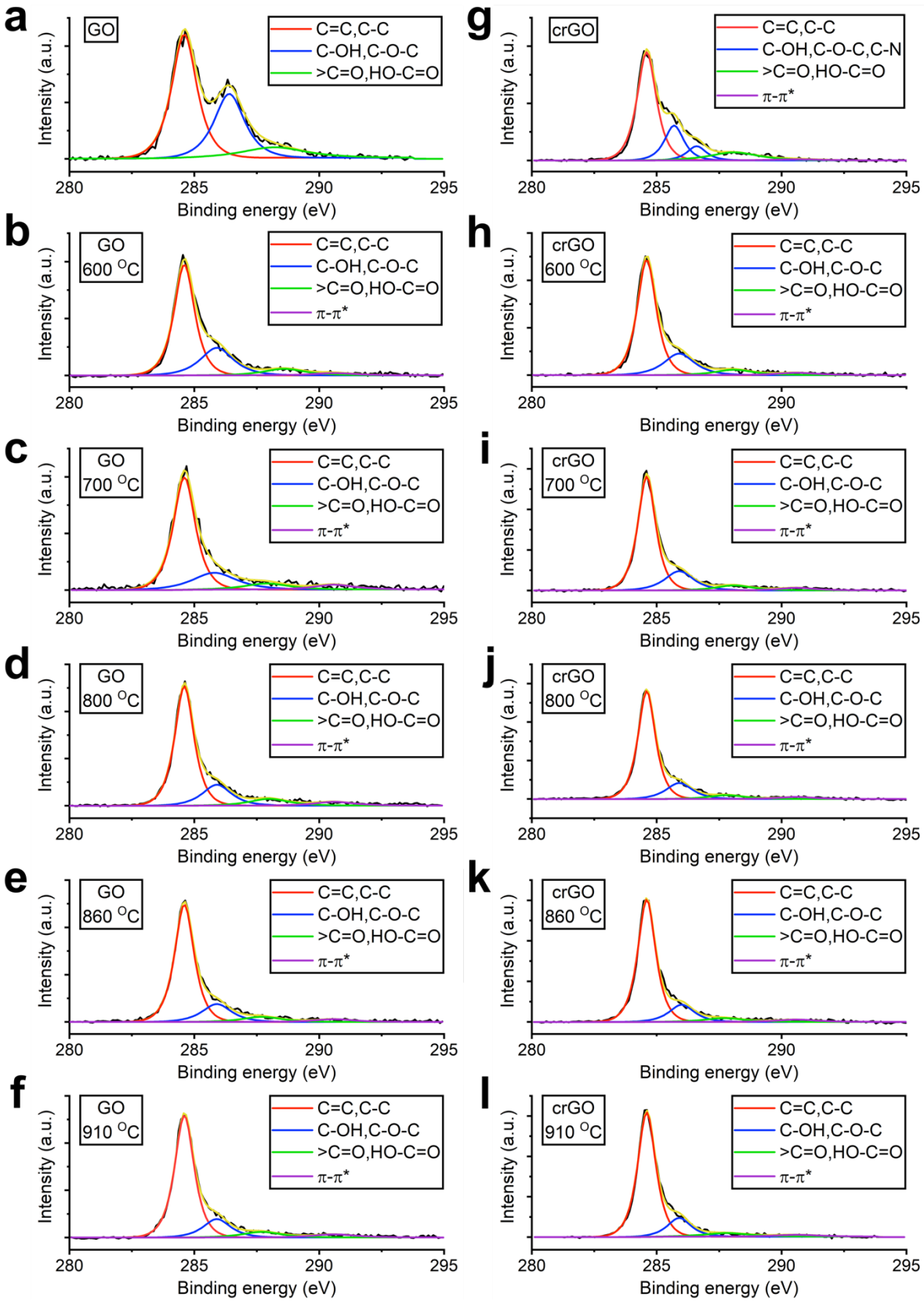

Figure 4D C1s XPS spectra of GO (a-f) and crGO (g-l) thermally annealed films at 600-910 ^{O}C for 1 h. The spectra was fitted using CasaXPS software, after a Shirley background subtraction and using a mixture of Guassian and Lorentzian functions (20:80 Guassian : Lorentzian).

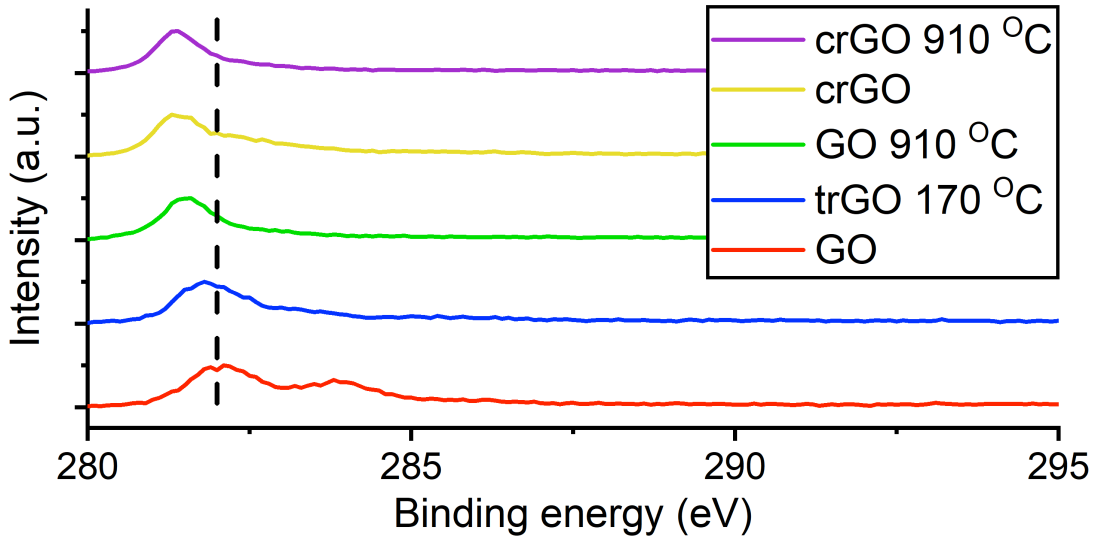

Figure 4E Selected examples of C1s components from the range of films investigated. Peak maxima show a shift to lower binding energy upon reduction from GO suggesting higher levels of graphitisation.

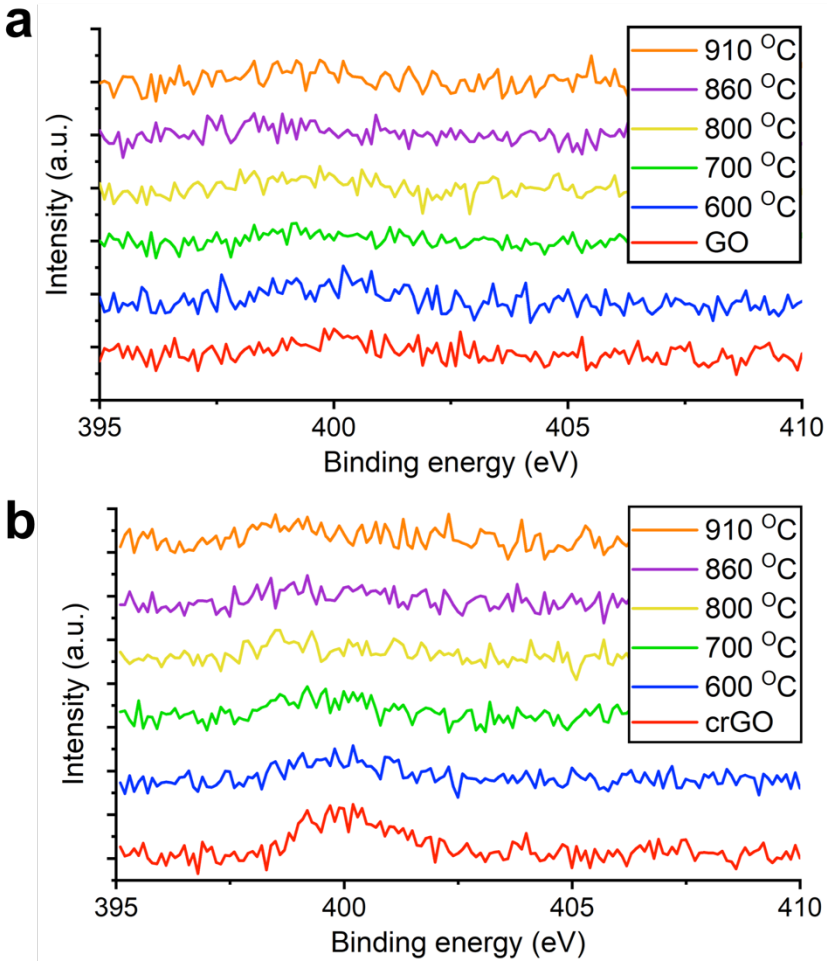

Figure 4F N1s XPS spectra of GO (a) and crGO (b) films after thermal annealing at temperatures ranging between 600-910 °C for 1 h. Only the pre-annealed crGO film shows any significant signal, demonstrating doping of rGO with nitrogen

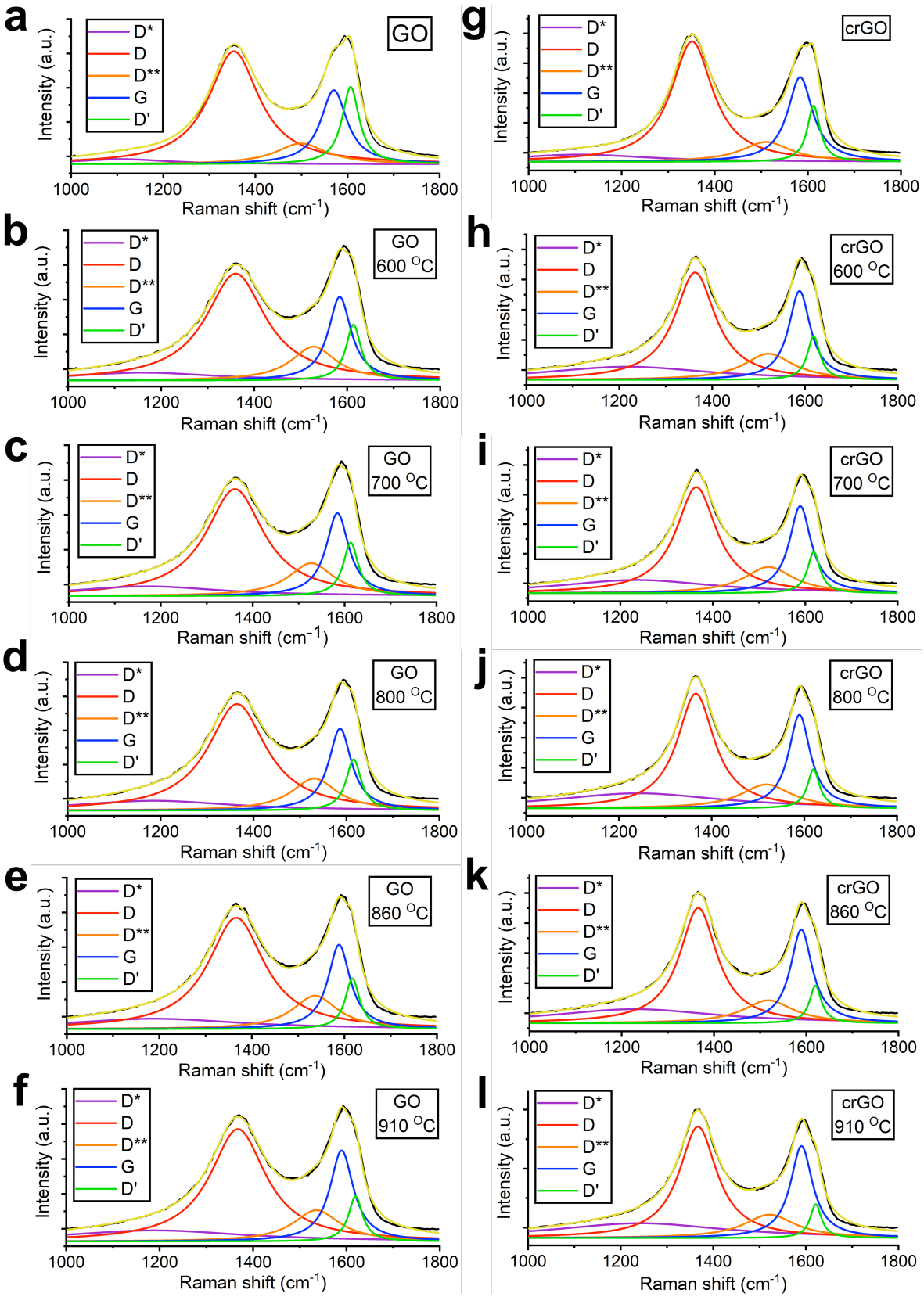

Figure 4G Raman spectra of D and G regions (1000-1800 cm^{-1}) of GO (a-f) and crGO (g-l) films before and after thermal annealing between 600-910 ^{O}C for 1 h. D and G bands have been deconvoluted into D*, D, D**, G and D' peaks according to Kaniyoor et al.[217]

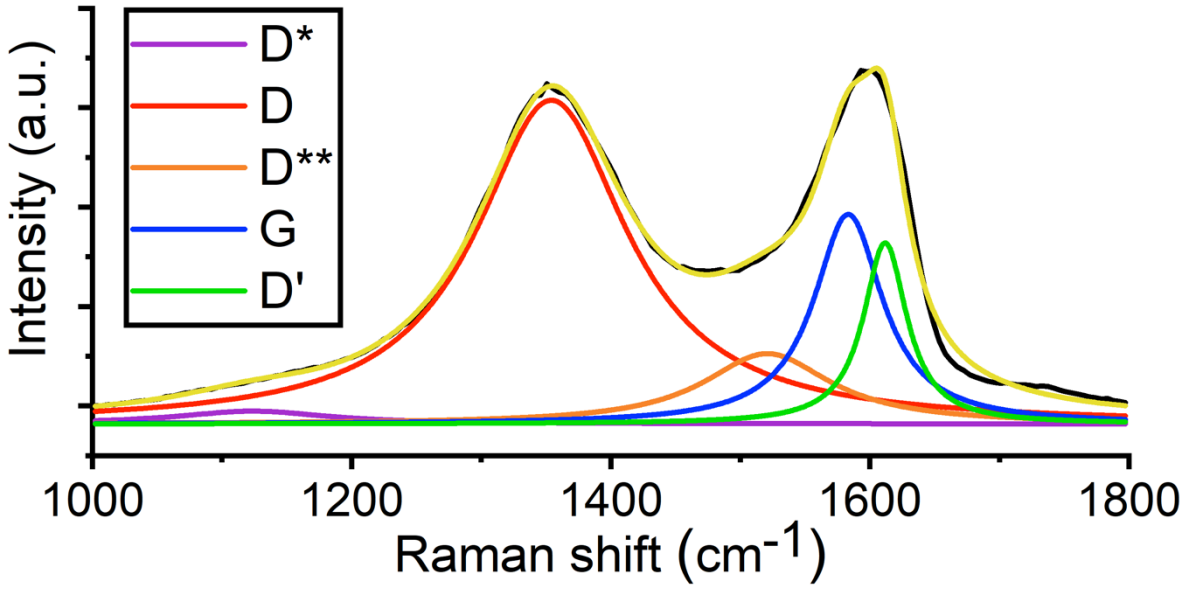

Figure 4H Raman spectrum of D and G regions, 1000-1800 cm^{-1}, for the trGO sample at 170^{O}C.

Temperature (^{O}C)		Sum of Squares	df	Mean Square	F	Sig. (*p*)
600	Between groups	0.029	1	0.029	72.216	0.001*
	Within groups	0.002	4	0.000		
	Total	0.030	5			
700	Between groups	0.015	1	0.015	23.570	0.008*
	Within groups	0.003	4	0.001		
	Total	0.018	5			
800	Between groups	0.009	1	0.009	13.626	0.021*
	Within groups	0.003	4	0.001		
	Total	0.012	5			
860	Between groups	0.013	1	0.013	14.150	0.020*
	Within groups	0.004	4	0.001		
	Total	0.017	5			
910	Between groups	0.014	1	0.014	23.942	0.008*
	Within groups	0.002	4	0.001		
	Total	0.016	5			

Table 4G One-way ANOVA between the I_D/I_G ratio of one and two-step rGO samples at each annealing temperature, calculated using SPSS software.

Temperature (^{O}C)		Sum of Squares	df	Mean Square	F	Sig. (*p*)
600	Between groups	14.727	1	14.727	552.250	0.000*
	Within groups	0.107	4	0.027		
	Total	14.833	5			
700	Between groups	10.140	1	10.140	121.680	0.000*
	Within groups	0.333	4	0.083		
	Total	10.473	5			
800	Between groups	1.602	1	1.602	16.569	0.015*
	Within groups	0.387	4	0.097		
	Total	1.988	5			
860	Between groups	0.042	1	0.042	1.471	0.292
	Within groups	0.113	4	0.028		
	Total	0.155	5			
910	Between groups	0.960	1	0.960	13.091	0.022*
	Within groups	0.293	4	0.073		
	Total	1.253	5			

Table 4H One-way ANOVA between the $I_{D'}/I_G$ ratio of one and two-step rGO samples at each annealing temperature, calculated using SPSS software.

Temperature (^{O}C)		Sum of Squares	df	Mean Square	F	Sig. (*p*)
600	Between groups	0.006	1	0.006	5.082	0.087
	Within groups	0.005	4	0.001		
	Total	0.011	5			
700	Between groups	0.013	1	0.013	127.589	0.000*
	Within groups	0.000	4	0.000		
	Total	0.014	5			
800	Between groups	0.048	1	0.048	70.487	0.001*
	Within groups	0.003	4	0.001		
	Total	0.051	5			
860	Between groups	0.024	1	0.024	47.336	0.002*
	Within groups	0.002	4	0.001		
	Total	0.026	5			
910	Between groups	0.021	1	0.021	8.095	0.047*
	Within groups	0.010	4	0.003		
	Total	0.031	5			

Table 4I One-way ANOVA between the D shift of one and two-step rGO samples at each annealing temperature, calculated using SPSS software.

Temperature (°C)		Sum of Squares	df	Mean Square	F	Sig. (*p*)
600	Between groups	46.482	1	46.482	108.941	0.000*
	Within groups	1.707	4	0.427		
	Total	48.188	5			
700	Between groups	37.002	1	37.002	70.256	0.001*
	Within groups	2.107	4	0.527		
	Total	39.108	5			
800	Between groups	23.602	1	23.602	91.955	0.001*
	Within groups	1.027	4	0.257		
	Total	24.628	5			
860	Between groups	14.415	1	14.415	13.685	0.021*
	Within groups	4.213	4	1.053		
	Total	18.628	5			
910	Between groups	7.260	1	7.260	13.570	0.021*
	Within groups	2.140	4	0.535		
	Total	9.400	5			

Table 4J One-way ANOVA between the G shift of one and two-step rGO samples at each annealing temperature, calculated using SPSS software.

Temperature (°C)		Sum of Squares	df	Mean Square	F	Sig. (*p*)
600	Between groups	29.040	1	29.040	77.786	0.001*
	Within groups	1.493	4	0.373		
	Total	30.533	5			
700	Between groups	24.402	1	24.402	76.654	0.001*
	Within groups	1.273	4	0.318		
	Total	25.675	5			
800	Between groups	12.615	1	12.615	43.006	0.003*
	Within groups	1.173	4	0.293		
	Total	13.788	5			
860	Between groups	1.402	1	1.402	2.168	0.215
	Within groups	2.587	4	0.647		
	Total	3.988	5			
910	Between groups	0.427	1	0.427	0.955	0.384
	Within groups	1.787	4	0.447		
	Total	2.213	5			

Table 4K One-way ANOVA between the D' shift of one and two-step rGO samples at each annealing temperature, calculated using SPSS software.

Temperature (°C)		Sum of Squares	df	Mean Square	F	Sig. (*p*)
600	Between groups	11.760	1	11.760	134.323	0.000*
	Within groups	0.350	4	0.088		
	Total	12.110	5			
700	Between groups	7.238	1	7.238	31.223	0.005*
	Within groups	0.927	4	0.232		
	Total	8.165	5			
800	Between groups	7.981	1	7.981	29.344	0.006*
	Within groups	1.088	4	0.272		
	Total	9.069	5			
860	Between groups	3.375	1	3.375	3.892	0.120
	Within groups	3.469	4	0.867		
	Total	6.844	5			
910	Between groups	7.129	1	7.129	28.614	0.006*
	Within groups	0.997	4	0.249		
	Total	8.125	5			

Table 4L One-way ANOVA between the D width of one and two-step rGO samples at each annealing temperature, calculated using SPSS software.

Temperature (°C)		Sum of Squares	df	Mean Square	F	Sig. (*p*)
600	Between groups	3601.500	1	3601.500	15111.189	0.000*
	Within groups	0.953	4	0.238		
	Total	3602.453	5			
700	Between groups	3141.882	1	3141.882	4446.059	0.000*
	Within groups	2.827	4	0.707		
	Total	3144.708	5			
800	Between groups	4471.740	1	4471.740	191646.000	0.000*
	Within groups	0.093	4	0.023		
	Total	4471.833	5			
860	Between groups	3432.042	1	3432.042	8303.327	0.000*
	Within groups	1.653	4	0.413		
	Total	3433.695	5			
910	Between groups	2973.936	1	2973.936	8519.679	0.000*
	Within groups	1.396	4	0.349		
	Total	2975.332	5			

Table 4M One-way ANOVA between the G width of one and two-step rGO samples at each annealing temperature, calculated using SPSS software.

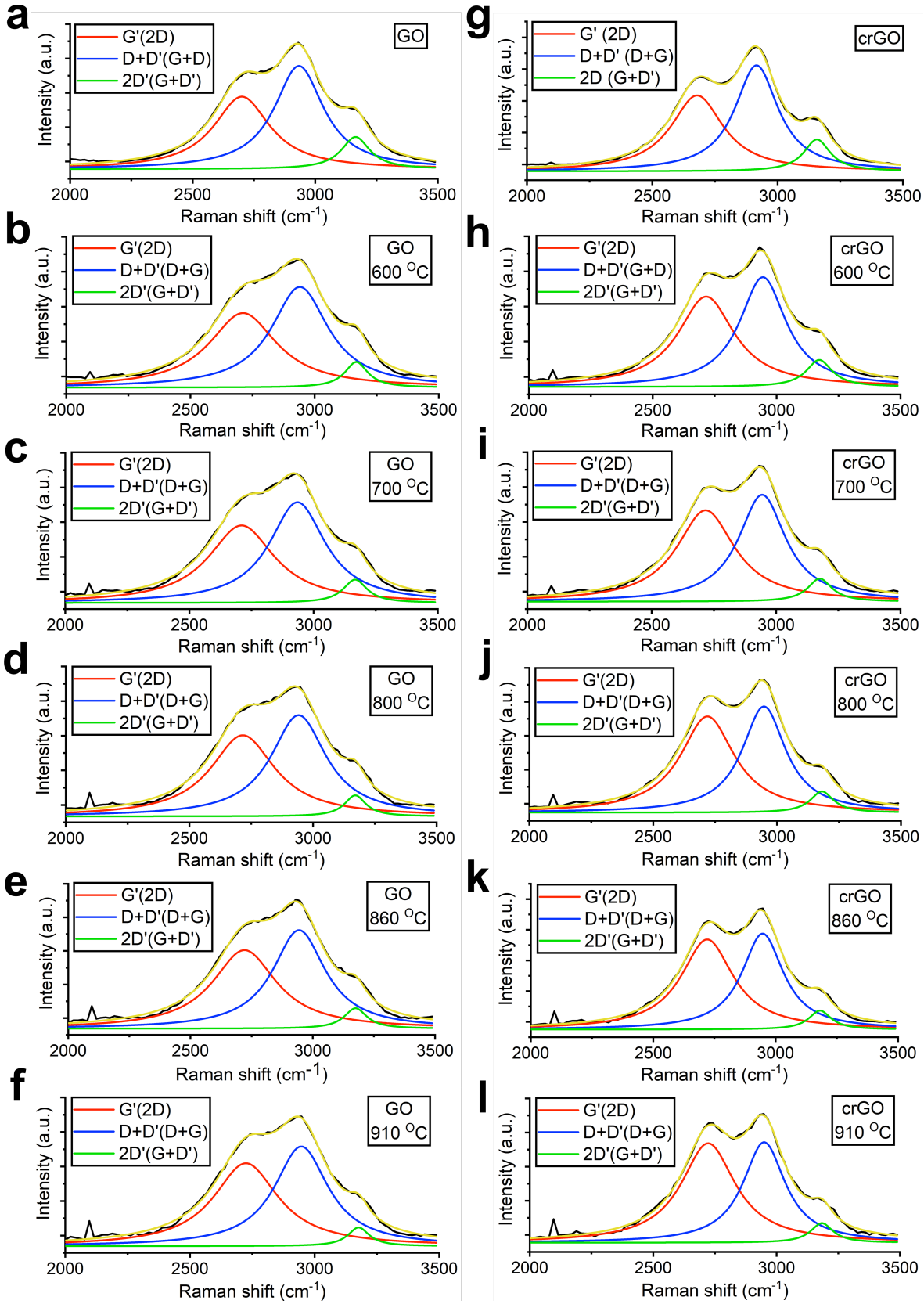

Figure 4l Raman spectra of the 2D region (2000-3500 cm^{-1}) of GO (a-f) and crGO (g-l) films before and after thermal annealing between 600-910 ^{O}C for 1 h. D and G bands have been deconvoluted into G', D+D' and 2D' peaks according to Kaniyoor et al.[217]

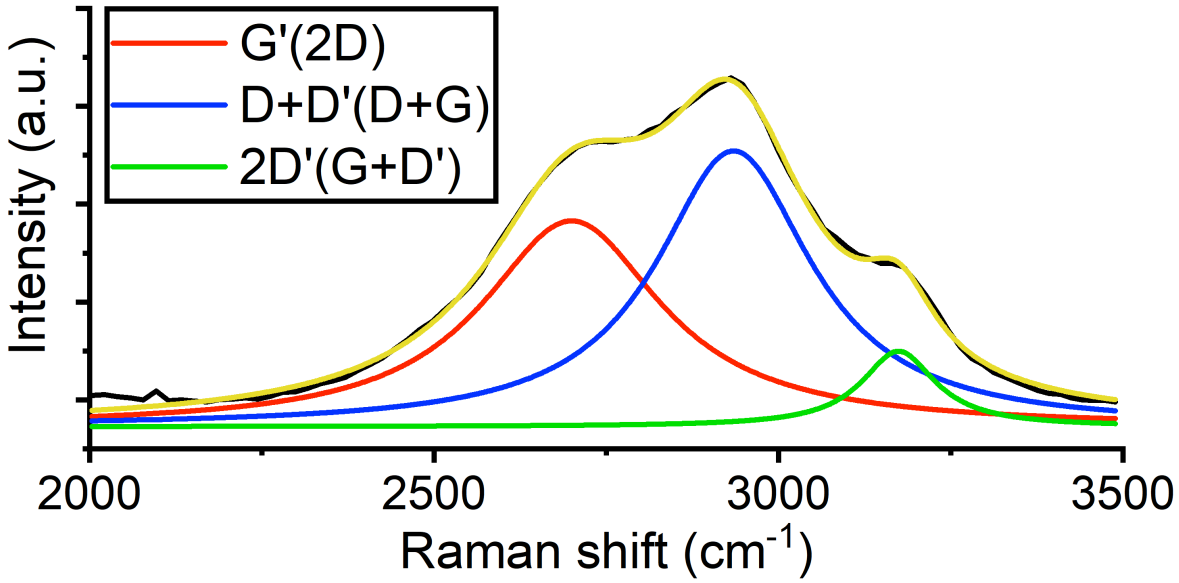

Figure 4J Raman spectrum of the 2D region (2000-3500 cm^{-1}) of trGO reduced at 170 ^{O}C (a-f). The 2D band has been deconvoluted into G', D+D' and 2D' peaks according to Kaniyoor et al.[217]

Temperature (^{O}C)		Sum of Squares	df	Mean Square	F	Sig. (*p*)
600	Between groups	0.006	1	0.006	5.082	0.087
	Within groups	0.005	4	0.001		
	Total	0.011	5			
700	Between groups	0.013	1	0.013	127.589	0.000*
	Within groups	0.000	4	0.000		
	Total	0.014	5			
800	Between groups	0.048	1	0.048	70.487	0.001*
	Within groups	0.003	4	0.001		
	Total	0.051	5			
860	Between groups	0.024	1	0.024	47.336	0.002*
	Within groups	0.002	4	0.001		
	Total	0.026	5			
910	Between groups	0.021	1	0.021	8.095	0.047*
	Within groups	0.010	4	0.003		
	Total	0.031	5			

Table 4N One-way ANOVA between the I_{2D}/I_{D+G} ratio of one and two-step rGO samples at each annealing temperature, calculated using SPSS software.

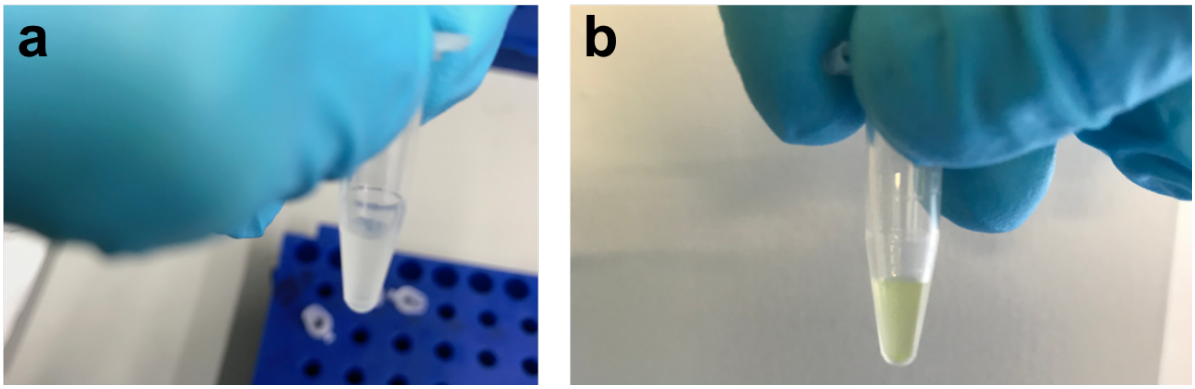

Figure 5A Colour of solution before (a) and after (b) the templating of CdS to DNA.

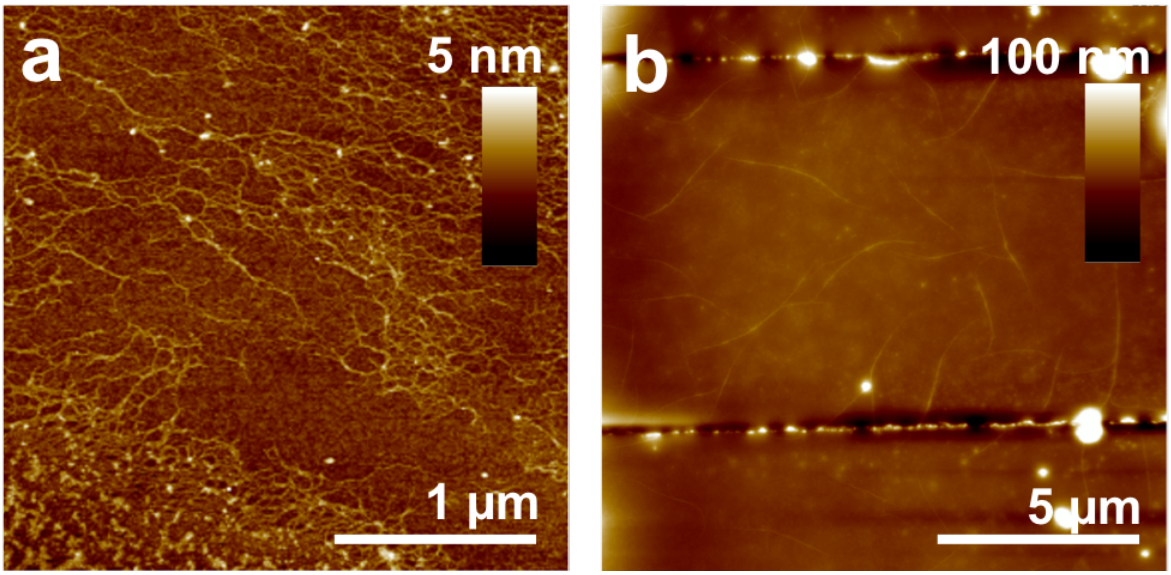

Figure 5B AFM images on CdS/λ.DNA deposited on Si (a) and over a Pt-on-glass IDE (b). Printing many layers leads to a dense network formation (a). From printing a few layers, individual wires can be identified and seen to exhibit extended conformations (b).

References

1 R. Das, K. Ghaffarzadeh and X. He, *IDTechEx Res.*, 2017.
2 F. Torrisi, T. Hasan, W. P. Wu, Z. P. Sun, A. Lombardo, T. S. Kulmala, G. W. Hsieh, S. J. Jung, F. Bonaccorso, P. J. Paul, D. P. Chu and A. C. Ferrari, *ACS Nano*, 2012, **6**, 2992–3006.
3 W. Yang and C. Wang, *J. Mater. Chem. C*, 2016, **4**, 7193–7207.
4 L. T. Le, M. H. Ervin, H. Qiu, B. E. Fuchs, J. Zunino and W. Y. Lee, in *Proceedings of the IEEE Conference on Nanotechnology*, 2011, pp. 67–71.
5 S. Lim, B. Kang, D. Kwak, W. H. Lee, J. A. Lim and K. Cho, *J. Phys. Chem. C*, 2012, **116**, 7520–7525.
6 K. Arapov, R. Abbel, G. De With and H. Friedrich, *Faraday Discuss.*, 2014, **173**, 323–336.
7 L. Huang, Y. Huang, J. J. Liang, X. J. Wan and Y. S. Chen, *Nano Res.*, 2011, **4**, 675–684.
8 N. Karim, S. Afroj, A. Malandraki, S. Butterworth, C. Beach, M. Rigout, K. S. Novoselov, A. J. Casson and S. G. Yeates, *J. Mater. Chem. C*, 2017, **5**, 11640.
9 Y. Xu, I. Hennig, D. Freyberg, A. James Strudwick, M. Georg Schwab, T. Weitz and K. Chih-Pei Cha, *J. Power Sources*, , DOI:10.1016/j.jpowsour.2013.09.096.
10 V. Dua, S. P. Surwade, S. Ammu, S. R. Agnihotra, S. Jain, K. E. Roberts, S. Park, R. S. Ruoff and S. K. Manohar, *Angew Chem Int Ed Engl*, 2010, **49**, 2154–2157.
11 D. Savastano, *Ink World*, 2015.
12 S. Bae, H. Kim, Y. Lee, X. Xu, J. S. Park, Y. Zheng, J. Balakrishnan, T. Lei, H. Ri Kim, Y. Il Song, Y. J. Kim, K. S. Kim, B. Özyilmaz, J. H. Ahn, B. H. Hong and S. Iijima, *Nat. Nanotechnol.*, 2010, **5**, 574–578.
13 B. N. Chandrashekar, B. Deng, A. S. Smitha, Y. Chen, C. Tan, H. Zhang, H. Peng and Z. Liu, *Adv. Mater.*, 2015, **27**, 5210–5216.
14 J. Sun, Z. Chen, L. Yuan, Y. Chen, J. Ning, S. Liu, D. Ma, X. Song, M. K. Priydarshi, A. Bachmatiuk, M. H. Rümmeli, T. Ma, L. Zhi, L. Huang, Y. Zhang and Z. Liu, *ACS Nano*, 2016, **10**, 11136–11144.
15 J. Sun, Y. Chen, X. Cai, B. Ma, Z. Chen, M. K. Priydarshi, K. Chen, T. Gao, X. Song, Q. Ji, X. Guo, D. Zou, Y. Zhang and Z. Liu, *Nano Res.*, 2015, **8**, 2496–3504.
16 W. H. Lin, T. H. Chen, J. K. Chang, J. I. Taur, Y. Y. Lo, W. L. Lee, C. S. Chang, W. Bin Su and C. I. Wu, *ACS Nano*, 2014, **8**, 1784–1791.
17 K. Ghaffarzadeh and R. Das, *Transparent Conductive Films and Materials 2019-2029: Forecasts, Technologies, Players*, 2018.
18 IHS markit, 2018.
19 Statista, 2017.
20 B. Fabbri, A. Gaiardo, V. Guidi, C. Malagù and A. Giberti, *Procedia Eng.*, 2014, **87**, 140–143.
21 K. W. Böer, *Energy Convers. Manag.*, 2011, **52**, 426–430.
22 A. K. Bansal, F. Antolini, S. Zhang, L. Stroea, L. Ortolani, M. Lanzi, E. Serra, S. Allard, U. Scherf and I. D. W. Samuel, *J. Phys. Chem. C*, 2016, **120**, 1871–1880.

23 J. Jia, J. Wu, J. Dong, L. Fan, M. Huang, J. Lin and L. Zhang, *Chem. Commun.*, 2018, **54**, 3170–3173.
24 O. S. Wolfbeis, *Chem. Soc. Rev.*, 2015, **44**, 4743–4768.
25 S. Chakraborty and M. Pal, *Sensors Actuators, B Chem.*, 2017, **242**, 1155–1164.
26 J. Reyes-Esparza, A. Martínez-Mena, I. Gutiérrez-Sancha, P. Rodríguez-Fragoso, G. G. Cruz, R. Mondragón and L. Rodríguez-Fragoso, *J. Nanobiotechnology*, 2015, **13**, 83.
27 N. Chilton, 2014.
28 M. Singh, H. M. Haverinen, P. Dhagat and G. E. Jabbour, *Adv. Mater.*, , DOI:10.1002/adma.200901141.
29 F. Bonaccorso, A. Lombardo, T. Hasan, Z. Sun, L. Colombo and A. C. Ferrari, *Mater. Today*, 2012, **15**, 564–589.
30 K. H. Lee, B. Lee, S.-J. Hwang, J.-U. Lee, H. Cheong, O.-S. Kwon, K. Shin and N. H. Hur, *Carbon N. Y.*, 2014, **69**, 327–335.
31 K. Y. Shin, J. Y. Hong and J. Jang, *Adv Mater*, 2011, **23**, 2113–2118.
32 G. Gao, S. Wen, W. Wucong, L. Yuanpeng and Y. Zhao, *Ind. Eng. Chem. Res.*, 2014, **53**, 16777–16784.
33 W. J. Hyun, E. B. Secor, M. C. Hersam, C. D. Frisbie and L. F. Francis, *Adv. Mater.*, 2015, **27**, 109–115.
34 S. Cinti and F. Arduini, *Biosens. Bioelectron.*, 2017, **89**, 107–122.
35 J. Baker, D. Deganello, D. T. Gethin and T. M. Watson, *Mater. Res. Innov.*, 2014, **18**, 86–90.
36 E. B. Secor, S. Lim, H. Zhang, C. D. Frisbie, L. F. Francis and M. C. Hersam, *Adv. Mater.*, 2014, **26**, 4533–4538.
37 M. Lahti, S. Leppävuori and V. Lantto, *Appl. Surf. Sci.*, 1999, **142**, 367–370.
38 L. Nilsson, M. Andersen, R. Balog, E. Lægsgaard, P. Hofmann, F. Besenbacher, B. Hammer, I. Stensgaard and L. Hornekær, *ACS Nano*, 2012, **6**, 10258–10266.
39 S. De and J. L. Lutkenhaus, *Green Chem.*, 2018, **20**, 506–514.
40 E. Kymakis, E. Stratakis, M. M. Stylianakis, E. Koudoumas and C. Fotakis, *Thin Solid Films*, 2011, **520**, 1238–1241.
41 J. Liu, L. Hua, S. Li and M. Yu, *Appl. Surf. Sci.*, 2015, **327**, 241–245.
42 Fujifilm, 2012.
43 N. Marjanovic, J. Hammerschmidt, J. Perelaer, S. Farnsworth, I. Rawson, M. Kus, E. Yenel, S. Tilki, U. S. Schubert and R. R. Baumann, *J. Mater. Chem.*, 2011, **21**, 13634.
44 J. Perelaer, M. Klokkenburg, C. E. Hendriks and U. S. Schubert, *Adv. Mater.*, 2009, **21**, 4830–4834.
45 R. Tortorich and J.-W. Choi, *Nanomaterials*, 2013, **3**, 453–468.
46 Y. Lee, J. R. Choi, K. J. Lee, N. E. Stott and D. Kim, *Nanotechnology*, 2008, **15**, 415604.
47 C. C. Caliman, A. F. Mesquita, D. F. Cipriano, J. C. C. Freitas, A. A. C. Cotta, W. A. A. Macedo and A. O. Porto, *RSC Adv.*, 2018, **8**, 6136–6145.
48 D. Li, W.-Y. Lai, Y.-Z. Zhang and W. Huang, *Adv. Mater.*, 2018, **30**, 1704738.

49 M. Michel, C. Biswas, C. S. Tiwary, G. A. Saenz, R. F. Hossain, P. Ajayan and A. B. Kaul, *2D Mater.*, 2017, **4**, 025076.
50 T. Juntunen, H. Jussila, M. Ruoho, S. Liu, G. Hu, T. Albrow-Owen, L. W. T. Ng, R. C. T. Howe, T. Hasan, Z. Sun and I. Tittonen, *Adv. Funct. Mater.*, 2018, **28**, 1800480.
51 E. B. Secor, B. Y. Ahn, T. Z. Gao, J. A. Lewis and M. C. Hersam, *Adv. Mater.*, 2015, **27**, 6683–6688.
52 B. Derby, *J. Eur. Ceram. Soc.*, 2011, **31**, 2543–2550.
53 D. Jang, D. Kim and J. Moon, *Langmuir*, 2009, **25**, 2629–2635.
54 J. E. Fromm, *IBM J. Res. Dev.*, 1984, **28**, 322–333.
55 P. He and B. Derby, *Adv. Mater. Interfaces*, 2017, **4**, 1700944.
56 P. He and B. Derby, *2D Mater.*, 2017, **4**, 021021.
57 M. H. U. Bhuiyan, R. Saidur, M. A. Amalina, R. M. Mostafizur and A. K. M. S. Islam, *Procedia Eng.*, 2015, **105**, 431–437.
58 R. N. Nurdillayeva, A. B. Oshido, T. A. Bamford, O. El-Zubir, A. Houlton, J. Hedley, A. R. Pike and B. R. Horrocks, *Nanotechnology*, 2018, **19**, 135704.
59 M. Rogala, I. Wlasny, P. Dabrowski, P. J. Kowalczyk, A. Busiakiewicz, W. Kozlowski, L. Lipinska, J. Jagiello, M. Aksienionek, W. Strupinski, A. Krajewska, Z. Sieradzki, I. Krucinska, M. Puchalski, E. Skrzetuska and Z. Klusek, *Appl. Phys. Lett.*, 2015, **106**, 041901.
60 Y. Su, J. H. Du, D. M. Sun, C. Liu and H. M. Cheng, *Nano Res.*, 2013, **6**, 842–852.
61 Y. Fang, J. G. D. Hester, W. Su, J. H. Chow, S. K. Sitaraman and M. M. Tentzeris, *Sci. Rep.*, 2016, **6**, 39909.
62 L. T. Le, M. H. Ervin, H. Qiu, B. E. Fuchs and W. Y. Lee, *Electrochem. commun.*, 2011, **13**, 355–358.
63 P. Reynolds, in *Colloid Science: Principles, Methods and Applications*, 2009.
64 T. Huhtamäki, X. Tian, J. T. Korhonen and R. H. A. Ras, *Nat. Protoc.*, 2018, **13**, 1521–1538.
65 R. J. Good, *J. Adhes. Sci. Technol.*, 1992, **6**, 1269–1302.
66 A. Kozbial, Z. Li, C. Conaway, R. McGinley, S. Dhingra, V. Vahdat, F. Zhou, B. D'Urso, H. Liu and L. Li, *Langmuir*, 2014, **30**, 8598–8606.
67 S. M. Smith, B. S. Taft and J. Moulton, *Front. Heat Mass Transf.*, 2014, **5**, 6.
68 D. Mampallil, *Resonance*, 2014, **19**, 123–134.
69 M. C. Phillips and A. C. Riddiford, *Nature*, 1965, **205**, 1005–1006.
70 D. H. Prajitno, A. Maulana and D. G. Syarif, *J. Phys. Conf. Ser.*, 2016, **739**, 012029.
71 L. Chen and E. Bonaccurso, *Phys. Rev. E - Stat. Nonlinear, Soft Matter Phys.*, 2014, **90**, 022401.
72 H. Kim, J. I. Jang, H. H. Kim, G. W. Lee, J. A. Lim, J. T. Han and K. Cho, *ACS Appl. Mater. Interfaces*, 2016, **8**, 3193–3199.
73 P. He, J. R. Brent, H. Ding, J. Yang, D. J. Lewis, P. O'Brien and B. Derby, *Nanoscale*, 2018, **10**, 5599.
74 D. Soltman and V. Subramanian, *Langmuir*, 2008, **24**, 2224–2231.
75 T. Wang, M. A. Roberts, I. A. Kinloch and B. Derby, *J. Phys. D. Appl. Phys.*, ,

DOI:10.1088/0022-3727/45/31/315304.
76 R. Tadmor, *J. Colloid Interface Sci.*, 2009, **332**, 451–454.
77 X. Xu and J. Luo, *Appl. Phys. Lett.*, 2007, **91**, 124102.
78 L. Zhang, H. Liu, Y. Zhao, X. Sun, Y. Wen, Y. Guo, X. Gao, C. A. Di, G. Yu and Y. Liu, *Adv. Mater.*, , DOI:10.1002/adma.201103620.
79 V. Slabov, A. V. Vinogradov and A. V. Yakovlev, *J. Mater. Chem. C*, 2018, **6**, 5269–5277.
80 S. Chung, M. A. U. Karim, M. Spencer, H. J. Kwon, C. P. Grigoropoulos, E. Alon and V. Subramanian, *Appl. Phys. Lett.*, 2014, **105**, 261901.
81 Y. Zhang, X. Chen, F. Liu, L. Li, J. Dai and T. Liu, *Adv. Condens. Matter Phys.*, , DOI:10.1155/2018/9795654.
82 H. Hu and R. G. Larson, *J. Phys. Chem. B*, 2006, **110**, 7090–7094.
83 C. Seo, D. Jang, J. Chae and S. Shin, *Sci. Rep.*, 2017, **7**, 500.
84 K. S. Novoselov, A. K. Geim, S. V Morozov, D. Jiang, Y. Zhang, S. V Dubonos, I. V Grigorieva and A. A. Firsov, *Science*, 2004, **306**, 666–669.
85 C. Lee, X. Wei, J. W. Kysar and J. Hone, *Science (80-.).*, 2008, **321**, 385–388.
86 F. Bonaccorso, L. Colombo, G. Yu, M. Stoller, V. Tozzini, A. C. Ferrari, R. S. Ruoff and V. Pellegrini, *Science (80-.).*, 2015, **347**, 1246501.
87 K. I. Bolotin, K. J. Sikes, Z. Jiang, M. Klima, G. Fudenberg, J. Hone, P. Kim and H. L. Stormer, *Solid State Commun.*, 2008, **146**, 351–355.
88 D. Kong, L. T. Le, Y. Li, J. L. Zunino and W. Lee, *Langmuir*, 2012, **28**, 13467–13472.
89 Y. Yu, H. Wada, J. Inoue, S. Imaizumi, Y. Kounosu, K. Tsuboi, H. Matsumoto, M. Ashizawa, T. Mori, M. Minagawa and A. Tanioka, *Appl. Phys. Express*, , DOI:10.1143/APEX.4.115101.
90 X. Miao, S. Tongay, M. K. Petterson, K. Berke, A. G. Rinzler, B. R. Appleton and A. F. Hebard, *Nano Lett.*, 2012, **12**, 2745–2750.
91 S. H. Song, M.-H. Jang, J. Chung, S. H. Jin, B. H. Kim, S.-H. Hur, S. Yoo, Y.-H. Cho and S. Jeon, *Adv. Opt. Mater.*, 2014, **2**, 1016–1023.
92 I. Rodriguez-Pastor, G. Ramos-Fernandez, H. Varela-Rizo, M. Terrones and I. Martin-Gullon, *Carbon N. Y.*, 2015, **84**, 299–309.
93 A. Lerf, H. He, M. Forster and J. Klinowski, *J. Phys. Chem. B*, 1998, **23**, 4477–4482.
94 H. He, J. Klinowski, M. Forster and A. Lerf, *Chem. Phys. Lett.*, 1998, **287**, 53–56.
95 N. I. Zaaba, K. L. Foo, U. Hashim, S. J. Tan, W. W. Liu and C. H. Voon, *Procedia Eng.*, 2017, **184**, 469–477.
96 H. Yu, B. Zhang, C. Bulin, R. Li and R. Xing, *Sci. Rep.*, 2016, **6**, 36143.
97 M. J. Kim, Y. Jeong, S. H. Sohn, S. Y. Lee, Y. J. Kim, K. Lee, Y. H. Kahng and J. H. Jang, *AIP Adv.*, 2013, **3**, 012117.
98 Y. Zhang, L. Guo, S. Wei, Y. He, H. Xia, Q. Chen, H. B. Sun and F. S. Xiao, *Nano Today*, 2010, **5**, 15–20.
99 M. Zhou, Y. Wang, Y. Zhai, J. Zhai, W. Ren, F. Wang and S. Dong, *Chem. - A Eur. J.*, 2009, **15**, 6116–6120.
100 X. Wang, L. Zhi and K. Müllen, *Nano Lett.*, 2008, **8**, 323–327.

101 S. Pei, J. Zhao, J. Du, W. Ren and H. M. Cheng, *Carbon N. Y.*, 2010, **48**, 4466–4474.
102 J. T. Li, F. Ye, S. Vaziri, M. Muhammed, M. C. Lemme and M. Ostling, *Adv Mater*, 2013, **25**, 3985–3992.
103 M. Yi and Z. Shen, *J. Mater. Chem. A*, 2015, **3**, 11700–11715.
104 H. Wang, S. Lu, Y. Zhang, F. Lan, X. Lu and Y. Xiang, *J. Mater. Chem. A*, 2015, **3**, 6282–6285.
105 M. H. Ervin, L. T. Le and W. Y. Lee, *Electrochim. Acta*, 2014, **147**, 610–616.
106 T. Le, V. Lakafosis, Z. Lin, C. P. Wong and M. M. Tentzeris, in *Proceedings - Electronic Components and Technology Conference*, 2012, pp. 1003–1008.
107 R. Rozada, J. I. Paredes, S. Villar-Rodil, A. Martínez-Alonso and J. M. D. Tascón, *Nano Res.*, 2013, **6**, 216–233.
108 I. K. Moon, J. Lee, R. S. Ruoff and H. Lee, *Nat. Commun.*, 2010, **1**, 73.
109 H. A. Becerril, J. Mao, Z. Liu, R. M. Stoltenberg, Z. Bao and Y. Chen, *ACS Nano*, 2008, **2**, 463–470.
110 R. Larciprete, S. Fabris, T. Sun, P. Lacovig, A. Baraldi and S. Lizzit, *J. Am. Chem. Soc.*, 2011, **133**, 17315–17321.
111 S. Pang, Y. Hernandez, X. Feng and K. Müllen, *Adv. Mater.*, 2011, **23**, 2779–2795.
112 M. He, J. Jung, F. Qiu and Z. Lin, *J. Mater. Chem.*, 2012, **22**, 24254–24264.
113 A. Kumar and C. Zhou, *ACS Nano*, 2010, **4**, 11–14.
114 D. H. Wang, A. K. K. Kyaw, V. Gupta, G. C. Bazan and A. J. Heeger, *Adv. Energy Mater.*, 2013, **3**, 1161–1165.
115 R. Arvidsson, D. Kushnir, S. Molander and B. A. Sandén, *J. Clean. Prod.*, 2016, **132**, 289–297.
116 D. R. Cairns, R. P. Witte, D. K. Sparacin, S. M. Sachsman, D. C. Paine, G. P. Crawford and R. R. Newton, *Appl. Phys. Lett.*, 2000, **76**, 1425–1427.
117 J. H. Bae, J. M. Moon, J. W. Kang, H. D. Park, J. J. Kim, W. Jo Cho and H. K. Kim, *J. Electrochem. Soc.*, 2007, **154**, 81–85.
118 S. Kaleemulla, A. S. Readdy, S. Uthanna and P. S. Reddy, *Optoelectron. Adv. Mater. Rapid Commun.*, 2008, **2**, 782–787.
119 A. Suzuki, T. Matsushita, Y. Sakamoto, N. Wada, T. Fukuda, H. Fujiwara and M. Okuda, *Japanese J. Appl. Physics, Part 1 Regul. Pap. Short Notes Rev. Pap.*, 1996, **35**, 5457–5461.
120 D. Liu, S. Ren, X. Ma, C. Liu, L. Wu, W. Li, J. Zhang and L. Feng, *RSC Adv.*, 2017, **7**, 8295–8302.
121 A. R. Madaria, A. Kumar, F. N. Ishikawa and C. Zhou, *Nano Res.*, 2010, **3**, 564–573.
122 Y. Xia, K. Sun and J. Ouyang, *Adv. Mater.*, 2012, **24**, 2436–2440.
123 H. Kang, S. Jung, S. Jeong, G. Kim and K. Lee, *Nat. Commun.*, 2015, **6**, 6503.
124 L. Kinner, S. Nau, K. Popovic, S. Sax, I. Burgués-Ceballos, F. Hermerschmidt, A. Lange, C. Boeffel, S. A. Choulis and E. J. W. List-Kratochvil, *Appl. Phys. Lett.*, 2017, **110**, 1011107.
125 K.-R. Chen, H.-F. Yeh, H.-C. Chen, T.-J. Liu, S.-J. Huang, P.-Y. Wu and C. Tiu, *Adv. Chem. Eng. Sci.*, 2013, **3**, 105–111.

126 F. Mirri, A. W. K. Ma, T. T. Hsu, N. Behabtu, S. L. Eichmann, C. C. Young, D. E. Tsentalovich and M. Pasquali, *ACS Nano*, 2012, **6**, 9737–9744.
127 S. Pei, J. Du, Y. Zeng, C. Liu and H. M. Cheng, *Nanotechnology*, 2009, **20**, 235707.
128 Q. Cao, S. H. Hur, Z. T. Zhu, Y. Sun, C. Wang, M. A. Meitl, M. Shim and J. A. Rogers, *Adv. Mater.*, 2006, **18**, 304–309.
129 R. R. Nair, P. Blake, A. N. Grigorenko, K. S. Novoselov, T. J. Booth, T. Stauber, N. M. R. Peres and A. K. Geim, *Science (80-.)*., 2008, **320**, 1308.
130 S. Majee, M. Song, S. L. Zhang and Z. Bin Zhang, *Carbon N. Y.*, 2016, **102**, 51–57.
131 S. Sharma, S. Shriwastava, S. Kumar, K. Bhatt and C. C. Tripathi, *Opto-electronics Rev.*, 2018, 223–235.
132 T. L. Chen, D. S. Ghosh, V. Mkhitaryan and V. Pruneri, *ACS Appl. Mater. Interfaces*, 2013, **5**, 11756–11761.
133 T. Qiu, B. Luo, M. Liang, J. Ning, B. Wang, X. Li and L. Zhi, *Carbon N. Y.*, 2015, **81**, 232–238.
134 V. C. Tung, L. M. Chen, M. J. Allen, J. K. Wassei, K. Nelson, R. B. Kaner and Y. Yang, *Nano Lett.*, 2009, **9**, 1949–1955.
135 T. Hu, H. Wang, Y. Shao, X. Zhang, G. Liu, M. Li, H. Chen and Y. Lee, *SID Symp. Dig. Tech. Pap.*, 2017, **48**, 972–975.
136 R. Chen, S. R. Das, C. Jeong, M. R. Khan, D. B. Janes and M. A. Alam, *Adv. Funct. Mater.*, 2013, **23**, 5150–5158.
137 H. G. Im, S. H. Jung, J. Jin, D. Lee, J. Lee, D. Lee, J. Y. Lee, I. D. Kim and B. S. Bae, *ACS Nano*, 2014, **8**, 10973–10979.
138 M. S. Lee, K. Lee, S. Y. Kim, H. Lee, J. Park, K. H. Choi, H. K. Kim, D. G. Kim, D. Y. Lee, S. Nam and J. U. Park, *Nano Lett.*, 2013, **13**, 2814–2821.
139 R. Jalili, S. H. Aboutalebi, D. Esrafilzadeh, K. Konstantinov, S. E. Moulton, J. M. Razal and G. G. Wallace, *ACS Nano*, 2013, **7**, 3981–3990.
140 P. Solís-Fernández, J. I. Paredes, S. Villar-Rodil, A. Martínez-Alonso and J. M. D. Tascón, *Carbon N. Y.*, 2010, **48**, 2657–2660.
141 K. Y. Shin, J. Y. Hong and J. Jang, *Chem. Commun.*, 2011, **47**, 8527–8529.
142 J. Zhang, H. Yang, G. Shen, P. Cheng, J. Zhang and S. Guo, *Chem. Commun. (Camb).*, 2010, **46**, 1112–1114.
143 C. J. Shearer, A. D. Slattery, A. J. Stapleton, J. G. Shapter and C. T. Gibson, *Nanotechnology*, 2016, **27**, 125704.
144 H. Lee and J. Y. Park, *Rev. Sci. Instrum.*, 2019, **90**, 103702.
145 J. M. Mativetsky, E. Treossi, E. Orgiu, M. Melucci, G. P. Veronese, P. Samorì and V. Palermo, *J. Am. Chem. Soc.*, 2010, **132**, 14130–14136.
146 M. Ahmad, S. A. Han, D. H. Tien, J. Jung and Y. Seo, *J. Appl. Phys.*, 2011, **110**, 054307.
147 J. M. P. Alaboson, Q. H. Wang, J. A. Kellar, J. Park, J. W. Elam, M. J. Pellin and M. C. Hersam, *Adv. Mater.*, 2011, **23**, 2181–2184.
148 M. M. Macinnes, S. Hlynchuk, S. Acharya, N. Lehnert and S. Maldonado, *ACS Appl. Mater. Interfaces*, 2018, **10**, 2004–2015.
149 Y. Zhu, X. Li, Q. Cai, Z. Sun, G. Casillas, M. Jose-Yacaman, R. Verduzco and

J. M. Tour, *J. Am. Chem. Soc.*, 2012, **91**, 266–274.
150 L. Pei and Y.-F. Li, *RSC Adv.*, 2017, **7**, 51711–51720.
151 T. H. Seo, S. Lee, H. Cho, S. Chandramohan, E. K. Suh, H. S. Lee, S. K. Bae, S. M. Kim, M. Park, J. K. Lee and M. J. Kim, *Sci. Rep.*, 2016, **6**, 24143.
152 L. Zhang, Y. Li, L. Zhang, D. W. Li, D. Karpuzov and Y. T. Long, *Int. J. Electrochem. Sci.*, 2011, **6**, 819–829.
153 A. Ganguly, S. Sharma, P. Papakonstantinou and J. Hamilton, *J. Phys. Chem. C*, 2011, **115**, 17009–17019.
154 F. Priante, M. Salim, L. Ottaviano and F. Perrozzi, *Nanotechnology*, 2018, **29**, 075704.
155 G. G. Jernigan, J. A. Nolde, N. A. Mahadik, E. R. Cleveland, J. E. Boercker, M. B. Katz, J. T. Robinson and E. H. Aifer, *J. Appl. Phys.*, , DOI:10.1063/1.4998812.
156 M. P. Araújo, O. S. G. P. Soares, A. J. S. Fernandes, M. F. R. Pereira and C. Freire, *RSC Adv.*, 2017, **7**, 14290–14301.
157 A. Bagri, C. Mattevi, M. Acik, Y. J. Chabal, M. Chhowalla and V. B. Shenoy, *Nat. Chem.*, 2010, **2**, 581–587.
158 N. Morimoto, T. Kubo and Y. Nishina, *Sci. Rep.*, 2016, **6**, 21715.
159 A. C. Ferrari and D. M. Basko, *Nat. Nanotechnol.*, 2013, **46**, 235–246.
160 L. M. Malard, M. A. Pimenta, G. Dresselhaus and M. S. Dresselhaus, *Phys. Rep.*, 2009, **473**, 51–57.
161 J. Schwan, S. Ulrich, V. Batori, H. Ehrhardt and S. R. P. Silva, *J. Appl. Phys.*, 1996, **80**, 440–447.
162 F. Tuinstra and J. L. Koenig, *J. Chem. Phys.*, 1970, **53**, 1126–1130.
163 K.-C. Jiang, S. Xin, J.-S. Lee, J. Kim, X.-L. Xiao and Y.-G. Guo, *Phys. Chem. Chem. Phys.*, 2012, **14**, 2934–2939.
164 L. G. Caŋado, K. Takai, T. Enoki, M. Endo, Y. A. Kim, H. Mizusaki, A. Jorio, L. N. Coelho, R. Magalhães-Paniago and M. A. Pimenta, *Appl. Phys. Lett.*, 2006, **88**, 163106.
165 J. I. Paredes, S. Villar-Rodil, P. Solís-Fernández, A. Martínez-Alonso and J. M. D. Tascón, *Langmuir*, 2009, **25**, 5957–5968.
166 C. Y. Su, Y. Xu, W. Zhang, J. Zhao, X. Tang, C. H. Tsai and L. J. Li, *Chem. Mater.*, 2009, **21**, 5674–5680.
167 I. Calizo, A. A. Balandin, W. Bao, F. Miao and C. N. Lau, *Nano Lett.*, 2007, **7**, 2645.
168 A. C. Ferrari, J. C. Meyer, V. Scardaci, C. Casiraghi, M. Lazzeri, F. Mauri, S. Piscanec, D. Jiang, K. S. Novoselov, S. Roth and A. K. Geim, *Phys. Rev. Lett.*, 2006, **97**, 187401.
169 M. A. Pimenta, G. Dresselhaus, M. S. Dresselhaus, L. G. Cançado, A. Jorio and R. Saito, *Phys. Chem. Chem. Phys.*, 2007, **9**, 1276–1291.
170 G. Yasin, M. Arif, M. Shakeel, Y. Dun, Y. Zuo, W. Q. Khan, Y. Tang, A. Khan and M. Nadeem, *Adv. Eng. Mater.*, 2018, **20**, 1701166.
171 T. F. Emiru and D. W. Ayele, *Egypt. J. Basic Appl. Sci.*, 2017, **4**, 74–79.
172 M. Grundmann, *The physics of semiconductors: An introduction including devices and nanophysics*, Springer, 2006.

173 M. A. Carter and J. Woods, *J. Phys. D. Appl. Phys.*, 1973, **6**, 337–349.
174 F. Schipani, C. M. Aldao and M. A. Ponce, *AIP Adv.*, 2012, **2**, 032138.
175 S. Adachi, *Properties of Semiconductor Alloys : Group-IV , III – V and II – VI Semiconductors*, Wiley, 2009.
176 T. Zhai, X. Fang, H. Zeng, X. Xu, Y. Bando and D. Golberg, *Pure Appl. Chem.*, 2010, **82**, 2027–2054.
177 H. Cao, G. Wang, S. Zhang, X. Zhang and D. Rabinovich, *Inorg. Chem.*, 2006, **45**, 5103–5108.
178 L. Zhu, C. Feng, F. Li, D. Zhang, C. Li, Y. Wang, Y. Lin, S. Ruan and Z. Chen, *RSC Adv.*, 2014, **4**, 61691.
179 X. Yue, S. Yi, R. Wang, Z. Zhang and S. Qiu, *Sci. Rep.*, 2016, **5**, 13593.
180 J. D. Watson and F. H. C. Crick, *Nature*, 1953, **171**, 737–738.
181 A. Houlton, A. R. Pike, M. Angel Galindo and B. R. Horrocks, *Chem. Commun.*, 2009, **0**, 1797–1806.
182 L. Dong, T. Hollis, B. A. Connolly, N. G. Wright, B. R. Horrocks and A. Houlton, *Adv. Mater.*, 2007, **19**, 1748–1751.
183 I. Turel and J. Kljun, *Curr. Top. Med. Chem.*, 2011, **11**, 2661–2687.
184 G. H. Clever and M. Shionoya, *Interplay between Met. Ions Nucleic Acids*, 2012, **10**, 269–294.
185 S. M. D. Watson, A. Houlton and B. R. Horrocks, *Nanotechnology*, 2012, **23**, 505603.
186 J. Westwater, *J. Vac. Sci. Technol. B Microelectron. Nanom. Struct.*, 1997, **15**, 554–557.
187 S. Pu, A. Zinchenko and S. Murata, *Nanotechnology*, 2011, **22**, 375604.
188 M. Husham, Z. Hassan and A. M. Selman, *Eur. Phys. J. Appl. Phys.*, 2016, **74**, 10101.
189 J. H. Im, H. R. Kim, B. G. An, Y. W. Chang, M. J. Kang, T. G. Lee, J. G. Son, J. G. Park and J. C. Pyun, *Biosens. Bioelectron.*, 2017, **92**, 221–228.
190 S. Veeranarayanan, A. C. Poulose, M. Sheikh Mohamed, Y. Nagaoka, S. Iwai, Y. Nakagame, S. Kashiwada, Y. Yoshida, T. Maekawa and D. Sakthi Kumar, *Int. J. Nanomedicine*, 2012, **7**, 3769–3786.
191 A. Bah, K. Y. Lim, F. Wei, A. Khursheed and C. H. Sow, *Sci. Rep.*, 2019, **9**, 9671.
192 S. Wu, B. Liu, X. Su and S. Zhang, *J. Phys. Chem. Lett.*, 2017, **8**, 2835–2841.
193 T. Goldmann and J. S. Gonzalez, *J. Biochem. Biophys. Methods*, 2000, **42**, 105–110.
194 N. Ogata, *Proc. SPIE*, 2012, **8464**, 846403.
195 V. Kumar, D. K. Sharma, M. K. Bansal, D. K. Dwivedi and T. P. Sharma, *Sci. Sinter.*, 2011, **43**, 335–341.
196 Y. C. Guo, X. F. Zhou, J. L. Sun, M. Q. Li and J. Hu, *Chinese Sci. Bull.*, 2004, **49**, 1574–1577.
197 R. N. Nurdillayeva, B. R. Horrocks and A. R. Pike, *Mater. Today Proc. INESS*, 2017, accepted.
198 S. Pruneanu, L. Dong, T. A. Hollis, N. G. Wright, M. A. Galindo, A. R. Pike, B. A. Connolly, B. R. Horrocks and A. Houlton, in *AIP Conference Proceedings*,

2008, pp. 33–42.
199 B. L. Baldock and J. E. Hutchison, *Anal. Chem.*, 2016, **88**, 12072–12080.
200 N. Soltani, E. Saion, M. Z. Hussein, M. Erfani, A. Abedini, G. Bahmanrokh, M. Navasery and P. Vaziri, *Int. J. Mol. Sci.*, 2012, **13**, 12242–12258.
201 M. C. Baykul and N. Orhan, *Thin Solid Films*, 2010, **518**, 1925–1928.
202 D. Patidar, R. Sharma, N. Jain, T. P. Sharma and N. S. Saxena, *Bull. Mater. Sci.*, 2006, **29**, 21–24.
203 P. Atkins and J. De Paula, *Atkins' physical chemistry*, Oxford, 2009.
204 V. Stsiapura, A. Sukhanova, A. Baranov, M. Artemyev, O. Kulakovich, V. Oleinikov, M. Pluot, J. H. M. Cohen and I. Nabiev, *Nanotechnology*, 2006, **17**, 581.
205 A. Aboulaich, D. Billaud, M. Abyan, L. Balan, J. J. Gaumet, G. Medjadhi, J. Ghanbaja and R. Schneider, *ACS Appl. Mater. Interfaces*, 2012, **4**, 2561–2569.
206 A. Veamatahau, B. Jiang, T. Seifert, S. Makuta, K. Latham, M. Kanehara, T. Teranishi and Y. Tachibana, *Phys. Chem. Chem. Phys.*, 2015, **17**, 2850–2858.
207 M. O'Neil, J. Marohn and G. McLendon, *J. Phys. Chem.*, 1990, **94**, 4356–4363.
208 R. Xu, Y. Wang, G. Jia, W. Xu, S. Liang and D. Yin, *J. Cryst. Growth*, 2007, **299**, 28–33.
209 S. R. Dhage, H. A. Colorado and T. Hahn, *Nanoscale Res. Lett.*, 2011, **6**, 420.
210 A. Dumbrava, C. Badea, G. Prodan and V. Ciupina, *Chalcogenide Lett.*, 2010, **7**, 111–118.
211 E. Dutková, P. Baláž and P. Pourghahramani, *J. Optoelectron. Adv. Mater.*, 2009, **11**, 2092–2097.
212 Z. R. Khan, M. Zulfequar and M. S. Khan, *Mater. Sci. Eng. B Solid-State Mater. Adv. Technol.*, 2010, **174**, 145–149.
213 M. A. Nusimovici and J. L. Birman, *Phys. Rev.*, 1967, **156**, 925–938.
214 V. Singh and P. Chauhan, *Chalcogenide Lett.*, 2009, **6**, 421–426.
215 A. Pillonnet, R. Ongaro and M. Garoum, *J. Phys. D-Applied Phys.*, 1995, **28**, 149.
216 S. F. Pei and H. M. Cheng, *Carbon N. Y.*, 2012, **50**, 3210–3228.
217 A. Kaniyoor and S. Ramaprabhu, *AIP Adv.*, 2012, **2**, 032183.
218 X. Zhang, B. Lou, D. Li, W. Hong, Y. Yu, J. Li and E. Wang, *Chem. Commun.*, 2015, **51**, 6788–6791.
219 T. Carey, S. Cacovich, G. Divitini, J. Ren, A. Mansouri, J. M. Kim, C. Wang, C. Ducati, R. Sordan and F. Torrisi, *Nat. Commun.*, 2017, **8**, 1202.
220 F. Miao, S. Majee, M. Song, J. Zhao, S. L. Zhang and Z. Bin Zhang, *Synth. Met.*, 2016, **220**, 318–322.
221 C. L. Lee, C. H. Chen and C. W. Chen, *Chem. Eng. J.*, 2013, **230**, 296–302.
222 K. Kim, S. Il Ahn and K. C. Choi, *Carbon N. Y.*, 2014, **66**, 172–177.
223 I. Wlasny, M. Rogala, P. Dabrowski, P. J. Kowalczyk, A. Busiakiewicz, W. Kozlowski, L. Lipinska, J. Jagiello, M. Aksienionek, Z. Sieradzki, I. Krucinska, M. Puchalski, E. Skrzetuska, Z. Draczynski and Z. Klusek, *Mater. Chem. Phys.*, 2016, **181**, 409–414.
224 Z. Pei, H. Hu, G. Liang and C. Ye, *Nano-Micro Lett.*, 2017, 9:19.
225 P. Sundriyal and S. Bhattacharya, *ACS Appl. Mater. Interfaces*, 2017, **9**,

38507–38521.
226 D. H. Lee, H. S. Cho, D. Han, R. Chand, T. J. Yoon and Y. S. Kim, *J. Mater. Chem. B*, 2017, **5**, 3580–3585.
227 D. S. Eom, J. Chang, Y. W. Song, J. A. Lim, J. T. Han, H. Kim and K. Cho, *J. Phys. Chem. C*, 2014, **118**, 27081–27090.
228 E. B. Secor, P. L. Prabhumirashi, K. Puntambekar, M. L. Geier and M. C. Hersam, *J. Phys. Chem. Lett.*, 2013, **4**, 1347–1351.
229 F. Tardani, W. Neri, C. Zakri, H. Kellay, A. Colin and P. Poulin, *Langmuir*, 2018, **34**, 2996–3002.
230 C. Gómez-Navarro, R. T. Weitz, A. M. Bittner, M. Scolari, A. Mews, M. Burghard and K. Kern, *Nano Lett.*, 2007, **7**, 3499–3503.
231 L. Dong, J. Yang, M. Chhowalla and K. P. Loh, *Chem. Soc. Rev.*, 2017, **46**, 7306–7316.
232 Q. Lai, S. Zhu, X. Luo, M. Zou and S. Huang, *AIP Adv.*, 2012, **2**, 032146.
233 J. I. Parades, S. Villar-Rodil, A. Martínez-Alonso and J. M. D. Tascón, *Langmuir*, 2008, **24**, 10560–10564.
234 W. Du, M. Wu, M. Zhang, G. Xu, T. Gao, L. Qian, X. Yu, F. Chi, C. Li and G. Shi, *Chem. Commun.*, 2017, **53**, 11005–11007.
235 Viscosity, Surface Tension, Specific Density and Molecular Weight of Selected Liquids, https://www.accudynetest.com/visc_table.html.
236 S. A. Peng, Z. Jin, P. Ma, D. Y. Zhang, J. Y. Shi, J. Bin Niu, X. Y. Wang, S. Q. Wang, M. Li, X. Y. Liu, T. C. Ye, Y. H. Zhang, Z. Y. Chen and G. H. Yu, *Carbon N. Y.*, 2015, **82**, 500–505.
237 O. Orkun and H. Y. Erbil, *Surf. Topogr. Metrol. Prop.*, 2017, **5**, 024002.
238 Common Organic Solvents: Table of Properties, https://www.organicdivision.org/orig/organic_solvents.html.
239 Ohnesorge for Inkjet, https://www.stevenabbott.co.uk/practical-coatings/ohnesorge.php.
240 MEGlobal, *Ethylene Glycol Product Guide*, 2008.
241 T. L. and J. W. Peiwen Li, Cheng-An Tao, Bangyun Wang, Jian Huang, *J. Nanosci. Nanotechnol.*, 2018, **18**, 713–718.
242 P. He and B. Derby, in *Materials Research Society Symposium Proceedings*, 2014, p. 1699.
243 S. E. Zhu, S. Yuan and G. C. A. M. Janssen, *EPL*, 2014, **108**, 17007.
244 A. A. K. King, B. R. Davies, N. Noorbehesht, P. Newman, T. L. Church, A. T. Harris, J. M. Razal and A. I. Minett, *Sci. Rep.*, 2016, **6**, 19491.
245 S. Eigler, S. Grimm, M. Enzelberger-Heim, P. Müller and A. Hirsch, *Chem. Commun.*, 2013, **49**, 7391–7393.
246 A. Ferrari and J. Robertson, *Phys. Rev. B - Condens. Matter Mater. Phys.*, 2000, **61**, 14095.
247 C. Xu, X. Shi, A. Ji, L. Shi, C. Zhou and Y. Cui, *PLoS One*, 2015, **10**, 0144842.
248 P. N. Nirmalraj, T. Lutz, S. Kumar, G. S. Duesberg and J. J. Boland, *Nano Lett*, 2011, **11**, 16–22.
249 J. Kauppila, P. Kunnas, P. Damlin, A. Viinikanoja and C. Kvarnström, *Electrochim. Acta*, 2013, **89**, 84–89.

250 A. Viinikanoja, J. Kauppila, P. Damlin, M. Suominen and C. Kvarnström, *Phys. Chem. Chem. Phys.*, 2015, **17**, 12115–12123.
251 S. Y. Toh, K. S. Loh, S. K. Kamarudin and W. R. W. Daud, *Chem. Eng. J.*, 2014, **251**, 422–434.
252 H.-L. Guo, X.-F. Wang, Q.-Y. Qian, F.-B. Wang and X.-H. Xia, *ACS Nano*, 2009, **3**, 2653–2659.
253 Z. Wang, X. Zhou, J. Zhang, F. Boey and H. Zhang, *J. Phys. Chem. C*, 2009, **113**, 14071–14075.
254 S. J. An, Y. Zhu, S. H. Lee, M. D. Stoller, T. Emilsson, S. Park, A. Velamakanni, J. An and R. S. Ruoff, *J. Phys. Chem. Lett.*, 2010, **1**, 1259–1263.
255 Y. Shao, J. Wang, M. Engelhard, C. Wang and Y. Lin, *J. Mater. Chem.*, 2010, **20**, 743–748.
256 R. Alcántara, J. M. Jiménez-Mateos, P. Lavela and J. L. Tirado, *Electrochem. commun.*, 2001, **3**, 639–642.
257 L. J. Cote, R. Cruz-Silva and J. Huang, *J. Am. Chem. Soc.*, 2009, **131**, 11027–11032.
258 Y. Zhu, S. Murali, M. D. Stoller, A. Velamakanni, R. D. Piner and R. S. Ruoff, *Carbon N. Y.*, 2010, **48**, 2118–2222.
259 Y. Tu, T. Utsunomiya, T. Ichii and H. Sugimura, *J. Vac. Sci. Technol. B, Nanotechnol. Microelectron. Mater. Process. Meas. Phenom.*, 2017, **35**, 03D110.
260 D. W. Wang, K. H. Wu, I. R. Gentle and G. Q. Lu, *Carbon N. Y.*, 2012, **50**, 3333–3341.
261 H. Wang, J. T. Robinson, X. Li and H. Dai, *J. Am. Chem. Soc.*, 2009, **131**, 9910–9111.
262 S. Dubin, S. Gilje, K. Wang, V. C. Tung, K. Cha, A. S. Hall, J. Farrar, R. Varshneya, Y. Yang and R. B. Kaner, *ACS Nano*, 2010, **4**, 3845–3852.
263 G. Williams, B. Seger and P. V. Kamt, *ACS Nano*, 2008, **2**, 1487–1491.
264 S. Stankovich, D. A. Dikin, R. D. Piner, K. A. Kohlhaas, A. Kleinhammes, Y. Jia, Y. Wu, S. B. T. Nguyen and R. S. Ruoff, *Carbon N. Y.*, 2007, **45**, 1558–1565.
265 H. Liu, L. Zhang, Y. Guo, C. Cheng, L. Yang, L. Jiang, G. Yu, W. Hu, Y. Liu and D. Zhu, *J. Mater. Chem. C*, 2013, **1**, 3104–3109.
266 M. J. Fernández-Merino, L. Guardia, J. I. Paredes, S. Villar-Rodil, P. Solís-Fernández, A. Martínez-Alonso and J. M. D. Tascón, *J. Phys. Chem. C*, 2010, **114**, 6426–6432.
267 A. Kumar and M. Khandelwal, *J. Mater. Chem. A*, 2014, **2**, 20345–20357.
268 D. R. Dreyer, S. Murali, Y. Zhu, R. S. Ruoff and C. W. Bielawski, *J. Mater. Chem.*, 2011, **21**, 3443–3447.
269 Y. Wang, L. Sun and B. Fugetsu, *Bull. Chem. Soc. Jpn.*, 2012, **85**, 1339–1344.
270 G. Wang, J. Yang, J. Park, X. Gou, B. Wang, H. Liu and J. Yao, *J. Phys. Chem. B*, 2008, **112**, 8192–8195.
271 X. Fan, W. Peng, Y. Li, X. Li, S. Wang, G. Zhang and F. Zhang, *Adv. Mater.*, 2008, **20**, 4490–4493.
272 W. Gao, L. B. Alemany, L. Ci and P. M. Ajayan, *Nat. Chem.*, 2009, **1**, 403–408.

273 A. Ambrosi, C. K. Chua, A. Bonanni and M. Pumera, *Chem. Mater.*, 2012, **24**, 2292–2298.
274 D. Yang, A. Velamakanni, G. Bozoklu, S. Park, M. Stoller, R. D. Piner, S. Stankovich, I. Jung, D. A. Field, C. A. Ventrice and R. S. Ruoff, *Carbon N. Y.*, 2009, **47**, 145–152.
275 X. Gao, J. Jang and S. Nagase, *J. Phys. Chem. C*, 2010, **114**, 832–842.
276 C. K. Chua and M. Pumera, *Chem. Commun.*, 2016, **52**, 72–75.
277 D. Yang, A. Velamakanni, G. Bozoklu, S. Park, M. Stoller, R. D. Piner, S. Stankovich, I. Jung, D. A. Field, C. A. Ventrice and R. S. Ruoff, *Carbon N. Y.*, , DOI:10.1016/j.carbon.2008.09.045.
278 M. Acik, G. Lee, C. Mattevi, A. Pirkle, R. M. Wallace, M. Chhowalla, K. Cho and Y. Chabal, *J. Phys. Chem. C*, 2011, **115**, 19761–19781.
279 A. Eckmann, A. Felten, A. Mishchenko, L. Britnell, R. Krupke, K. S. Novoselov and C. Casiraghi, *Nano Lett.*, 2012, **12**, 3925–3930.
280 X. Díez-Betriu, S. Álvarez-García, C. Botas, P. Álvarez, J. Sánchez-Marcos, C. Prieto, R. Menéndez and A. De Andrés, *J. Mater. Chem. C*, 2013, **1**, 6905–6912.
281 H. Yang, Y. Cao, J. He, Y. Zhang, B. Jin, J. L. Sun, Y. Wang and Z. Zhao, *Carbon N. Y.*, 2017, **115**, 561–570.
282 H. C. Schniepp, J. L. Li, M. J. McAllister, H. Sai, M. Herrera-Alonson, D. H. Adamson, R. K. Prud'homme, R. Car, D. A. Seville and I. A. Aksay, *J. Phys. Chem. B*, 2006, **110**, 8535–8359.
283 Y. Sekimoto, R. Ohtani, M. Nakamura, M. Koinuma, L. F. Lindoy and S. Hayami, *Sci. Rep.*, 2017, **7**, 12159.
284 G. Lopez-Polin, J. Gomez-Herrero and C. Gomez-Navarro, *Nano Lett.*, 2015, **15**, 2050–2054.
285 G. Eda, G. Fanchini and M. Chhowalla, *Nat. Nanotechnol.*, 2008, **3**, 270–274.
286 M. M. Qin, W. Ji, Y. Y. Feng and W. Feng, *Chinese Phys. B*, 2014, **23**, 028103.
287 Y. Si and E. T. Samulski, *Nano Lett.*, 2008, **8**, 1679–1682.
288 D. Soltman and V. Subramanian, *Langmuir*, 2008, **24**, 2224–2231.
289 E. V. Gorb, N. Hosoda, C. Miksch and S. N. Gorb, *J. R. Soc. Interface*, 2010, **7**, 1571–1579.
290 Q. Pan, C.-C. Chung, N. He, J. L. Jones and W. Gao, *J. Phys. Chem. C*, 2016, **120**, 14984–14990.
291 H. J. Shin, K. K. Kim, A. Benayad, S. M. Yoon, H. K. Park, I. S. Jung, M. H. Jin, H. K. Jeong, J. M. Kim, J. Y. Choi and Y. H. Lee, *Adv. Funct. Mater.*, 2009, **19**, 1987–1992.
292 R. S. Rajaura, S. Srivastava, V. Sharma, P. K. Sharma, C. Lal, M. Singh, H. S. Palsania and Y. K. Vijay, *Int. J. Hydrogen Energy*, 2016, **41**, 9454–9461.
293 A. Y. Nugraheni, D. N. Jayanti, Kurniasari, S. Soontaranon, E. G. Rachman Putra and Darminto, *IOP Conf. Ser. Mater. Sci. Eng.*, 2017, **196**, 012007.
294 H. H. Huang, K. K. H. De Silva, G. R. A. Kumara and M. Yoshimura, *Sci. Rep.*, 2018, **8**, 6849.
295 L. Dong, J. Yang, M. Chhowalla and K. P. Loh, *Chem. Soc. Rev.*, 2017, **46**, 7306–7316.

296 D. Yoon, Y.-W. Son and H. Cheong, *Nano Lett.*, 2011, **11**, 3227–3231.
297 W. M. Yim and R. J. Paff, *J. Appl. Phys.*, 1974, **45**, 1456.
298 S. Ryu, L. Liu, S. Berciaud, Y. J. Yu, H. Liu, P. Kim, G. W. Flynn and L. E. Brus, *Nano Lett.*, 2010, **10**, 4944–4951.
299 X. Wei, L. Mao, R. A. Soler-Crespo, J. T. Paci, J. Huang, S. T. Nguyen and H. D. Espinosa, *Nat. Commun.*, 2015, **6**, 8029.
300 G. G. Jernigan, J. A. Nolde, N. A. Mahadik, E. R. Cleveland, J. E. Boercker, M. B. Katz, J. T. Robinson and E. H. Aifer, *J. Appl. Phys.*, 2017, **122**, 075301.
301 W. Chen and L. Yan, *Nanoscale*, 2010, **2**, 559–563.
302 V. Kampars and M. Legzdina, *IOP Conf. Ser. Mater. Sci. Eng.*, 2015, **77**, 012033.
303 H. Chen, M. B. Müller, K. J. Gilmore, G. G. Wallace and D. Li, *Adv. Mater.*, 2008, **20**, 3557–3561.
304 C. Feng, K. Liu, J. S. Wu, L. Liu, J. S. Cheng, Y. Zhang, Y. Sun, Q. Li, S. Fan and K. Jiang, *Adv. Funct. Mater.*, 2010, **20**, 885–891.
305 X. Lin, J. Jia, N. Yousefi, X. Shen and J. K. Kim, in *14th International Conference on Electronic Materials and Packaging, EMAP 2012*, 2012, p. 13485128.
306 P. Meenakshi, R. Karthick, M. Selvaraj and S. Ramu, *Sol. Energy Mater. Sol. Cells*, 2014, **128**, 264–269.
307 J. B. Gilbert, M. F. Rubner and R. E. Cohen, *Proc. Natl. Acad. Sci. U. S. A.*, 2013, **110**, 6651–6656.
308 C. Mattevi, G. Eda, S. Agnoli, S. Miller, K. A. Mkhoyan, O. Celik, D. Mastrogiovanni, G. Granozzi, E. Carfunkel and M. Chhowalla, *Adv. Funct. Mater.*, 2009, **19**, 2577–2583.
309 M. Fan, C. Zhu, Z. Q. Feng, J. Yang, L. Liu and D. Sun, *Nanoscale*, 2014, **6**, 4882–4888.
310 Y. E. Shin, Y. J. Sa, S. Park, J. Lee, K. H. Shin, S. H. Joo and H. Ko, *Nanoscale*, 2014, **6**, 9734–9741.
311 L. Dong, J. Yang, M. Chhowalla and K. P. Loh, *Chem. Soc. Rev.*, 2017, **46**, 7306–7316.
312 S. Park, Y. Hu, J. O. Hwang, E. S. Lee, L. B. Casabianca, W. Cai, J. R. Potts, H. W. Ha, S. Chen, J. Oh, S. O. Kim, Y. H. Kim, Y. Ishii and R. S. Ruoff, *Nat. Commun.*, 2012, **3**, 638.
313 O. Akhavan, *Carbon N. Y.*, 2010, **48**, 509–519.
314 A. Bhaumik, A. Haque, M. Taufique, P. Karnati, R. Patel, M. Nath and K. Ghosh, *J. Mater. Sci. Eng.*, 2017, **6**, 1000364.
315 S. Drewniak, R. Muzyka, A. Stolarczyk, T. Pustelny, M. Kotyczka-Morańska and M. Setkiewicz, *Sensors*, 2016, **16**, 103.
316 S. Y. Huang, B. Zhao, K. Zhang, M. M. F. Yuen, J. Bin Xu, X. Z. Fu, R. Sun and C. P. Wong, *Sci. Rep.*, 2015, **5**, 14260.
317 A. Ferrari and J. Robertson, *Phys. Rev. B - Condens. Matter Mater. Phys.*, 2000, **61**, 14095–14107.
318 R. Shroder, R. Nemanich and J. Glass, *Phys. Rev. B*, 1990, **41**, 3738–3745.
319 M. S. Dresselhaus, A. Jorio, A. G. Souza Filho and R. Saito, *Philos. Trans. R.*

Soc. A Math. Phys. Eng. Sci., 2010, **368**, 5355–5377.
320 A. A. K. King, B. R. Davies, N. Noorbehesht, P. Newman, T. L. Church, A. T. Harris, J. M. Razal and A. I. Minett, *Sci. Rep.*, 2016, **6**, 19491.
321 J. E. Proctor, E. Gregoryanz, K. S. Novoselov, M. Lotya, J. N. Coleman and M. P. Halsall, *Phys. Rev. B*, 2009, **80**, 073408.
322 Z. Ni, Y. Wang, T. Yu and Z. Shen, *Nano Res.*, 2010, **1**, 273–291.
323 R. He, L. Zhao, N. Petrone, K. S. Kim, M. Roth, J. Hone, P. Kim, A. Pasupathy and A. Pinczuk, *Nano Lett.*, 2012, **12**, 2408–2413.
324 N. D. K. Tu, J. Choi, C. R. Park and H. Kim, *Chem. Mater.*, 2015, **27**, 7362–7369.
325 B. Tang, H. Guoxin and H. Gao, *Appl. Spectrosc. Rev.*, 2010, **45**, 369–407.
326 R. J. Nemanich and S. A. Solin, *Phys. Rev. B*, 1979, **20**, 392–401.
327 A. A. Dubale, W.-N. Su, A. G. Tamirat, C.-J. Pan, B. A. Aragaw, H.-M. Chen, C.-H. Chen and B.-J. Hwang, *J. Mater. Chem. A*, 2014, **2**, 18383–18397.
328 K. N. Kudin, B. Ozbas, H. C. Schniepp, R. K. Prud'homme, I. A. Aksay and R. Car, *Nano Lett.*, 2008, **8**, 36–41.
329 A. Wróblewska, A. Dużyńska, J. Judek, L. Stobiński, K. Zerańska, A. P. Gertych and M. Zdrojek, *J. Phys. Condens. Matter*, 2017, **29**, 475201.
330 L. G. Cançado, A. Jorio, E. H. M. Ferreira, F. Stavale, C. A. Achete, R. B. Capaz, M. V. O. Moutinho, A. Lombardo, T. S. Kulmala and A. C. Ferrari, *Nano Lett.*, 2011, **11**, 3190–3196.
331 E. H. Martins Ferreira, M. V. O. Moutinho, F. Stavale, M. M. Lucchese, R. B. Capaz, C. A. Achete and A. Jorio, *Phys. Rev. B - Condens. Matter Mater. Phys.*, 2010, **82**, 125429.
332 H. A. Becerril, R. M. Stoltenberg, D. R. Wheeler, R. C. Davis, J. N. Harb and A. T. Woolley, *J. Am. Chem. Soc.*, 2005, **127**, 2828–2829.
333 C. F. Monson and A. T. Woolley, *Nano Lett.*, 2003, **3**, 359–363.
334 J. Su, F. Gao and L. Hou, *Mater. Lett.*, 2013, **92**, 206–209.
335 W. U. Dittmer and F. C. Simmel, *Appl. Phys. Lett.*, 2004, **85**, 633–635.
336 H. D. A. Mohamed, S. M. D. Watson, B. R. Horrocks and A. Houlton, *Nanoscale*, 2012, **4**, 5936–5945.
337 S. N. Sarangi, S. Rath, K. Goswami, S. Nozaki and S. N. Sahu, *Phys. E Low-Dimensional Syst. Nanostructures*, 2010, **42**, 1670–1674.
338 H. D. A. Mohamed, S. M. D. Watson, B. R. Horrocks and A. Houlton, *J. Mater. Chem. C*, 2015, **3**, 438–446.
339 E. Braun, Y. Eichen, U. Sivan and G. Ben-Yoseph, *Nature*, 1998, **391**, 775–778.
340 H. Yan, S. H. Park, G. Finkelstein, J. H. Reif and T. H. LaBean, *Science (80-.).*, 2003, **301**, 1882–1884.
341 M. Mertig, L. C. Ciacchi, R. Seidel, W. Pompe and A. De Vita, *Nano Lett.*, 2002, **2**, 841–844.
342 Y. Ma, J. Zhang, G. Zhang and H. He, *J. Am. Chem. Soc.*, 2004, **126**, 7097–7101.
343 J. Liu, B. Uprety, S. Gyawali, A. T. Woolley, N. V. Myung and J. N. Harb, *Langmuir*, 2013, **29**, 11176–11184.

344 C. M. Phan and H. M. Nguyen, *J. Phys. Chem. A*, 2017, **121**, 3213–3219.
345 G. Van Der Snickt, J. Dik, M. Cotte, K. Janssens, J. Jaroszewicz, W. De Nolf, J. Groenewegen and L. Van Der Loeff, *Anal. Chem.*, 2009, **81**, 2600–2610.
346 W. G. Huckle, G. F. Swigert and S. E. Wiberley, *Ind. Eng. Chem. Prod. Res. Dev.*, 1966, **5**, 362–366.
347 Y. J. Yuan, D. Chen, Z. T. Yu and Z. G. Zou, *J. Mater. Chem. A*, 2018, **6**, 11606–11630.
348 A. Gaiardo, B. Fabbri, V. Guidi, P. Bellutti, A. Giberti, S. Gherardi, L. Vanzetti, C. Malagù and G. Zonta, *Sensors (Switzerland)*, 2016, **16**, 296.
349 O. Roslyak and A. Piryatinski, *J. Appl. Phys.*, 2016, **3**, 1600524.
350 F. Güell, P. R. Martínez-Alanis, S. Khachadorian, R. R. Zamani, A. Franke, A. Hoffmann, M. R. Wagner and G. Santana, *Mater. Res. Express*, 2016, **3**, 025010.
351 T. Ye, L. Jun, L. Kun, W. Hu, C. Ping, D. Ya-Hui, C. Zheng, L. Yun-Fei, W. Hao-Ran and D. Yu, *Org. Electron. physics, Mater. Appl.*, 2017, **41**, 179–185.
352 M. Xie, H. Lu, L. Zhang, J. Wang, Q. Luo, J. Lin, L. Ba, H. Liu, W. Shen, L. Shi and C.-Q. Ma, *Sol. RRL*, 2018, **2**, 1–10.
353 A. Chiolerio, S. Bocchini, F. Scaravaggi, S. Porro, D. Perrone, D. Beretta, M. Caironi and C. Fabrizio Pirri, *Semicond. Sci. Technol.*, 2015, **30**, 104001.
354 D. L. Daniels, J. R. de Wet and F. R. Blattner, *J. Virol.*, 1980, **33**, 390–400.
355 R. K. Duchaniya, *Int. J. Mining, Metall. Mech. Eng.*, 2014, **2**, 54–56.
356 M. T. Walsh and X. Huang, *Nucleic Acids Res.*, 2017, **45**, e175.
357 S. Engelen, S. F. Møller and M. Hubert, *Chemom. Intell. Lab. Syst.*, 2007, **86**, 35–51.
358 N. Chestnoy, T. D. Harris, R. Hull and L. E. Brus, *J. Phys. Chem.*, 1986, **90**, 3393–3399.
359 W. J. Danaher, L. E. Lyons, M. Marychurch and G. C. Morris, *Appl. Surf. Sci.*, 1986, **27**, 338–354.
360 D. M. Poirier and J. H. Weaver, *Surf. Sci. Spectra*, 1993, **2**, 249.
361 A. Roche, H. Montes, J. Brissot, M. Romand, P. Josseaux and A. K. De Mesmaeker, *Appl. Surf. Sci.*, 1985, **21**, 12.
362 S. Ptasińska, A. Stypczyńska, T. Nixon, N. J. Mason, D. V. Klyachko and L. Sanche, *J. Chem. Phys.*, 2008, **129**, 065102.
363 G. Mattogno, C. Ferragina, M. A. Massucci, P. Patrono and A. La Ginestra, *J. Electron Spectros. Relat. Phenomena*, 1988, **46**, 285–295.
364 J. Marmur and P. Doty, *J. Mol. Biol.*, 1962, **5**, 109–118.
365 B. Porsch, R. Laga, J. Horský, Č. Koňák and K. Ulbrich, *Biomacromolecules*, 2009, **10**, 3148–3150.
366 L. Daasch and D. Smith, *Anal. Chem.*, 1951, **23**, 853–868.
367 D. M. Adams and J. B. Cornell, *J. Chem. Soc. A Inorganic, Phys. Theor. Chem.*, 1967, 884–889.
368 R. P. Lopes, R. Valero, J. Tomkinson, M. P. M. Marques and L. A. E. Batista de Carvalho, *New J. Chem.*, 2013, **37**, 2691--2699.
369 C. Yamahata, D. Collard, T. Takekawa, M. Kumemura, G. Hashiguchi and H. Fujita, *Biophys. J.*, 2008, **94**, 63–70.

370 J. Li, C. Bai, C. Wang, C. Zhu, Z. Lin, Q. Li and E. Cao, *Nucleic Acids Res.*, 1998, **26**, 4785–4786.
371 M. Zahn, Y. Ohki, D. B. Fenneman, R. J. Gripshover and V. H. Gehman, *Proc. IEEE*, 1986, **74**, 1182–1221.
372 D. B. Fenneman, *J. Appl. Phys.*, 1982, **53**, 8961–8968.
373 MEGlobal, Ethylene Glycol Product Guide, http://www.meglobal.biz/media/product_guides/MEGlobal_MEG.pdf.
374 M. Klenk, O. Schenker, U. Probst and E. Bucher, *Sol. Energy Mater. Sol. Cells*, 1999, **58**, 299–319.
375 R. D. Deegan, O. Bakajin, T. F. Dupont, G. Huber, S. R. Nagel and T. A. Witten, *Nature*, 1997, **389**, 827–829.
376 Y. Ooi, I. Hanasaki, D. Mizumura and Y. Matsuda, *Sci. Technol. Adv. Mater.*, 2017, **18**, 316–324.
377 R. A. Leese and E. L. Wehry, *Anal. Chem.*, 1978, **50**, 1193–1197.
378 R. A. Erb, *J. Phys. Chem.*, 1965, **69**, 1306–1309.
379 D. H. Prajitno, A. Maulana and D. G. Syarif, in *Journal of Physics: Conference Series*, 2016, p. 739 012029.
380 M. H. Zhao, X. P. Chen and Q. Wang, *Sci. Rep.*, 2014, **4**, 5376.
381 R. S. Crandall, *Phys. Rev.*, 1968, **169**, 577–584.
382 H. Elhadidy, J. Sikula and J. Franc, *Semicond. Sci. Technol.*, 2012, **27**, 015006.
383 S. Nandy, G. Gonçalves, J. V. Pinto, T. Busani, V. Figueiredo, L. Pereira, R. F. Paiva Martins and E. Fortunato, *Nanoscale*, 2013, **5**, 11699–11709.
384 F. Raissi and R. Farivar, *Appl. Phys. Lett.*, 2005, **87**, 164101.
385 V. Simakov, O. Yakusheva, A. Grebennikov and V. Kisin, *Sensors Actuators, B Chem.*, 2006, **31**, 339–340.
386 S. Pitcher, J. A. Thiele, H. Ren and J. F. Vetelino, *Sensors Actuators, B Chem.*, 2003, **93**, 454–462.
387 H. Mitsuhashi, *J. Phys. Chem. Solids*, 1961, **22**, 223–226.